

Multi-mode Two-dimensional Infrared Spectroscopy of Peptides and Proteins

by

Lauren P. DeFlores

B.A. Cornell University, 2002

Submitted to the Department of Chemistry
in partial fulfillment of the requirements for the degree of

Doctor of Philosophy

at the

MASSACHUSETTS INSTITUTE OF TECHNOLOGY

February 2008

© 2008 Massachusetts Institute of Technology. All rights reserved.

Signature of Author.....

Department of Chemistry
February 25, 2008

Certified by.....

Andrei Tokmakoff
Professor of Chemistry
Thesis Supervisor

Accepted by.....

Robert W. Field
Haslam And Dewey Professor Of Chemistry
Chairman, Departmental Committee on Graduate Students

This doctoral thesis has been examined by a Committee of the Department of Chemistry that included,

Professor Robert G. Griffin.....
Thesis Chair

Professor Robert W. Field.....

Professor Andrei Tokmakoff.....
Thesis Supervisor

Multi-mode Two-dimensional Infrared Spectroscopy of Peptides and Proteins

by

Lauren P. DeFlores

Submitted to the Department of Chemistry
on February, 2008 in partial fulfillment of the
requirements for the degree of
Doctor of Philosophy

Abstract

In this thesis, a methodology for understanding structural stability of proteins through multi-mode two-dimensional infrared (2D IR) spectroscopy is developed. The experimental framework for generation of broadband infrared lasers and robust new approaches to 2D IR spectroscopy are demonstrated. Long-term phase stability is achieved through the development of a passively stabilized diffractive optic and wedge interferometer. A new approach for acquisition of 2D IR spectra in the pump-probe geometry reduces overall experimental complexity. These technological advances extend the capabilities of 2D IR to further resolve inter- and intramolecular couplings, relaxation pathways and structural kinetics in complex systems. Characterization of multi-mode spectra is first performed on model protein systems to reveal detailed information on the effects of solvation and structure on the amide vibrations. Differences in vibrational coupling, transition dipole angles and the anharmonic potential of the amide vibrations of isotopologues of *N*-methylacetamide arise from significant change in the local mode composition of the amide II band due to isotopic substitution of the peptide group. Extension of multi-mode 2D IR to study the amide I'-II' spectra of an ideal protein system, poly-L-lysine, provides direct evidence for the structural sensitivity of the amide II' vibration, particularly to the α -helix moiety. This structural sensitivity arises from through bond coupling and structure induced symmetry and orientation of adjacent residues. Integration of these tools with hydrogen exchange techniques allows for the protein structural kinetics and stability to be observed through protein-solvent interactions with enhanced structural sensitivity relative to amide I spectroscopy alone. The amide II' diagonal provides a measure of the degree of exchange and the cross peaks between the structurally sensitive amide I/I' vibration and the solvent exposure sensitive amide II and II' modes reveal the location of exchange. Partial exchange of the secondary structure of ubiquitin is revealed by correlation of the different amide signatures through analysis of cross peak line shapes, positions and amplitudes. Results provide direct evidence for a highly stable helix and labile β -sheet structure.

Thesis Supervisor: Andrei Tokmakoff
Title: Professor of Chemistry

To

*those that inspire
and
never doubt what **one** can do...*

Acknowledgements

I would like to thank Andrei, my advisor, for always inspiring me to be a better experimentalist and scientist. To a wonderful group of friends and colleagues in the Tokmakoff group; Adam, Anne, Becky, Ben, Hoi Sung, Josh, Kevin, Krupa, Poul, Sean, and Ziad. For all of their endless listening. To Matt and Joe for their guidance and friendship. To all of those that supported me along the way. Thank you.

And my infinite thanks...

To the one I will experience the world with, my best friend and the source of consistent calmness and patience in my life. Only forever to go. To the one who is always there and for whom I could not be *me* without. To the one that just wants to know if I am happy? Yes. To the two that keep me in check and I could not imagine this world without. To my girls who's little faces keep me company. To my other *sister*. And to my furry kids who always keep me smiling.

Table of Contents

List of Figures.....	10
List of Tables	22
1. Introduction.....	23
1.1 Multidimensional Spectroscopy.....	24
1.1.1 Multi-Mode Vibrational Spectroscopy of Proteins and Peptides.....	25
1.2 Experimental Considerations for Multi-mode 2D IR Spectroscopy.....	28
1.2.1 Phase Stability.....	29
1.2.2 Phasing.....	30
1.3 Thesis Outline.....	31
References.....	35
2. Passively Stabilized Two-dimensional Infrared Spectroscopy using a Diffractive Optic and Wedge Interferometer.....	39
2.1 Experimental Design.....	41
2.1.1 Diffractive Optics.....	43
2.1.2 ZnSe Wedges and Pulse Timing.....	44
2.1.3 System Alignment.....	46
2.1.4 Stage Calibration.....	49
2.1.5 Fast Scanning.....	51
2.1.6 Improved Heterodyned Detection using a Hollow Waveguide.....	52
2.1.7 Array Calibration.....	53
2.2 Passively Stabilized Two Dimensional Infrared Spectroscopy.....	54
2.3 Conclusion.....	57
References.....	59
3. Two-dimensional Infrared Spectroscopy in the Pump-Probe Geometry .	61
3.1 Traditional 2D FT versus 2D FT in the Pump-Probe Geometry.....	63
3.2 The 2D FT Spectrometer.....	65
3.3 Results.....	70
Conclusion.....	77
References.....	78
4. The Anharmonic Vibrational Potential and Relaxation Pathways of the Amide I and II Modes of <i>N</i> -methylacetamide.....	81
4.1 Introduction.....	81

4.2	Amide I/II 2D IR Spectroscopy	84
4.3	Results.....	86
4.4	Discussion.....	93
4.4.1	The Anharmonic Potential and Vibrational Couplings.....	93
4.4.2	Vibrational Relaxation	95
4.4.3	Transition Dipole Orientation and Amide Mode Composition.....	100
4.5	Conclusion	107
	References.....	109
5.	Secondary Structural Sensitivity of the Amide II' Vibration of Proteins	113
5.1	Introduction.....	113
5.2	Experimental	118
5.3	Linear Spectroscopy of the Amide Fingerprint Region.....	119
5.4	2D IR Spectroscopy of Amide II'	120
5.4.1	Amide I' and II' Diagonal Resonances of Poly-L-lysine.....	120
5.4.2	Amide I'-II' Cross Peaks of Poly-L-lysine	124
5.5	Model Calculations of the Amide II' Sensitivity to Secondary Structure.....	129
5.5.1	Local Amide Hamiltonian.....	130
5.5.2	Doorway Mode Analysis.....	137
5.6	Amide II' Spectroscopy of Globular Proteins.....	140
5.6.1	Myoglobin	141
5.6.2	Ubiquitin.....	143
5.7	Conclusion	145
	References.....	147
6.	Side Chain Absorptions in the Amide Finger Print Region of Proteins. 149	
6.1	Two-Dimensional Infrared Spectroscopy of Protein Side Chains	149
6.1.1	Aspartic Acid.....	151
6.1.2	Tyrosine.....	153
6.1.3	Arginine.....	154
6.2	Side Chain Absorptions seen in FTIR Spectroscopy of Proteins and Hairpins. 155	
	References.....	166
7.	Hydrogen-Deuterium Exchange FTIR of Ubiquitin.....	167
7.1	Background: Hydrogen-Deuterium Exchange.....	167
7.1.1	Hydrogen Exchange Chemistry.....	170
7.1.2	Linderstrom-Lang Steady State Theory of HX Kinetics	174
7.1.3	Mechanism of Hydrogen Exchange in Proteins	178
7.2	Hydrogen-Deuterium Exchange Kinetics of Ubiquitin: An FTIR Study	185
7.2.1	Temperature Dependent Hydrogen Exchange.....	186
7.2.2	Time Dependence of Hydrogen Exchange.....	189
7.3	Conclusion	196
	References.....	198

8. Hydrogen Exchange Multi-Mode Two-Dimensional Infrared (2D IR) Spectroscopy	201
8.1 Equilibrium Hydrogen Exchange Two-dimensional Infrared Spectroscopy.....	201
8.1.1 Amide I/II HX Spectroscopy.....	203
8.1.2 Amide I/II/II' HX Spectroscopy.....	212
8.2 Looking Forward.....	227
References.....	231
Appendix 1: Wedges.....	233
Curriculum Vitae.....	237

List of Figures

Fig. 1.1.1.1 Representations of double-resonance 2D IR spectroscopy (top), dual-frequency Fourier transform 2D IR spectroscopy (middle) and multi-mode Fourier transform 2D IR spectroscopy (bottom).	27
Fig. 2.1.1.1 3D layout of the diffractive optic interferometer using ZnSe wedge delay lines for intrinsically phased match 2D IR spectroscopy.	42
Fig. 2.1.2.1 Illustration of wedge pair and the design parameters presented in Eq. 2-4... 45	
Fig. 2.1.3.1 Alignment procedure for diffractive optic and wedge set up. The image to the right of the second spherical mirror shows the end on view of the HeNe spot.	47
Fig. 2.1.3.2 Rotation of the box (red Gaussian beams) for free translation of the wedges (orange).	48
Fig. 2.1.3.3 Alignment procedure for ZnSe wedges.	49
Fig. 2.1.4.1 (Top) Experimental set up for stage calibration depicting a second diffractive optic in the sample position. (Bottom) Acquired spectral interferogram versus time delay, the Fourier transformed spectrum and extracted phase.	50
Fig. 2.1.7.1 (Top) Experimental set up for array calibration using non-resonant response of a ZnSe window at the sample position. (Bottom) Depicts collection of the array as a function of time. Each pixel is independently Fourier transformed to give frequency calibration.	53
Fig. 2.2.1.1 2D IR step scan spectra of methyl methacrylate in acetonitrile and ethanol. 55	
Fig. 2.2.1.2 (Left) 2D IR surface of an idealized helical homopolymers of PBG in CDCl ₃ . The 20 average surface is plotted with 5 times more contours between +/-10%. (Right) Rephasing and non-rephasing time traces at $\omega_3 = 1735 \text{ cm}^{-1}$ are shown. Significant improvement in SNR is observed.	56

Fig. 3.1.1.1 Experimental geometry of traditional 2D IR Spectroscopy and the experimental unknowns and constraints intrinsic to the set up.....	64
Fig. 3.2.1.1 Experimental geometry of 2D FT Spectroscopy in the pump-probe geometry and the experimental unknowns and constraints intrinsic to the set up. Spectral detection is required for acquisition of correlation spectrum.	66
Fig. 3.2.1.2 Experimental set up of 2D IR spectrometer, including acquisition of 2D spectra (A), interferometric autocorrelation (B) and stage calibration (C).....	67
Fig. 3.2.1.3 Flow chart of stage calibration and acquisition and phasing of a 2D FT spectrum.....	69
Fig. 3.3.1.1 2D FT spectrum of RDC in hexane showing the polarization selectivity and the 2D FT waiting time series of RDC in CDCl ₃	71
Fig. 3.3.1.2 ZZZZ and ZZYY 2D IR waiting time series of RDC in CDCl ₃ . Bottom panel is the integrated area of the ZZZZ cross peak region versus waiting time.....	73
Fig. 3.3.1.3 ZZZZ and ZZYY 2D IR waiting time series of RDC in hexane.....	74
Fig. 3.3.1.4 ZZYY 2D FT spectrum of concanavalin A.	75
Fig. 3.3.1.5 Experimental set up for 2-Color 2D FT spectrometer with modification from the current experimental design.	76
Fig. 4.3.1.1 FTIR spectra of NMA-h ₇ (dot-dashed), NMA-d ₇ (solid) and NMA-d ₁ (dashed) in DMSO-d ₆ , CDCl ₃ , and D ₂ O. Prime denotes amide vibration with a deuterated amide group.....	87
Fig. 4.3.1.2 Experimental absorptive 2DIR spectrum of NMA-d ₇ /D ₂ O obtained at $\tau_2 = 80$ fs for parallel (a) and perpendicular (c) polarization, and for NMA-h ₇ /DMSO-d ₆ (e,g). Corresponding fits, (b,d) and (f,h) respectively, are plotted to their right. For each normalized amide I spectrum, twenty-six equally spaced contours are plotted from $\pm 60\%$ for NMA-d ₇ /D ₂ O and from $\pm 30\%$ for NMA-h ₇ /DMSO-d ₆ . The fit	

parameters of NMA-d₇/D₂O for the six level system are $\omega_{AI'} = 1598 \text{ cm}^{-1}$, $\omega_{AII'} = 1495 \text{ cm}^{-1}$, $\Delta_{AI'} = 15 \text{ cm}^{-1}$, $\Delta_{AII'} = 11 \text{ cm}^{-1}$, $\Delta_{AI',AII'} = 11 \text{ cm}^{-1}$, $\mu_{AI'} = 1$, $\mu_{AII'} = 0.58$, $\mu_{2AI',AI'} = 1.51(1.41)$, $\mu_{2AII',AII'} = 0.68 (0.82)$, $\mu_{AI',AII'} = 1.0 (1.0)$, $\mu_{AII', AI'} = 0.58 (0.58)$, and $\Theta = 75^\circ$. For NMA-h₇/DMSO-d₆ the fit parameters are $\omega_{AI} = 1665 \text{ cm}^{-1}$, $\omega_{AII} = 1555 \text{ cm}^{-1}$, $\Delta_{AI} = 12 \text{ cm}^{-1}$, $\Delta_{AII} = 10 \text{ cm}^{-1}$, $\Delta_{AI,AII} = 3.8 \text{ cm}^{-1}$, $\mu_{AI} = 1$, $\mu_{AII} = 0.84$, $\mu_{2AI,AI} = 1.41 (1.41)$, $\mu_{2AII,AII} = 1.09 (1.19)$, $\mu_{AI,AII} = 0.98 (1.0)$, $\mu_{AII,AI} = 0.84 (0.84)$, and $\Theta = 40^\circ$. ω is the vibrational frequency, Δ is the anharmonicity and μ is the transition moment amplitude. Harmonic scaling values are given by parentheses. 88

Fig. 4.3.1.3 Magic-angle broadband dispersed pump-probes detected at the amide I and II frequencies. Amide I detected signals (top) are shown with a bi-exponential fit with time scales of 0.38 and 2.1 ps for NMA-d₇/D₂O and 0.43 and 2.1 ps for NMA-h₇/DMSO-d₆. The amide II detected signals (bottom) are shown with a fit to a damped cosine plus bi-exponential. The beats have a period of 0.38 ps and damp with time scales of approximately 0.15 and 0.30 ps for NMA-d₇/D₂O and NMA-h₇/DMSO-d₆. The long time tails of are 5.2 ps and 3.3 ps for the respective systems. 90

Fig. 4.3.1.4 Integrated resonances of absolute value rephasing spectrum along τ_2 are plotted for the diagonal and cross peak regions of NMA-d₇/D₂O and NMA-h₇/DMSO-d₆. Diagonal resonances refer to the amide I and II modes and are fit to bi-exponentials. The amide II to I (upward) cross peak and amide I to II (downward) cross peak are fit to a damped cosine plus bi-exponential..... 91

Fig. 4.3.1.5 Time series of the magic angle absolute value rephasing spectra of NMA-h₇ in DMSO-d₆ scaled to the amide I dispersed pump-probe decay. Thirteen contour levels plotted from 0 to 30% of the normalized projected amide I peak. Time series of the magic angle absolute value rephasing spectra of NMA-d₇ in D₂O scaled to the amide I dispersed pump-probe decay. Thirteen contour levels plotted from 0 to 60% of the normalized projected amide I peaks. 92

Fig. 4.4.2.1 Vibrational relaxation pathway of the amide I and II vibrations.	97
Fig. 4.4.2.2 Amide A spectrum of NMA-h ₇ in CDCl ₃ including free and hydrogen bound NH.	99
Fig. 4.4.3.1 Hydrogen bonding environment of NMA in DMSO-d ₆ and D ₂ O including the dominant contributions to the vibrational modes and the angles of the transition dipole moments relative to the CO bond.	103
Fig. 4.4.3.2 (Top, Middle) Normal mode displacements of the amide I and II vibrational bands of NMA-d ₇ in the gas phase. (Bottom) The amide I/II transition dipole angles for NMA-d ₇ /D ₂ O (blue dashed arrow) and NMA-h ₇ in DMSO-d ₆ (black solid arrow) where Θ defines the experimentally determined angle from the polarization 2DIR spectra given in Table 4.4.3.1.	104
Fig. 4.4.3.3 FTIR spectra (top), parallel (middle) and perpendicular (bottom) absorptive 2DIR spectrum of NMA-h ₇ in CDCl ₃ and NMA-d ₁ in D ₂ O at $\tau_2 = 0$ fs. Twenty-six equally spaced contours are plotted from $\pm 25\%$ for NMA-h ₇ /CDCl ₃ and from $\pm 50\%$ for NMA-d ₁ /D ₂ O of the normalized amide I spectral amplitude.	106
Fig. 5.1.1.1 The unit cell of the AP β sheet contains for amide groups. The position and orientation of the amide I' (red) and amide II' (blue) transition dipole moments are also pictured.	114
Fig. 5.3.1.1 FTIR spectra of poly-L-lysine as a function of pH and temperature of preparation showing the β -sheet (pH=12, T=46°C), α -helix (pH=12, T<20°C) and random coil (pH=4, T=20°C) form of the homopolymer.	120
Fig. 5.4.1.1 FTIR and ZZZZ and ZZZY Amide I' 2D IR spectra of poly-L-lysine as a function of pH and temperature of preparation showing the β -sheet (pH=12, T=46°C), α -helix (pH=12, T<20°C) and random coil (pH=4, T=20°C) form of the polypeptide.	121

- Fig. 5.4.1.2 FTIR and ZZZZ and ZZYY Amide II' 2D IR spectra of poly-L-lysine as a function of pH and temperature of preparation showing the β -sheet (pH=12,T=46°C), α -helix (pH=12,T<20°C) and random coil (pH=4,T=20°C)..... 122
- Fig. 5.4.2.1 ZZZZ and ZZYY Amide I'-II' 2D IR spectra of poly-L-lysine as a function of pH and temperature of preparation showing the β -sheet (pH=12,T=46°C), α -helix (pH=12,T<20°C) and random coil (pH=4,T=20°C) forms..... 126
- Fig. 5.4.2.2 (a,b) FTIR of the amide II' and amide I' regions of PLL. (c,d) Projection along ω_1 of the diagonal peaks of amide II' (1420-1500 cm^{-1}) and amide I' (1600-1700 cm^{-1}). (e,f) Projections of the downward (amide I'-II') and upward (amide II'-I') 2D IR cross peaks. Distinct signatures for the α -helix and random coil are seen in both the diagonal (c) and cross peaks (e) of the amide II' 2D projections..... 128
- Fig. 5.5.1.1 Pictorial representation of the Local Amide I'-II' Hamiltonian for an α helix. The amide I' block contains through space coupling depicted by n+1 diagonal elements. The amide II' block (red) only contains nearest neighbor couplings. 132
- Fig. 5.5.1.2 Comparison of calculated FTIR and 2D spectra comparing coupling effects. Amide I'-II' on-site coupling induces a shift in the peak frequency of 6 cm^{-1} while nearest neighbor coupling splits the vibrational mode. 133
- Fig. 5.5.1.3 Calculated FTIR and Amide I'/II' 2D IR spectra of AP β sheet, α helix and random coil in both ZZZZ and ZZYY polarization. 134
- Fig. 5.5.1.4 Comparison of the calculated and experimental ZZYY 2D IR spectra. Projections of the β sheet, α helix and random coil of the amide II' diagonal (1420-1500 cm^{-1}) and the amide I'-II' downward cross peak (1600-1700 cm^{-1}). Projections show identical band structures with inclusion of negative nearest neighbor couplings. 135
- Fig. 5.5.1.5 Calculated size-dependence of the FTIR spectra for the idealized β -sheet (top) and β -hairpin (middle). N represents the number of unit cells in the calculation.

(Bottom) Frequency dependence of the most intense amide II' and I' modes vs. N.
 137

Fig. 5.5.2.1 (Top) Amide II' β -sheet and α -helix doorway modes of idealized systems. The visualization map has hydrogen bonded oscillators (n and $n+3$ for the α helix) aligned vertically. (Bottom) Relationship of the amide I' and II' transition dipole (eigenstates) relative to the secondary structure axis. For each mode, the frequency range of the doorway mode is given (for single frequencies the angle of the eigenstates is used), the dipole moment intensity and the angle relative to the +Y (for β -sheet) and +Z (for α -helix). Note that coordinate arrows represent the direction of residue addition. 138

Fig. 5.6.1.1 ZZZY 2D IR Spectra of myoglobin at pH =7 at T = 10°C before (Left) and after (Right) being heated to above the unfolding temperature (T = 80°C). Heated spectra shows aggregation of myoglobin into AP β sheet..... 141

Fig. 5.6.1.2 Projection along ω_1 axis of ZZZY 2D IR Spectra of myoglobin at pH =7 at T = 10°C before (Black) and after (Red) being heated to above the unfolding temperature (T = 80°C). Heated spectra shows aggregation of myoglobin into AP β -sheet in the amide I' diagonal (top), amide II' diagonal (middle) and amide I'-II' downward cross peaks (bottom) projections..... 142

Fig. 5.6.2.1 Temperature dependent Amide II' 2D IR spectra and projections of ubiquitin at T = 5°C (red), 20°C (blue), and 80°C(black)..... 144

Fig. 6.1.1.1 FTIR and 2DIR spectra showcasing the aspartic acid side chain absorption in ubiquitin, concanavalin A and myoglobin. 152

Fig. 6.1.2.1 FTIR and 2DIR spectrum of ribonuclease A exhibiting the tyrosine absorption at 1515 cm^{-1} 153

Fig. 6.1.3.1 FTIR and 2D IR spectra of ubiquitin and lysozyme that show the symmetric and asymmetric stretch of the guanidyl group of the arginine side chain. 154

- Fig. 6.1.3.2 Position and structure of the guanidyl group in ubiquitin. The guanidinium groups are fully exchanged due to solvent exposure of the protein. The stick spectra shown under the FTIR represent the position of the side chains in D₂O (top) and H₂O (bottom) at pH=1. 155
- Fig. 6.2.1.1 (Top) Atomic structures of predominant side chains in the amide finger region. (Bottom) Stick plots of side chain absorption from Table 1 in the amide finger print region as a function of solvent and pH. Major changes occur due to the protonation state of ASP, GLU and HIS. Isotopic sensitivity of the vibrational absorption is seen in TRP, ARG, GLU and ASP. 157
- Fig. 6.2.1.2 FTIR of concanavalin A at pH = 9 (pH>pK_a) and pH = 1 (pH<pK_a) and the corresponding side chain stick plots from Table 1. Intensities of stick plots are given side chain are scaled relative to the total number of amide I oscillators in the protein assuming an amide I extinction coefficient of 300 M⁻¹cm⁻¹. 158
- Fig. 6.2.1.3 FTIR of ribonuclease A at pH = 9 (pH>pK_a) and pH = 1 (pH<pK_a) and the corresponding side chain stick plots from Table 1. Intensities of stick plots are given side chain are scaled relative to the total number of amide I oscillators in the protein assuming an amide I extinction coefficient of 300 M⁻¹cm⁻¹. 159
- Fig. 6.2.1.4 FTIR of ubiquitin at pH = 9 (pH>pK_a) and pH = 1 (pH<pK_a) and the corresponding side chain stick plots from Table 1. Intensities of stick plots are given side chain are scaled relative to the total number of amide I oscillators in the protein assuming an amide I extinction coefficient of 300 M⁻¹cm⁻¹. 160
- Fig. 6.2.1.5 FTIR of lysozyme at pH = 9 (pH>pK_a) and pH = 1 (pH<pK_a) and the corresponding side chain stick plots from Table 1. Intensities of stick plots are given side chain are scaled relative to the total number of amide I oscillators in the protein assuming an amide I extinction coefficient of 300 M⁻¹cm⁻¹. 161
- Fig. 6.2.1.6 FTIR of myoglobin at pH = 9 (pH>pK_a) and pH = 1 (pH<pK_a) and the corresponding side chain stick plots from Table 1. Intensities of stick plots are given

side chain are scaled relative to the total number of amide I oscillators in the protein assuming an amide I extinction coefficient of $300 \text{ M}^{-1}\text{cm}^{-1}$	162
Fig. 6.2.1.7 FTIR of β -lactoglobulin at $\text{pH} = 9$ ($\text{pH} > \text{pK}_a$) and $\text{pH} = 1$ ($\text{pH} < \text{pK}_a$) and the corresponding side chain stick plots from Table 1. Intensities of stick plots are given side chain are scaled relative to the total number of amide I oscillators in the protein assuming an amide I extinction coefficient of $300 \text{ M}^{-1}\text{cm}^{-1}$	163
Fig. 6.2.1.8 FTIR of albumin at $\text{pH} = 7$ and the corresponding side chain stick plots from Table 1. Intensities of stick plots are given side chain are scaled relative to the total number of amide I oscillators in the protein assuming an amide I extinction coefficient of $300 \text{ M}^{-1}\text{cm}^{-1}$	164
Fig. 6.2.1.9 FTIR of TrpZip2 at $\text{pH} = 7$ and the corresponding side chain stick plots from Table 1. Intensities of stick plots are given side chain are scaled relative to the total number of amide I oscillators in the protein assuming an amide I extinction coefficient of $300 \text{ M}^{-1}\text{cm}^{-1}$	164
Fig. 6.2.1.10 FTIR of PG12 at $\text{pH} = 7$ and the corresponding side chain stick plots from Table 1. Intensities of stick plots are given side chain are scaled relative to the total number of amide I oscillators in the protein assuming an amide I extinction coefficient of $300 \text{ M}^{-1}\text{cm}^{-1}$	165
Fig. 6.2.1.11 FTIR of GB1 at $\text{pH} = 7$ and the corresponding side chain stick plots from Table 1. Intensities of stick plots are given side chain are scaled relative to the total number of amide I oscillators in the protein assuming an amide I extinction coefficient of $300 \text{ M}^{-1}\text{cm}^{-1}$	165
Fig. 7.1.1.0 Illustration of a solvated hydrogenated protein in a bath of D_2O . (a) Exchange of surface protons (blue) or those in highly labile regions ($k_{\text{ch}} \sim 10^{-3}\text{-}10^{12} \text{ s}^{-1}$) (b) Protein fluctuations lead to opening events through breaking of hydrogen bonds and exposure of imbedded residues to solvent ($k_{\text{op/cl}} \sim 10^{-5}\text{-}10^{12} \text{ s}^{-1}$) (c) Exchange of a internal proton via water penetration into the protein structure (k_{ch}) (d) The overall	

exchange of an structurally hindered proton (green) will have a rate constant (k_{ex}) proportional to the chemical exchange and protein dynamics..... 169

Fig. 7.1.1.1 Possible mechanisms for (a) acid and (b) base catalyzed reactions for hydrogen-deuterium exchange of amide groups in proteins..... 171

Fig. 7.1.1.2 Effects of primary structure of the calculated hydrogen exchange rate of a disordered homopolymer of poly-L-alanine. At low and high pH, away from pH min, the rate is dominated by the acid and base catalyzed mechanism that scales with the concentration of catalyst. Here k_a and k_b are the acid and base catalyzed rates respectively. As steric effects increase, the overall rate of exchange decreases due to accessibility of catalyst to the exchange site (blue trace and arrow). Inductive effects act to decrease the rate of the acid catalysis mechanism and increase the rate of the base catalysis mechanism due to electron withdrawing effects of the side chain (red trace and arrow). This excludes the effects on exchange due to burial of amino acids in the protein core or residues partaking in hydrogen bonded contacts of secondary structure. Figure adapted from reference.⁶..... 173

Fig. 7.1.2.1 pH dependence of the hydrogen exchange rate (black curve). The EX1 limit dominates at high pH where the protein fluctuations dictate the exchange rate. At low pH, or the EX2 limit, the exchange shows pH dependence..... 176

Fig. 7.1.3.1 Free energy dependence on protein destabilization conditions. (a) Free energy as a function of denaturant concentration from Eq. 7 and 8 where $\Delta G_o = 9.7$ kcal/mol, $T = 300K$, $\Delta n = 4$, $K_{op}(g) = 1$, and $K_{op}(l) = 0, 10^2, 10^4, 10^6, 10^7$. The dotted traces represent the effect of protection of exchangeable sites. (b) Free energy as a function of temperature from Eq. 9 and 10 where $\Delta S = 0.27$ kcal/mol·T, $C_p = 1.8$ kcal/mol·T, $T_m = 77^\circ C$ and $\Delta H = 100, 84, 69$ and 67 kcal/mol. The dotted trace represents the effects on free energy with high entropy..... 181

Fig. 7.2.1.1 Temperature induced hydrogen-exchange FTIR spectra of ubiquitin at pH 1 and pH 9. FTIR spectra of partially exchanged ubiquitin of the amide I/II/II' spectral region (left) and amide A mode (middle) and the temperature dependent difference

FTIR at pH 9 (top) and pH 1 (bottom) are shown. Note the temperature-dependent difference spectra are colored from cold (blue) to hot (red). The right panel shows the temperature dependent traces of exchange for the amide A (red), amide II (blue) and amide II' (black) bands. 187

Fig. 7.2.2.1 Time-dependent hydrogen exchange of ubiquitin at pH 9 at T=30°C, 40°C and 50°C 190

Fig. 7.2.2.2 (a) Normalized hydrogen exchange traces of the amide II mode are plotted for pH 9 (black/blue) and pH 1 (red). pH 1 traces show significant temperature dependence of decay. (b) Direct comparison of pH 1 (red) and 9 (black) hydrogen exchange traces of amide II at T = 30°C, 40°C and 50°C. 193

Fig. 7.2.2.3 Comparison of 2D IR projection to FTIR pH 1 and T = 50°C. 195

Fig. 7.2.2.4 ZZZY 2D IR spectrum of ubiquitin at pH 1. Arrow represents the related projection of the 2D surface over the amide II region seen in the FTIR kinetic trace of Fig. 7.2.2.3. 196

Fig. 8.1.1.1 FTIR and absorptive amide I/I'-II 2DIR spectra of a) Con A, b) myoglobin, c) RNaseA and d) ubiquitin. The spectral regions corresponding to the amide I/I', amide II, and various side chain absorptions are labeled in the middle. Dashes mark the amide I and amide II regions over which the slices in Fig. 8.1.1.3 were integrated. Contour levels are plotted to emphasize the cross peak region of the spectra. Contours for Con A and RNaseA are plotted in 1% increments for ±8% and 4.3% from ±8% to ±60% peak amplitude of the amide I fundamental. Ubiquitin and myoglobin are plotted with 1.5% increments for ±12% and 4% from ±12% to ±60% peak amplitude of the amide I fundamental. 204

Fig. 8.1.1.2 FTIR and absorptive 2D IR spectra of proteins concanavalin A, β-lactoglobulin, ribonuclease A, ubiquitin, lysozyme, myoglobin, albumin and an idealized α-helix homopolymers PBG in CDCl₃. Contours for Con A, BLG and RNaseA are plotted in 1% increments for ±8% and 4.3% from ±8% to ±60% peak

amplitude of the amide I fundamental. Ubiquitin, lysozyme, myoglobin and albumin are plotted with 1.5% increments for $\pm 12\%$ and 4% from $\pm 12\%$ to $\pm 60\%$ peak amplitude of the amide I fundamental. 206

Fig. 8.1.1.3 Normalized slices taken along $\omega_1 = \omega_{AI}$ (blue) overlapped with the amide I slice (red) and amide I FTIR (black dashed)..... 209

Fig. 8.1.1.4 FTIR and 2DIR spectra of ubiquitin before exchange and after full exchange. Note disappearance of the amide II peak that is only present when the amide mode is protonated..... 211

Fig. 8.1.2.1 ZZYY 2D IR Spectra of ubiquitin at pH = 7 (a,b) under partial exchange conditions (5°C) and after full exchange (heated to 80°C and cooled back to 5°C). FTIR kinetic traces of ubiquitin at pH 7 and 30°C. The amide II' cross peaks (3 and 4) report on secondary structure that has exchanged during sample preparation and data acquisition. The amide II cross peaks (1 and 2) report on solvent inaccessible regions of the protein. 214

Fig. 8.1.2.2 ZZYY 2D IR Spectra of ubiquitin at pH = 9 (d, e) under partial exchange conditions (5°C) and after full exchange (heated to 80°C and cooled back to 5°C). FTIR kinetic traces of ubiquitin at pH 9 and 30°C. The amide II' cross peaks (3 and 4) report on secondary structure that has exchanged during sample preparation and data acquisition. The amide II cross peaks (1 and 2) report on solvent inaccessible regions of the protein. 215

Fig. 8.1.2.3 (a-d) Projection along ω_1 axis of ZZYY 2D IR spectra of ubiquitin at pH = 1 (black) and pH 9 (green) under partial exchange conditions (5°C, dotted) and after full exchange (heated to 80°C and cooled to 5°C, solid). The changes to the projection of the amide II' diagonal (a,b), amide II' and amide I/I'-II' downward cross peak (c,d) show increase β -sheet structure. (e,f) Projection of the amide I' diagonal (black), amide I/I'-II upward cross peak (red, dotted), amide I/I'-II' upward cross peak (blue, dotted) show partially exchange secondary structure..... 217

Fig. 8.1.2.4 Tabulated results of water proximity to amide backbone protons from a 40 ps molecular dynamics simulation of Ubiquitin. Bar-plot represents the fraction of water molecules within a 3Å radius of the amide proton. Visualization of the exchange sites is spatially mapped onto the Ubiquitin structure. Results show isolated residues have higher susceptibility to exchange.....	220
Fig. 8.1.2.5 pH dependence of the AI/II/II' 2D IR spectrum and integrated projections of Concanavalin A.....	223
Fig. 8.1.2.6 pH dependence of the AI/II/II' 2D IR spectrum and projections of myoglobin.	224
Fig. 8.1.2.7 pH dependence of the AI/II/II' 2D IR spectrum and projections of lysozyme.	225
Fig. 8.1.2.8 pH dependence of the AI/II/II' 2D IR spectrum and projections of Ribonuclease A.....	226
Fig A1.1 Full experimental set up of DO/Wedge 2D IR spectrometer.....	233
Fig A1.2 Design of the ZnSe wedge used to control pulse delay in experimental set up of Chapter 2.....	234
Fig A1.3 Compression mounts for thin wedges with bulk dimensions of 6 cm wide, 2 cm tall and >2 mm thick. Blue lines represent location of silicon compression material.	234
Fig A1.4 Design vertical and horizontal slides for mounting wedges to vertically mounted stages.....	235
Fig A1.5 Full experimental set up of wedge mounts. The box geometry of the input laser beams is shown (red). The rotation of the box allows for full translation of the wedges.	236

List of Tables

Table 4.4.3.1 Amide I (AI) and amide II (AII) transition frequencies and transition dipole angles for isotopic species of NMA in the gas phase, D₂O, and DMSO-d₆. Experimental frequencies are extracted from FTIR spectra and ‡ are frequencies obtained from Mayne et al.²². Calculated frequencies are the harmonic normal mode frequencies from DFT calculations. The amide I-II projection angle Θ is that between the eigenvectors extracted from fits to the 2DIR spectra, and the calculated angle θ is that between the normal mode coordinates. Also given are the calculated angles of amide I transition moment relative to the CO bond (\angle CO-AI) and the amide II transition moment relative to the CN bond (\angle CN-AII). Potential energy distribution calculations are given for amide I contributions $\geq 4\%$ and amide II contributions $\geq 5\%$. Mode definitions are defined by: s = stretch, d = deformation, ib = in-plane bend (peptide bond). All methyl motions were combined into a single methyl deformation mode for simplicity and Me₁ is the C terminus and Me₂ is the N terminus methyl. For definitions of internal coordinate system see Pulay et al.⁴⁰ 97

Table. 5.5.2.1 Calculated angles between the amide I' and II' doorway modes (for frequency ranges) and eigenstates (single frequency). Angles in gray are the angle of the transition dipole relative to the dominate axis of the secondary structure. Bolded angles represent modes with the strongest cross peaks observed in ZZYY 2D IR. 135

Table 6.1.1.1 Extinction coefficients and peak frequencies of amino acids that absorb between 1200 cm⁻¹ and 1800 cm⁻¹ in H₂O and D₂O. Frequencies are tabulated as a function of pH relative to the pK_a value determined from the isolated amino acid. For vibrations with no pH dependence appear in the central column. 145

Table 7.2.2.1 Fit parameters from FTIR time-dependent hydrogen exchange of ubiquitin at pH1 and 9 at T=30°C, 40°C and 50°C. Traces are fit to a bi-exponential function equal to $A_1 \exp(t/T_1) + A_2 \exp(t/T_2) + B$ 186

Chapter 1

Introduction

“Our species needs, and deserves, a citizenry with minds wide awake and a basic understanding of how the world works” --Carl Sagan

Encoded in the structure of proteins is the ability to conduct and regulate their function. Proteins perform a wide range of functions in cells including catalysis of biological reactions, regulation of other proteins, transport and storage of essential molecules, acting as motors in cellular motility and being the structural foundation of the cell. Rarely is this function directly dictated by the amino acid sequence but, in fact, by the three-dimensional structure formed through inter- and intra-molecular interactions. Some of the dominant influences on protein structure include side chains interactions, hydrogen bonded contacts of the protein backbone and solvent interactions. In addition to the overall structure of proteins, local fluctuations and structural rearrangements play an integral role in protein function and biochemical reactions.¹⁻³

Hydrophobic collapse is a proposed mechanism by which proteins fold into their native state.⁴⁻⁷ The importance of hydrophobicity in folding points to the significant interaction between a protein and its local solvent environment. The solvent can provide an indirect means to observed protein stability and the structure of the hydrophobic core through hydrogen-deuterium exchange techniques.^{8,9} The degree of stability can be assessed by solvent penetration into the protein core and exchange with sterically hindered protons. Therefore, what is required is a molecular probe that is sensitive to both protein solvation and secondary structure.

In this thesis, the protein-solvent interaction is used to enhance the structural resolution of non-linear two-dimensional infrared (2D IR) spectroscopy. Due to the ability of this spectroscopy to correlate molecular signatures through coupling, this technique is ideal for addressing these multi-coordinate and complex questions. New experimental manifestations of 2D IR and a robust framework for acquisition of multi-mode spectra are demonstrated. The stability of proteins and the hydrophobic core is elucidated for ubiquitin by correlation of the solvent and structural sensitivity of the amide vibrations of proteins. This work establishes 2D IR spectroscopy as a structurally sensitive tool for the study of protein dynamics and structure.

1.1 Multidimensional Spectroscopy

Multidimensional spectroscopy reports on molecular connectivity via coupling of nuclear spins, electronic states or vibrational modes depending on the excitation mechanism. Two-dimensional nuclear magnetic resonance (NMR) and X-ray crystallography have provided a wealth of information on atomistic protein structure in both the solid and condensed phases.¹⁰⁻¹³ However, in practice, structure resolution and

temporal resolution are often mutually exclusive. NMR has the capability of inferring structural kinetics on the picosecond to nanosecond time scale. But, to obtain dynamical information, or the structural evolution of molecules along an energetic coordinate, a technique is required that can directly observe structural rearrangements on these timescales.¹⁴

To this point, the structural sensitivity of the optical analogs of 2D NMR is limited due to the nature of the observed transitions. However, these methods have addressed a wide variety of important molecular questions ranging from understanding coupling of electronic states,¹⁵ collective dynamics in the condensed phase,¹⁶ spectral diffusion,¹⁷ vibrational relaxation and couplings,¹⁸⁻²² conformational fluctuations,^{23,24} chemical reaction dynamics,^{25,26} and transient structural changes after photoinitiation.^{27,28} Ultrafast vibrational spectroscopy is ideally suited for studying fast molecular dynamics due to the nature of the molecular probe. Molecular vibrations are sensitive to the chemical connectivity and local environment. The vibrational modes experience frequency shifts, line width broadening and amplitude variations due to vibrational coupling, hydrogen bonding and electrostatics of the larger protein and solvent.^{29,30} High order non-linear vibrational measurements are capable of accessing the vibrational manifold of states providing direct information about vibrational coupling, anharmonicity and dynamics.^{21,31} In this thesis, the ability of multi-dimensional spectroscopy to correlate vibrations will be used to enhance structural sensitivity of the technique.

1.1.1 Multi-Mode Vibrational Spectroscopy of Proteins and Peptides

Despite the sensitivity of a molecular vibration to its local environment, high structural resolution is limited by spectral congestion that impedes the ability to

spectroscopically isolate structural elements. Using 2D vibrational spectroscopy, spectroscopic information is spread over two frequency axes reducing overall spectral congestion. Due to the collective nature of most vibrational modes, correlating specific vibrational signatures, or normal modes, to local structure requires the ability to properly characterize the local mode composition of vibrational eigenstates. The anharmonic potential can be extracted with this method to fully characterize a vibration.²¹ Increased structural information is obtained using polarization selective measurements that extract the relative angle between transition dipole moments.³²

This view of spectral congestion often comes from examination of a single vibrational band. The full vibrational spectrum of proteins spans nearly a 2000 cm^{-1} window in the mid-infrared and has a large number of distinct backbone vibrations. With vibrational line widths ranging from 30-100 cm^{-1} , most vibrations are split sufficiently and are spectrally distinct. The amide I vibration, a predominately carbonyl stretch, is centered at $\sim 1650 \text{ cm}^{-1}$ when protonated. The amide II vibration, which is a mixed vibration of CN stretch and NH in-plane bend, appears at $\sim 1550 \text{ cm}^{-1}$ and when the amide group is deuterated shifts 100 cm^{-1} to $\sim 1450 \text{ cm}^{-1}$. In addition to backbone vibrations, side chains also absorb in this region and will be detailed in Chapter 6. Correlating the sensitivities of vibrations in the amide finger print regions provides increase structural information and dramatically reduced congestion.

Dual-frequency 2D IR experiments have been implemented by a number of groups and successfully performed on model peptides systems by Hochstrasser and co-workers using two independently tunable laser sources.³³ Over the past decade, the

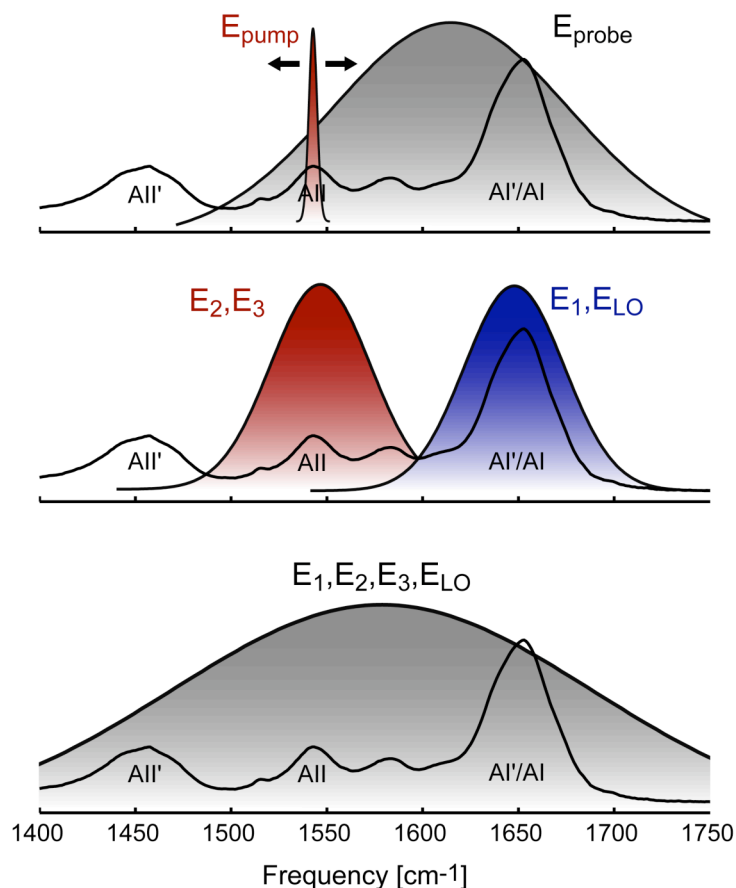


Fig. 1.1.1.1 Representations of double-resonance 2D IR spectroscopy (top), dual-frequency Fourier transform 2D IR spectroscopy (middle) and multi-mode Fourier transform 2D IR spectroscopy (bottom).

availability of ultrafast lasers with sub 100 fs pulse durations in the infrared permit broader bandwidth experiments to be performed. For the experiments presented in this thesis, an optical parametric amplifier was constructed with a tunable bandwidth of up to 400 cm^{-1} . This system is specifically designed to cover the amide I-II region of proteins. Over the $1350\text{-}1750\text{ cm}^{-1}$ range, multiple backbone vibrations are probed with high time resolution. Fig. 1.1.1.1 is a pictorial representation of this experiment. In this thesis, the use of a single laser pulse to cover multiple vibrations will be referred to as multi-mode Fourier transform 2D IR spectroscopy. The distinct difference between these techniques is that two-color experiment measures coupling terms only while the multi-mode 2D IR

measures the full spectrum thus characterizing the full anharmonic potential of all vibrations under the laser bandwidth.

Multi-mode 2D IR spectroscopy will be used to determine secondary structure stability in proteins and solvent penetration into the protein structure.³⁴ The sensitivity of the amide I band to secondary structure moieties is used in conjunction with the solvent sensitivity of the amide II vibration to probe protein-solvent interactions. The structural sensitivity of the amide I vibrations arises from its intrinsic sensitivity to its local environment. Correlated frequency shifts and line shape changes arise from vibrational coupling of adjacent oscillators and those involved in hydrogen-bonded contacts of the extended protein structure. Therefore, the amide I line shape reflects the underlying three-dimensional structure.^{35,36} Partial exchange of proteins with hydrogen-deuterium exchange methods reveals information about amide protons involved in stable secondary structure protected through strong hydrogen bonds and those protected in the hydrophobic core. Thereby correlating the structural sensitivity of the amide I mode with protonation state sensitivity of amide II band, direct information about solvent exposed residues can be accessed. Extension of the spectral bandwidth to cover the amide II' band allows for structural information about solvent accessible and inaccessible residues to be measured simultaneously. In addition, the structural sensitivity of the amide II' band is observed for the first time.

1.2 Experimental Considerations for Multi-mode 2D IR Spectroscopy

A number of technical challenges of 2D IR spectroscopy are addressed in this thesis. 2D IR is a third-order nonlinear technique that maps vibrational frequency evolution through three independently controlled time periods. An ultrafast laser pulse

interacting with the sample initiates the evolution period. This interaction creates a vibrational coherence that evolves on the excited vibrational state potential. After some time, a second pulse interacts with the sample to generate a population. During this waiting period, the population relaxes via vibrational couplings and solvent interactions. A final third pulse probes the population and determines where the vibrational energy has dissipated. To extract phase and amplitude information, the resulting molecular response can be heterodyned detected, or cross-correlated with a known electric field. This is known as the detection period. Performing a numerical Fourier transform over the evolution and detection periods generates a two-dimensional correlation surface. This map provides an intuitive picture of the anharmonic potential, as well as the dynamics of the system. Frequency-structure correlation is established through vibrational couplings or alternatively viewed as the projection of the spectral sensitivities of one coordinate onto that of another.

1.2.1 Phase Stability

Phase sensitive detection requires interferometric stability over the time scale of the experiment. Errors in stage position, vibrations of optical mounts, temperature, humidity and air currents can give rise to phase errors. These errors manifest themselves as ghost peaks in the Fourier transform that interfere with the 2D IR line shape. Above is the description of time/time acquisition of a 2D IR surface. This method requires exceptionally high laser and interferometric stability. Only recently in our group has this method been experimentally realized as a practical approach of 2D IR spectroscopy. Traditionally, these experiments have been performed in time/frequency where the signal plus heterodyning field is optically transformed through a monochromator and collected

on an array detector.³⁷ Multiplexing the signal dramatically reduces the required time for data acquisition. This, however, still is an interferometric measurement and relies on phase stability through the course of the experiment. A number of groups have actively approached this problem through passive stabilization methods in which pulse pairs are generated off a diffractive optic and stage delays are controlled by wedged windows that are far less sensitive to external vibrations.^{38,39} Chapter 2 demonstrates the use of diffractive optics and transmissive delay lines for 2D IR experiments. Alternatively, a quasi-frequency domain approach has been implemented by Hochstrasser, which establishes the two frequency axes by spectrally tuning the pump pulse.⁴⁰

1.2.2 Phasing

In the aforementioned methods, obtaining an intuitive view of the molecular evolution requires the ability to separate real and imaginary contributions to the 2D signal as well as the coherence pathways through phase matching or pulse ordering. Absolute time zero for both the first and third time periods and the relative timing between rephasing and non-rephasing responses in the evolution period need to be well defined to properly construct the absorptive 2D surface. In non-linear optical and infrared techniques a central problem in constructing purely absorptive spectra comes from these phase errors. “Phasing” spectra corrects for errors in relative and absolute pulse timings that in the numerical transform mix the absorptive and dispersive components, as well as, altering the absolute peak shift. Pulse timing techniques, such as second harmonic autocorrelations, are only accurate to within an optical cycle at best and are insufficient for alias-free Fourier transform measurements. With multiple pulse interactions and independent time delays, the problem is underdetermined.

A number experimental techniques have been employed to address and ideally eliminate the need for phasing, however, generally at the cost of less spectroscopic information and versatility. Early experiments performed by Hamm, et. al. use two broadband laser pulses in which the pump frequency is spectrally selected with a Fabry-Perot filter. Hamm showed that double resonance techniques provide similar information as the real 2D FT correlation spectrum except the pump axis is convolved with the pulse spectral bandwidth.⁴¹ The simplicity of the experimental set up is at the expense of spectral and temporal resolution and the ability separate coherence pathways.

To improve phase control between pulses and simplify the experimental set up, Warren and co-workers implemented a collinear 2D FT technique in which pulse timings and phase of three collinear visible beams are controlled by an acousto-optic pulse shaper. Despite the high degree of control over the pulse sequence, acousto-optic pulse shapers can produce spurious pulses that can amplitude modulate the signal. Recently, the Zanni group demonstrated the ability to collect 2D surfaces in the infrared with a germanium acousto-optic modulator.⁴² This demonstrated the ability of performing both time and frequency domain techniques using a pump-probe geometry with one shaped pulse. Despite minor set backs in efficiencies and spurious pulses using pulse shapers, this is an exciting field which opens opportunities in coherent control of populations as well as methods in which one can selectively control the coherence pathways in the 2D signal.

1.3 Thesis Outline

The ability to acquire high fidelity 2D IR line shapes on complex systems in the condensed phase requires a diverse and robust experimental design. Often there are trade-

offs between experimental complexity and the wealth of information obtained from the designed experiment. The emphasis of this thesis is on extending the current capabilities of 2D IR to explore much more complex scientific questions through the use of multi-mode vibrational spectroscopy. However, this advance is not at the expense of experimental involvedness due to the new experimental manifestation of 2D IR described in chapter 3. Applications of multi-mode 2D IR to study protein structural stability and solvation are observed for the first time

To address the technical challenge of interferometric phase stability in 2D IR experiments, a passively stabilized 2D IR spectrometer is discussed and demonstrated in **Chapter 2**. The use of a single diffractive optic to generate four pulse replicas in a compact design substantially improves phase stability over hours to days. Stage timings are controlled by zinc selenide (ZnSe) wedged windows to an accuracy of less than 50 attoseconds.

Chapter 3 details a new method for acquisition of two-dimensional Fourier transform (2D FT) spectra.⁴³ In contrast to the methods described above which employ a non-collinear geometry, this method uses a collinear pulse pair and probe geometry to induce a molecular response. This implementation has been discussed previously in the theoretical literature^{15,44-46} and the geometry demonstrated experimentally.⁴⁵ Simultaneous collection of the molecular response and pulse timing and characteristics permit real time phasing and rapid acquisition of spectra. This method demonstrates the ability to acquire information on molecular dynamics, couplings and structure in a simple apparatus.

Earlier work in our group laid the framework for extraction of the vibrational potential by modeling it as two coupled anharmonic oscillators. This framework is extended to the vibrational coupling of the amide I and II modes in the model peptide group *N*-methylacetamide in **Chapter 4**.⁴⁷ The model is used to characterize the effects of solvation and isotopic substitution of the anharmonic potential and vibrational relaxation pathways of the amide vibrations. The experiments are validated by density functional theory calculations and are used to dissect the amide normal modes into a local mode picture. Variations in this local mode description of the vibrations gives rise to the fundamental difference between the isotopically substituted amide group.

With a fundamental understanding of the local mode nature of amide vibrations in a model group, the amide II' is further investigated in globular proteins in **Chapter 5**.³⁴ The structural sensitivity of the amide II' is elucidated for the first time in 2D IR spectroscopy. Experimental 2D IR spectra of poly-L-lysine, in the anti-parallel β -sheet, α -helix and random coil forms, are compared to model calculations for idealized structures. The origin of amide II' structural sensitivity arises from nearest neighbor couplings. Results are further validated through thermal denaturation and aggregation of other proteins systems.

Chapter 6 aims to spectroscopically identify vibrations due to side chain absorptions in the amide finger print region between 1350 and 1720 cm^{-1} . The major side chain contributions to the vibrational spectrum over this range are arginine, aspartic acid, glutamic acid, tyrtophan and tyrosine. 2D IR spectra of a number of side chains are presented.

Chapter 7 presents a background to hydrogen-deuterium exchange spectroscopy including results of hydrogen exchange kinetics of ubiquitin using linear Fourier transform infrared spectroscopy. Expanding on this and the instrumental and scientific progress made in chapters 2-5, hydrogen exchange multi-mode 2D IR spectroscopy is performed on a series of globular proteins in **Chapter 8**. By exploiting the fact that protons of the amide backbone that are protected through hydrogen bonds of secondary structure and the tertiary structure of proteins, one can spectroscopically isolate solvent accessible and inaccessible residues of a protein through vibrational coupling of the amide I mode to the amide II and II' vibrations. Using the structural sensitivity of amide I/I' and II', the stable forms of secondary structure are identified.

References

- (1) Lu, H. P.; Xun, L. Y.; Xie, X. S. *Biophysical Journal* **1999**, *76*, A136-A136.
- (2) Warshel, A. *Proc. Nat. Acad. Sci., USA* **1984**, *81*, 444-448.
- (3) Jimenez, M. A.; Salazar, G.; Yin, J.; Taiha, J.; Romesberg, F. E. *Proc. Nat. Acad. Sci.* **2004**, *10*, 3803-3808.
- (4) Kauzmann, W. *Adv. Protein Chem.* **1959**, *14*, 1-63.
- (5) Kuntz, I. D.; Kauzmann, W. *Adv. Protein Chem.* **1974**, *28*, 239.
- (6) Dill, K. A.; Truskett, T. M.; Vlachy, V.; Hribar-Lee, B. *Ann. Rev. Biophys. Biomol. Str.* **2005**, *34*, 173-199.
- (7) Dill, K. A. *Biochemistry* **1990**, *29*, 7133.
- (8) Bai, Y.; Milne, C. J.; Mayne, L.; Englander, S. W. *Proteins* **1982**, *20*, 4-14.
- (9) Englander, S. W.; Krishna, M. M. G. *Nature Structural Biology* **2001**, *8*, 741-742.
- (10) Palmer III, A. G. *Chem. Rev.* **2004**, *104*, 3623-3640.
- (11) Doniach, S. *Chem. Rev.* **2001**, *101*, 1763-1778.
- (12) Cavalleri, A.; Siders, C. W.; Sokolowski-Tinten, K.; Toth, C.; Blome, C.; Squier, J. A.; von der Linde, D.; Barty, C. P. J.; Wilson, K. R. *Optics and Photonics News* **2001**, *May 2001*, 29-33.
- (13) Stockman, B. J.; Euvrard, A.; Scahill, T. A. *J. Biomol. NMR* **1993**, *3*, 285-296.
- (14) Calhoun, D. B.; Englander, S. W. *Biochemistry* **1985**, *24*, 2095-2100.
- (15) Jonas, D. M. *Annu. Rev. Phys. Chem.* **2003**, *54*, 397-424.
- (16) Joo, T.; Jia, Y.; Fleming, G. R. *J. Chem. Phys.* **1995**, *102*, 4063.
- (17) Deak, J. C.; Rhea, S. T.; Iwaki, L. K.; Dlott, D. D. *J. Phys. Chem. A* **2000**, *104*, 4866-4875.

- (18) Hamm, P.; Lim, M.; Hochstrasser, R. M. *J. Chem. Phys.* **1997**, *107*, 10523.
- (19) Deak, J. C.; Iwaki, L. K.; Dlott, D. D. *Chem. Phys. Lett.* **1998**, *293*, 405.
- (20) Khalil, M.; Demirdöven, N.; Tokmakoff, A. *J. Phys. Chem. A* **2003**, *107*, 5258-5279.
- (21) Golonzka, O.; Khalil, M.; Demirdöven, N.; Tokmakoff, A. *Phys. Rev. Lett.* **2001**, *86*, 2154-2157.
- (22) Golonzka, O.; Khalil, M.; Demirdöven, N.; Tokmakoff, A. *J. Chem. Phys.* **2001**, *115*, 10814-10828.
- (23) Woutersen, S.; Pfister, R.; Hamm, P.; Mu, Y. G.; Kosov, D. S.; Stock, G. *J. Chem. Phys.* **2002**, *117*, 6833-6840.
- (24) Hamm, P.; Hochstrasser, R. M. In *Ultrafast Infrared and Raman Spectroscopy*; Fayer, M. D., Ed.; Marcel Dekker, Inc.: New York, 2001, p 273-347.
- (25) Kwak, K.; Asbury, J.; Chen, X.; Piletic, I. R.; Fayer, M. D. *Science* **2005**, *309*, 1338-1343.
- (26) Kim, Y. S.; Hochstrasser, R. M. *Proc. Nat. Acad. Sci.* **2005**, *102*, 11185-11190.
- (27) Bredenbeck, J.; Helbing, J.; Kumita, J. R.; Woolley, G. A.; Hamm, P. *PNAS* **2005**, *102*, 2379-2384.
- (28) Chung, H. S.; Khalil, M.; Smith, A. W.; Tokmakoff, A. *Rev. Sci. Instr.* **2007**, *78*.
- (29) Joo, T.; Jia, Y.; Yu, J.-Y.; Lang, M. J.; Fleming, G. R. *J. Chem. Phys.* **1996**, *104*, 6089-6107.
- (30) DeCamp, M. F.; DeFlores, L. P.; McCracken, J. M.; Tokmakoff, A.; Kwac, K.; Cho, M. *J. Phys. Chem. B* **2005**, *109*, 11016.

- (31) Demirdöven, N.; Khalil, M.; Tokmakoff, A. *Phys. Rev. Lett.* **2002**, *89*, 237401-237401.
- (32) Golonzka, O.; Tokmakoff, A. *J. Chem. Phys.* **2001**, *115*, 297-309.
- (33) Rubtsov, I. V.; Wang, J.; Hochstrasser, R. M. *Proc. Natl. Acad. Sci. USA* **2003**, *100*, 5601-5606.
- (34) DeFlores, L. P.; Tokmakoff, A. *J. Am. Chem. Soc.* **2006**, *128*, 16520-16521.
- (35) Cheatum, C. M.; Tokmakoff, A.; Knoester, J. *J. Chem. Phys.* **2004**, *120*, 8201-8215.
- (36) Demirdöven, N.; Cheatum, C. M.; Chung, H. S.; Khalil, M.; Knoester, J.; Tokmakoff, A. *J. Am. Chem. Soc.* **2004**, *126*, 7981-7990.
- (37) Khalil, M.; Demirdöven, N.; Tokmakoff, A. In *Ultrafast Phenomena XIII*; Miller, R. J. D., Murnane, M. M., Scherer, N. F., Weiner, A. M., Eds.; Springer Verlag: Vancouver, Canada, 2002; Vol. 71, p 583-585.
- (38) Brixner, T.; Stoipkin, I. V.; Fleming, G. R. *Opt. Lett.* **2004**, *29*, 884-886.
- (39) Goodno, G. D.; Astinov, V.; Miller, R. J. D. *J. Phys. Chem. B* **1999**, *103*, 603.
- (40) Hamm, P.; Lim, M.; Hochstrasser, R. M. *J. Phys. Chem. B* **1998**, *102*, 6123-6138.
- (41) Cervetto, V.; Helbing, J.; Bredenbeck, J.; Hamm, P. *J. Chem. Phys.* **2004**, *121*, 5935-5942.
- (42) Shim, S. H.; Strasfeld, D. B.; Zanni, M. T. *Proc. Nat. Acad. Sci.* **2007**, *Special Feature*.
- (43) DeFlores, L.; Nicodemus, R. A.; Tokmakoff, A. *Opt. Lett.* **2007**, *32*, 2966.
- (44) de Boeij, W. P.; Pshenichnikov, M. S.; Wiersma, D. A. *Annu. Rev. Phys. Chem.* **1998**, *49*, 99-123.

- (45) Emde, M. F.; de Boeij, W. P.; Pshenichnikov, M. S.; Wiersma, D. A. *Opt. Lett.* **1997**, *22*, 1338.
- (46) Gallagher Faeder, S. M.; Jonas, D. M. *J. Phys. Chem. A* **1999**, *103*, 10489-10505.
- (47) DeFlores, L. P.; Ganim, Z.; Ackley, S. F.; Chung, H. S.; Tokmakoff, A. *J. Phys. Chem. B* **2006**, *110*, 18973-18980.

Chapter 2

Passively Stabilized Two-dimensional Infrared Spectroscopy using a Diffractive Optic and Wedge Interferometer

“Where we have strong emotions, we're liable to fool ourselves.” – Carl Sagan

Fourier transform multi-dimensional ultrafast spectroscopy is finding a wide range of applications in studying chemical and biological dynamics spanning spectral regions from optical to terahertz.¹ Across the entire spectra range, interferometric stability and timing accuracy is required to minimize Fourier transform artifacts that plague the time domain techniques. For these multidimensional techniques, the time domain signal is commonly sampled at discrete points for each interacting laser pulse. The dominant spectral artifacts are (1) aliasing due to inaccurate time steps and phase drifts and (2) line shape distortion caused by mixing of the real and imaginary

components of the molecular response due to absolute timing errors. The errors result in reduced signal strength and ones ability to accurately separate the absorptive and dispersive components of the nonlinear polarization. What is required are improved methods of data acquisition through system robustness that improve phase stability, time resolution, and data collection time.

Traditionally, multidimensional spectroscopy is preformed in the time domain with a Mach-Zehnder interferometer that includes beam splitters, retro-reflectors and high accuracy translation stages.² Without phase stabilization, particularly in the visible region where path length instabilities lead to more substantial phase errors, Fourier transform artifacts are unavoidable. Active phase stabilization has been implemented previously, but as experimental complexity increases, this method becomes far less feasible.^{3,4} Two ideal approaches to avoid phase stability problems in multidimensional techniques are to perform purely frequency domain experiments or to passively stabilize signals in the time domain. Hochstrasser and co-workers have implemented the former by using a spectrally narrowed pump and broadband probe in which the pump frequency is scanned to establish the second dimension.^{5,6} Alternatively, in the time domain, a number of groups have developed methods for passive phase stabilization of pulse pairs for two-dimensional electronic spectroscopy.⁷⁻¹⁰ The methods commonly employ a common optic for generation of pulse replicas, either through use of a diffractive optics^{7,11,12} or pulse shapers.^{10,13}

Fleming and co-workers have addressed these issues by implementing a passively stabilized diffractive optic set up creating two sets of pulse pairs and time delays that are controlled by transmission through translating thin fused silica wedges.¹⁴ The use of

diffractive optics to perform heterodyned transient grating spectroscopy was first presented by Goodno and Miller.¹² In addition to the inherent passive stabilization imposed by the diffractive optic, they also have the distinct advantage of fully overlapping pulse fronts when used in a 2f imaging configuration.¹⁵

In this chapter, we discuss the extension of these techniques to two-dimensional infrared spectroscopy (2D IR). We generate a mid-infrared boxcar from a single laser pulse incident on a diffractive optic for passive phase stabilization of pulse replicas. Implementation of zinc selenide (ZnSe) wedges allow for highly accurate and reproducible pulse timings. The advantages of this technique significantly improve phase stability and pulse timing that dramatically reduces aliasing in the Fourier transformed spectra. In addition, by using a single diffractive optic, the experiment is intrinsically phase matched for the non-collinear 2D IR experiment. These advances allow for acquisition of rapid surfaces by scanning the stages at constant velocity and therefore reducing the effects of long-term drift. The improved phase stability, time resolution and acquisition time allow for averaging in the time domain which greatly improves signal-to-noise. However, due to the compactness of the set up and designs of the diffractive optic element, pulse dispersion and alignment flexibility are notable disadvantages.

2.1 Experimental Design

Femtosecond mid-infrared pulses for 2D IR spectroscopy are obtained from a home-built oscillator/amplifier Ti:Sapphire system pumping a home-built optical parametric amplifier (OPA). An 86 MHz repetition rate Ti:sapphire oscillator seeds the 1 kHz regenerative amplifier producing 1.2 mJ of 38 fs, 790 nm light. The near-infrared light is down converted into the mid-infrared through optical parametric amplification

and difference frequency generation. The OPA generates mid-infrared light that peaks between $2500\text{-}1400\text{ cm}^{-1}$ with a bandwidth of $250\text{-}400\text{ cm}^{-1}$ and with pulse durations between $65\text{-}90\text{ fs}$. To minimize pulse dispersion, the remainder of the experimental set up is designed to be entirely reflective except for two potassium bromide (KBr) lenses and the ZnSe wedge delay lines. KBr is an ideal material for the mid-infrared due to the extremely low material dispersion properties. The infrared is overlapped with a Helium-Neon (HeNe) laser, which acts as a tracer beam for aligning the diffractive optic interferometer.

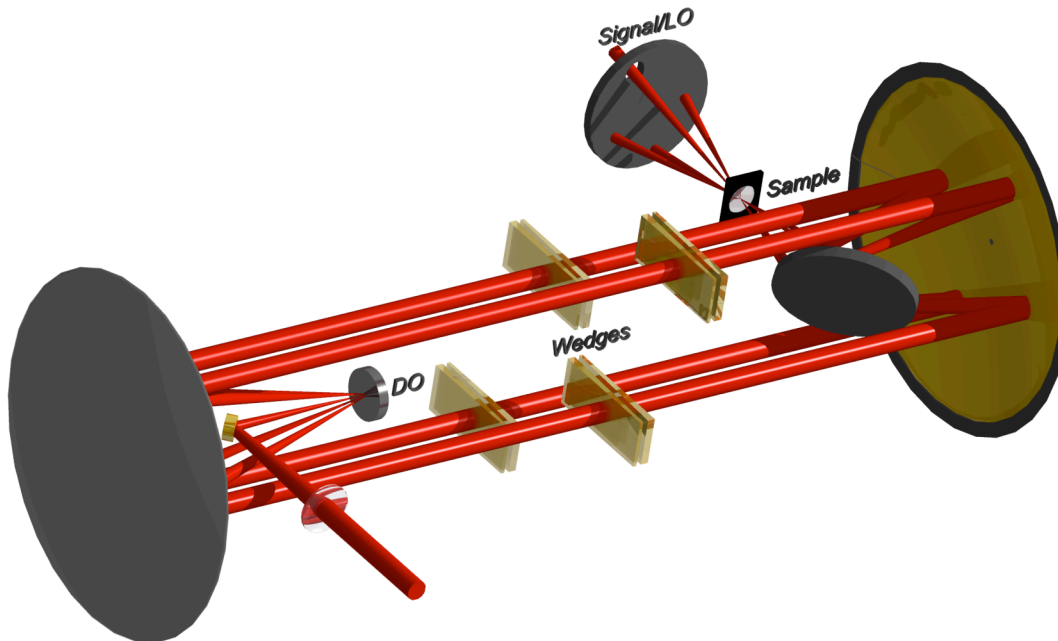


Fig. 2.1.1.1 3D layout of the diffractive optic interferometer using ZnSe wedge delay lines for intrinsically phased match 2D IR spectroscopy.

Fig. 2.1.1.1 shows the design of the diffractive optic (DO) interferometer. A 1 cm diameter single mid-infrared beam is focused onto the DO using a 6-inch focal length potassium bromide lens. Currently, all techniques employing diffractive optics in higher order spectroscopy use a two-beam design with two independent incident beams

generated by a beam splitter before the DO.¹² In the 2D IR experiment, the first and last pulse pair creates a vibrational coherence and therefore requires a well-defined phase relationship. A single incident beam DO that creates four-replica pulse pairs in the box geometry thereby creating four passively phase locked pulses. By generating all four beams in a box from a single incident light source, the 2D IR experiment is intrinsically phase matched. This single optic further simplifies the design and alignment procedure removing the need for beam splitters prior to the set up and has been made to be reflective to reduce cost and minimize pulse dispersion.

2.1.1 Diffractive Optics

The reflective diffractive optical elements (DO) were purchased from INO on fused silica substrates with a reflective gold coating. Given normal incidence to the DO, the angle of the optimized order, θ_m , is given by:

$$\theta_m = \sin^{-1}\left(\frac{m\lambda}{a}\right) \quad (1)$$

where m is the order, λ is the wavelength and a is the grating spacing. DO were optimized to an efficiency of 65% in the first orders at 6 μm with $\theta_m = 15^\circ$ giving a grating spacing of approximately 32.75 μm . The divergence angle of the first order beams was set to be 15° off normal to create a 2.25 inch x 2.25 inch box at a focal length of 6 inches from the collecting mirror.

An important consideration occurs for broadband mid-infrared pulses; θ_m varies dramatically across the bandwidth, as one gets longer in wavelength. This results from a large $\Delta\lambda/\lambda$ and therefore a large $\Delta\theta_m/\theta$. This establishes a critical limitation in the design and implementation of a DO interferometer using optically controlled delay lines. For a

pulse centered at 1550 cm^{-1} with a full width half max of 400 cm^{-1} , the angular dispersion, $\Delta\theta_m$, is 4.36° resulting in substantial spatial dispersion as the beams propagate through the interferometer. This divergence over the 6-inch focal length results in a widening of the FWHM beam diameter by 2.5 cm. The current design is limited to a pulse bandwidth of $\sim 200 \text{ cm}^{-1}$ due to the geometry of the optics and wedge dimensions. Inversion of the sign of the cross peaks is seen in poor alignment of this interferometer and can be attributed to spatial dispersion.

2.1.2 ZnSe Wedges and Pulse Timing

Pulse timings are controlled by a pair of anti-reflection coated ZnSe wedges mounted to mechanical stages that translate along the wedge face. The resolution of the wedges (R in $\text{fs}/\mu\text{m}$) is defined as the change in optical path length ($\Delta\text{OPL} = \Delta n \cdot \Delta l$) per linear translation of the mechanical stage (d) where $\Delta n = n_{\text{ZnSe}} - n_{\text{Air}}$ and Δl is the change in material thickness.

$$R = \frac{\Delta\text{OPL}}{c \cdot d} \quad (2)$$

Wedges were designed with a desired resolution of $0.1 \text{ fs}/\mu\text{m}$ and a total optical path length delay per translation of a single wedge (OPL) of 5000 fs. The dimensionality of the wedge (Fig. 2.1.2.1) are related to these parameters by

$$\theta = \arctan\left(\frac{R \cdot c}{\Delta n}\right) \quad (3)$$

and

$$Y = \frac{\text{OPL}}{R} \quad (4)$$

where θ is the angle of the wedge face, Y is the length of the wedge, and c is the speed of light. The strength of using wedges can clearly be seen as a downshifting of the optical delay of the mechanical stages, therefore no longer relying on high precision stages and reducing cost. In addition to the increased resolution, since these optics are transmissive, they are minimally sensitive to external vibrations as seen in retro-reflectors and therefore do not limit the phase stability in the experimental set up.

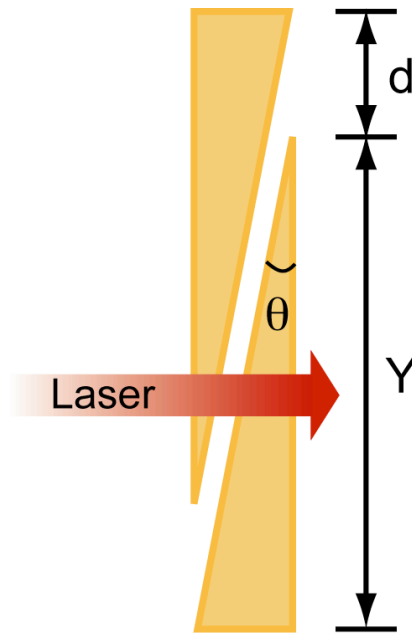


Fig. 2.1.2.1 Illustration of wedge pair and the design parameters presented in Eq. 2-4.

Using the above expressions, the wedge dimensions are determined to be 5 cm long and have a wedge angle of 1.2° (Fig. 2.1.2.1). In order to optically delay a 1 cm diameter beam the length of the wedges was increased by 1 cm. ZnSe wedges were purchased from Crystan as a trapezoid with physical dimensions of 6 cm x 2 cm x (2 mm to 3.2 mm). Surfaces are anti-reflection coated over the 2-8 μm mid-infrared range to minimize loss of power due to four reflections. Wedges are held in home-built compression mounts to reduce strain effects on the thin material and to leave the wedge

face unobstructed by the mount allowing for free motion along the wedge face. The wedge face is aligned along the axis of translation of the stage to avoid collision of the wedge faces. CAD drawings of wedge designs, compression mounts, and stage adapters are contained in Appendix 1.

2.1.3 System Alignment

For the initial alignment of the diffractive optics interferometer, the HeNe is initially used to optimize the set up. This procedure is pictured in Fig. 2.1.3.1. The incident beam from the HeNe/IR overlap set up is aligned, unfocused through the first turning mirror of the set up towards the second large collecting spherical mirror. The height of the large spherical mirror is adjusted such that the incoming beam hits the middle of the optic. In step 2, the beam is focused and reflected back onto a pinhole to ensure planar alignment of the second spherical mirror. Then, in 3, the KBr lens is put in place to establish correct focusing through the system and avoids misalignment at a later stage. The DO is put in place (step 4) at the focus of the HeNe. Since the DO is not designed for a high degree of flatness at 632 nm, there is a large amount of scatter that is collected by the first spherical mirror. This scatter is collimated and aligned to map exactly onto the second spherical mirror in step 5. This adjusts the collimation of the box as well as the height of the mirror. To improve alignment, the iris used to align the first beam (step 6) can be used to ensure the focus of the HeNe is at the proper height for this imaging configuration. In step 7, the pick off mirror is put in place and the sample and detection set up can then be aligned. The HeNe is further optimized by using a pinhole of decreasing size in which the translation of the input lens and first spherical mirrors (or DO if it is on a stage) can be adjusted.

The diffractive optic is precisely placed at the focus of both the incoming transmission lens and the large spherical mirror. This ensures collimation of both the box and individual beams. These lenses create a telescope and a mis-match in focal lengths can be used to reduce the individual beam diameter if desired. Additionally, varying the

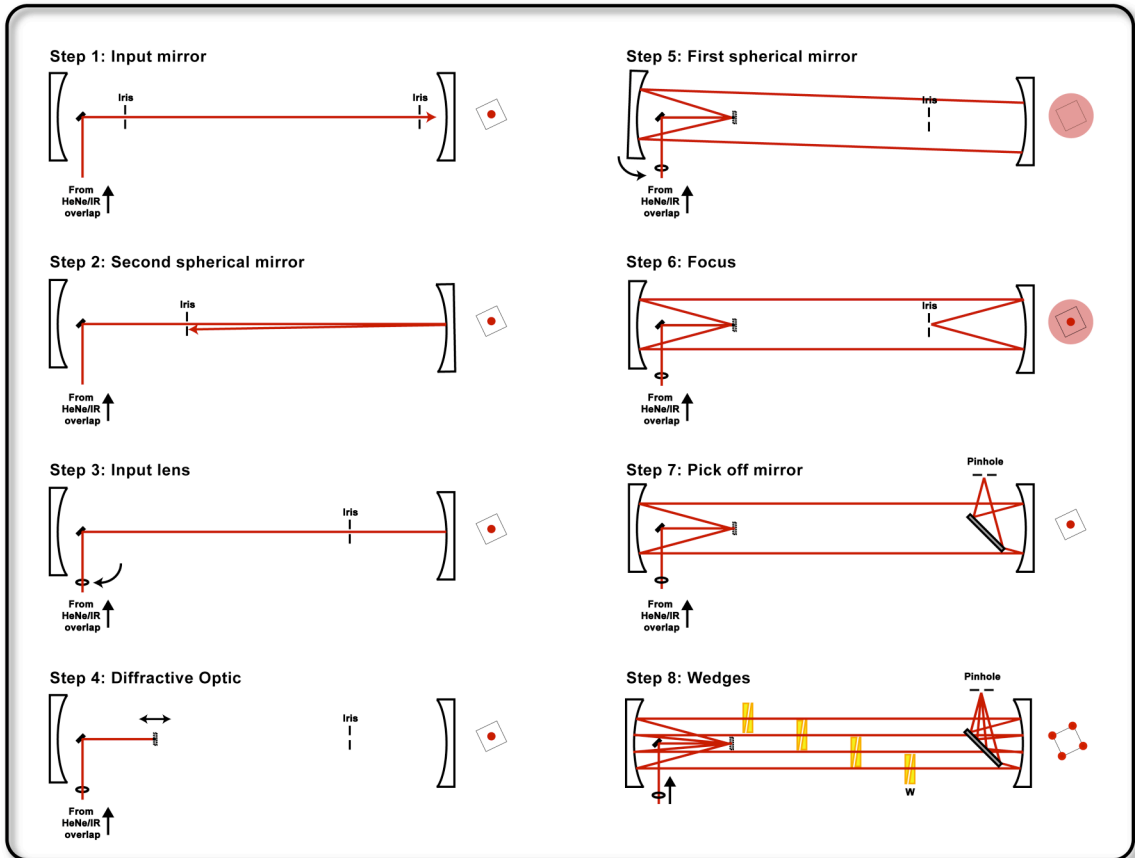


Fig. 2.1.3.1 Alignment procedure for diffractive optic and wedge set up. The image to the right of the second spherical mirror shows the end on view of the HeNe spot.

focal length of the first spherical mirror can be used to control the size of the box and may be required if a given diffractive optic is used for different wavelengths. The divergence angle will be determined by the wavelength as described in Eq. 1. This particular geometry was chosen in order to properly propagate 1 cm diameter beams

through the optical delay lines to avoid clipping of the beams. Additionally, the DO is rotated by 26.5° ($\arctan \frac{1}{2}$) to allow for full translation of the horizontally mounted wedges to avoid clipping of adjacent beams (Fig. 2.1.3.2).

Beam Propagation through wedges

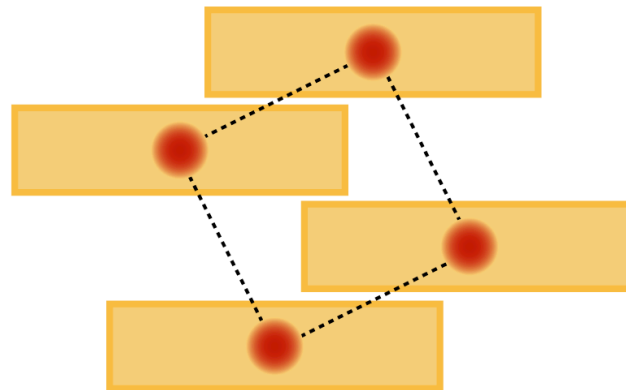


Fig. 2.1.3.2 Rotation of the box (red Gaussian beams) for free translation of the wedges (orange).

Alignment of the IR through the wedges can be done by visualization of the HeNe (Fig 2.1.3.1, step 8 and Fig. 2.1.3.3). Since the wedges are not AR coated for the HeNe, at each interface the beam will reflect onto itself making a diffraction-like pattern. The major parameters that will control proper alignment of the wedges and therefore free translation across the wedge face is the short and long face rotation and the displacement between the wedge pairs. The displacement between the wedge pairs will cause walk off of the IR beam however as long as the wedge faces are parallel this will not generate a problem in the imaging the DO set up. This is because the displacement will be much smaller than the beam diameter, generally kept to about 1 mm or less. This is calibrated by measuring the horizontal distance between the HeNe spots seen in the bottom panel of Fig. 2.1.3.3. Poor wedge alignment, shown in the top panel of Fig. 2.1.3.3, arises when

the wedge faces are not parallel. Rotation about the short face causes each horizontally displaced HeNe spot to have horizontal replicas fanning out. Rotation about the long face causes these spots to fan out vertically. Therefore, by minimizing these effects, the wedge faces can be made parallel with high precision. Alignment is critical to avoid collision of the wedges over the full time delay.

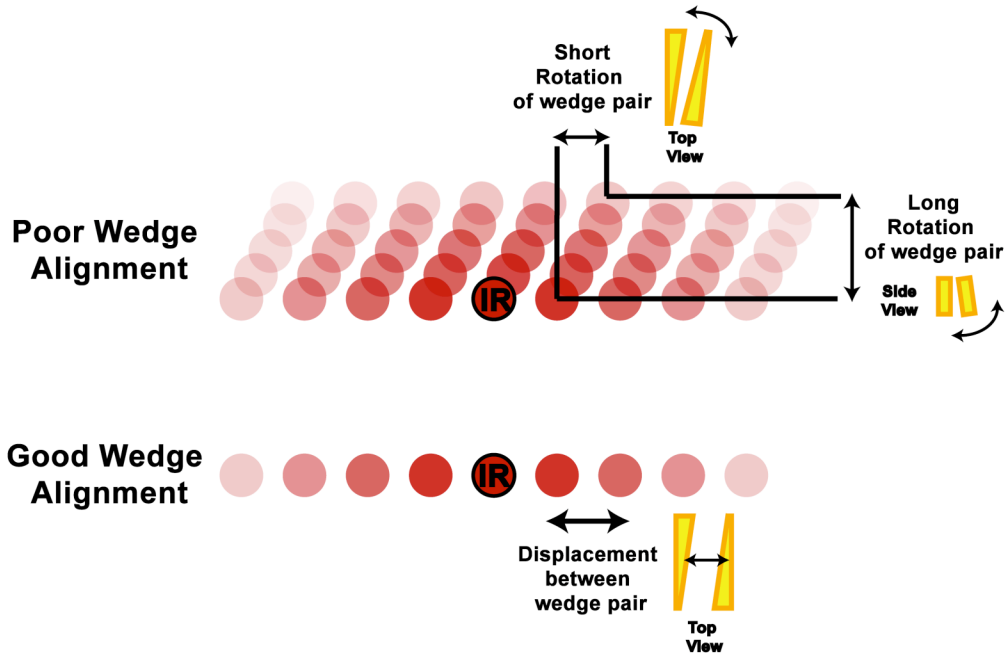


Fig. 2.1.3.3 Alignment procedure for ZnSe wedges.

2.1.4 Stage Calibration

To accurately determine the stage position and step size, the wedges are calibrated by acquiring a spectral interferogram (Fig. 2.1.4.1). Spectral interferometry is performed by co-propagating pulse replicas and spectrally dispersing the pulse-pair into a monochromator. The pulse delay generates a fringing pattern in the frequency spectrum in which the fringe separation is directly related to the time delay. Monochromatic detection of the spectral interferogram will oscillate at a frequency corresponding to the

monochromator position as the pulse-pair is delayed. Therefore, a calibrated monochromator can be used for the stage calibration.

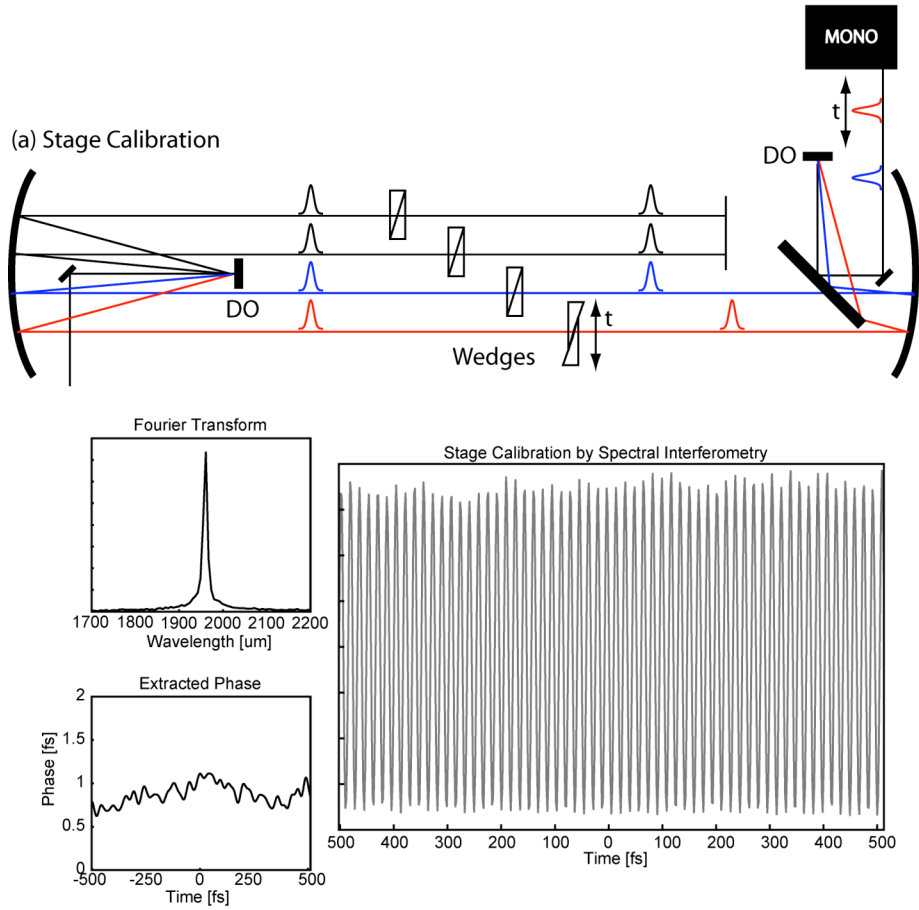


Fig. 2.1.4.1 (Top) Experimental set up for stage calibration depicting a second diffractive optic in the sample position. (Bottom) Acquired spectral interferogram versus time delay, the Fourier transformed spectrum and extracted phase.

For stage calibration, pulse pairs are combined onto an identical DO at the sample position and the beams propagate back along the zero order axis of the optic. For each stage, a beam pair is sent through a monochromator set to a known wavelength and signal is collected on a cooled MCT detector as a function of pulse delay. The monochromator slits are set to (100 μm) giving a frequency resolution of $\sim 1 \text{ cm}^{-1}$. The full interferogram is collected over a 4 ps range therefore limiting the spectral resolution to $\sim 3.7 \text{ cm}^{-1}$.

Comparison of the frequency of the interferogram with the monochromator position gives a unitless calibration constant ($W_c = \frac{\omega_{mono}}{\omega_{int}}$), which is the down-conversion constant for that stage. From this constant, the resolution of the stages is given by $R = \frac{2}{c \cdot W_c}$, where c is the speed of light in $\mu\text{m}/\text{fs}$ and the factor of two arises from comparison with a retro-reflector. The calibration factors were determined to be 66.56, 66.65, 66.55, and 66.39 (ideally 66.66) for beams 1-4 respectively giving R values of 0.1002, 0.1001, 0.1002 and 0.1005 $\text{fs}/\mu\text{m}$. It is important to note that these R -values within 3 decimal places match the wedge design specification of 0.1 $\text{fs}/\mu\text{m}$.

2.1.5 Fast Scanning

The stage can be scanned at constant velocity (up to 2 mm/s) to decrease data acquisition time by removing the need for equilibration at each point during a step scan. It is important, however, that the signal and stage position are acquired simultaneously. For the single axis data acquisition, the integrated detector signal is acquired using a boxcar integrator and the digital output is fed into the stage driver. Both the stage position and the external input are acquired using an external kHz trigger to ensure the signal and stage position are identical.

The velocity (V) of the stage is dictated by the time window or “step” size (Δt), the repetition rate of the laser (f), the resolution of the wedges (R), sample averaging or shots per point (S_p).

$$V = \frac{\Delta t \cdot f}{S_p \cdot R} \quad (5)$$

The total time required for a single scan is given by:

$$t = \frac{d_t}{R \cdot V} \quad (6)$$

where d_t is the total pulse time delay in fs given by the stage displacement of $d_s = d_t/R$. Therefore, the total time of a scan is dictated by the sampling rate, the number of points and the resolution of the wedges.

2.1.6 Improved Heterodyned Detection using a Hollow Waveguide

After beam propagation through the optical delay lines, the box is imaged into the sample using an identical 6-inch focal length spherical mirror. Due to the phase matching conditions imposed by the DO, the 2D IR experiment is properly phase matched. At the sample position, the pulse wave fronts are fully overlapped¹⁵ and the signal field propagates out in the phase matching direction, overlapping the fourth corner of the box and the local oscillator, $k_{LO} = k_{sig} = k_1 + k_2 + k_3$ (Fig. 2.1.1.1). In practice, however, propagation effects through sample windows and wedges can slightly misalign the third-order signal relative to the LO. This mismatch in overlap results in a reduction in the efficiency of heterodyne detection. Additionally, the mismatch in alignment also introduces spatial mismatch in the phase relationship between the spatially dispersed signal field and LO. The alignment and overlap of signal and LO was improved by imaging into a 2 cm long, 300 μm inner diameter hollow wave-guide fiber made of fused silica with the internal surface coating of silver. This ensured proper mode matching of the two fields. Ideally, the fiber core is single mode and on the order of the diffractive limited spot to avoid temporal walk-off of the pulses through the fiber if not propagating collinearly. This drastically improves the spatial overlap, and the heterodyne signal increases by up to an order of magnitude. The fiber is mounted at the entrance slit to a

monochromator imaged onto a 64 channel MCT array detector (Infrared Systems Development and Infrared Associates Incorporated).

2.1.7 Array Calibration

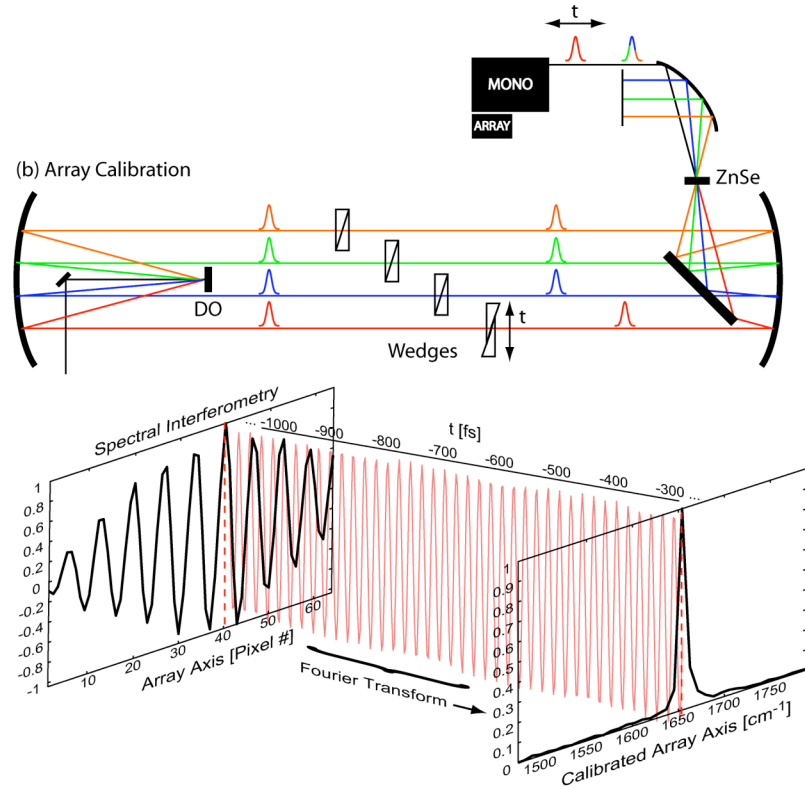


Fig. 2.1.7.1 (Top) Experimental set up for array calibration using non-resonant response of a ZnSe window at the sample position. (Bottom) Depicts collection of the array as a function of time. Each pixel is independently Fourier transformed to give frequency calibration.

The 64-channel MCT array is calibrated by placing a ZnSe window in the sample position and performing spectral interferometry between the non-resonant response from the crystal and the LO beam (shown in Fig. 2.1.7.1). The LO field is scanned using the optically controlled delay line over a total time delay of 4 ps giving a resolution of 3.7 cm⁻¹. The resolution in this case is limited by the dispersion of the grating in the monochromator, which is determined to be 4.2 cm⁻¹/pixel. Each pixel is independently

transformed and the peak frequency defines the pixel calibration and the width defines the resolution (Fig. 2.1.7.1). Data and stage positions are both acquired at 1 kHz and then binned after acquisition to sample each fringe at 10 points per cycle. This binning results in an average over a displacement window of ~ 17 μm and therefore ~ 1.7 fs optical delay. The transform of both fast and step scans were compared and showed no artifacts arising from binning of the stage position. Additionally, with this high reproducibility in stage position, multiple time traces can be averaged sequentially to improve signal to noise.

2.2 Passively Stabilized Two Dimensional Infrared Spectroscopy

Absorptive two-dimensional infrared spectra were acquired with the experimental set up described above. The pulse spectrum was tuned such that the bandwidth of 280 cm^{-1} at FWHM is centered to cover the vibrations of interest. The absorptive 2DIR spectrum is obtained by collecting the rephasing ($k_R = -k_1 + k_2 + k_3$) and non-rephasing ($k_{NR} = k_1 - k_2 + k_3$) spectra and taking a numerical Fourier transform along τ_1 of their sum. Data is acquired in an identical manor to the array calibration and the signal and LO are overlapped in a hollow wave-guide. To remove non-desired third-order signals arising from pump-probes with beams 1, 2 and 3, the LO is set to arrive 1 ps earlier to ensure that these signals decay before the other pulses arrive. By using spectral interferometry, the desired signal field is collected. The phase along τ_3 is retrieved by multiplying the rephasing and non-rephasing contributions by:

$$\phi_R = \exp(i2\pi\omega_1 c\Delta T_R) \cdot \exp(i2\pi\omega_3 c\Delta T_3), \quad (7)$$

and

$$\phi_{NR} = \exp(i2\pi\omega_1 c\Delta T_{NR}) \cdot \exp(i2\pi\omega_3 c\Delta T_3). \quad (8)$$

ω_1 and ω_3 are the frequency axes, ΔT is the respective time delay for the LO delay. The signal is given by $S=(R_{\text{real}}+R_{\text{imag}})\phi_R+(NR_{\text{real}}+NR_{\text{imag}})\phi_{NR}$.

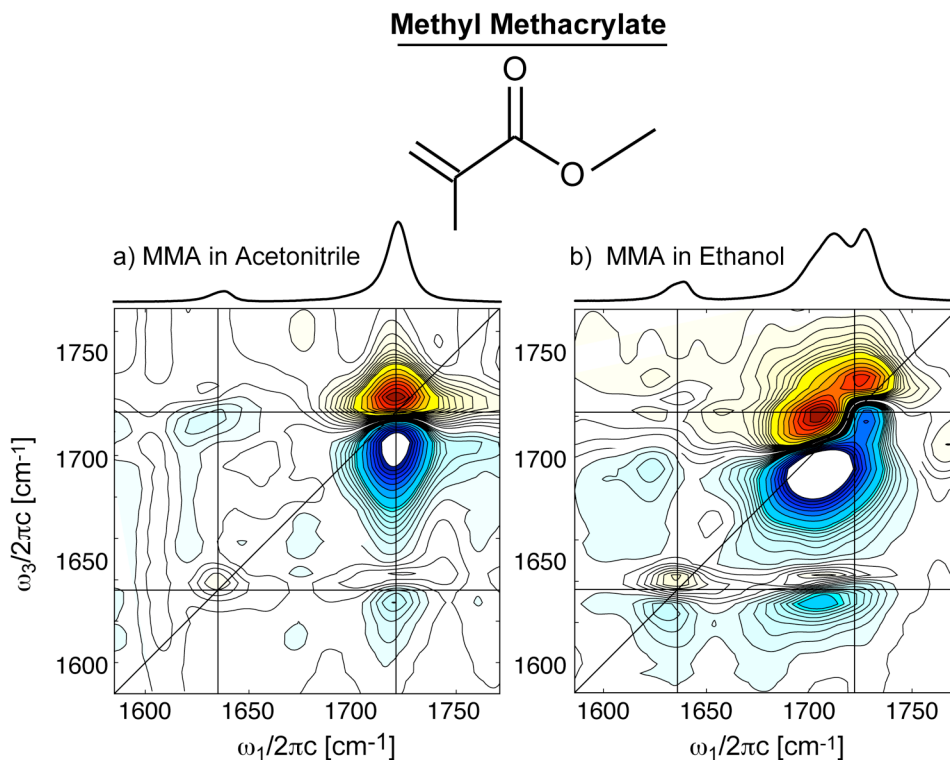


Fig. 2.2.1.1 2D IR step scan spectra of methyl methacrylate in acetonitrile and ethanol.

To demonstrate the method, we take 2D spectra of methyl methacrylate in the finger print region. Fig. 2.2.1.1 shows the phase corrected 2D IR spectrum of methyl methacrylate in acetonitrile and in ethanol taken in step scan mode. The FTIR and 2D IR spectra of MMA in ethanol show a doublet (CO stretch) in the high frequency band due to different number of hydrogen bonds to the carbonyl oxygen. Similar effects are seen in NMA in methanol (Chapter 4). The spectra show distinct cross peaks arising from coupling of the vibrational modes of the CO s (1720 cm^{-1}) and CC s (1640 cm^{-1}).

Fast scanning leads to considerable decrease in data acquisition time. A single step scan spectrum sampling in the time domain at 10 points per cycle over a $T = 4$ ps window requires ~ 16 minutes of data collection averaging at 10 ms per point. A fast scan,

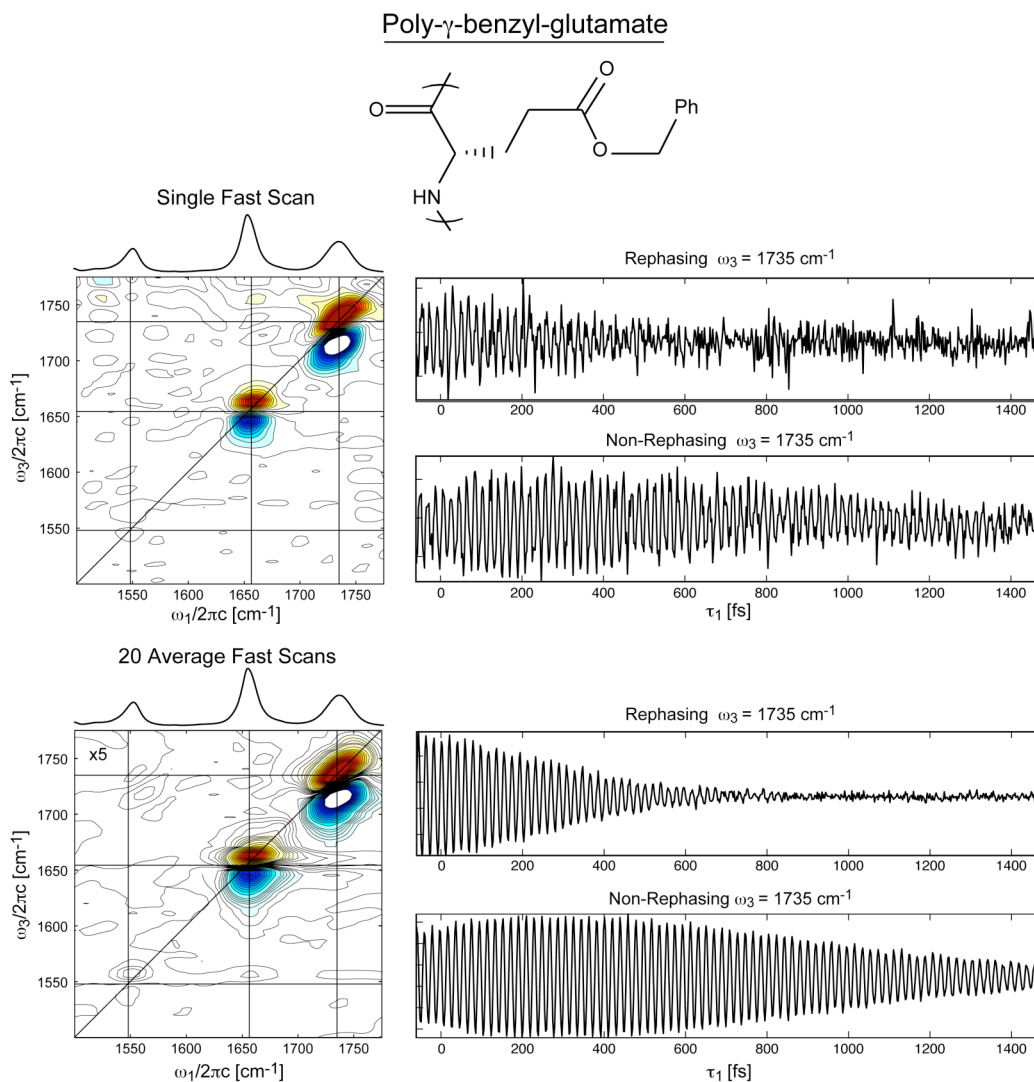


Fig. 2.2.1.2 (Left) 2D IR surface of an idealized helical homopolymers of PBG in CDCl_3 . The 20 average surface is plotted with 5 times more contours between $\pm 10\%$. (Right) Rephasing and non-rephasing time traces at $\omega_3 = 1735 \text{ cm}^{-1}$ are shown. Significant improvement in SNR is observed.

on the other hand, sampling at 10 points per cycle and 10 ms per point over the same window requires only ~ 20 seconds, which is $\sim 48x$ improvement in data collection time.

While step scanning requires the stage to equilibrate its position prior to acquisition, fast

scanning removes this need. For slow noise, this method provides significant improvements in signal to noise. In addition, by averaging more fast scans one can obtain better signal-to-noise in comparable time to step scan. Fig. 2.2.1.2 compares a single fast scan to the average of 20 fast scans of an α -helical forming homopolymer, poly- γ -benzyl glutamate in CDCl_3 , of the ester (1735 cm^{-1}), amide I (1655 cm^{-1}) and amide II (1550 cm^{-1}) transitions. Significant improvement in signal to noise is seen in the rephasing and non-rephasing time traces when 20 fast scans are averaged.

2.3 Conclusion

Phase stability is the most notable advantage of common path interferometers where all beams experience the same environmental disturbances. Phase drifts in pulse timings give rise to ripples that distort the spectral signatures upon Fourier transform. We demonstrated a passively stabilized 2D IR spectrometer using diffractive optics and wedge-pair controlled time delays. The use of a single diffractive optic element to generate the non-collinear box geometry establishes a well-defined phase relationship between pulse replicas and intrinsically phase matches the 2D experiment. The use of transmissive optics to control time delays prevents phase noise due to unstable stages. ZnSe wedges provide exceptionally high time resolution ($0.1\text{ fs}/\mu\text{m}$). Large amplitude ($>10\ \mu\text{m}$) environmental vibrations along the direction of stage motion would be required to induce substantial phase errors. These high amplitude motions are unlikely and the other degrees of freedom of the wedge, including torsion or tilt, are also insignificant.

These advantages lead to a compact diffractive optic/wedge interferometer with sub-fringe phase stability over hours to days, even with minor steering of the input mid-infrared laser due to instabilities in the source. The experimental set up is ideal for long

term studies that require sequential acquisition of 2D surfaces or those that require a high degree of averaging due to weak signal intensity. In addition, high stage reproducibility and resolution allows for fast scanning for improved data collection times and signal-to-noise of 2D IR surfaces.

The wavelength dependence of the diffraction angle of gratings is a significant design constraint for the diffractive optic set up. The tunability of the DO/wedge interferometer is limited to the size of the collection optics and geometry of the wedges. This requires wavelength specific diffractive optics or an adjustable interferometer set up, both with advantages and drawbacks, including cost and system robustness.

As laser spectroscopy advances, the desire for faster pulses and therefore broad spectral bandwidth begin to push the limitations of this experimental design due to the spatial dispersion. The experimental set up described above is ideally suited for less than 200 cm^{-1} of bandwidth, above which pulses are broadened through spectral filtering by clipping of beams. This presents a challenge for overlap between the signal and LO field. Minor misalignment can be compensated using a hollow waveguide to overlap and improved heterodyne detection. An open question remains in regards to the phase and frequency relationship of the signal and LO. This can be resolved through full characterization of the spatial modes and spectral dispersion. This characterization can be performed through up conversion of the mid-infrared into the visible and imaged onto a CCD camera or by controlled masking of the beam profile.¹⁶ Overall system compactness through the use of a four-beam diffractive optics and wedge delay lines allows for long-term stability limited only by the laser source. Often, however, system robustness is at the expense of system versatility and alignment degrees of freedom.

References

- (1) Hochstrasser, R. *Proc. Nat. Acad. Sci.* **2007**, *104*, 14190-14196.
- (2) Hybl, J. D.; Albrecht, A. W.; Gallager-Faeder, S. M.; Jonas, D. M. *Chem. Phys. Lett.* **1998**, *297*, 307-313.
- (3) Scherer, N. F.; Carlson, R. J.; Matro, A.; Du, M.; Ruggiero, A. J.; Romero-Rochin, V.; Cina, J. A.; Fleming, G. R.; Rice, S. A. *J. Chem. Phys.* **1991**, *95*, 1487 -1511.
- (4) Zhang, T.; Borca, C. N.; Li, X.; Cundiff, S. T. *Optics Express* **2005**, *13*, 7432-7441.
- (5) Cervetto, V.; Helbing, J.; Bredenbeck, J.; Hamm, P. *J. Chem. Phys.* **2004**, *121*, 5935-5942.
- (6) Hamm, P.; Lim, M.; Hochstrasser, R. M. *J. Phys. Chem. B* **1998**, *102*, 6123-6138.
- (7) Brixner, T.; Mancal, T.; Stioipkin, I. V.; Fleming, G. R. *J. Chem. Phys.* **2004**, *121*, 4221-4236.
- (8) Goodno, G. D.; Astinov, V.; Miller, R. J. D. *J. Phys. Chem. B* **1999**, *103*, 603.
- (9) Astinov, V.; Kubarych, K. J.; Milne, C. J.; Miller, R. J. D. *Opt. Lett.* **2000**, *25*, 853.
- (10) Shim, S. H.; Strasfeld, D. B.; Zanni, M. T. *Proc. Nat. Acad. Sci.* **2007**, *104*, 14197-14202.
- (11) Cowan, M. L.; Ogilvie, J. P.; Miller, R. J. D. *Chem. Phys. Lett.* **2004**, *386*, 184-189.
- (12) Goodno, G. D.; Dadusc, G.; Miller, R. J. D. *J. Opt. Soc. Am. B* **1998**, *15*, 1791.
- (13) Tian, P.; Keusters, D.; Suzuki, Y.; Warren, W. S. *Science* **2003**, *300*, 1553-1555.
- (14) Brixner, T.; Stoipkin, I. V.; Fleming, G. R. *Opt. Lett.* **2004**, *29*, 884-886.

- (15) Maznev, A. A.; Crimmins, T. F.; Nelson, K. A. *Opt. Lett.* **1998**, *23*, 1378.
- (16) DeCamp, M. F.; DeFlores, L. P.; Jones, K. C.; Tokmakoff, A. *Opt. Express* **2006**, *15*, 233-241.

Chapter 3

Two-dimensional Infrared Spectroscopy in the Pump-Probe Geometry

“The truth may be puzzling. It may take some work to grapple with. It may be counterintuitive. It may contradict deeply held prejudices. It may not be consonant with what we desperately want to be true. But our preferences do not determine what's true. We have a method, and that method helps us to reach not absolute truth, only asymptotic approaches to the truth - never there, just closer and closer, always finding vast new oceans of undiscovered possibilities. Cleverly designed experiments are the key.”-Carl Sagan

The work presented in this chapter has been published in the following paper:

- *L. P. DeFlores, R. N. Nicodemus and A. Tokmakoff, Optics Letters, Vol. 32, No. 20, pp. 2966-2968, 2007.*

Two-dimensional optical and infrared spectroscopy have emerged as important tools for describing molecular dynamics, electronic and vibrational couplings, and structure in applications ranging from biology to materials.¹⁻⁹ Two-dimensional Fourier transform (2D FT) methods transform a third-order nonlinear signal field acquired as a function of an initial excitation and a final detection periods to establish the axes of the

2D spectrum that correlates the frequency evolution. In its different implementations, obtaining maximum frequency resolution and retaining relative phase information across the spectrum requires the ability to separate real and imaginary contributions to the 2D signal and the ability to selectively separate rephasing (R) and non-rephasing (NR) coherence pathways through phase matching or pulse ordering.¹⁰ Present 2D FT methods face the time consuming problem of post-collection “phasing” in constructing absorptive spectra. Phasing is used to correct sub-wavelength errors in relative and absolute pulse timings that in the Fourier transforms mix the absorptive and dispersive components. Using the projection-slice theorem, experiments are commonly constrained by fitting the projection of the 2D absorptive surface to a dispersed pump-probe spectrum.¹⁰ In time domain techniques, this applies one constraint to a problem with three unknowns: the relative timing of R and NR and the absolute τ_1 and τ_3 timings. Alternatively, methods such as double resonance experiments eliminate the need for phasing by using a spectrally narrowed pump and broadband probe at the cost of losing the distinct advantages intrinsic to FT techniques.¹¹ Additional control over pulse phases and timings has been achieved by use of acousto-optic pulse shaping in both the visible and infrared.^{12,13} With these methods one balances the advantage of a high level of control over pulse timing and phase with the disadvantage of low efficiencies and cost.

In this chapter, we demonstrate a method for performing 2D FT spectroscopy in the time domain using a pulse-pair pump and probe geometry that greatly simplifies phasing and readily provides absorptive 2D spectra. This implementation has been discussed previously in the theoretical literature^{10,14-16} and the experimental set up has been demonstrated using an alternate pulse sequence for acquisition of the transient non-

linear polarization.¹⁶ However, despite its simplicity, demonstration as a viable 2D FT technique has not been shown with conventional optics.

3.1 Traditional 2D FT versus 2D FT in the Pump-Probe Geometry

In traditional 2D FT experiments, 2D surfaces are acquired by scanning the delay between the first and second pulse, the excitation period τ_1 , as a function of delay between the third pulse and a local oscillator, which define the detection period τ_3 . Numerical transformation of the signal as a function of τ_1 and τ_3 leads to a 2D spectrum in the conjugate variables ω_1 and ω_3 as a function of τ_2 . In the boxcar geometry, R and NR coherence pathways are separated through pulse time orderings and phase matching conditions.^{10,17} This is pictured in Fig. 3.1.1.1. Time reversal of the independently Fourier transformed R and NR spectra allows the dispersive lobes of the R and NR spectra to properly cancel yielding absorptive line shapes.¹⁸ To improve acquisition time, spectral interferometry of the overlapped signal and local oscillator (reference field) has been implemented by a number of research groups. By performing an optical transform, only the positive frequencies are acquired and the real R and real NR spectra can be added and transformed or visa verse to produce absorptive line shapes. It is critical that the R and NR experiments be properly “phased.” Not only do the relative timings between R and NR need to be determined but also the absolute time zero which determines the peak-shift of the system. In long lived systems with small peak shifts, these errors are less critical; however, studies in systems such as water, these errors strongly affect line shapes. Our group has implemented a number of experimental improvements to accurately correct stage errors and pulse timings in these shortly lived systems.

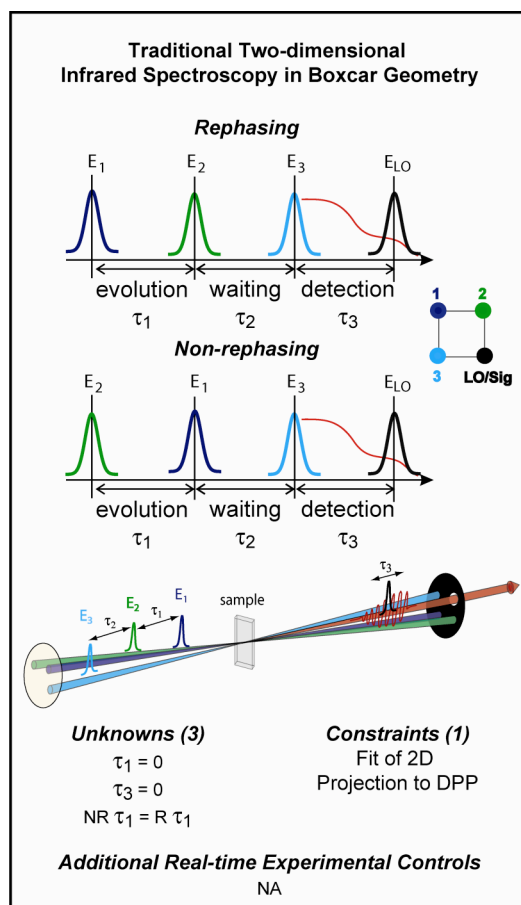


Fig. 3.1.1.1 Experimental geometry of traditional 2D IR Spectroscopy and the experimental unknowns and constraints intrinsic to the set up.

A number of experimental techniques have been employed by other groups to address and ideally eliminate the need for “phasing,” however, generally at the cost of less spectroscopic information and versatility. Early experiments performed by Hamm, et. al. used two broadband laser pulses in which the pump frequency is spectrally selected by using a Fabry-Perot filter. Hamm showed that double resonance techniques provide similar information as the real 2D FT correlation spectrum where the pump axis is convolved with the pulse spectral bandwidth. The simplicity of the experimental set up is at the expense of spectral and temporal resolution and the ability separate coherence pathways.

To improve phase stability between pulses and simplify the experimental set up, Warren and co-workers implemented a collinear 2D FT technique in which pulse timings and phase of three collinear beams are controlled by an acusto-optic pulse shaper to acquire optical 2D spectra. Despite the high degree of control over the pulse sequence, acusto-optic pulse shapers can produce spurious pulses that can amplitude modulate the signal. Recently, the ability to collect 2D surfaces in the infrared using a germanium acusto-optic modulator (AOM) has been demonstrated by the Zanni group.¹² This demonstrated the ability to perform both time and frequency domain techniques using a pump-probe geometry in which one pulse was shaped. Despite minor set backs in efficiencies and spurious pulses using pulse shapers, this is an exciting field which opens opportunities in coherent control of populations as well as methods in which one can selectively control the coherence pathways in the 2D signal.

3.2 The 2D FT Spectrometer

Our 2D FT method uses crossed-beam geometry between a collinear pulse-pair pump and a probe beam and is shown in Fig. 3.2.1.1 The pulse-pair induced change to the probe intensity that is measured by spectral interferometry as a function of the pulse-pair delay τ_1 . Fourier transformation along τ_1 provides identical information to the real part of the 2D correlation experiment performed in the boxcar geometry.^{10,16} Since the pulse pair is collinear and indistinguishable with respect to time ordering, both R and NR coherence pathways contribute to the signal thus removing the need for relative phasing of these two signals. The probe field not only acts as an interaction field but also intrinsically heterodynes the signal, thus eliminating the need for absolute τ_3 phasing. This leaves absolute τ_1 timing as the only unknown to be constrained by the pump-probe fit. With the

τ_3 timing fixed and both coherence orders contributing, spectrally dispersed detection of the probe can be used to directly obtain the absorptive 2D FT spectrum. The single technical disadvantage of this geometry is the inability to independently control the local oscillator intensity for optimizing the heterodyne signal. However, our results show that there is sufficient signal to noise for rapid acquisition of 2D spectra.

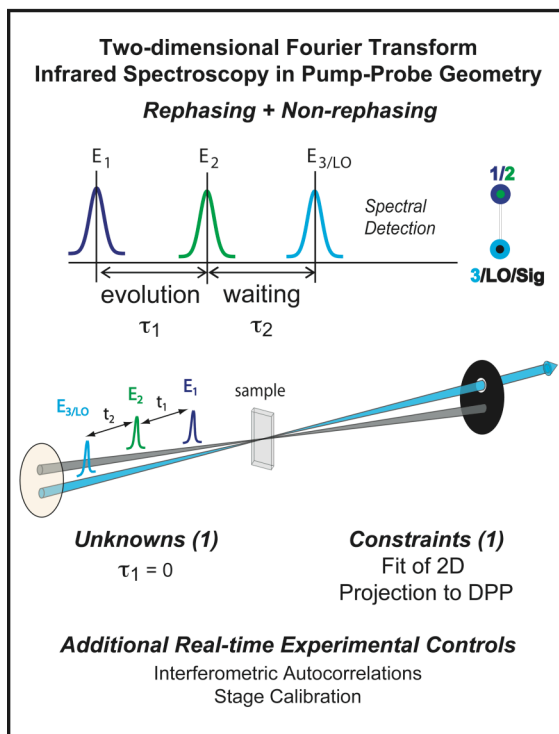


Fig. 3.2.1.1 Experimental geometry of 2D FT Spectroscopy in the pump-probe geometry and the experimental unknowns and constraints intrinsic to the set up. Spectral detection is required for acquisition of correlation spectrum.

Fig. 3.2.1.2 shows the design and layout of the 2D FT IR spectrometer. The home-built laser system used to generate the infrared pulses consists of an amplified Ti:sapphire system (650 μJ , 40 fs, 800 nm, 1 kHz) pumping an optical parametric amplifier after which mid-IR light is generated through difference frequency generation. The output infrared laser is centered at 2050 cm^{-1} with 90 fs pulse duration and 8 μJ of

energy. The IR source is split into three beams using 50/50 KBr beam splitters (BS) and the pulse-pair pump is created by combining beams 1 and 2 onto a third BS. Pulse timings are controlled through translation of ZnSe wedges (W) giving a time step accuracy of $0.01 \text{ fs}/\mu\text{m}$,¹⁹ and a zero-order wave-plate (Karl Lambrecht Corp) and wire-grid polarizer (Thorlabs Inc.) (WP/P) pair controls polarization and pulse intensity. After the sample, the probe beam is spectrally dispersed using a monochromator equipped with a 100 groove/mm grating and imaged onto a 64 channel MCT array. Intensity changes are collected as a function of delay between the pulse pair. To remove the contribution of one pump-probe signal, beam 2 is chopped (C) at 500 Hz and consecutive shots are subtracted. The pulse-pair time delay is generated by stepping or scanning stage 1

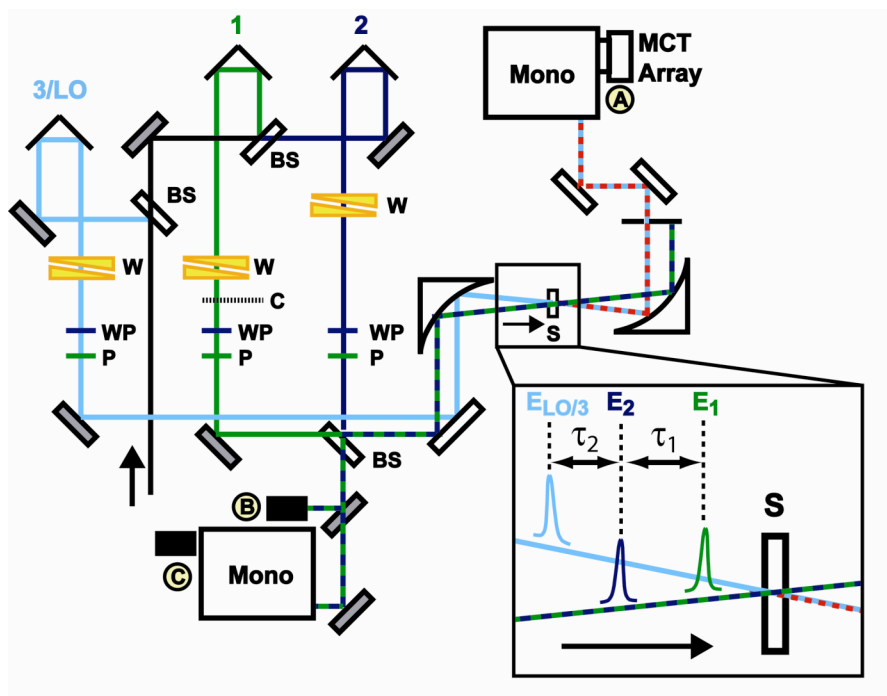


Fig. 3.2.1.2 Experimental set up of 2D IR spectrometer, including acquisition of 2D spectra (A), interferometric autocorrelation (B) and stage calibration (C).

relative to the other pulses. The scanning method allows for rapid acquisition of 2D spectra at a rate of ~ 1 ps delay/15 seconds. The other pump-probe signal generated between beams 1 and 3 is removed by the final Fourier transform along τ_1 .

In conjunction with acquisition of the 2D spectrum, the interferometric autocorrelation and interference fringes for stage calibration are simultaneously collected to achieve sub-fringe timings in τ_1 . An out-of-phase replica of the pulse pair is generated off the back side of the third beam splitter. A small reflection of the pulse pair is directly monitored using a single channel MCT to collect the interferometric autocorrelation. The signal measured here defines an absolute time zero for the experiment, which is required for accurate phasing of the 2D FT spectrum. The detailed procedure for phasing the 2D spectrum is given in Fig. 3.2.1.3 The interference fringes generated by imaging the remaining IR pulse pair through a monochromator centered at 2050 cm^{-1} with a resolution of 1 cm^{-1} are collected by a single channel MCT detector. The stage calibration is determined by performing a fast Fourier transform (FFT) of this interference trace as a function of τ_1 . The frequency of the transformed trace is compared with the position of the monochromator to determine the overall stage calibration. The individual and overall stage corrections are applied to the original time axis, as is the absolute time zero correction determined by the interferometric autocorrelation (see Chapter 2 for more details). Since an interferometric autocorrelation is symmetric in time, the symmetry point of this interference defines time zero. This correction is applied the τ_1 axis and a new axis is made. The raw 2D data is interpolated onto the new time axis and a FFT is performed to acquire the frequency-frequency 2D surface. The ω_1 frequency axis is

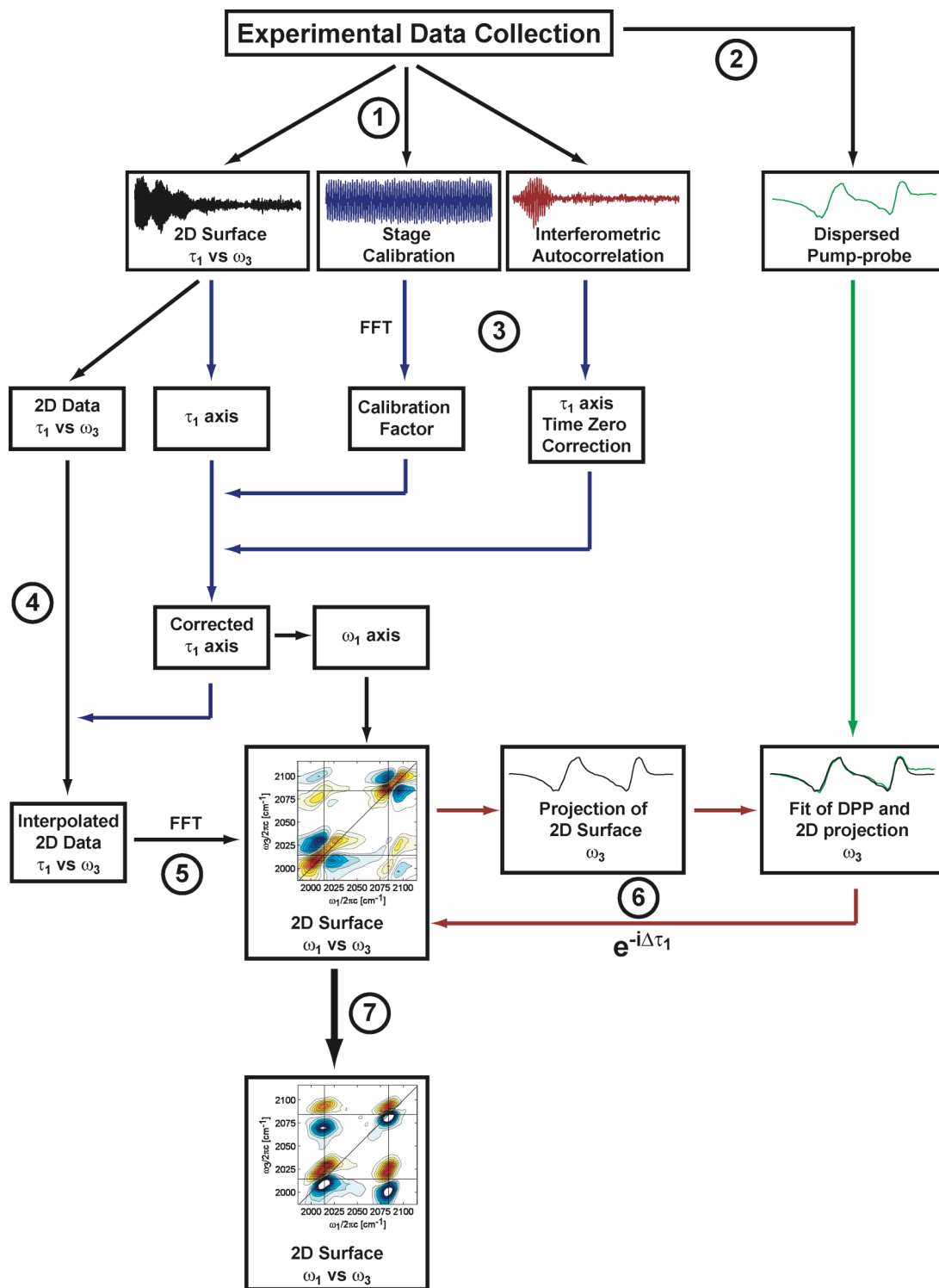


Fig. 3.2.1.3 Flow chart of stage calibration and acquisition and phasing of a 2D FT spectrum

determined from the corrected time axis. The ω_3 axis is determined from calibration of the array through spectral interferometry. This is performed independent of the actual experiment. Once the frequency-frequency surface is obtained, the surface is projected onto the ω_3 axis and compared to the dispersed pump-probe. The dispersed pump probe can be collected prior to the experiment at a given waiting time by blocking beam *I* (the non-chopped beam). The surface is corrected by iterating a phase factor along ω_1 that is proportional to the error in absolute timing of τ_1 . This factor is multiplied by the transformed data and the fit is iterated to minimize the difference using a least squares method. Once the fit is determined, the final 2D surface is acquired. Using this method, the stage positions can be determined with better than $\lambda/100$ precision. These additional elements allow for real-time data acquisition and calibration of pulse timing, which to this point have been a major obstacle of 2D FT spectroscopy.

3.3 Results

In Fig. 3.2.1.4, we present polarization 2D IR spectra of dicarbonyl-acetylacetonato-rhodium (RDC) in hexane and deuterated chloroform (CDCl_3). Time-frequency (ω_3 vs. τ_1) 2D surfaces are collected in approximately one minute by scanning stage *I* from τ_1 of -250 fs to 4250 fs and surfaces are numerically Fourier transformed to acquire the real part of the 2D correlation spectrum. Due to the constraints of the wedge design, the longest relative stage delay achieved was 4500 fs, thus truncation of the time scans relative to the inverse line width of the symmetric and asymmetric modes causes small aliasing peaks appear in ω_1 in the case of RDC in hexane. Absolute zero is determined from the interferometric autocorrelation to better than a fringe and the

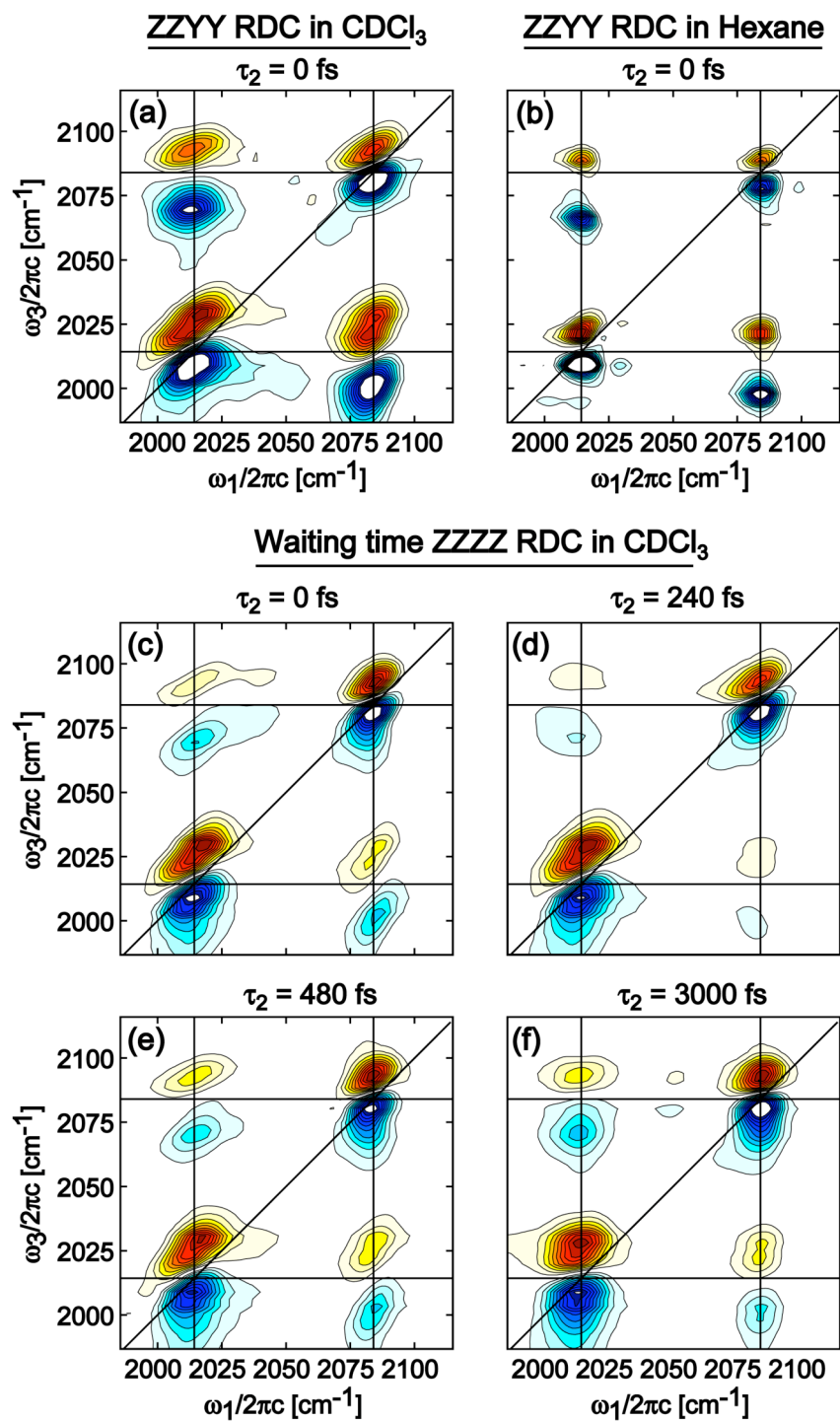


Fig. 3.3.1.1 2D FT spectrum of RDC in hexane showing the polarization selectivity and the 2D FT waiting time series of RDC in CDCl_3 .

projection of the 2D surface onto the ω_3 axis is then fit to the dispersed pump-probe to achieve sub fs timing. This reduces the phasing problem to one variable, the absolute τ_1 timing, to fit one constraint, the data projected onto ω_3 . Alternatively, symmetric scanning of the pulse pair can be performed to define absolute zero. This however requires the use of two choppers to properly remove the pump-probe response.

By comparing the line shapes in 2D spectra of RDC in hexane and CDCl_3 , the degree of inhomogeneity in these systems can be seen. In agreement with previous studies,² the peak structure of RDC in hexane is narrow and symmetric (Fig. 3.2.1.4b) while RDC in CDCl_3 is diagonally elongated indicative of inhomogeneous broadening (Fig. 3.2.1.4a). In addition, the appearance of cross peaks, arising from vibrational coupling, is seen in all these spectra, as well as the diagonal elongation attributed to correlated inhomogeneous broadening.

Spectra reflecting vibrational dynamics and relaxation are acquired by controlling the waiting time delay between the pulse pair and the probe beam. In Fig. 3.2.1.4c-f, waiting spectra of $\tau_2 = 0$ fs, 240 fs, 480 fs and 3000 fs in the ZZZZ polarization are shown. In this system, energy coherently transfers between the modes in RDC with an oscillation period of 480 fs.²⁰ The intensities and tilts of the cross peaks, reflecting correlated broadening, are modulated at this period, as seen in the $\tau_2 = 240$ fs and 480 fs spectra. At a waiting time of 3000 fs, the off-diagonal peaks grow in and the diagonal resonances become symmetric. Both are salient features of vibrational relaxation in a 2D spectrum. Fig. 3.2.1.5 and 3.2.1.6 show the full waiting time series for ZZZZ and ZZYY of RDC in hexane and CDCl_3 respectively.

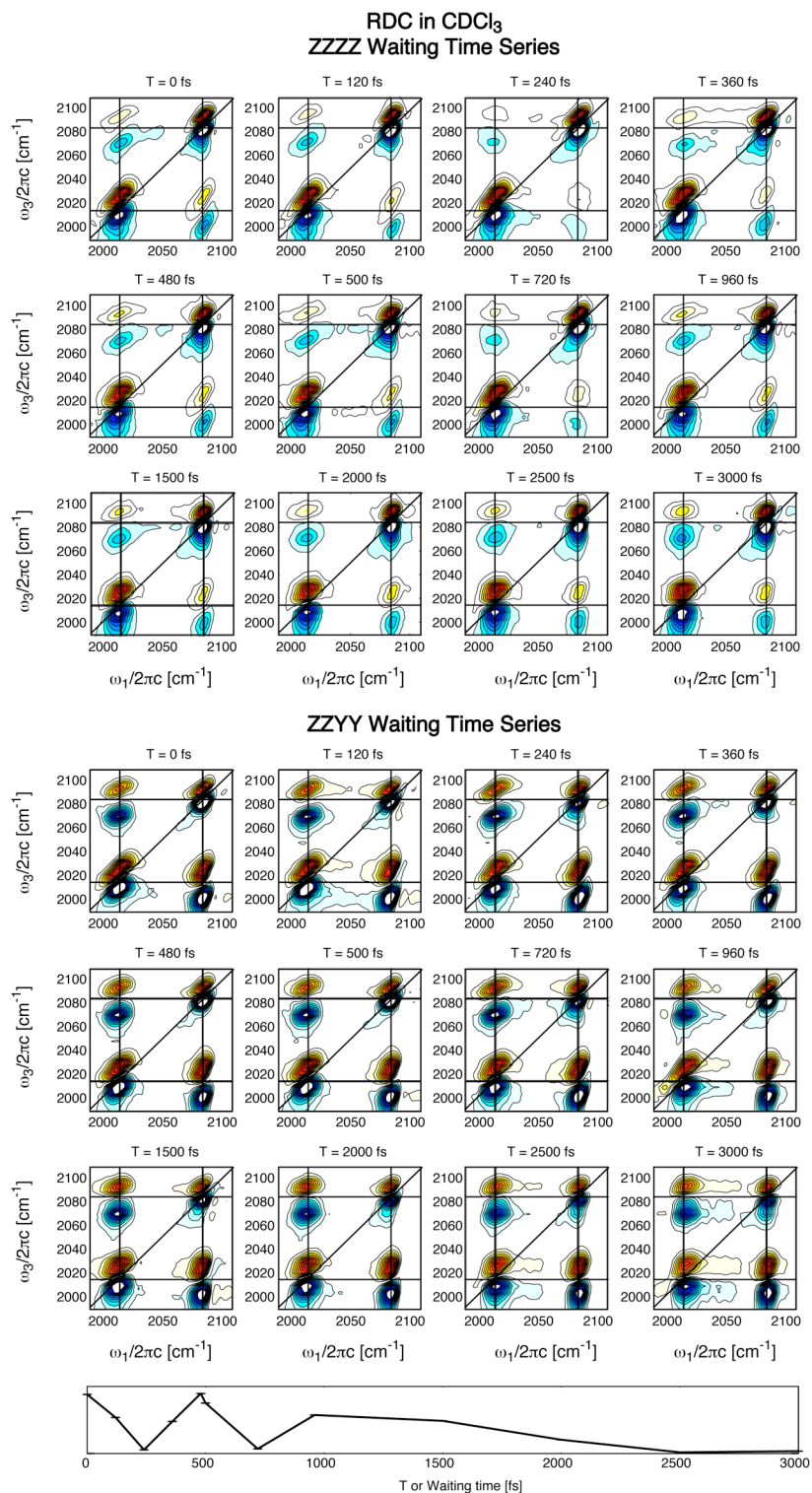
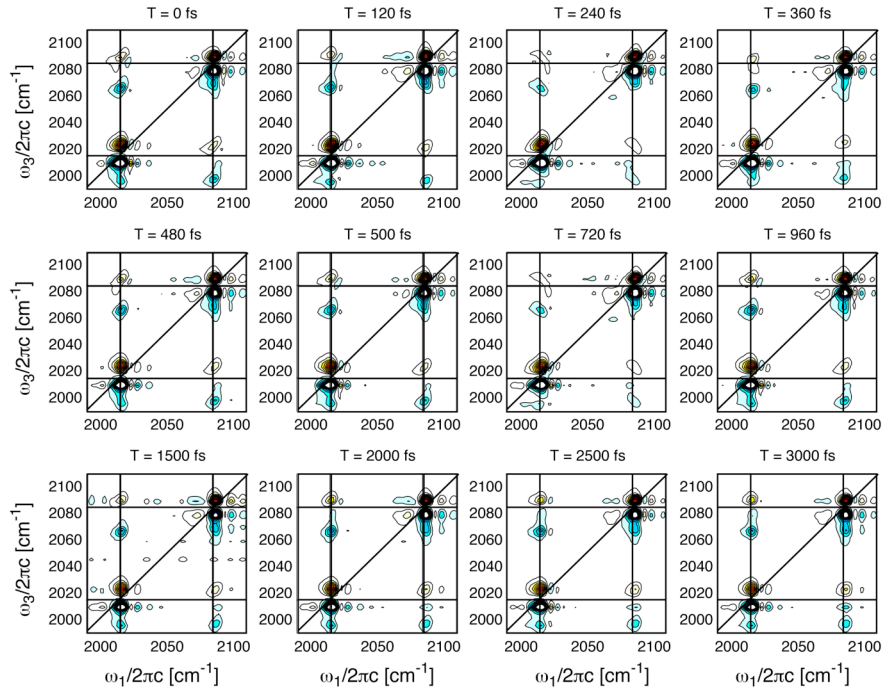


Fig. 3.3.1.2 ZZZZ and ZZYY 2D IR waiting time series of RDC in CDCl_3 . Bottom panel is the integrated area of the ZZZZ cross peak region versus waiting time.

RDC in Hexane
ZZZZ Waiting Time Series



ZZYY Waiting Time Series

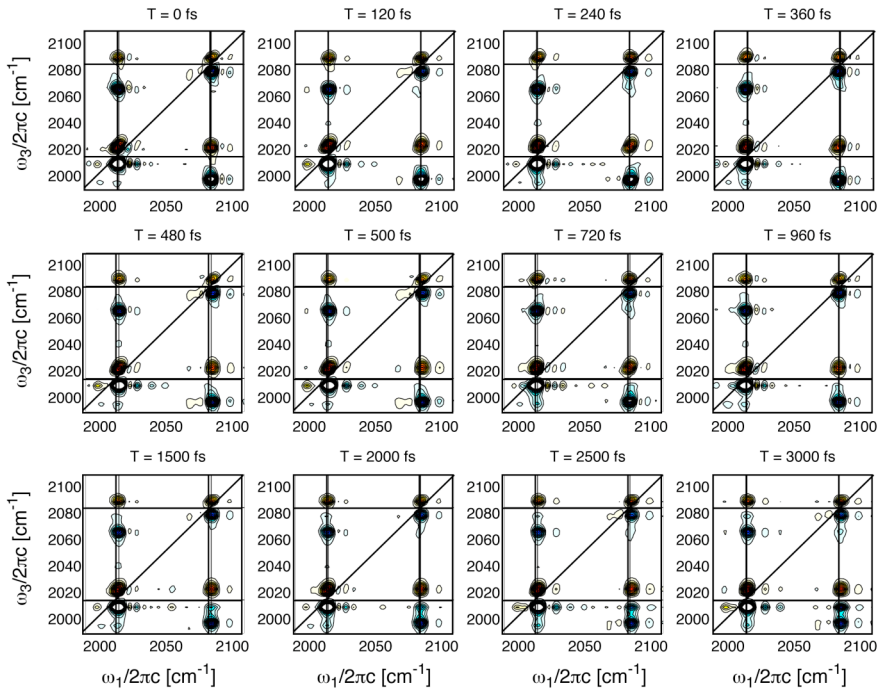


Fig. 3.3.1.3 ZZZZ and ZZYY 2D IR waiting time series of RDC in hexane.

We have also demonstrated the capability to acquire polarization-sensitive 2D spectra that provides information about dipole orientation and molecular structure. This is seen by comparison of the off-diagonal resonance intensities in the ZZYY and ZZZZ $2=0$ surfaces (Fig. 3.2.1.4a and c). The relative increase in intensity of the ZZYY cross peaks arises from the $\sim 90^\circ$ angle between the transition dipole moments of the symmetric and asymmetric modes of the RDC molecule. All tensor elements of the third order polarization can be obtained by implementing schemes used in transient dichroism and birefringence techniques. The ZYZY element is obtained by placing the pump pulse pair 45° and 135° and the analyzer approximately 90° with respect to the probe. This allows for the analyzer to act as the heterodyning field with a small misalignment of the polarization. In principle, introduction of a quarter wave plate in the path of beam 3 using the above polarization scheme, allows for the dispersive component of the third order polarization to be acquired, making this technique highly versatile with few experimental drawbacks. In practice, this requires polarizers with high extinction ratios to fully

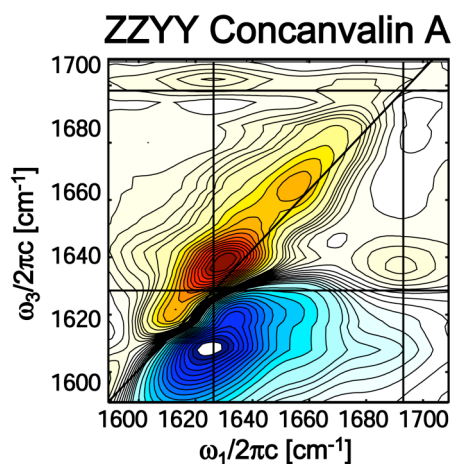


Fig. 3.3.1.4 ZZYY 2D FT spectrum of concanavalin A.

extinguish the probe beam to acquire pure heterodyne signal. The enhancement seen with 100:1 extinction is approximately 2-3 times in heterodyne signal intensity.

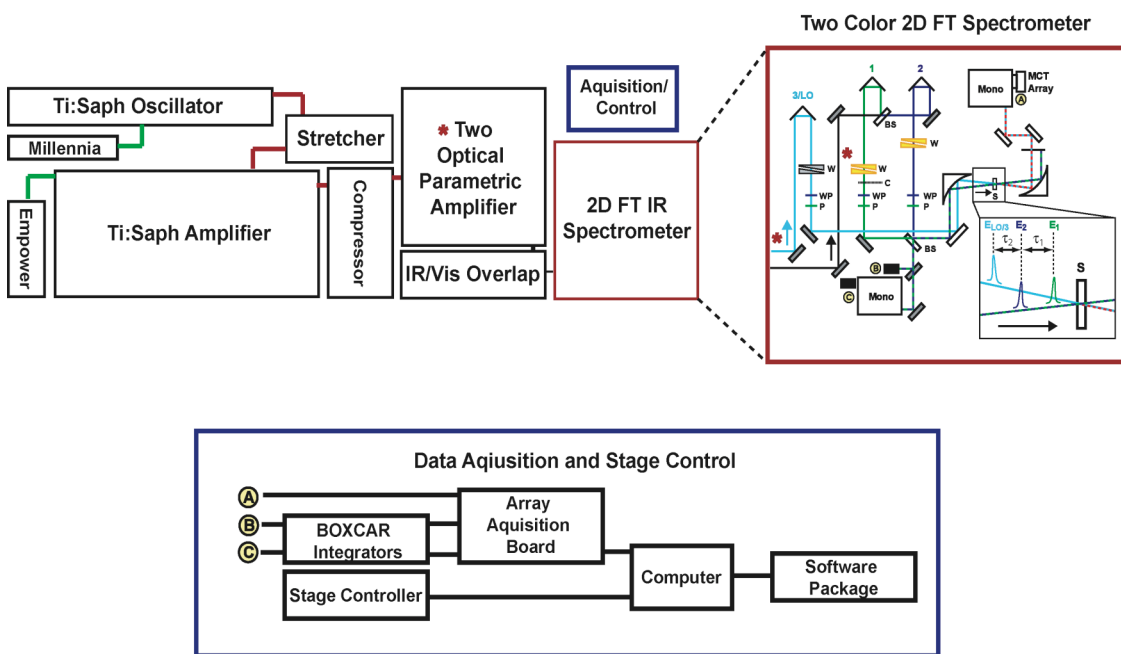


Fig. 3.3.1.5 Experimental set up for 2-Color 2D FT spectrometer with modification from the current experimental design.

As a further test of the simplicity and reliability of the technique and the ability to measure weaker signals, we show a 2D spectrum of the β -sheet protein concanavalin A in D_2O in Fig. 3.2.1.7 with a pulse spectrum centered at 1650 cm^{-1} . The amide I 2D spectrum shows the characteristic features of an anti-parallel β sheet with strong cross peaks between the ν_{\perp} and ν_{\parallel} modes as well as a high degree of inhomogeneous broadening along the diagonal.²¹ The appearance of inhomogeneous broadening in all these spectra implies the proper balance of R and NR signals. In later chapters, the use of 2D FT spectroscopy with broadband mid-IR will be demonstrated with a bandwidth that covers the entire amide finger print region.

Conclusion

Here we have demonstrated a simplified implementation of 2D IR spectroscopy in the pump-probe geometry using conventional optics without loss of spectral and temporal resolution or of quantitative information. Due to the indistinguishability of the pulse pair with respect to time ordering and phase matching, and the third field acting as a probe and reference field, the underdetermined phasing problem is eliminated. This method also provides opportunities for a simple extension of 2D FT spectroscopy to multi-color and broadband continuum experiments without the need to account for phase matching conditions as shown in Fig. 3.2.1.8. Modifications are shown by the red stars, which indicate the use of multiple OPAs for generation of separate wavelengths. The initial beam splitter is no longer required as the second color is now used as the probe (or beams 3 and LO). The rest of the set up will remain identical, as will acquisition of the 2D surface and stage positioning. Due to the nature of the experiment in which there is no need for phase matching, two-color and broadband experiments are intrinsically phased matched. Minor modifications can be made for single color applications in the UV, optical, infrared and terahertz regions. This requires beam splitters and mirrors with different optical coatings and detectors with different sensitivities but the overall set up is still applicable. Therefore, 2D FT spectroscopy in the pump-probe geometry is an exceptionally versatile tool opening up the accessibility of 2D IR to the broader scientific audience.

References

- (1) Hamm, P.; Lim, M.; Hochstrasser, R. M. *J. Phys. Chem. B* **1998**, *102*, 6123-6138.
- (2) Khalil, M.; Demirdoven, N.; Tokmakoff, A. *J. Phys. Chem. A* **2003**, *107*, 5258-5279.
- (3) Krummel, A. T.; Mukherjee, P.; Zanni, M. T. *J. Phys. Chem. B* **2003**, *107*, 9165-9169.
- (4) Chung, H. S.; Khalil, M.; Smith, A. W.; Ganim, Z.; Tokmakoff, A. *Proc. Natl. Acad. Sci. USA* **2005**, *102*, 612-617.
- (5) Brixner, T.; Stenger, J.; Vaswani, H. M.; Cho, M.; Blankenship, R. E.; Fleming, G. R. *Nature* **2005**, *434*, 625-628.
- (6) Bredenbeck, J.; Helbing, J.; Kumita, J. R.; Woolley, G. A.; Hamm, P. *PNAS* **2005**, *102*, 2379-2384.
- (7) Borca, C. N.; Zhang, T.; Li, X.; Cundiff, S. T. *Chem. Phys. Lett.* **2005**, *416*, 311-315.
- (8) Zheng, J. R.; Kwak, K.; Asbury, J.; Chen, X.; Piletic, I. R.; Fayer, M. D. *Science* **2005**, *309*, 1338-1343.
- (9) Loparo, J. J.; Roberts, S. T.; Tokmakoff, A. *J. Chem. Phys.* **2006**, *125*, 194521.
- (10) Gallagher Faeder, S. M.; Jonas, D. M. *J. Phys. Chem. A* **1999**, *103*, 10489-10505.
- (11) Cervetto, V.; Helbing, J.; Bredenbeck, J.; Hamm, P. *J. Chem. Phys.* **2004**, *121*, 5935-5942.
- (12) Shim, S. H.; Strasfeld, D. B.; Zanni, M. T. *Proc. Nat. Acad. Sci.* **2007**, *104*, 14197-14202.
- (13) Tian, P.; Keusters, D.; Suzuki, Y.; Warren, W. S. *Science* **2003**, *300*, 1553-1555.

- (14) Jonas, D. M. *Annu. Rev. Phys. Chem.* **2003**, *54*, 397-424.
- (15) de Boeij, W. P.; Pshenichnikov, M. S.; Wiersma, D. A. *Annu. Rev. Phys. Chem.* **1998**, *49*, 99-123.
- (16) Emde, M. F.; de Boeij, W. P.; Pshenichnikov, M. S.; Wiersma, D. A. *Opt. Lett.* **1997**, *22*, 1338.
- (17) Khalil, M.; Demirdöven, N.; Tokmakoff, A. *Phys. Rev. Lett.* **2003**, *90*, 47401-47404.
- (18) Ernst, R. R.; Bodenhausen, G.; Wokaun, A. *Principles of Nuclear Magnetic Resonance in One and Two Dimensions*; Oxford University Press: Oxford, 1987.
- (19) Brixner, T.; Stoipkin, I. V.; Fleming, G. R. *Opt. Lett.* **2004**, *29*, 884-886.
- (20) Khalil, M.; Demirdöven, N.; Tokmakoff, A. *J. Chem. Phys.* **2004**, *121*, 362.
- (21) Demirdöven, N.; Cheatum, C. M.; Chung, H. S.; Khalil, M.; Knoester, J.; Tokmakoff, A. *J. Am. Chem. Soc.* **2004**, *126*, 7981-7990.

Chapter 4

The Anharmonic Vibrational Potential and Relaxation Pathways of the Amide I and II Modes of *N*-methylacetamide

“In order to make an apple pie from scratch, you must first create the universe.”-Carl Sagan

The work presented in this chapter has been published in the following paper:

- *L. P. DeFlores, Z. Ganim, S. F. Ackley, H.S. Chung and A. Tokmakoff, JPCB, 110, pp. 18973, 2006*

4.1 Introduction

The influence of isotopic substitution and solvation of *N*-methylacetamide (NMA) on anharmonic vibrational coupling and vibrational relaxation of the amide I and amide II modes is investigated. Differences in the anharmonic potential of isotopic derivatives of NMA in D₂O and DMSO-d₆ are quantified by extraction of the anharmonic parameters and the transition dipole moment angles from cross peaks in the two-dimensional infrared

(2DIR) spectra. To interpret the effects of isotopic substitution and solvent interaction on the anharmonic potential, density functional theory (DFT) and potential energy distribution (PED) calculations are performed. It is shown that the origin of anharmonic variation arises from differing local mode contributions to the normal modes of the NMA isotopologues, particularly in amide II. The time domain manifestation of the coupling is the coherent exchange of excitation between amide modes seen as the quantum beats in femtosecond pump-probes. The biphasic behavior of population relaxation of the pump-probe and 2DIR experiments can be understood the rapid exchange of strongly coupled modes within the peptide backbone, followed by picosecond dissipation into weakly coupled modes of the bath.

NMA is a widely used model compound for investigations into the physical and chemical properties of the amide group, particularly for the purpose of understanding the behavior of one of many peptide linkages in proteins and peptides. Studies of the amide I vibration of NMA have provided insight for vibrational relaxation pathways within peptides,^{1,2} peptide solvation and peptide-solvent hydrogen bonding interactions.^{1,3-9} Vibrational techniques show that polar solvents cause large solvatochromic shifts of the amide I and II modes from the gas phase depending on the solvent by stabilizing the ionic resonance structure of NMA.¹⁰ The infrared spectroscopy of the amide I vibration is also of interest for its role in understanding the origin of the sensitivity of protein amide I spectroscopy to secondary structure. Many amide I spectroscopic models are based on coupled amide I oscillators,^{1,11} in which NMA is used as a model for the individual sites. Less studied are the couplings between vibrations of the amide group, and their consequences for vibrational relaxation pathways.^{1,12} Most descriptions of the vibrational

motion in proteins and peptides assume the backbone is described by weakly coupled normal modes. However, little has been done to test such notions and fundamental questions still remain: What is the inherent anharmonic nature of the amide vibrations? How does this manifest itself in terms of vibrational relaxation processes? How is this influenced by the solvent environment and molecular composition?

The connection between vibrational eigenstates and local atomic displacements provides a direct link from spectroscopic observables to structure of the protein and peptide backbone. Uniformly, the analysis of NMA and protein vibrations is treated in a harmonic basis, a largely untested assumption that the normal modes are only weakly anharmonic and show negligible coupling. *Ab initio* calculations of NMA in the gas phase and condensed phase have been used to describe the composition of the spectroscopically observable normal modes in a local, or atomic, mode picture,^{10,13-15} addressing the role of anharmonicity through various frequency scaling techniques.¹⁶⁻¹⁸ Similarly, NMA experimental studies are interpreted with an amide normal mode picture whose coordinates may vary with different isotopic species,^{14,19-21} but anharmonicity of the potential remains largely untested.²² Some theoretical efforts have been made towards calculating protein vibrational spectroscopy directly from anharmonic potential energy surfaces^{13,23,24} and these studies argue that harmonic force fields are inadequate to describe their spectroscopy. Recent work by Hayashi and co-workers have developed a detailed DFT electrostatic map for predicting the fundamental and combination bands of many amide modes including electrostatic induced solvent effects.²⁵ In the same spirit of these calculations, to appropriately capture intramolecular dynamics and energy flow

within the vibrational modes, experimental techniques sensitive to anharmonic properties of a system are required.

In this chapter, we examine the anharmonic nature of amide I and II vibrations of NMA using two-dimensional infrared (2DIR) spectroscopy, a technique inherently sensitive to the anharmonic vibrational potential of the molecule and ultrafast vibrational relaxation. 2DIR is a femtosecond Fourier transform spectroscopy, which characterizes how vibrational excitation of a mode at frequency ω_1 evolves and is detected in a mode at frequency ω_3 . Cross peaks in a 2DIR spectrum are an indication of coupled vibrations, and the pattern of peaks in a 2DIR spectrum can be used to characterize their anharmonic potential.^{26,27} 2DIR spectra acquired as a function of waiting time τ_2 between excitation and detection allow for vibrational relaxation pathways to be unraveled.²⁸ Here we quantify the amide I/amide II anharmonic coupling strength, the projection angle between their transition dipole moments, and explore pathways for energy relaxation through the use of pump-probe and transient 2DIR experiments. Specifically, these experiments explore the role of solvent and isotopic labeling of NMA on these properties, finding that both of these variables introduce important effects. We will emphasize the need for more explicit models that account for anharmonic coupling that can capture more appropriate dynamics in the protein backbone.

4.2 Amide I/II 2D IR Spectroscopy

Absorptive two-dimensional infrared spectra were acquired as described in detail elsewhere.²⁷ Briefly, the Fourier transform 2DIR experiments were performed with pulsed mid-IR radiation derived from an amplified Ti:sapphire pumped optical parametric amplifier. The pulse spectrum was tuned such that the $\sim 185\text{ cm}^{-1}$ bandwidth

(FWHM) is centered to cover both the fundamental ($\nu=0\rightarrow 1$) and anharmonically shifted ($\nu=1\rightarrow 2$) overtones of both the amide I and amide II modes of NMA. Three femtosecond pulses sequentially drive the resonant transitions, giving rise to a radiated signal that is heterodyne-detected through spectral interferometry with a local oscillator pulse. A 2D spectrum is obtained from a signal acquired as a function of initial pulse delay τ_1 and detection frequency ω_3 by numerically Fourier transforming with respect to τ_1 . The absorptive 2DIR spectrum is obtained from a sum of rephasing ($k_R = -k_1+k_2+k_3$) and nonrephasing ($k_{NR} = k_1-k_2+k_3$) 2D spectra. The polarization of the mid-IR pulses was controlled with pairs of $\lambda/2$ waveplates and wire-grid polarizers. Polarization-selective 2DIR experiments were performed in the parallel (ZZZZ) and perpendicular (ZZYY) geometries, and magic angle spectra were reconstructed for each by summing ZZZZ + 2·ZZYY. For relaxation studies, diagonal and cross peaks for the absolute-value magic angle rephasing spectra are integrated for multiple spectra acquired as a function of delay time τ_2 between excitation and detection.

Polarization-selective pump-probe measurements were taken using identical conditions as the 2DIR experiments, by spectrally dispersing the transmitted probe pulse onto an array detector. Dispersed pump-probe spectra are used to phase the 2DIR spectra. Also, pump-probe transient signals are detected as a function of delay τ_2 at the amide I and II fundamental transition frequency. Signals are acquired for the parallel and perpendicular polarizations, and the magic-angle pump-probe is reconstructed for each.

All chemical were purchased from Aldrich and used without further purification. *N*-methylacetamide- d_7 (NMA- d_7) and *N*-methylacetamide- h_7 (NMA- h_7) were dissolved in D_2O , dimethylsulfoxide- d_6 (DMSO- d_6) and chloroform- d_1 ($CDCl_3$), and held in a CaF_2

sample cell with a 50 μm spacer. Only in the case of NMA-h₇ prepared in D₂O will the amide hydrogen exchange with the solvent giving NMA-d₁. Sample concentrations (~ 0.10 mM) were chosen to maintain a peak optical density of ~ 0.4 for the amide I and amide I' transitions and ~ 0.1 for the amide II and amide II'. For clarity in the remainder of paper, the conventional amide notation where primes denote deuterated species will be replaced by explicitly defining the isotopic species of NMA with (-h₇, -d₇, -d₁).

4.3 Results

The FTIR spectra of isotopologues of NMA in DMSO-d₆, CDCl₃, and D₂O are given in Fig. 4.3.1.1. Solvation and isotope labeling strongly dictate the vibrational frequencies, intensities, and line widths of the linear spectrum. The amide I vibration red shifts with increasing interaction and polarity of solvent and the amide II vibration blue shifts correspondingly from the gas phase values. The anti-correlated frequency shifts can be understood as an increased stabilization of the resonance form of NMA by polar solvents.^{10,14} The lengthening of the carbonyl bond in the resonance structure reduces the vibrational frequency of the amide I mode, while shortening the CN bond and inducing a blue shift of the amide II mode.

Labeling the amide hydrogen weakly red shifts the amide I and strongly red shifts the amide II band due to the different contribution of ND in-plane bending (ib). The affect of methyl group deuteration, seen by comparing NMA-d₇ in D₂O with NMA-d₁ in D₂O, is to red shift both amide I and II transitions. This is a result of the methyl deformation contribution to these modes. An interesting feature seen in the NMA-d₁/D₂O spectrum is the presence of the amide II doublet between 1492 and 1514 cm^{-1} . The

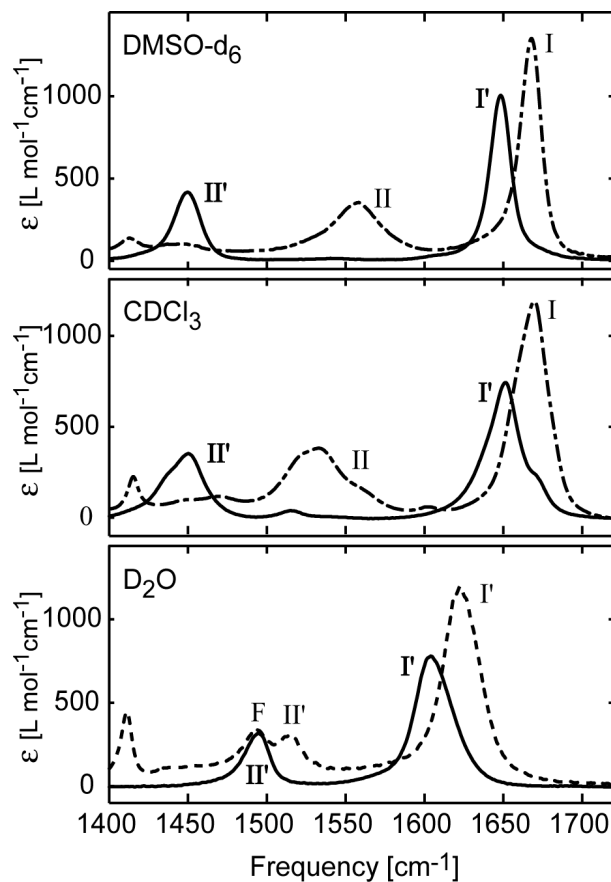


Fig. 4.3.1.1 FTIR spectra of NMA-h₇ (dot-dashed), NMA-d₇ (solid) and NMA-d₁ (dashed) in DMSO-d₆, CDCl₃, and D₂O. Prime denotes amide vibration with a deuterated amide group.

doublet arises from mixing of a combination band of low energy backbone modes with the amide II vibration (1514 cm⁻¹), giving rise to a Fermi resonance at 1492 cm⁻¹.²⁰ The Fermi resonance is not seen in other spectra in which the splitting may be small and only appear as a shoulder on the amide II peak. This may be the case for NMA in CDCl₃ where the amide II region appears as overlapping resonances.

To further examine the effects of solvent and isotopes on the vibrational spectrum of NMA, the left column in Fig. 4.3.1.2 shows polarization selective 2DIR surfaces of NMA-d₇ in D₂O (NMA-d₇/D₂O) and NMA-h₇ in DMSO-d₆ (NMA-h₇/DMSO-d₆). In all

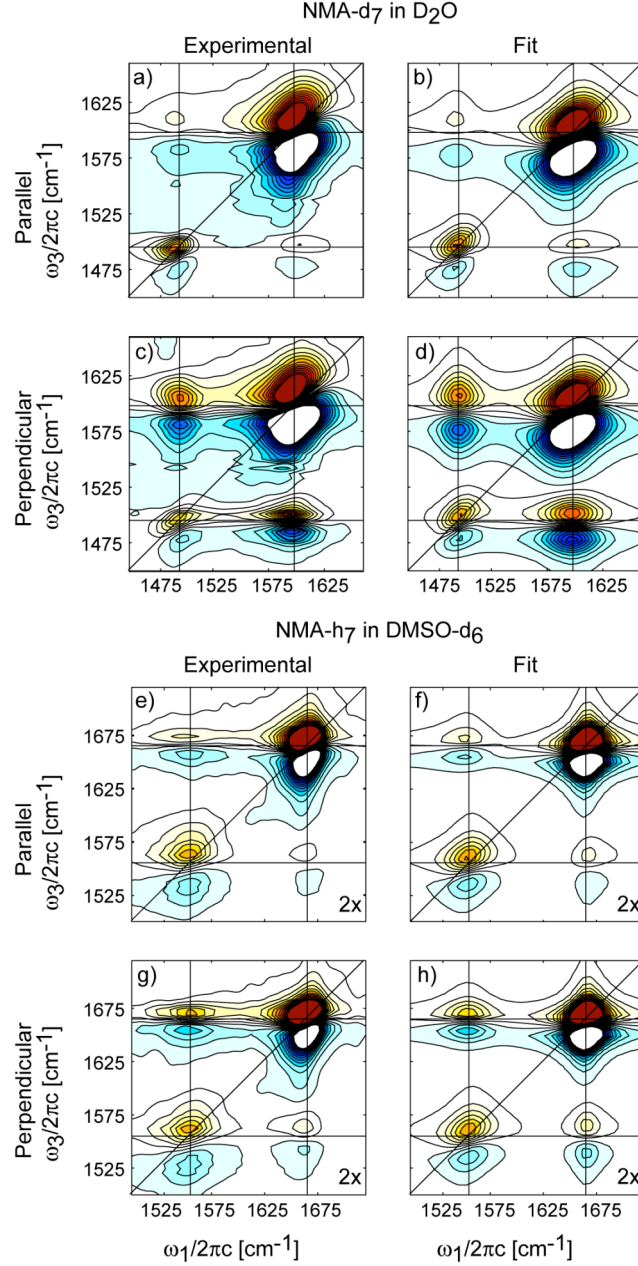


Fig. 4.3.1.2 Experimental absorptive 2DIR spectrum of NMA-d₇/D₂O obtained at $\tau_2 = 80$ fs for parallel (a) and perpendicular (c) polarization, and for NMA-h₇/DMSO-d₆ (e,g). Corresponding fits, (b,d) and (f,h) respectively, are plotted to their right. For each normalized amide I spectrum, twenty-six equally spaced contours are plotted from $\pm 60\%$ for NMA-d₇/D₂O and from $\pm 30\%$ for NMA-h₇/DMSO-d₆. The fit parameters of NMA-d₇/D₂O for the six level system are $\omega_{AI'} = 1598$ cm⁻¹, $\omega_{AII'} = 1495$ cm⁻¹, $\Delta_{AI'} = 15$ cm⁻¹, $\Delta_{AII'} = 11$ cm⁻¹, $\Delta_{AI',AII'} = 11$ cm⁻¹, $\mu_{AI'} = 1$, $\mu_{AII'} = 0.58$, $\mu_{2AI',AI'} = 1.51(1.41)$, $\mu_{2AII',AII'} = 0.68(0.82)$, $\mu_{AI',AII'} = 1.0(1.0)$, $\mu_{AII',AI'} = 0.58(0.58)$, and $\Theta = 75^\circ$. For NMA-h₇/DMSO-d₆ the fit parameters are $\omega_{AI} = 1665$ cm⁻¹, $\omega_{AII} = 1555$ cm⁻¹, $\Delta_{AI} = 12$ cm⁻¹, $\Delta_{AII} = 10$ cm⁻¹, $\Delta_{AI,AII} = 3.8$ cm⁻¹, $\mu_{AI} = 1$, $\mu_{AII} = 0.84$, $\mu_{2AI,AI} = 1.41(1.41)$, $\mu_{2AII,AII} = 1.09(1.19)$, $\mu_{AI,AII} = 0.98(1.0)$, $\mu_{AII,AI} = 0.84(0.84)$, and $\Theta = 40^\circ$. ω is the vibrational frequency, Δ is the anharmonicity and μ is the transition moment amplitude. Harmonic scaling values are given by parentheses.

spectra, we observe amide I and II diagonal peaks and cross peaks, and each appears as an oppositely signed doublet. The diagonal features in the 2DIR spectrum provide information about the nuclear potential of a single vibrational coordinate, here the amide I and II modes. The positive and negative peaks along the diagonal arise from ground state bleach and excited state absorption, respectively. The splitting of the doublet along ω_3 gives the difference between the fundamental and overtone transitions, and is therefore a measure of the diagonal anharmonicity. Ellipticity or diagonal elongation of the peak, seen clearly for the diagonal amide I peak of NMA-d₇/D₂O, is an indication of the inhomogeneous broadening. This arises from variation of local solvent environments and their dynamics, and is discussed in detail elsewhere.²⁹ Cross-peaks reflect the case where excitation of one resonance influences another transition, and arises from couplings between different vibrational coordinates. The splitting of the cross peaks along ω_3 gives the off-diagonal anharmonicity of the system.²⁶ However, the interference between these positive and negative features when the splitting are on the order of the line widths impairs the ability to directly infer parameters from the peak spacing without a fitting algorithm.

Transition dipole moment magnitudes are reflected in the intensities of the eight-peak structure of the 2D spectrum, with diagonal peaks scaling roughly as the fourth power of the transition moment and cross peaks scaling as the second power in each of the transitions involved. The projection angle between transition moments is reflected in the variation of cross peak amplitudes in the parallel and crossed spectra. Non-harmonic scaling of the $v=0 \rightarrow 1$ and $v=1 \rightarrow 2$ transition dipole moments arises predominately from the presence of electrical anharmonicity, the non-linear expansion of the dipole moment

in the normal mode coordinate.³⁰ This can be seen by comparing intensities of oppositely signed peaks referring to the fundamental and overtone transitions.²⁶ Electrical anharmonicity is apparent in these systems predominately in the amide II vibration.

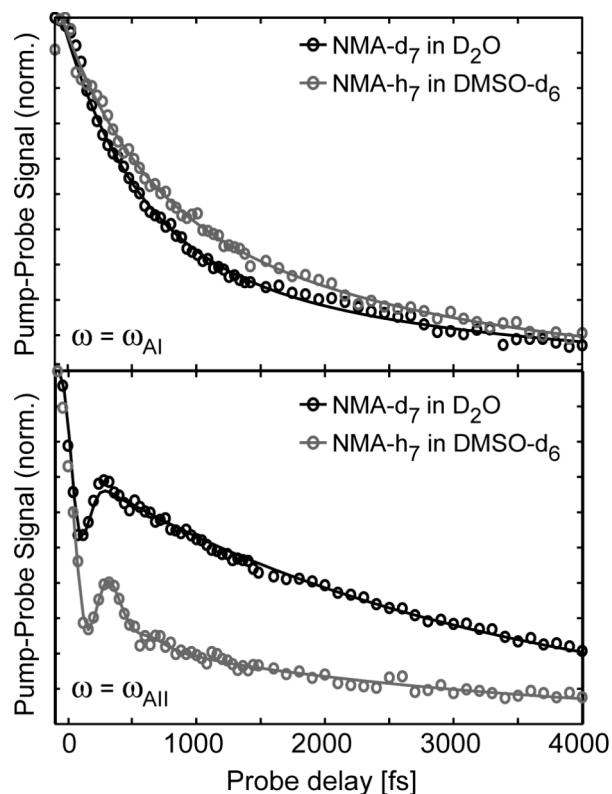


Fig. 4.3.1.3 Magic-angle broadband dispersed pump-probes detected at the amide I and II frequencies. Amide I detected signals (top) are shown with a bi-exponential fit with time scales of 0.38 and 2.1 ps for NMA-d₇/D₂O and 0.43 and 2.1 ps for NMA-h₇/DMSO-d₆. The amide II detected signals (bottom) are shown with a fit to a damped cosine plus bi-exponential. The beats have a period of 0.38 ps and damp with time scales of approximately 0.15 and 0.30 ps for NMA-d₇/D₂O and NMA-h₇/DMSO-d₆. The long time tails of are 5.2 ps and 3.3 ps for the respective systems.

The presence of cross peaks in the 2DIR spectrum is a direct indication of coupling between amide I and II modes. In the time domain, this coherent exchange of vibrational excitation manifests itself as a quantum beat at the Rabi frequency (or the frequency splitting between eigenstates). Fig. 4.3.1.3 shows magic-angle dispersed pump probes of NMA-h₇/DMSO-d₆ and NMA-d₇/D₂O detected at the amide I and II fundamental frequencies. Similar to previous studies performed with only amide I

excitation,^{1,3} the pump-probe detected at the amide I frequency exhibits a biphasic relaxation whose origin is not understood in detail. The amide II pump-probe shows distinctive beats indicative of coherent exchange between modes. The damping of the quantum beats indicates the loss of coherence of the amide I-II energy exchange process, either as a result of vibrational relaxation to dark states or solvent-induced dephasing. The common longer tail seen in the relaxation at both frequencies suggests a slower relaxation to the bath (solute or solvent) following exchange between amide modes.

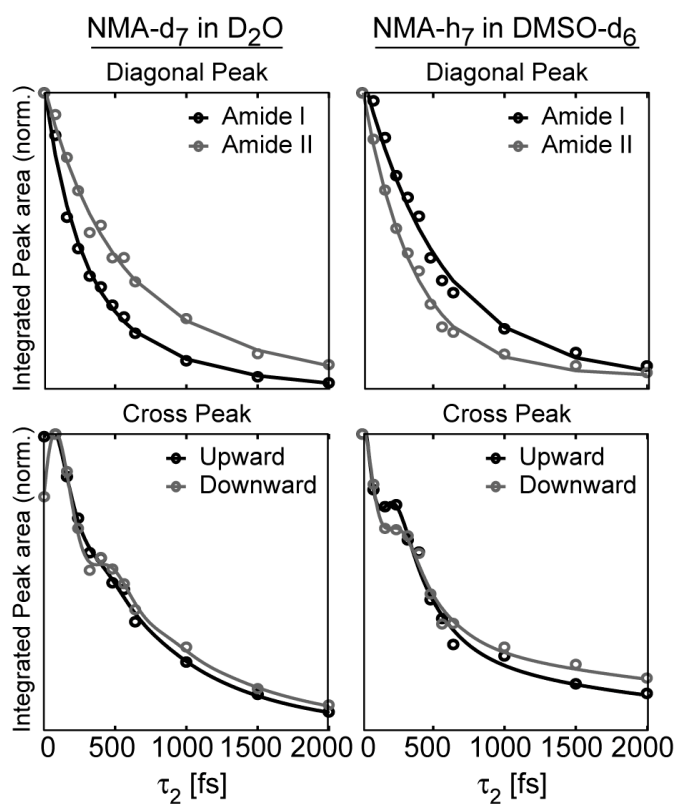


Fig. 4.3.1.4 Integrated resonances of absolute value rephasing spectrum along τ_2 are plotted for the diagonal and cross peak regions of NMA-d₇/D₂O and NMA-h₇/DMSO-d₆. Diagonal resonances refer to the amide I and II modes and are fit to bi-exponentials. The amide II to I (upward) cross peak and amide I to II (downward) cross peak are fit to a damped cosine plus bi-exponential.

To gain a more accurate picture of the vibrational relaxation, the diagonal and cross peaks of the magic angle absolute value rephasing spectrum are integrated

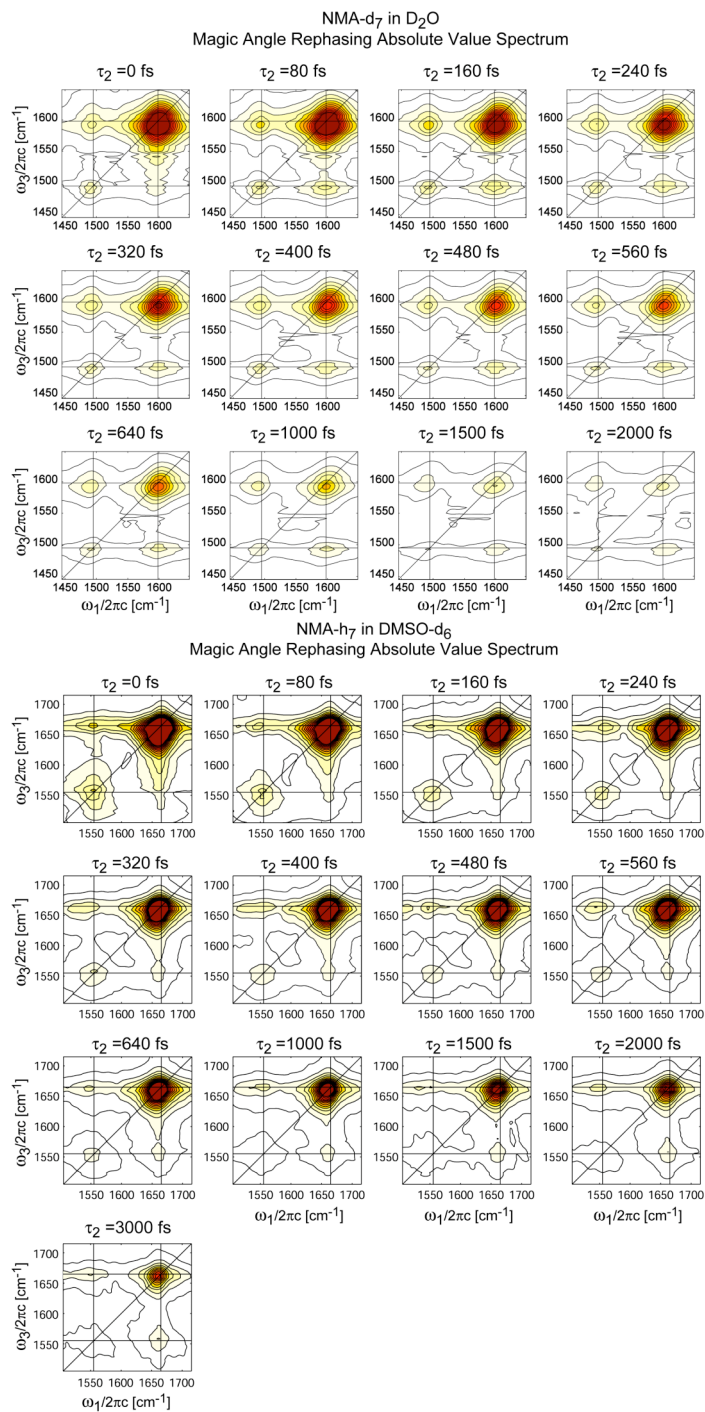


Fig. 4.3.1.5 Time series of the magic angle absolute value rephasing spectra of NMA-h₇ in DMSO-d₆ scaled to the amide I dispersed pump-probe decay. Thirteen contour levels plotted from 0 to 30% of the normalized projected amide I peak. Time series of the magic angle absolute value rephasing spectra of NMA-d₇ in D₂O scaled to the amide I dispersed pump-probe decay. Thirteen contour levels plotted from 0 to 60% of the normalized projected amide I peaks.

separately as a function of τ_2 , shown in Fig. 4.3.1.4 and the full 2D surfaces are seen in Fig. 4.3.1.5.²⁸ These traces show that both diagonal and cross peaks decay from a maximum at $\tau_2=0$ with biphasic relaxation. The diagonal peak amplitudes, which indicate the loss of population from the amide modes, relax faster for amide II than for amide I in the case of NMA-h₇/DMSO-d₆, but faster for amide I in the case of NMA-d₇/D₂O. As expected from the light-matter interaction pathways in the non-rephasing spectrum, beats are only present in the cross peak time traces.²⁸ These data are consistent with a strong coupling that exchanges excitation between amide I, amide II and other peptide modes, followed by a slower dissipation to the bath.

4.4 Discussion

4.4.1 The Anharmonic Potential and Vibrational Couplings

To quantify the information on the amide I/II anharmonic nuclear potential and projection angle in these systems, the data in Fig. 4.3.1.2 were fit using a response function formalism for the amide I and II normal modes of NMA and includes diagonal and off-diagonal anharmonicity.^{26,27,31} This model accounts for resonant transitions between six vibrational states: a ground state, one-quantum amide I and II states, doubly excited amide I and II states, and a combination state. The energy gaps between infrared allowed transitions are taken to interact stochastically with a harmonic bath. This system-bath interaction is parameterized using exponential auto- and cross-correlation functions using methods described in detail elsewhere.²⁹ We also allow for diffusive orientational relaxation, which we have previously characterized for NMA.³ The orientational response function is a joint probability distribution that reflects sequential interactions of the

polarized light fields with transition moments oriented in fixed directions in the molecular frame interlaced with orientational diffusion.^{27,32}

The parameters extracted from the 2D spectra describe the anharmonic potential surface for the amide vibrational modes. Parallel and perpendicular experimental data are fit simultaneously using the model described above to extract anharmonicities, orientation, and coupling constants for both NMA-d₇/D₂O and NMA-h₇/DMSO-d₆. The results of this fit are shown to the right of the data in Fig. 4.3.1.2. The extracted diagonal anharmonicity for amide I/II modes from the fits of the parallel 2DIR spectra, are $\Delta_{AI'}$ = 15 cm⁻¹ and $\Delta_{AII'}$ = 11 cm⁻¹ respectively for NMA-d₇/D₂O, and Δ_{AI} = 12 cm⁻¹ and Δ_{AII} = 10 cm⁻¹ for NMA-h₇/DMSO-d₆. The off-diagonal anharmonicities obtained are $\Delta_{AI',AII'}$ = 11 cm⁻¹ for NMA-d₇/D₂O and $\Delta_{AI,AII}$ = 3.8 cm⁻¹ for NMA-h₇/DMSO-d₆. The trends of the experimental amide I and II anharmonicities are consistent with the DFT studies of NMA in the condensed and gas phase.^{25,33} The anharmonic splitting that we measure for NMA-h₇ compare favorably with those found by Hayashi, et al.³⁴ using a DFT derived potential with an electrostatic map for solvent effects: Δ_{AI} = 14.3 cm⁻¹, Δ_{AII} = 13 cm⁻¹ and $\Delta_{AI,AII}$ = 3.1 cm⁻¹.³⁴ In the case of NMA-h₇/DMSO-d₆, the experimental anharmonic parameters and transition dipole angles are comparable to those found by two-color 2DIR using two spectrally distinct laser pulses.¹²

We find the observed coupling between the amide I and II vibrational modes to be quite strong. The magnitude and significance of the coupling can be illustrated by interpreting the transition frequencies between the six eigenstates through a model of two bi-linearly coupled anharmonic oscillators.²⁷ Fitting this Hamiltonian to the experimentally determined eigenstates, the bilinear coupling term is determined to be V_{12}

= 39 cm⁻¹ and 29 cm⁻¹ for NMA-d₇/D₂O and NMA-h₇/DMSO-d₆, respectively. Using the obtained zero-order frequencies with peak splitting of $(\omega_1 - \omega_2)/2\pi c = 64$ cm⁻¹ and 96 cm⁻¹, the Rabi period for exchange between the two vibrations is 0.32 ps and 0.30 ps in the two respective samples. Comparison of the zero-order frequency peak splitting with the bilinear coupling clearly shows that the weak coupling approximation ($\omega_1 - \omega_2 \gg 4V_{12}$) is not appropriate for the amide I/II system. These findings support the study of Gerber and co-workers, who have argued for the importance of anharmonic effects in protein force fields.^{24,35} They find that the anharmonic effects in NMA computed from high-order terms of the potential using the AMBER semi-empirical force field are negligible, and do not agree well with MP2 *ab initio* calculations or experiment.¹³

4.4.2 Vibrational Relaxation

The time domain manifestation of the coherent exchange of vibrational excitation between amide I/II is seen by the quantum beats in the dispersed pump probe of NMA-d₇/D₂O and NMA-h₇/DMSO-d₆ in Fig. 4.3.1.3. These time traces probe the amide I and II modes following abrupt excitation of both amide modes. The amide II pump-probes show clear quantum beating with a period of ~0.38 ps which is similar to the peak splitting between vibrational eigenstates and consistent with the Rabi periods calculated from the anharmonic potential parameters. From the projection relationship between the dispersed pump-probed and 2DIR spectrum and the relative amplitudes of peaks in the 2D spectra, one sees that the amide II pump-probe signal is dominated by the cross peak signal contributions, and thereby better reflects the oscillating probability of exchanging vibrational excitation. The beats damp with time scales of approximately 0.15 ps and 0.30 ps for NMA-d₇/D₂O and NMA-h₇/DMSO-d₆ respectively, indicating a very rapid

dephasing of the exchange of vibrational excitation either through solvation effects, but more likely as a result of vibrational relaxation to other amide modes. The amide I traces exhibit a biphasic relaxation, with a fast time scale less than 0.5 ps and a long time component of roughly 2.1 ps. From the 2D spectrum it is clear that this trace is dominated by signal contributions from the amide I diagonal peak, and therefore reflect loss of population from the amide I state.

Previous studies have attributed these timescales to the fast amide I fluctuations and/or dissipation of energy through intramolecular vibrational-energy redistribution (IVR) and a slow rearrangement of the hydrogen bonding environment of the solute-solvent system.^{1,3} The beats and biphasic relaxation suggest that there is rapid exchange of vibrational excitation, not only between the amide I and II bright states, but also other dark amide modes through anharmonic interactions. This would account for the rapid drop in amplitude during the first few hundred femtoseconds and damping of the beats. The longer time relaxation would then be a slower dissipation to the more weakly coupled elements of the bath, presumably in large part the solvent. Non-equilibrium molecular dynamics simulations used to study the vibrational energy transfer of peptides in water offer support for this picture.² Amide I relaxation dynamics were also found to be biphasic, and shown to depend sensitively on the initially prepared state. With pure CO vibrational excitation, the amide I energy shows rapid oscillatory exchange between CO and CN stretches, among other beats, as well as rapid damping. These calculations show early time behaviors in which the excited mode rapidly relaxes into local vibrations through coupling since it is not an eigenstate of the system. Similarly here, our

experiments prepare an abrupt excitation of bright amide backbone modes that evolve through coherent and irreversible pathways.

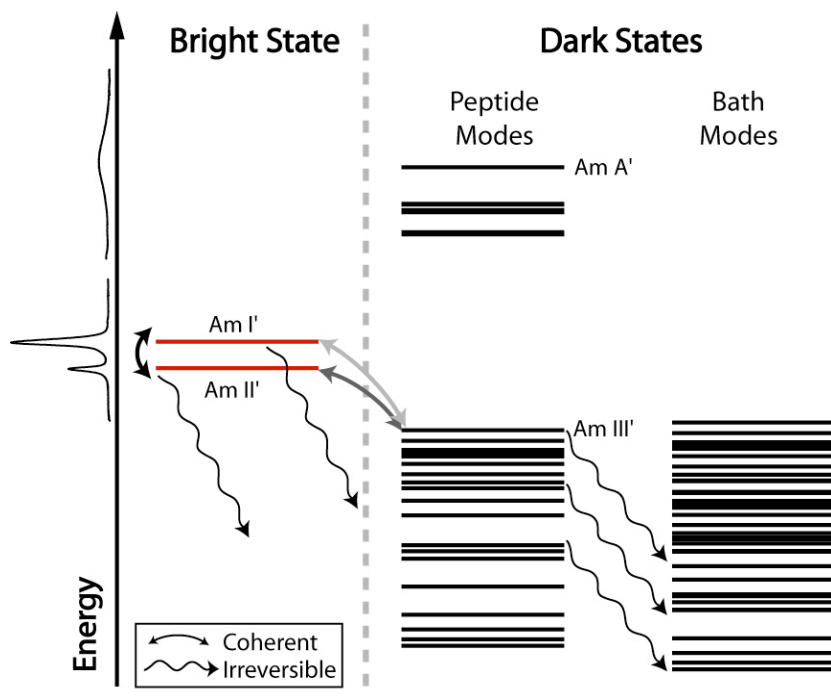


Fig. 4.4.2.1 Vibrational relaxation pathway of the amide I and II vibrations.

While broad-band pump-probe experiments involve a single abrupt excitation, the 2DIR data spectrally resolves amide I and amide II frequencies through the Fourier transform of the initial evolution period τ_1 . The pump-probe data integrates over several relaxation pathways, whereas the 2D peaks can be interpreted in terms of conditional probabilities of preparing the system at ω_1 and detecting at ω_3 . Therefore, detailed information about the system's anharmonic states and their temporal evolution can be extracted from a single waiting-time dependent 2D experiment. When only the peak position and amplitudes are of interest, comparable information can be obtained from a series of narrow band pump-probe experiments with two independently tunable laser sources.

In Fig. 4.3.1.4, vibrational relaxation in these systems is presented by integrating the amplitude of the diagonal and cross peaks of the 2D spectrum (Fig. 4.3.1.5) as a function of waiting time. The relaxation of amplitude in all peaks of the magic angle rephasing spectra proceeds from a maximum at $\tau_2 \approx 0$, implying that during the evolution period τ_1 , the amide I and II vibrations have already efficiently exchanged excitation. If the coupling were weak between the two modes, the cross peak amplitude would grow in as population exchanged during τ_2 . The amplitude decay of diagonal and cross peaks is seen to be biphasic with a few-hundred-femtosecond short component, and a longer ~ 1 ps decay for NMA-d₇/D₂O and >2 ps for NMA-h₇/DMSO-d₆. These observations are also consistent with rapid exchange between a manifold of strongly coupled modes within the peptide, followed by a slower dissipation from these to the bath - primarily to the solvent. In the case of NMA-h₇/DMSO-d₆, the amide II diagonal peak initially relaxes faster (0.35 ps) than the amide I (0.45 ps), suggesting that amide II is more strongly coupled to the other backbone vibrations for NMA-h₇.¹ For NMA-d₇/D₂O the amide I mode relaxes faster (0.21 ps) than amide II (0.38 ps), suggesting a change in intramolecular vibrational-energy redistribution pathway between the two systems. All indications suggest that the fast time scale for vibrational relaxation is intramolecular energy redistribution and that the relaxation process is a property of the peptide unit solely.

Vibrational energy exchange with close lying Fermi resonances and the amide III mode provides energetically favorable relaxation pathways to lower frequency amide modes. Fermi resonances are seen in the spectra of NMA-d₁ in D₂O (Fig. 4.1.3.3), and offer direct evidence of anharmonic couplings to lower frequency NMA modes. This conclusion has been drawn previously based on vibrational relaxation data of the amide I

mode of NMA-d₁/D₂O.¹ The recent computational study of the amide I, II, III, and A anharmonic potential of NMA-h₇ by Hayashi, et al.³⁴ can be used to argue that the amide III mode is one of the dominant relaxation pathways from amide I/II. If the eigenstates obtained from their DFT calculations for the amide I/III and amide II/III systems are interpreted within the model of coupled anharmonic oscillators described above, the zero-order frequency splitting is determined to be 398 cm⁻¹ and 150 cm⁻¹ with bilinear coupling terms of 12 cm⁻¹ and 97 cm⁻¹ respectively. These results show the amide II mode can be expected to couple strongly to amide III mode in the case of NMA-h₇.

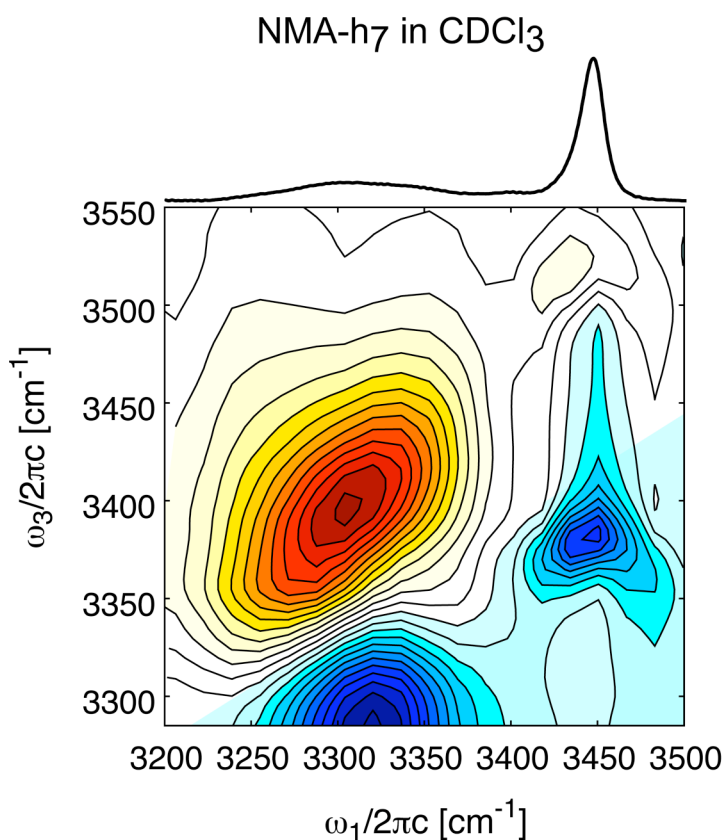


Fig. 4.4.2.2 Amide A spectrum of NMA-h₇ in CDCl₃ including free and hydrogen bound NH.

Vibrational relaxation pathways can be determined through multicolor pump-probe and 2-color 2D IR experiments. Broader bandwidth or two independently tunable

OPAs are required to achieve this. Fig. 4.4.2.2 shows the 2D IR spectrum of Amide A at 3300 cm^{-1} of NMA-h₇ in CDCl₃. The spectrum reveals a free NH and hydrogen bound NH mode. Coupling between these vibrations and the amide finger print region would provide much more detailed information about the relaxation pathways of NMA.

4.4.3 Transition Dipole Orientation and Amide Mode Composition

One of the prominent differences between NMA-d₇/D₂O and NMA-h₇/DMSO-d₆ is the variation of cross peak amplitude between parallel and perpendicular polarization data. A comparison of cross peak intensities in the two spectra gives direct information about the projection angle Θ between the $\nu=0\rightarrow 1$ transition dipole moments of the amide I and II eigenstates.^{27,36} The strong enhancement of the cross peak amplitude for NMA-d₇/D₂O in the perpendicular geometry is an immediate indicator that the projection angle varies considerably between the two species. By fitting the parallel and perpendicular 2D spectra simultaneously to the formalism described above, the projection angles are determined to be 75° for NMA-d₇/D₂O and 40° for NMA-h₇/DMSO-d₆.

The variation of the angle and anharmonic coupling between the transition moments raises an important question about the intrinsic nature of normal modes in NMA as a function of solvent and isotope effects. To construct a better picture of the normal modes, DFT calculations using the Gaussian³⁷ implementation of the B3LYP with the 6-311++G(d,p) basis set were performed to determine the normal modes of NMA-h₇, NMA-d₇, and NMA-d₁ in the gas phase. The MOLVIB³⁸ module in CHARMM³⁹ was used to compute the potential energy distribution (PED) by projecting the DFT-calculated normal modes onto an internal coordinate system detailed by Pulay et al.⁴⁰ The results are summarized in Table 4.4.3.1.

		$\omega/2\pi c$ [cm ⁻¹]	$\omega/2\pi c$ [cm ⁻¹]	Θ [°]	θ [°]	$\angle\text{CO-AI}$ [°]	Potential Energy Distribution	
		(exp)	(calc)	(exp)	(calc)	$\angle\text{CN-AII}$ [°]		
Gas Phase	NMA-h ₇	AI	1728 [‡]	1744	-	54	13	CO s (81), CCN d (4)
		AII	1500 [‡]	1559	-		10	NH ib (42), Me ₁ d (22), CN s (19)
	NMA-d ₁	AI'	1717 [‡]	1739	-	54	16	CO s (83), CCN d (4), CN s (4)
		AII'	1440 [‡]	1517	-		12	Me ₁ d (81), CN s (7)
	NMA-d ₇	AI'	-	1733	-	62	15	CO s (86), CCN d (4)
		AII'	-	1432	-		20	CN s (49), ND ib (16), CO ib (9)
D ₂ O	NMA-h ₇	AI	-	1655	-	45	18	CO s (62), CN s (11), Me ₂ d (10), NH ib (8), CCN d (5)
		AII	-	1617	-		6	NH ib (58), CN ₁ s (26)
	NMA-d ₁	AI'	1623	1650	-	90	26	CO s (60), CN s (20), Me ₂ d (11), CCN d (5)
		AII'	1493	1521	-		59	Me ₁ d (38), CO s (13), CN s (10), ND ib (8), CC s (7), Me ₂ d (6)
	NMA-d ₇	AI'	1604	1634			24	CO s (70), CN s (18), CCN d (5)
		AII'	1495	1499	75	72	39	CN s (45), ND ib (15), CC s (11), CO ib (9), NC s (8), CO s (8)
DMSO-d ₆	NMA-h ₇	AI	1668	1679	40	41	11	CO s (63), NH ib (18), Me ₂ d (6), CCN d (4), CN s (4)
		AII	1558	1624			-5	NH ib (60), CN s (22), CO s (6)
	NMA-d ₁	AI'	-	1667	-	81	11	CO s (71), CN s (12), Me ₂ d (7), CCN d (5)
		AII'	-	1509	-		45	Me ₁ d (85), CN s (5)
	NMA-d ₇	AI'	1648	1655	-	64	19	CO s (78), CN s (10), CCN d (4)
		AII'	1450	1474	-		27	CN s (49), ND ib (18), NC s (9), CC s (9), CO ib (8)

Table 4.4.3.1 Amide I (AI) and amide II (AII) transition frequencies and transition dipole angles for isotopic species of NMA in the gas phase, D₂O, and DMSO-d₆. Experimental frequencies are extracted from FTIR spectra and [‡] are frequencies obtained from Mayne et al.²². Calculated frequencies are the harmonic normal mode frequencies from DFT calculations. The amide I-II projection angle Θ is that between the eigenvectors extracted from fits to the 2DIR spectra, and the calculated angle θ is that between the normal mode coordinates. Also given are the calculated angles of amide I transition moment relative to the CO bond ($\angle\text{CO-AI}$) and the amide II transition moment relative to the CN bond ($\angle\text{CN-AII}$). Potential energy distribution calculations are given for amide I contributions $\geq 4\%$ and amide II contributions $\geq 5\%$. Mode definitions are defined by: s = stretch, d = deformation, ib = in-plane bend (peptide bond). All methyl motions were combined into a single methyl deformation mode for simplicity and Me₁ is the C terminus and Me₂ is the N terminus methyl. For definitions of internal coordinate system see Pulay et al.⁴⁰

PED analysis of the amide I and II modes in the gas phase indicate a distinct variation in normal mode composition upon isotopic substitution of the amide and methyl groups of NMA. The amide I PED analysis gives the mode composed of 81-86% CO stretch (s) for NMA-h₇, NMA-d₇, and NMA-d₁. All isotopic species have dipole moments for the amide I vibration to be between 12-15° off the carbonyl bond, which is consistent with the value of 20° commonly used in the literature.⁴¹ Since methyl deformations and N-H modes contribute weakly to the amide I transition, isotopic effects minimally contribute to the mode composition and transition moment angle. The amide II vibration is cited as being mostly CN s with NH in-plane bend (ib), leading to a transition moment approximately 68 degrees from the NH bond.⁴¹ The mode decomposition of amide II in the gas phase shows drastically different local mode distributions for the isotopic species. Deuteration of the methyl groups reduces the effective influence of methyl deformation on the amide II vibration therefore localizing the mode to the peptide backbone. This effect is consistent with assumptions made in large protein systems in which the normal modes are localized to their respective peptide unit, where in this study, the neighboring side chains are mimicked by heavier methyl capping groups. The remaining isotopologues show different mode composition where NMA-d₁ is dominated by methyl deformations and NMA-h₇ is predominately NH ib. The large variations in projection angles of the gas phase isotopologues is explained by these differences in the amide II local mode character. The calculated projection angle between the normal mode transition moments, θ , is tabulated in Table 4.4.3.1.

Solute-solvent interactions play a vital role in the amide spectroscopy of proteins and peptides. Prior theoretical^{6-8,25,42-44} and experimental studies^{1,3,5,9} have concentrated

on the influence of solvent motions and hydrogen bonding on NMA's amide I transition frequency. In our prior analysis of the τ_2 -dependent amide I 2DIR lineshape, we concluded that the influence of the local hydrogen bonding environment and solvent motions on amide I frequency is well modeled by electrostatic models for the system-bath interaction.³ Solvatochromic shifts are also observed from FTIR spectra for the amide II mode of NMA (Fig. 4.3.1.1 and Table 4.4.3.1), although in this case a blue shift is observed with increasingly strong hydrogen bonding interactions that act to stabilize the zwitterionic form of NMA.

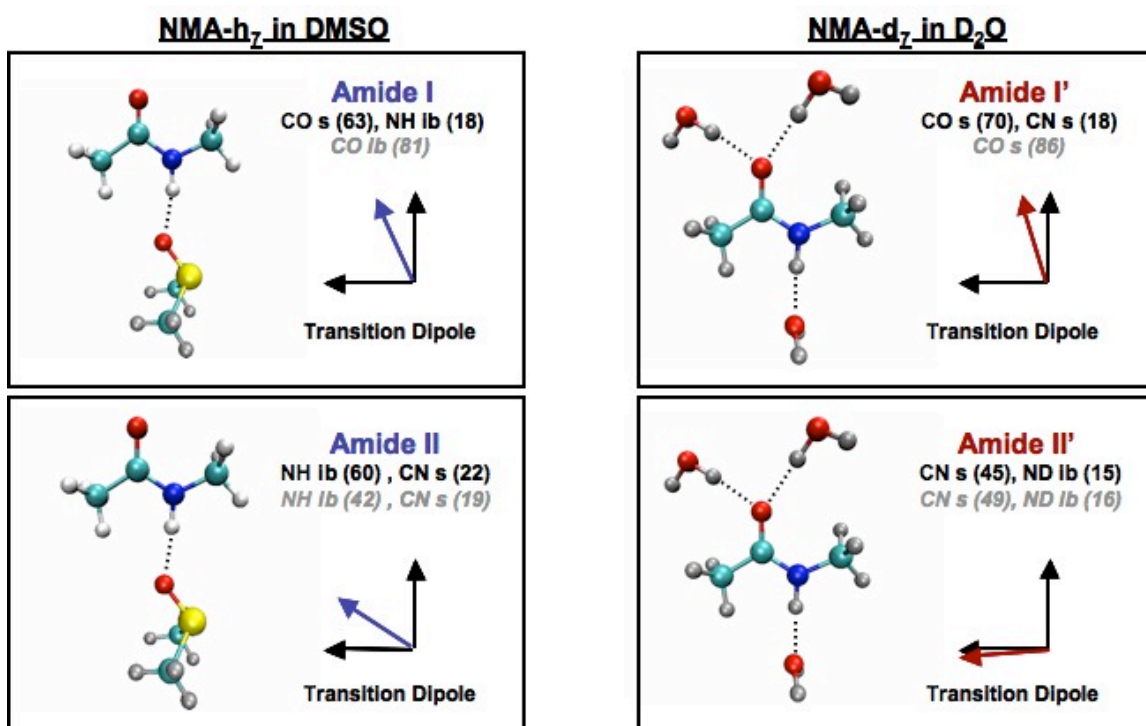


Fig. 4.4.3.1 Hydrogen bonding environment of NMA in DMSO-d₆ and D₂O including the dominant contributions to the vibrational modes and the angles of the transition dipole moments relative to the CO bond.

These earlier studies concentrated on the time-dependent amide I energies for the system-solvent interaction. To turn to characterization of the solvation effect on the amide eigenvectors, the DFT calculations and PED analysis of the amide I and II modes

were recalculated using an explicit solvent model for the first solvation shell and treating the remaining solvent implicitly. Calculations of NMA-h₇, NMA-d₇, and NMA-d₁ were done for NMA-(D₂O)₃ and NMA-DMSO-d₆ clusters, embedded in a dielectric continuum matching the static dielectric constant for each solvent.^{10,14,15,45} The coordination of NMA-d₇ to D₂O is through three hydrogen-bonding sites: two on the carbonyl oxygen and one on the ND group of the peptide and NMA-h₇/DMSO-d₆ has a single hydrogen-bonding site to the NH.

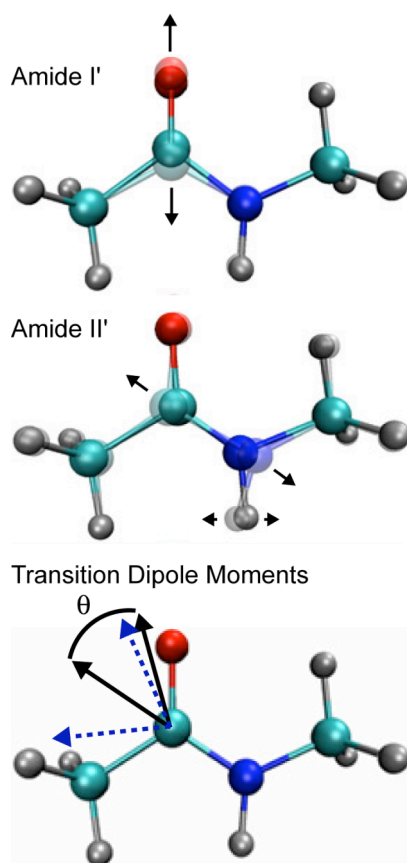


Fig. 4.4.3.2 (Top, Middle) Normal mode displacements of the amide I and II vibrational bands of NMA-d₇ in the gas phase. (Bottom) The amide I/II transition dipole angles for NMA-d₇/D₂O (blue dashed arrow) and NMA-h₇ in DMSO-d₆ (black solid arrow), where Θ defines the experimentally determined angle from the polarization 2DIR spectra given in Table 4.4.3.1.

Upon hydrogen bonding to the solvent, the amide I and II mode composition shows a small change. The amide II mode becomes more delocalized, picking up more

backbone stretches and bends. The amide I mode composition in both DMSO-d₆ and D₂O changes from the gas phase similarly, reducing the CO s local mode by approximately 10-15% and increasing the localization of the mode on the CN s. This effect explains the increased coupling of the amide vibrations in NMA-d₇/D₂O in which the amide II is dominated by the CN stretch for fully deuterated NMA. This trend of isotopic effects on the transition moment directions and projection angles of NMA-d₇/D₂O and NMA-h₇/DMSO-d₆ is pictured in the bottom panel of Fig. 4.4.3.2. These values are close to the experimentally determined projection values, although we note that these are not directly comparable, since they are represented in a normal mode basis as opposed to the eigen basis.

PED calculations strongly suggest that the isotopic substitution of NMA, not solvation, governs the large variations in observed 2DIR spectral features. For additional comparison of solvation and isotope effects, the 2DIR polarization-selective spectra were taken for NMA-d₁ in D₂O and NMA-h₇ in CDCl₃, and all spectra are shown in Fig. 4.4.3.3. The large off-diagonal anharmonicity and cross peak enhancement of the NMA-d₇/D₂O is not seen in the NMA-d₁ in D₂O spectra, which have identical solvation environments. NMA-h₇ in CDCl₃ shows similar spectral features to the NMA-h₇/DMSO-d₆ system. DMSO-d₆ and CDCl₃ have very different solvation characteristics in which DMSO-d₆ hydrogen bonds to the NH of the amide group and roughly two CDCl₃ molecules weakly hydrogen bond to the carbonyl.³ This clearly shows that the isotope effects are dictating the intramolecular coupling and transition moment variation in these samples.

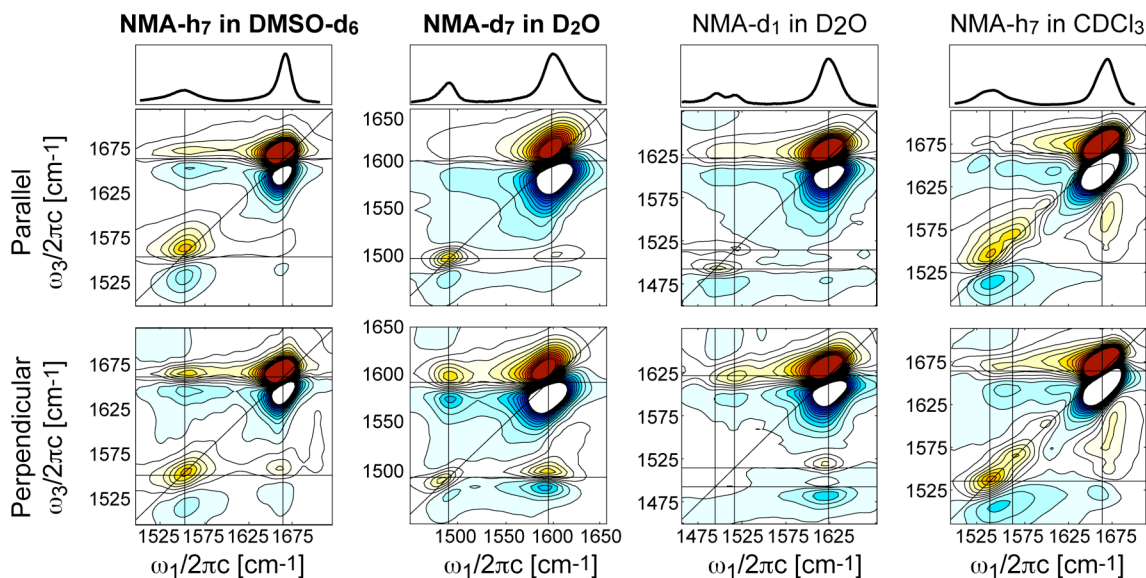


Fig. 4.4.3.3 FTIR spectra (top), parallel (middle) and perpendicular (bottom) absorptive 2DIR spectrum of NMA-h₇ in CDCl₃ and NMA-d₁ in D₂O at $\tau_2 = 0$ fs. Twenty-six equally spaced contours are plotted from $\pm 25\%$ for NMA-h₇/CDCl₃ and from $\pm 50\%$ for NMA-d₁/D₂O of the normalized amide I spectral amplitude.

PED analysis of the normal modes has been used to assign Fermi resonances in the NMA vibrational spectra, which provide energetically favorable pathways for vibrational relaxation. For the amide II doublet of NMA-d₁/D₂O, it has been proposed that the 1492 cm⁻¹ peak arises from a Fermi resonance between amide II and a combination band of the amide IV and peptide skeletal deformation modes.²⁰ In the case of NMA-h₇ in CDCl₃, the assignment of the somewhat structured and asymmetric resonance at ~ 1530 cm⁻¹ is not possible from FTIR, however, the 2DIR spectrum indicates clearly that this absorption feature involves two overlapping resonances at 1558 cm⁻¹ and 1532 cm⁻¹. The 2DIR spectrum of NMA-h₇ in CDCl₃ also exhibits strong similarity to the amide II and cross peak region with that of NMA-d₁/D₂O. The cross peak enhancement in the perpendicular polarized 2DIR spectrum is primarily between amide I and II at 1623 cm⁻¹ and 1514 cm⁻¹ respectively. The similarity between the 2DIR spectra in Fig. 4.4.3.3, showing that the dominant cross peak to amide I with the shoulder

of the 1558 cm^{-1} transition, suggests that this higher energy shoulder is the amide II mode and the 1532 cm^{-1} transition arises from a Fermi resonance.

4.5 Conclusion

Our study of the effects of solute-solvent interactions and deuteration on the amide I and II vibrational couplings, mode composition, and vibrational relaxation for isotopic species of NMA indicates that anharmonicity plays an important role in understanding the structure and energy exchange processes of peptides. The cross peaks in 2DIR spectra and quantum beats in pump-probe experiments are indicators of a rapid coherent exchange of energy between these coordinates. Thus, the common picture of weakly coupled normal modes, an assumption within most empirical potentials for biomolecules, does not properly describe the nuclear potential of a peptide linkage. The degree of coupling, mode composition, transition dipole moment orientation, and vibrational relaxation time scales for NMA is governed by the isotopic substitution of the amide and methyl groups, with the most significant effects on the amide II mode. The rapid vibrational relaxation processes observed argue for rapid intramolecular vibrational energy redistribution among a set of coupled peptide backbone modes followed by a slower energy dissipation into weakly coupled vibrations of the peptide and solvent motions. These results also indicate that NMA- h_7 is perhaps the least representative of a peptide group in a protein, due to the relatively light terminal methyl groups. Rather than deuterating the methyls, it may be better to study an amide with more massive terminal groups, for instance N-ethyl-propionamide.

The consequences of strong couplings could be significant for modeling protein vibrational spectroscopy, particularly for efforts to model the amide I spectroscopy of

proteins and understand its sensitivity to secondary structure. Structure-based spectroscopic models of the amide I spectrum are often based on a Hamiltonian formulated in a local mode amide I basis, where amide I oscillators parameterized from NMA interact with one another with through-space and through-bond couplings.^{1,11} The magnitude of the couplings observed here are no less than short-range through-space electrostatic interactions, suggesting that amide I vibrational couplings between bonded peptide groups may originate in their mutual coupling to amide backbone vibrations, such as the amide II. In fact, the importance of through-bond interaction in modeling amide I spectroscopy is already well-known, but has to now only been treated by deducing amide I couplings from *ab initio* and DFT calculations of dipeptides as a function of torsion angles.^{11,46,47} Currently there are conflicting accounts of amide II couplings between peptide units, with experiments arguing for negligible coupling⁴⁸ and theory arguing for strong interactions.⁴⁹ Experiments on amide I and II couplings in dipeptides would help resolve this issue, and would offer insight into the elements of a more robust protein spectroscopic model.

References

- (1) Hamm, P.; Lim, M.; Hochstrasser, R. M. *J. Phys. Chem. B* **1998**, *102*, 6123-6138.
- (2) Nguyen, P. H.; Stock, G. *J. Chem. Phys.* **2003**, *119*, 11350.
- (3) DeCamp, M. F.; DeFlores, L. P.; McCracken, J. M.; Tokmakoff, A.; Kwac, K.; Cho, M. *J. Phys. Chem. B* **2005**, *109*, 11016.
- (4) Rubtsov, I. V.; Kumar, K.; Hochstrasser, R. M. *Chemical Physics Letters* **2005**, *402*, 439-443.
- (5) Woutersen, S.; Mu, Y.; Stock, G.; Hamm, P. *Chem. Phys.* **2001**, *266*, 137.
- (6) Kwac, K.; Cho, M. *J. Chem. Phys.* **2003**, *119*, 2247-2255.
- (7) Schmidt, J. R.; Corcelli, S. A.; Skinner, J. L. *J. Chem. Phys.* **2004**, *121*, 8887-8896.
- (8) Bour, P.; Keiderling, T. A. *J. Chem. Phys.* **2003**, *119*, 11253-11262.
- (9) Zanni, M. T.; Asplund, M. C.; Hochstrasser, R. M. *J. Chem. Phys.* **2001**, *114*, 4579-4590.
- (10) Besley, N. A. *J. Phys. Chem. A* **2004**, *108*, 10794-10800.
- (11) Woutersen, S.; Hamm, P. *Journal of Physics: Condensed Matter* **2002**, *14*, 1035-1062.
- (12) Rubtsov, I. V.; Wang, J.; Hochstrasser, R. M. *Proc. Natl. Acad. Sci. USA* **2003**, *100*, 5601-5606.
- (13) Gregurick, S. K.; Chaban, G. M.; Gerber, R. B. *J. Phys. Chem. A* **2002**, *106*, 8696-8707.
- (14) Kubelka, J.; Keideling, T. A. *J. Phys. Chem. A* **2001**, *105*, 10922-10928.
- (15) Mirkin, N. G.; Krimm, S. *J. Mol. Struct.* **1996**, *377*, 219-234.

- (16) Scott, A. P.; Radom, L. J. *J. Phys. Chem. A* **1996**, *100*, 16502.
- (17) Pulay, P.; Fogarasi, G.; Pongor, G.; Boggs, J. E.; Vargha, A. *J. Am. Chem. Soc.* **1983**, *105*, 7037.
- (18) Allen, W. D.; Csaszar, A. G.; Horner, D. A. *J. Am. Chem. Soc.* **1992**, *114*, 6834.
- (19) Mix, G.; Schweitzer-Stenner, R.; Asher, S. A. *J. Am. Chem. Soc.* **2000**, *122*.
- (20) Chen, X. G.; Schweitzer-Stenner, R.; Asher, S. A.; Mirkin, N. G.; Krimm, S. *J. Phys. Chem.* **1995**, *99*, 3074-3083.
- (21) Torii, H.; Tatsumi, T.; Kanazawa, T.; Tasumi, M. *J. Phys. Chem. B* **1998**, *102*, 309-314.
- (22) Mayne, L. C.; Hudson, B. *J. Phys. Chem.* **1991**, *95*, 2962-2967.
- (23) Roitberg, A.; Gerber, R. B.; Elber, R.; Ratner, M. A. *Science* **1995**, *268*, 1319.
- (24) Gerber, R. B.; Brauer, B.; Gregurick, S. K.; Chaban, G. M. *PhysChemComm* **2002**, 142-150.
- (25) Hayashi, T.; Jansen, T. I. C.; Zhuang, W.; Mukamel, S. *J. Phys. Chem. A* **2005**, *109*, 64-82.
- (26) Golonzka, O.; Khalil, M.; Demirdöven, N.; Tokmakoff, A. *Phys. Rev. Lett.* **2001**, *86*, 2154-2157.
- (27) Khalil, M.; Demirdöven, N.; Tokmakoff, A. *J. Phys. Chem. A* **2003**, *107*, 5258-5279.
- (28) Khalil, M.; Demirdöven, N.; Tokmakoff, A. *J. Chem. Phys.* **2004**, *121*, 362.
- (29) Demirdöven, N.; Khalil, M.; Tokmakoff, A. *Phys. Rev. Lett.* **2002**, *89*, 237401-237401.
- (30) Khalil, M.; Tokmakoff, A. *Chem. Phys.* **2001**, *266*, 213-230.

- (31) Sung, J.; Silbey, R. J. *J. Chem. Phys.* **2001**, *115*, 9266-9287.
- (32) Golonzka, O.; Tokmakoff, A. *J. Chem. Phys.* **2001**, *115*, 297-309.
- (33) Wang, J.; Chen, X.; Clarke, M. L.; Chen, Z. *PNAS* **2005**, *102*, 4978-4983.
- (34) Hayashi, T.; Zhuang, W.; Mukamel, S. *J. Phys. Chem. A*, *109*, 9757-9759.
- (35) Roitberg, A.; Gerber, R. B.; Elber, R.; Ratner, M. A. *Science* **1995**, *268*, 1319-1322.
- (36) Golonzka, O.; Khalil, M.; Demirdöven, N.; Tokmakoff, A. *J. Chem. Phys.* **2001**, *115*, 10814-10828.
- (37) Frisch, M. J.; Trucks, G. W.; Schlegel, H. B.; Scuseria, G. E.; Robb, M. A.; Cheeseman, J. R.; Zakrzewski, V. G.; Montgomery, J. A.; Stratmann, R. E.; C. Burant, J.; Dapprich, S.; Millam, J. M.; Daniels, A. D.; Kudin, K. N.; Strain, M. C.; Farkas, O.; Tomasi, J.; Barone, V.; Cossi, M.; Cammi, R.; Mennucci, B.; Pomelli, C.; Adamo, C.; Clifford, S.; Ochterski, J.; Petersson, G. A.; Ayala, P. Y.; Cui, Q.; Morokuma, K.; Malick, D. K.; Rabuck, A. D.; Raghavachari, K.; Foresman, J. B.; Cioslowski, J.; Ortiz, J. V.; Stefanov, B. B.; G. Liu, A. L.; Piskorz, P.; Komaromi, I.; Gomperts, R.; Martin, R. L.; Fox, D. J.; Keith, T.; Al-Laham, M. A.; Peng, C. Y.; Nanayakkara, A.; Gonzalez, C.; Challacombe, M.; Gill, P. M. W.; G. Johnson, B.; Chen, W.; Wong, M. W.; Andres, J. L.; Head-Gordon, M.; Replogle, E. S.; Pople, J. A.; Gaussian, Inc.: Pittsburgh PA, 1994.
- (38) Kuczera, K.; Wiorkiewicz, J. K.; Karplus, M. *MOLVIB: Program for the Analysis of Molecular Vibrations; CHARMM; Harvard University* **1993**.
- (39) A. D. MacKerell, J.; Bashford, D.; Bellott, M.; R. L. Dunbrack, J.; Evanseck, J. D.; Field, M. J.; Fischer, S.; Gao, J.; Guo, H.; Ha, S.; Joseph-McCarthy, D.; Kuchnir, L.; Kuczera, K.; Lau, F. T. K.; Mattos, C.; Michnick, S.; Ngo, T.; Nguyen, D. T.; Prodhom,

- B.; W. E. Reiher, I.; Roux, B.; Schlenkrich, M.; Smith, J. C.; Stote, R.; Straub, J.; Watanabe, M.; Wiorkiewicz-Kuczera, J.; Yin, D.; Karplus, M. *J. Phys. Chem. B* **1998**, *102*, 3586.
- (40) Pulay, P.; Fogarasi, G.; Pang, F.; Boggs, J. E. *J. Am. Chem. Soc.* **1979**, *101*, 10814.
- (41) Moore, W. H.; Krimm, S. *Biopolymers* **1976**, *101*, 2550.
- (42) Bour, P. *J. Chem. Phys.* **2004**, *121*, 7545.
- (43) Kwac, K.; Lee, H.; Cho, M. *J. Chem. Phys.* **2004**, *120*, 1477.
- (44) Jansen, T. I. C.; Knoester, J. *J. Chem. Phys.* **2006**, *124*, 044502.
- (45) Guo, H.; Karplus, M. *J. Phys. Chem.* **1992**, *96*, 7273-7287.
- (46) Torii, H.; Tasumi, M. *J. Raman Spectrosc.* **1998**, *29*, 81-86.
- (47) Cha, S.; Ham, S.; Cho, M. *J. Chem. Phys.* **2002**, *117*, 740-750.
- (48) Mikhonin, A. V.; Asher, S. A. *J. Am. Chem. Soc.* **2005**, *109*, 3047.
- (49) Moran, A.; Mukamel, S. *Proc. Nat. Acad. Sci.* **2004**, *101*, 506-510.

Chapter 5

Secondary Structural Sensitivity of the Amide II' Vibration of Proteins

"Somewhere, something incredible is waiting to be known." –Carl Sagan

5.1 Introduction

Amide vibrational spectroscopy is an ideal tool for understanding protein dynamics, structure and molecular couplings. The amide vibrations of proteins have been heavily studied to provide molecular insight into protein function, stability and structure. Due to sensitivity to intra- and intermolecular couplings, the amide I mode yields secondary structural sensitivity that can be probed with picosecond time resolution.¹ The amide II mode shows particular sensitivity to the protonation state of the amide group and has been used in hydrogen-deuterium exchange experiments to reveal information about the stability and solvation of proteins.² Recently, UV resonance Raman spectroscopy revealed correlation between the amide III modes and the ψ Ramachandran angle.³

The most highly studied of these vibrations is the amide I vibration; a normal mode composed of predominately carbonyl stretch (80%) with modest contribution of the NH in-plane bend and out of phase CN stretch. The seminal work of Miyazawa first noted the structure sensitivity of the amide vibrations from the intrinsic sensitivity of vibrations to the symmetry of the local environment.⁴ Vibrational coupling arising from inter- and intra-molecular interactions via through-bond or cross-strand hydrogen bond couplings arising from the structural arrangement of the protein, gives rise to a delocalized vibrational state. This delocalized or excitonic state reports directly on the symmetry size of the secondary structure, and have shown particular sensitivity in the structural determination of anti-parallel β sheets.⁵

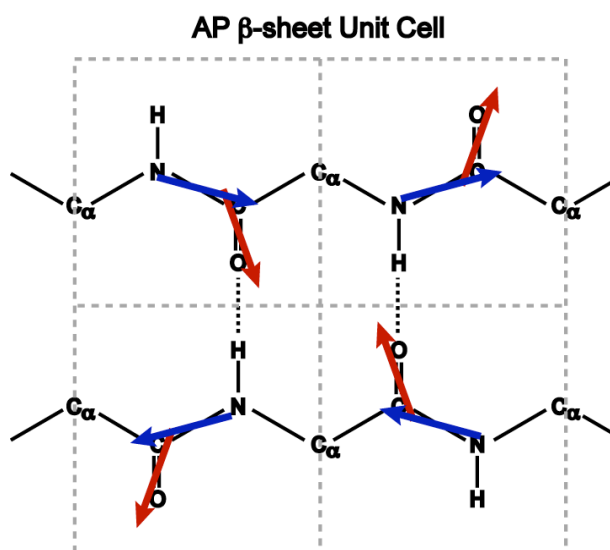


Fig. 5.1.1.1 The unit cell of the AP β sheet contains four amide groups. The position and orientation of the amide I' (red) and amide II' (blue) transition dipole moments are also pictured.

The simplest unit of an anti-parallel (AP) β -sheet contains a tetramer of the amide I local vibration (Fig. 5.1.1.1).⁵ The amide I transition dipole moment is at an angle of 20° off the carbonyl vibration and with strong coupling through hydrogen bonded

contacts, an intuitive picture of two vibrational eigenstates can be seen. One excitonic vibration, ν_{\perp} , will be the amide I transition dipole perpendicular to the β -sheet strands. This vibration contains most of the oscillator strength of the amide I band. The parallel vibration, ν_{\parallel} , with amide I transition dipole along the β -sheet strands, will be significantly weaker. These vibrations are clearly seen in the amide I FTIR spectrum of poly-L-lysine as a strong IR absorption at 1610 cm^{-1} and a weaker transition at 1690 cm^{-1} (Fig. 5.3.1.1). The size-dependent structural trends of these signatures are explained in detail elsewhere.⁵

To this point, the vibrational signatures of other secondary structure moieties are less resolvable under the amide I line shape. The α -helical structure is predicted to have three IR active vibrations, a strong vibration with transition dipole parallel to the axis of the helix, the A mode, and a significantly weaker doubly-degenerate set of the E_1 modes that are perpendicular. Despite the existence of these two vibrations, with the peak splitting is on the order of a few cm^{-1} , the amide I vibrational signature of α helices is dominated by the A mode absorption around 1650 cm^{-1} . In addition to the inability to spectrally resolve the two modes of the helix, this region of the amide I spectrum is overlapped with the random coil absorption.

The amide II vibration is predominately known for its sensitivity to the protonation state of the amide backbone.⁶ Early work of Miyazawa and Blout⁴ predicated that the amide II vibration, composed of NH in-plane bend and CN stretch, would also exhibit secondary structural sensitivity. Unlike the distinct signatures of the amide I vibrational sensitivity to anti-parallel β sheets, the amide II experimental spectrum does not exhibit similar sensitivity. However, Miyazawa predicted the use of amide I and II together allow

for a means to assign parallel and anti-parallel sheets, since amide II will exhibit a 20 cm^{-1} splitting of the band only in the case of parallel β -sheets.⁴

For an ideal helix, it is expected that the amide II band will also show two distinct vibrations with transition dipoles oriented perpendicular and parallel to the axis of the helix. In an oriented film of a homopolymer that forms extended helices, the observed amide II vibrations appear at 1516 and 1546 cm^{-1} . The stronger transition at high energy is the perpendicular vibration, while the weaker transition is predicted to run parallel to the helix axis. For random coils, the amide II vibration is expected to absorb at 1536 cm^{-1} giving a potential signature for differentiating between coils and helices.

Condensed phase experiments give rise to a significant amount of spectral broadening due to the inhomogeneous environment. Therefore, the ability to resolve spectral shifts on the order of the line width is nearly impossible with linear measurements. The ability to resolve details hidden by spectral congestion of vibrational line shapes has been significantly improved since the implementation of two-dimensional infrared spectroscopy (2D IR). 2D IR spreads vibrational bands over two frequency axes to allow separation of line broadening mechanisms and direct measurement of cross peaks and therefore vibrational couplings. In this chapter, the amide II' vibration will be dissected through its 2D IR lineshape and the amide I'-II' cross peak. Despite the widely made assumptions that the amide vibrations are orthogonal and therefore energetically isolated, Chapter 4 demonstrated and quantified the coupling of the amide I and II vibrations. In this chapter, by correlating the amide II' band with the known sensitivities of the amide I' vibration, structural assignments of the amide II' band can be made. Experiments were first performed on a model protein system of poly-L-lysine (PLL).

This synthetic polypeptide is documented to adopt extended secondary structure conformations under various experimental conditions.⁷ The anti-parallel β -sheet, α -helix and random coil moieties have been characterized by optical rotatory dispersion (ORD) and circular dichroism (CD) studies.⁸⁻¹⁰ Extension of these results to globular protein systems under denaturing conditions further examine line shape dependence of the amide I' diagonal and cross peak region. It is found that the amide II' 2D line shape gives rise to distinctive signatures for α helices and random coil regions, which, when combined with the β sheet sensitivity of the amide I region, allow for separation of all the common secondary structural motifs. In addition, the amide II band shifts 100 cm^{-1} upon deuteration of the amide proton and allows for solvent exposure and stability of protein secondary structure to be determined. The latter is discussed in detail in Chapter 7 and 8.

Similar to these early experiments of Miyazawa, much of the theoretical literature on the amide II vibration has concentrated on the protonated species. It has been seen that the amide II vibration changes significantly upon deuteration of the amide group. For the deuterated peptide group, the amide II' normal mode is dominated by the CN stretch and vibrational coupling to amide I' significantly increases.¹¹ This brings into question what the dominant mechanism of coupling for the amide II vibration is: through space coupling via hydrogen bonds, indirect coupling through the amide I vibration, or simply through bond coupling of nearest neighbors. By comparing the experimental amide I'/II' 2DIR spectra to model calculations of different structural motifs, it is concluded that the dominant coupling between amide II' modes is the through-bond nearest neighbor interaction dictated by backbone symmetry and the dihedral ϕ/ψ angles. Using only this amide II' coupling mechanism, a model is developed to calculate amide I'/II' 2D IR

spectra that yields qualitative agreement for α helices, β sheets, and random coils and allows amide I'/II' protein spectra to be calculated.

5.2 Experimental

To unravel the molecular structure sensitivity of the amide II' line shape, broadband 2D IR experiments are performed. The experimental set up for the 2D FT spectrometer is described in full detail in Chapter 3 and will only be discussed here briefly. The mid-infrared laser pulse is centered at 1550 cm^{-1} with a FWHM bandwidth of approximately 350 cm^{-1} . This is sufficient bandwidth to cover the fundamental and overtones of the amide I' and II' vibrations of the model protein and real protein systems. The pulse bandwidth is compressed to sub 90 fs in duration. Both the ZZZZ and ZZYY 2D IR spectra are acquired in step scan mode to improve signal-to-noise based on the noise characteristics of the laser system. Additionally, spectra are collected in high-resolution strips using a 75-groove/mm grating. This improves the overall resolution along ω_3 by a factor of 2 resulting in 1.9 cm^{-1} per pixel. Due to the limited number of pixels on the array detector (64), the ω_3 axis is limited to 120 cm^{-1} . The signal measured is a modulation of the probe beam and the detection sensitivity is therefore only limited by the dynamic range of the detector.

All samples are purchased from Sigma-Aldrich (St. Louis, MO) and fully exchanged between $45\text{-}65^\circ\text{C}$ before use. Concentrations of the proteins are selected such that the infrared absorbance of the amide I band is less than 0.5, this insures no pulse propagation effects or loss of signal from high OD samples. Poly-L-lysine (PLL) samples are prepared under different conditions to generate the desired secondary structure motif. The random coil species is generated by dissolving the protein in neat D_2O at 20°C and

pH = 4.02. The α -helical conformation is prepared by dissolving PLL into neat D₂O and raising the pH to 12 using 1M NaOD solution. If the sample windows are not clean, the homopolymers will begin to aggregate, this can be resolved by cleaning the windows using a pepsin solution or slightly reducing the pH to 11-11.5. The β -sheet form of PLL is simply prepared by raising the temperature of the α -helical solution to 46°C over 30 minutes. For these spectra, the helical and sheet moieties were taken consecutively on identical samples. Myoglobin and ubiquitin were prepared in unbuffered solutions at the desired pH.

5.3 Linear Spectroscopy of the Amide Fingerprint Region

The FTIR spectrum of poly-L-lysine is shown in Fig. 5.3.1.1. In acidic solution at ambient temperatures, poly-L-lysine is in the random coil form.¹⁰ A small shoulder appears on the blue side of the amide I band and the amide II' band shows a three peak structure. In basic conditions at low temperatures, the polypeptide takes on an α -helical structure, which red shifts the amide I' and II' bands and gives a low energy amide II' shoulder. As the temperature is increased, PLL undergoes a structural transition into a large-scale anti-parallel β -sheet aggregate. The amide I' band splits into the signature high and low intensity β -sheet modes. This drastic change in the amide I' band is not seen in amide II', which has a triangular, four-peak structure. It is similar in appearance to the random coil with an additional, sharp peak at 1440 cm⁻¹. The origin of the differences of the amide II' band can be attributed to secondary structure, which can be confirmed by a comparison of the amide II and II' bands of the single amide unit, *N*-methylacetamide, presented in Chapter 4, where no significant structure is seen in the linear vibrational or 2D IR spectra.

In addition to amide II' absorption at 1450 cm^{-1} , it is expected that there will be a significant contribution of the HOD bend due to water contamination at 1464 cm^{-1} . This will influence the overall intensity and structure of the band. In the next section, we show that 2D IR is able to clearly distinguish these vibrations, exploiting the fourth power scaling of 2D IR intensities with transition dipole to distinguish amide II' versus HOD bend.

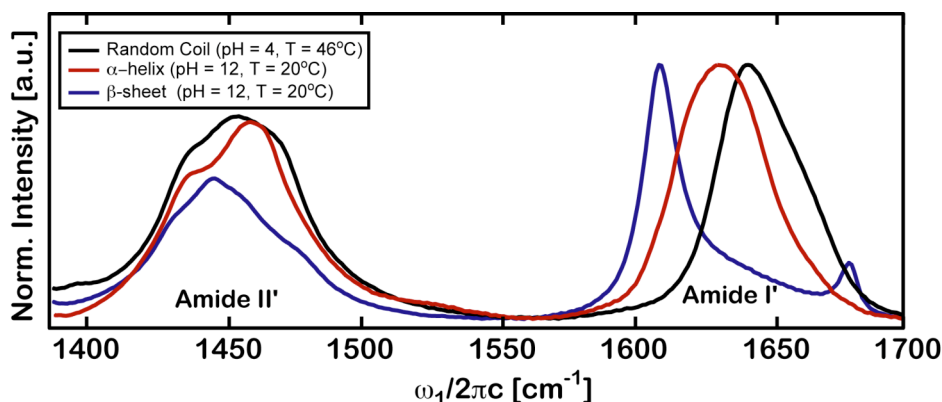


Fig. 5.3.1.1 FTIR spectra of poly-L-lysine as a function of pH and temperature of preparation showing the β -sheet (pH=12, T=46°C), α -helix (pH=12, T<20°C) and random coil (pH=4, T=20°C) form of the homopolymer.

5.4 2D IR Spectroscopy of Amide II'

5.4.1 Amide I' and II' Diagonal Resonances of Poly-L-lysine

Two-dimensional infrared spectroscopy has previously been used to detail the structural sensitivity of the amide I' line shape using the idealized polypeptide, PLL.¹² In Fig. 5.4.1.1 and 5.4.1.2, the 2D IR spectra of the amide I' and II' regions of PLL are presented in parallel and cross polarization. The diagonal regions, where $\omega_1 = \omega_3$, show positive and negative resonances attributed to the fundamental and overtones of the vibrational potential respectively. The details of the amide I' line shape will briefly be discussed here.¹

Amide I' 2D IR Spectra of Poly-L-Lysine

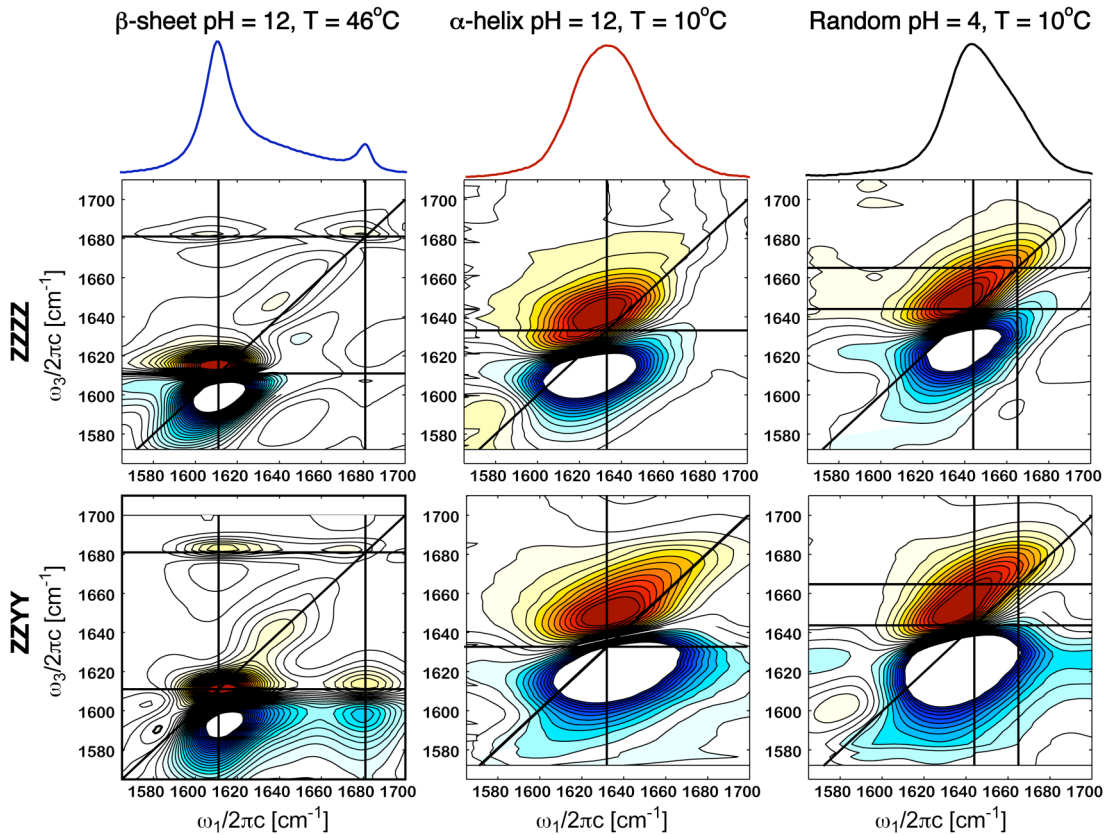


Fig. 5.4.1.1 FTIR and ZZZZ and ZZYY Amide I' 2D IR spectra of poly-L-lysine as a function of pH and temperature of preparation showing the β -sheet (pH=12, T=46°C), α -helix (pH=12, T=20°C) and random coil (pH=4, T=20°C) form of the polypeptide.

The ZZZZ 2D IR spectra of PLL in the various secondary structure conditions are shown in Fig. 5.4.1.1. The first amide I' spectra shows the characteristic 8-peak structure for the β -sheet conformation. The diagonal doublets are the fundamental and overtone transitions of the perpendicular (ν_{\perp}) and parallel (ν_{\parallel}) vibrations. The off-diagonal intensity of the amide I' band shows that these excitons are vibrationally coupled. This off-diagonal doublet reports on the strength of coupling through the anharmonicity or splitting between the positive and negative lobes, which is a direct measure of the frequency of the combination and overtone bands. The ZZYY (cross polarized) spectra

are shown in the lower panel for the corresponding systems. Since the cross peaks scale with the cosine of the angle between the transition dipoles, the enhancement seen in the cross polarized spectra signifies an orthogonal orientation between the two vibrations. By comparison of the *ZZZZ* and *ZZYY* spectra and quantitative value of the relative angle can be determined. For the amide I' vibration, this has been experimental determined to be 65° and these results are in good agreement.¹

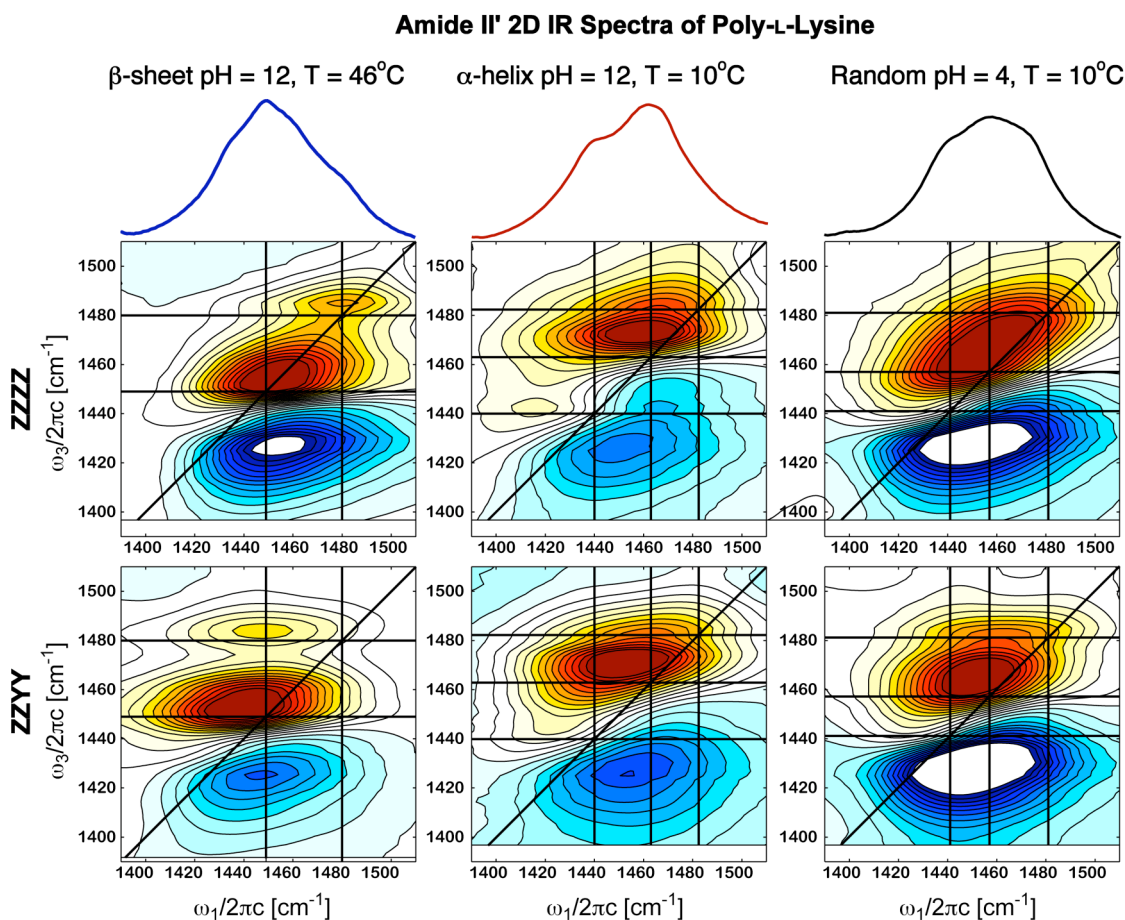


Fig. 5.4.1.2 FTIR and *ZZZZ* and *ZZYY* Amide II' 2D IR spectra of poly-L-lysine as a function of pH and temperature of preparation showing the β -sheet (pH=12,T=46°C), α -helix (pH=12,T<20°C) and random coil (pH=4,T=20°C).

The α -helix and random coil 2D amide I' spectra show very similar features and only exhibit a small relative blue shift as seen in the FTIRs. Both vibrations are

inhomogeneously broadened due to heterogeneity of the molecular structure. Even in this idealized system, the ability to spectrally distinguish these motifs is exceptionally difficult. However, by qualitative examination of the amide II' diagonal in Fig. 5.4.1.2, a significant difference in line shape exist between these moieties; the random coil line shape is more diagonally elongated while the α helix shows some off-diagonal structure, indicative of its underline A and E₁ mode structure.

Figure 5.4.1.2 shows the amide II' spectra of PLL with varying secondary structure conditions. Similar to the amide I' diagonal spectra, the 2D amide II' line shape shows a two-peak structure with the higher intensity peak appearing at lower frequency and a clear cross peak in seen in the ZZYY spectrum. To confirm the extra peak is in fact the contribution of the amide II' band and not the HOD bend, a sample of 1% HOD in D₂O was placed in the spectrometer in the identical sample cell and position of the PLL solution. There was no appreciable signal from the HOD and therefore it is concluded that the absorption at 1450 cm⁻¹ is purely amide II'. This is expected due to difference in the extinction coefficient of the HOD bend (~20 M⁻¹cm⁻¹) and the amide II' mode (~100 M⁻¹cm⁻¹).

The substantial difference in the amide II' 2D line shapes is seen in the α -helical PLL aggregate. The diagonal resonance is very sharp with a minor shoulder at lower frequencies. There is also a significant difference in the intensity scaling of the fundamental and overtone transitions in comparison to the other secondary structure. This non-harmonic scaling is may be attributed to electrical anharmonicity in the system or interference effects between positive and negative going features. This difference is not apparent in the amide I' overtones for any of the experimental systems. This represents

an important spectral differentiation between helices and coils in protein systems, something to this point has been difficult to isolate without spectral decomposition methods.

In all the ZZYY spectra, there is appreciable coupling between the modes of the amide II' vibration seen in the off-diagonal elements of the 2D spectra and implies these modes have a relative transition dipole moment angle greater than 45°. If the angle were precisely 45°, the intensity between the parallel and perpendicular spectra would show little to no difference in the off-diagonal contribution, if the angle is less than 45°, the ZZZZ would show more significant cross peak intensity.^{13,14}

One of the major observations of the diagonal amide II' line shapes, is the appearance of a two-peak structure of the random coil band. If the random coil truly samples all conformational microstates and solvation environments without bias, what causes the structure of its amide II' band? This imposes an important question of what is truly implied by “random.” Under the assumption that the random coil is a statistical sampling of all possible conformations in an extended form, one would expect to see a single inhomogeneously broadened vibrational mode as seen in the amide I' spectrum. Is this due to structural biases caused by steric hindrance and side chains imposing preferential ϕ and ψ geometries on the protein backbone? Or is it that while the configurations are random, the average vibrational coupling is non-zero. If non-zero, is the average coupling positive or negative?

5.4.2 Amide I'-II' Cross Peaks of Poly-L-lysine

To further understand the structural significance of the amide II' band, broadband 2D IR experiments that cover the entire amide I'/II' spectral region are performed. With

sufficient bandwidth to cover all the vibrational states of interests, this mutli-mode technique allows for cross correlation of vibrational sensitivities to be determined.

Figure 5.4.2.1 shows the 2D IR spectra of PLL from 1350-1700 cm^{-1} . The amide I' and II' strips are plotted above one another to represent the full spectrum. The upward cross peak defined vibrational energy transfer from amide II' to amide I' and is seen in the upper left quadrant. This is termed “upward” because its existence due to the induced absorption processes of the incident light field transfers energy in a direction that opposes vibrational relaxation from lower frequency to higher frequency. The downward cross peak, observed in the lower right quadrant of the 2D spectra, represents induced vibrational energy transfer from the amide I' mode “downhill” to amide II'. The line shapes and intensities of these cross peaks provide the correlation between the spectroscopic signatures of amide I' against amide II'.

The cross peak pattern of the β -sheet PLL shows an eight-peak structure in both the upward and downward regions of the ZZYY 2D IR spectra. This arises from coupling between all pairs of the amide I' and II' modes and the corresponding combination band (negative peak) states. The strongest cross peak appears between the two high intensity (1611 cm^{-1} and 1447 cm^{-1}) modes of the amide I' and II' bands. The cross peak intensity scales with the product of the square of the respective coupled transition dipole moments and the cosine of the relative angle between the dipoles. This scaling is clearly seen in the downward cross peak in which the cross peaks that correlate with ν_{\perp} are much more intense than those corresponding to ν_{\parallel} . The orientation of the transition dipoles can be seen through a qualitative comparison of the ZZZZ and ZZYY 2D spectrum. For the β -sheet PLL spectra, comparison of the peak positions of the upward cross peak show that

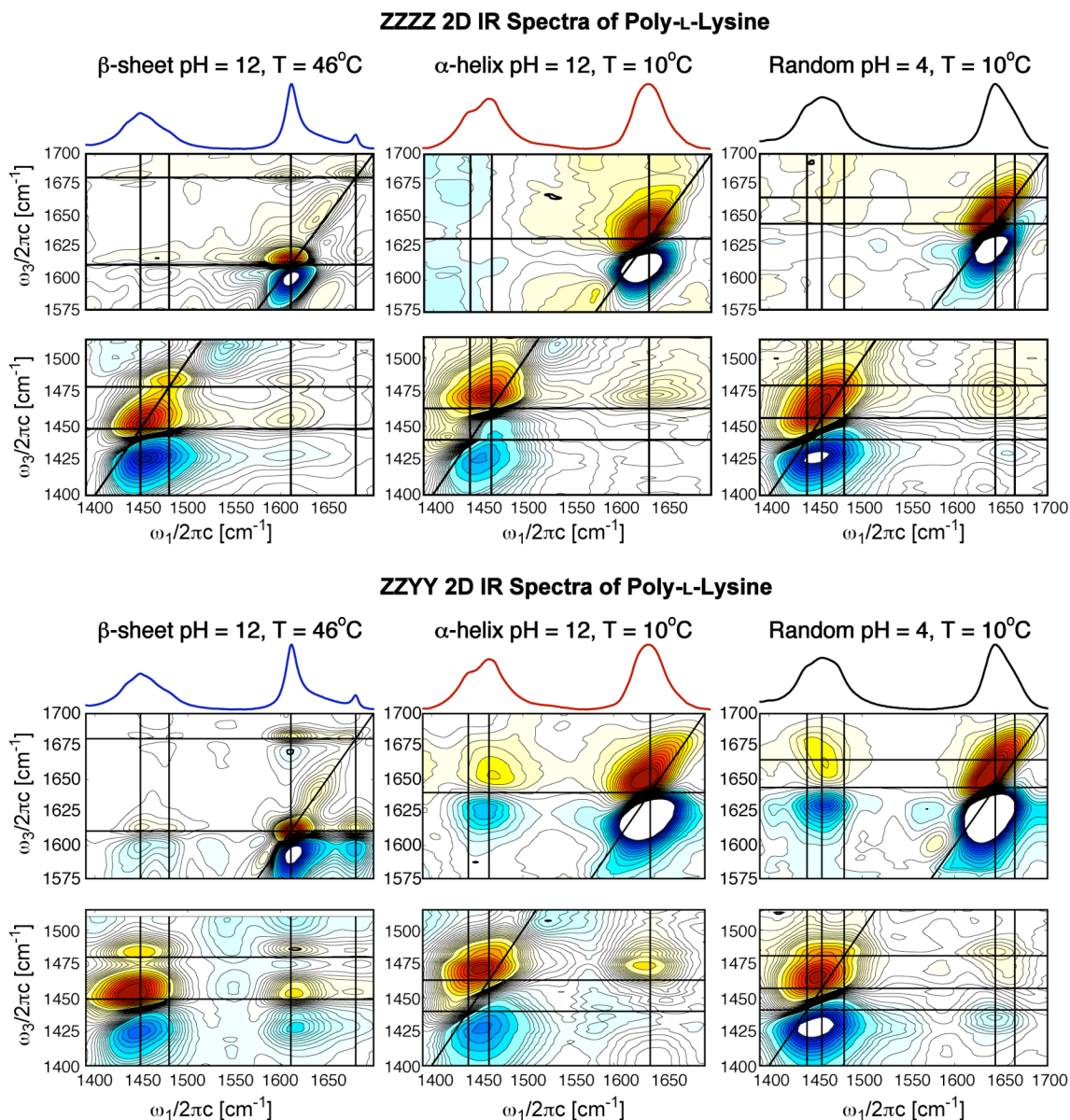


Fig. 5.4.2.1 ZZZZ and ZZYY Amide I'-II' 2D IR spectra of poly-L-lysine as a function of pH and temperature of preparation showing the β -sheet (pH=12, T=46°C), α -helix (pH=12, T<20°C) and random coil (pH=4, T=20°C) forms.

in ZZYY, the cross peak between ν_{\perp} amide I' band (1611 cm^{-1}) and 1447 cm^{-1} amide II' is more intense and in ZZZZ the cross peak between ν_{\perp} (1611 cm^{-1}) peak to the higher energy amide II' band at 1470 cm^{-1} is more intense. This effect is much more subtle in the coupling of ν_{\parallel} band of amide I' with the respective modes of amide II', where a stronger

cross peak in the *ZZZZ* polarization between the 1447 cm^{-1} amide II' band and the ν_{II} amide I' peak. The alternating intensity of the upward cross peaks between amide I' and II' suggests that the amide II' modes are orthogonal to amide I'. These results are consistent with the geometric relationship in which the 1447 cm^{-1} amide II' band is orthogonal to the ν_{\perp} mode and aligned to the ν_{\parallel} mode and the low intensity shoulder at 1470 cm^{-1} is aligned to ν_{\perp} and orthogonal to ν_{\parallel} . Relative to the proteins, this means the more intense mode of amide I' is aligned across the β -sheet strands and the more intense (1447 cm^{-1}) runs along the β -sheet strands as expected in Fig. 5.1.1.1. It is important to note though, that this qualitative assessment is strictly based on the relative angle being greater or less than 45° .

The amide II' 2D IR spectra of the α -helical PLL show substantially different coupling pattern between the amide I' and II' modes. Both cross peaks appear as a single sharp doublet. The upward cross peak shows an anti-diagonal tilt, implying that the molecular vibrations are anti-correlated. In addition, the downward cross peak shows little to no negative transition of the combination band, which may indicate non-harmonic scaling of the overtone transition dipole moment. In addition, the relative intensity increase of the downward cross peak between *ZZZZ* and *ZZYY* implies a substantial angle between the transition dipoles of the helical modes. It is known that the observed amide I' for the α helix is the A mode that lies along the axis of the helix. Results of Marsh and coworkers¹⁵ tabulate the relative angles of the amide I, II and A modes relative to the helix axis. The angles are given as $29\text{-}40^{\circ}$, $73\text{-}77^{\circ}$, and $18\text{-}29^{\circ}$ respectively. Integrating these results for the protonated amide vibrations and those from Chapter 4 in which the angle of amide I to I' is small and the amide II to II' is approximately 35° can

provide structural insight. From this, one would predict that the amide II' angle relative to the helix axis would be between 108-112° giving a relative angle between the helical amide I' and II' to be within 72-79° which would be consistent with the results observed here. Therefore, the amide II' band of α -helical PLL lies predominately perpendicular to the helix axis, and represents the E_1 helical mode.

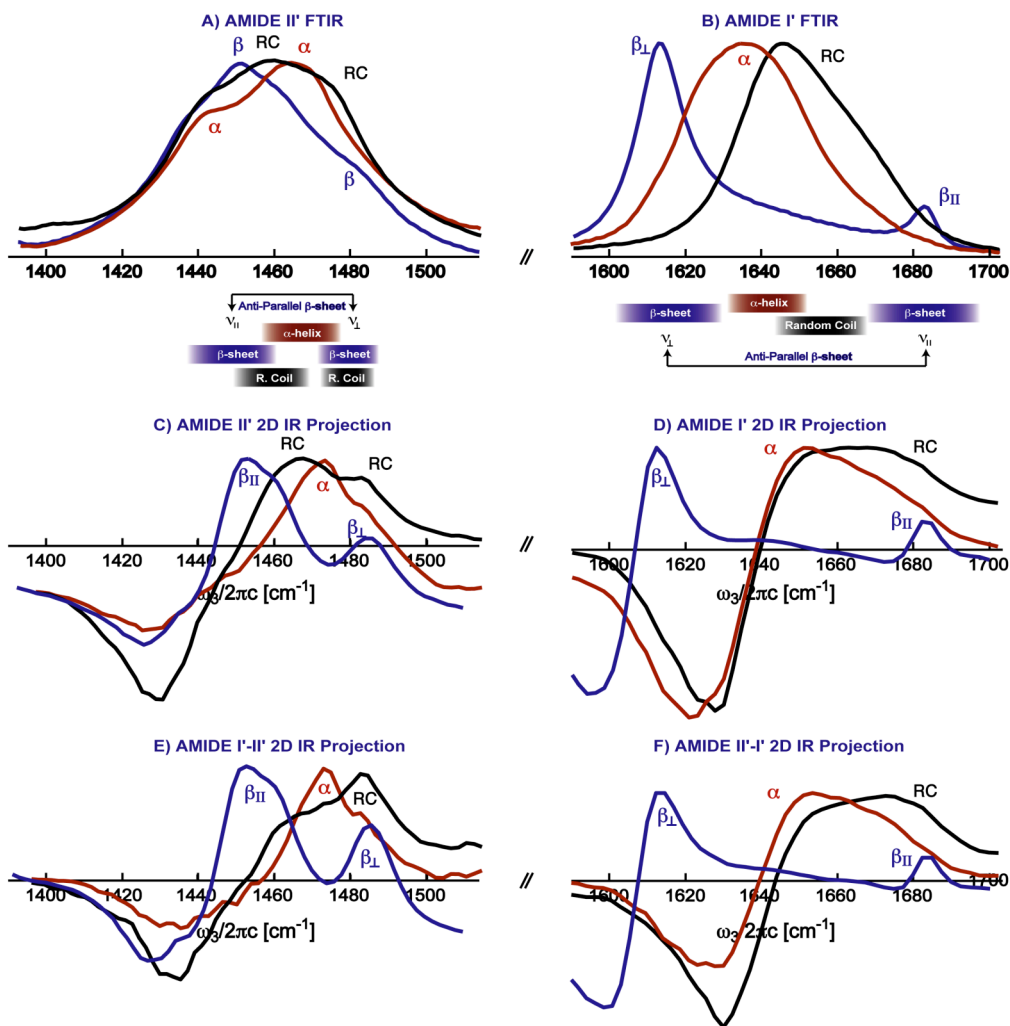


Fig. 5.4.2.2 (a,b) FTIR of the amide II' and amide I' regions of PLL. (c,d) Projection along ω_1 of the diagonal peaks of amide II' (1420-1500 cm^{-1}) and amide I' (1600-1700 cm^{-1}). (e,f) Projections of the downward (amide I'-II') and upward (amide II'-I') 2D IR cross peaks. Distinct signatures for the α -helix and random coil are seen in both the diagonal (c) and cross peaks (e) of the amide II' 2D projections.

Similar to amide I', the amide II' line shapes of the β sheet and α helix are distinct enough to allow simple separation. Additionally, amide II' complements amide I' with the ability to easily separate α -helix and random coil signatures. The random coil and β -sheet line shapes, however, appear similar. But differences can be resolved by inspecting the distinct cross-peaks to amide I'. In both ZZZZ and ZZZY polarizations, the strongest coupling is observed between the high-energy shoulder of amide II' band and the main peak of amide I' implying the angle between these transition is near 45°. There is a large apparent mismatch in intensities between the amide II' fundamental and overtone, which may be due to off diagonal anharmonicity or interference between the amide I' coupling with the 1450 cm⁻¹ mode.

To better compare signatures of the ZZZY surfaces, projections of the amide I' diagonal, the amide II' diagonal and the amide I'-II' downward cross peak are compared in Fig. 5.4.2.2 against the FTIR spectra. Here, the projections of the cross peak across the entire band along ω_1 show the distinct 2 peak structure of the β -sheet motif, a single sharp transition for the helical system and a sharp peak at 1481 cm⁻¹ and a broad shoulder of the random coil structure. Using these results, structural assignments based upon the amide I'/II' cross peak are made for the amide II' diagonal resonance. These results point to the ability to spectroscopically isolate all forms of secondary structure through the use of amide I'-II' coupling.

5.5 Model Calculations of the Amide II' Sensitivity to Secondary Structure

The multi-mode 2D IR experimental results provide insight into the interactions and structural relationship of the amide transition dipole moments of PLL in extended, idealized secondary structures. This is seen through correlated frequency shifts and

vibrational coupling extracted from the shape and amplitude of the cross peaks. To gain further molecular insight into how these dipoles, and therefore spectral features, project onto the molecular structure, calculations using the local amide mode Hamiltonian are performed. This model describes the amide I'/II' manifold of vibrations as linear combinations of unit amide I' and II' oscillators for each peptide group. Each oscillator has a site energy, corresponding to the vibrational frequency of that isolated oscillator and coupling between oscillators that can depend on the distance and orientation. This Hamiltonian and transition dipoles can be constructed for different idealized secondary structures and used to predict FTIR and 2D IR spectra. This type of modeling provides a frequency-structural correlation and has been very successful in capturing the amide I vibrational line shape. Finally, doorway mode analysis is performed on the amide II' eigenstates to provide a spatial map of the phase and amplitude relationships of the residue specific oscillators that give rise to vibrational delocalization or excitons.

5.5.1 Local Amide Hamiltonian

The Local Amide Hamiltonian (LAH) provides a method that relates experimental observables to structure through transformation from a local mode to a normal mode basis set. Established by the groups of Miyazawa¹⁶ and Krimm¹⁷ and later applied to 2D IR spectroscopy by Hamm and Hochstrasser,¹⁸ the LAH is an exceptionally simple and spectroscopically relevant method for understanding the nature of protein vibrations and their structural correlation. This approach has primarily been used for modeling amide I spectroscopy. Here, we extend the LAH to describe the secondary structure sensitivity of the amide II' vibration. The LAH is constructed in the amide I' and II' local basis and the amide II' block is related to the idealized structure through nearest neighbor coupling and

amide I'-II' on-site coupling. The idealized structure for the anti-parallel β sheet has six strands with 12 oscillators generated by repeating $\phi=-139^\circ$ and $\psi=135^\circ$ and the cross-strand groups are 3.04 Å apart. The α helix has 20 oscillators generated with repeating $\phi=-57^\circ$ and $\psi=-47^\circ$ yielding a 1.80 Å separation of hydrogen bonded O-H. The random coil is generated by 5000 snapshots of an MD simulation of an 18-oscillator peptide in vacuum at 1000°C, where it samples all ϕ and ψ equally.

The amide I vibrations are characterized by anharmonically coupled oscillators with all degenerate site energies of 1675 cm^{-1} and anharmonicity of 16 cm^{-1} . Using the orientation of the amide I' vibration of 20° off the C=O bond, with the dipole center located 0.868 Å along the carbonyl axis, and a normalized unit dipole strength of 1.0, dipole interactions and couplings are determined through transition dipole coupling, which senses the orientation and distance between amide I' oscillators.¹⁹

The amide II' band is primarily localized to the CN stretch with minimal ND in-plane bend contribution. Experimental obtained results from Chapter 4 on NMA-d₇ in D₂O are used for the amide I'/II' on-site coupling (39 cm^{-1}), amide II' vibrational anharmonicity (10 cm^{-1}), and site energy (1450 cm^{-1}). It is further assumed that the amide II' vibration only coupled to the amide I' vibration located on the site and the covalently bonded nearest neighbor amide II' sites. While the amide I'/II' coupling is fixed, amide II'/II' nearest neighbor couplings were empirically set to -8.5 cm^{-1} for the β sheet, -8.7 cm^{-1} for the α helix and randomly sampled from a normal distribution (mean = -5 cm^{-1} and standard deviation = 3 cm^{-1}). For the random coil, the site energies are also sampled from a normal distribution with standard deviation of 10 cm^{-1} from the above values for

amide I' and II'. The physical motivation for this is due to the overall bias towards negative coupling across the ϕ/ψ map seen for amide II in the work by Hayashi et al.²⁰ Through space coupling is neglected for the amide II' vibration since the vibration lies predominately along the backbone and observed to be inessential to reproduce the experimental line shapes.

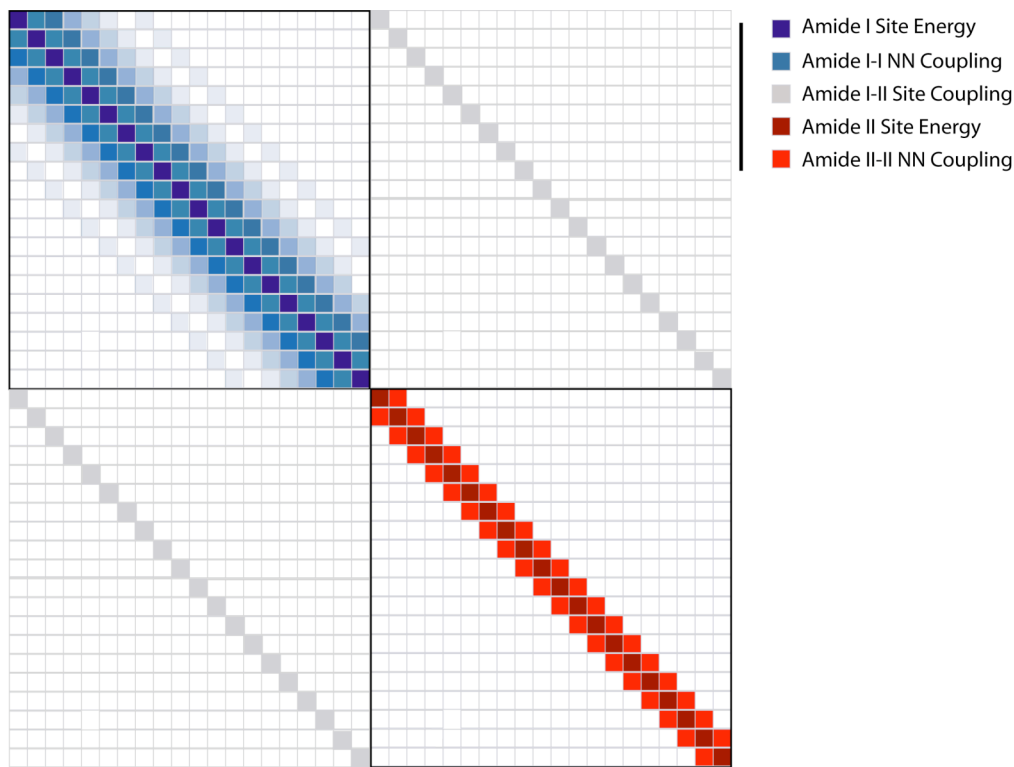


Fig. 5.5.1.1 Pictorial representation of the Local Amide I'-II' Hamiltonian for an α helix. The amide I' block contains through space coupling depicted by $n+1$ diagonal elements. The amide II' block (red) only contains nearest neighbor couplings.

Figure 5.5.1.1 shows a pictorial representation of the LAH for the amide I-II Hamiltonian. The diagonal elements are the site-specific energies of the individual residues and the off-diagonal elements are the vibrational coupling terms between residues. More sophisticated treatments that allow the site energies and couplings to vary,

show how these methods can be used to obtain amide I'/II' spectra of proteins using MD simulation.²¹⁻²³

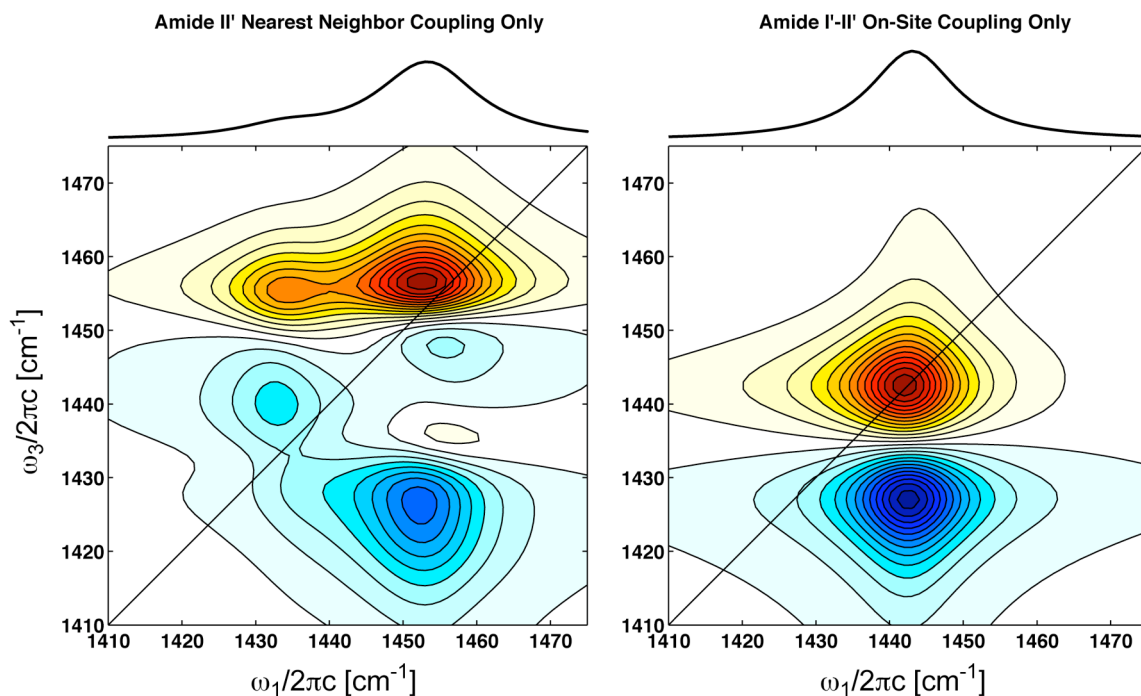


Fig. 5.5.1.2 Comparison of calculated FTIR and 2D spectra comparing coupling effects. Amide I'-II' on-site coupling induces a shift in the peak frequency of 6 cm^{-1} while nearest neighbor coupling splits the vibrational mode.

Control calculations of FTIR and 2D IR spectra with and without coupling are used to examine the origin of spectral features. Fig. 5.5.1.2 shows a comparison of the nearest neighbor coupling and amide I-II coupling on both the linear and 2D IR spectra of an idealized α helix. A single resonance is observed in the cases for no coupling and amide I'-II' site coupling only where the latter is shifted off the degenerate site energy by 6 cm^{-1} . Only introduction of nearest neighbor couplings in both cases split the vibrational band and the sign of the nearest neighbor coupling dictates the relative peak intensities. Therefore we conclude that amide II' oscillators couple directly to one another. A

coupling mechanism where amide II' oscillators are only indirectly coupled through the amide I' manifold is insufficient to produce any peak structure.

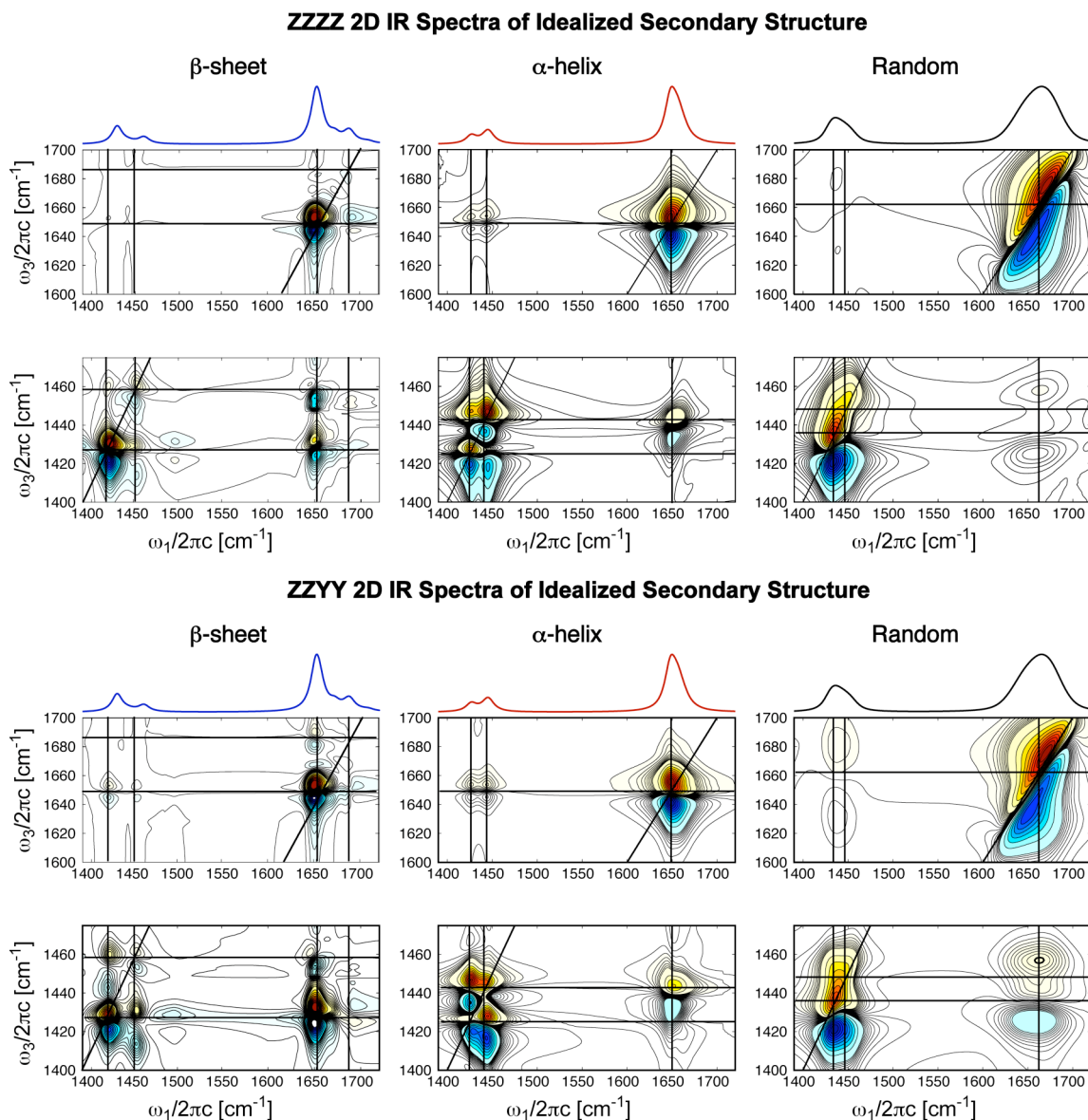


Fig. 5.5.1.3 Calculated FTIR and Amide I'/II' 2D IR spectra of AP β sheet, α helix and random coil in both ZZZZ and ZZYY polarization.

Figure 5.5.1.3 shows the calculated linear and 2D IR (ZZZZ and ZZYY) spectra for the AP β sheet, α helix and random coil. As described above, the experimental data shows splitting of the amide II' band, a signature only seen when including nearest

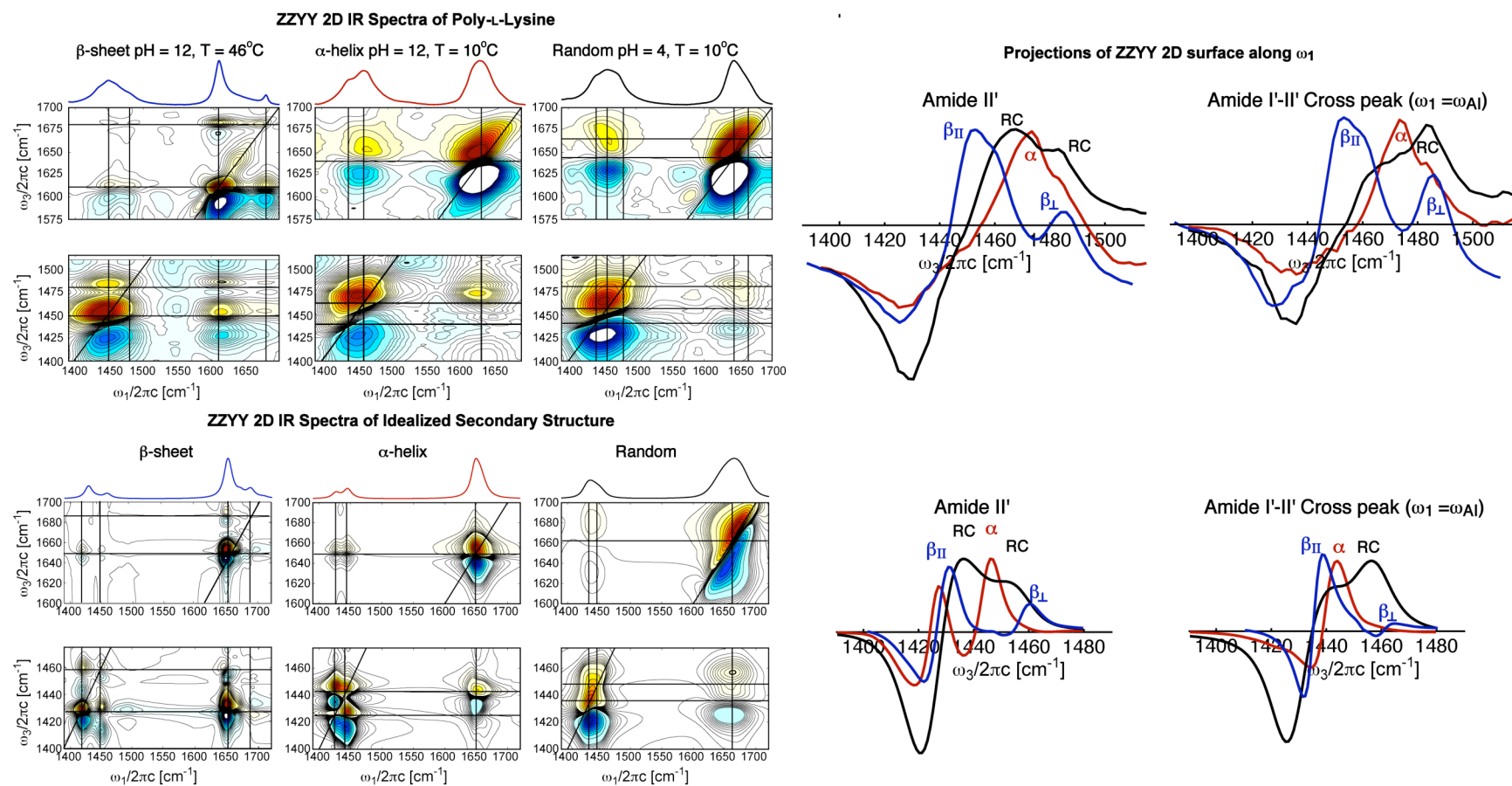


Fig. 5.5.1.4 Comparison of the calculated and experimental ZZYY 2D IR spectra. Projections of the β sheet, α helix and random coil of the amide II' diagonal (1420-1500 cm^{-1}) and the amide I'-II' downward cross peak (1600-1700 cm^{-1}). Projections show identical band structures with inclusion of negative nearest neighbor couplings.

neighbor couplings. This confirms that the origin of peak splitting is dictated by nearest neighbor coupling and ϕ/ψ angles of the protein structure. Furthermore, positive coupling can be definitely ruled out as it leads to the wrong intensity ratio between the high and low frequency peaks. The α -helical calculated 2D IR spectra show a weak shoulder on the red side of the amide II' band. This feature is observed as a weak resonance in the experimental PLL data and these results are compared in Fig. 5.5.1.4. Similarly, the β -sheet idealized structure shows two peaks in which the higher frequency vibration has a smaller transition. Inversion of the β -sheet cross peak arises from transform interference artifacts for interpolating narrow features on a low-resolution grid. The random coil 2D IR spectra show the qualitatively correct splitting in the amide II' line shape and changes from ZZZZ to ZZYY. The amide I'/II' cross-peak region almost fully captures the line shapes and intensities of the positive and negative contributions of the experimental random coil spectrum. Since these model calculations do not include the effects of electrical anharmonicity, it explains the observed mismatch in fundamental and overtone intensities as the result of interference due to static averaging. The simple modeling in these calculations demonstrates two points. First, that only nearest neighbor coupling is required to understand the splitting between amide II' vibrations. The second is that the sign and approximate magnitude of this nearest neighbor coupling can be unambiguously obtained from the intensity ratio and splitting observed in the amide II' 2D IR spectra.

To further capture the secondary structure size dependence of the amide II' vibration, linear FTIR spectra are calculated for NxN β -sheet and 1xN β -hairpins. The results are presented in Fig. 5.5.1.5. N is limited to 3 for these calculations due to the computation time of the NxN sheet. As expected for the amide I' band, ν_{\perp} shifts to lower

frequency as N increases for β -sheets and shift to higher frequency for increased hairpin length.⁵ For both β -sheets and β -hairpins, the amide II' doublet splits identically implying the addition of strands has limited to no effect on the band structure. This further elucidates the role of nearest neighbor coupling on the spectral signatures of amide II'.

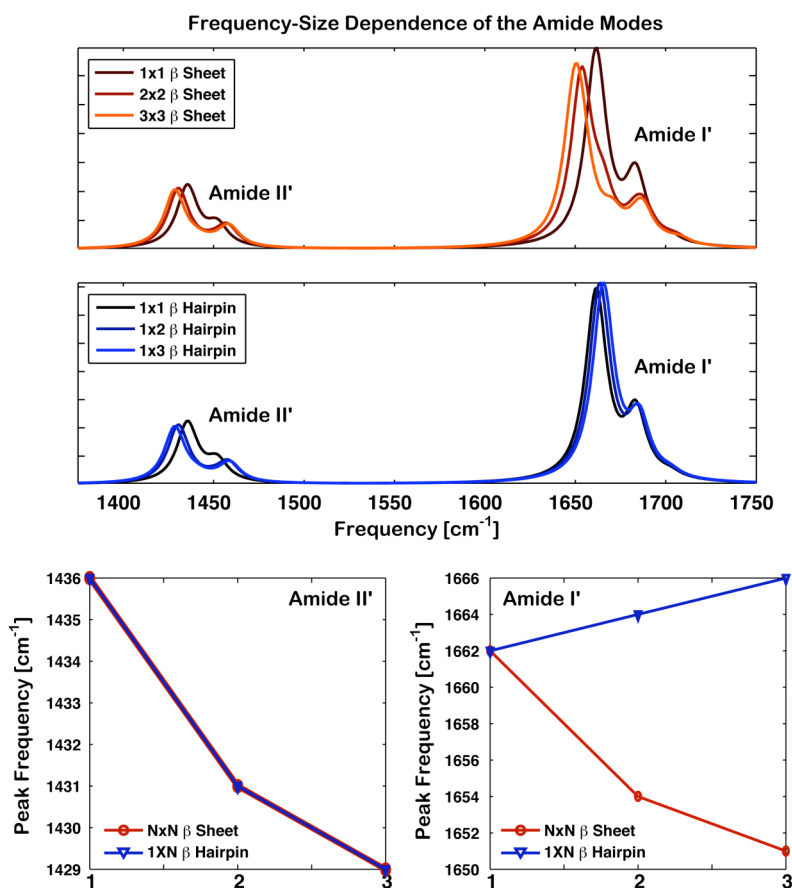


Fig. 5.5.1.5 Calculated size-dependence of the FTIR spectra for the idealized β -sheet (top) and β -hairpin (middle). N represents the number of unit cells in the calculation. (Bottom) Frequency dependence of the most intense amide II' and I' modes vs. N.

5.5.2 Doorway Mode Analysis

The correlation between spectral signatures and protein structure is obtained through building a molecular view of the vibrational eigenstates. However, vibrational

modes comprise a dense manifold of states that, for any one molecule, evolve rapidly in

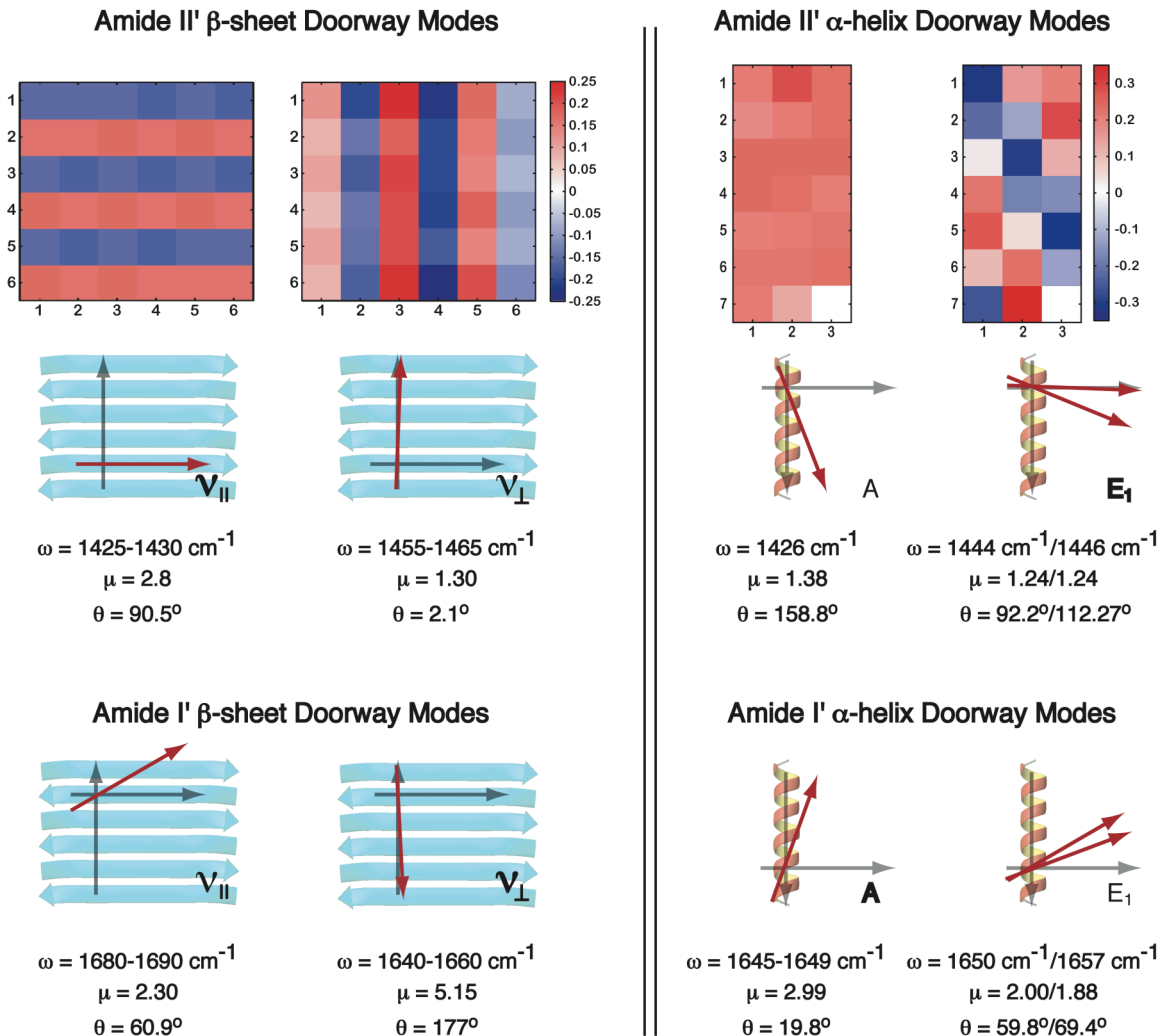


Fig. 5.5.2.1 (Top) Amide II' β -sheet and α -helix doorway modes of idealized systems. The visualization map has hydrogen bonded oscillators (n and $n+3$ for the α helix) aligned vertically. (Bottom) Relationship of the amide I' and II' transition dipole (eigenstates) relative to the secondary structure axis. For each mode, the frequency range of the doorway mode is given (for single frequencies the angle of the eigenstates is used), the dipole moment intensity and the angle relative to the +Y (for β -sheet) and +Z (for α -helix). Note that coordinate arrows represent the direction of residue addition.

time. One way to overcome this challenge of visualization is to identify bright states in a frequency region. Doorway mode analysis is a way of transforming a subset of the eigenvectors in a given frequency range into a bright state basis, which concisely describes the modes that carry the most transition dipole strength and therefore, best

signify the chosen frequency region. Our method²⁴ extends that of Torii and Tasumi²⁵ and visualizes these bright states by showing the participation amplitude and phase of all oscillators in the mode.

		Amide II'					
		θ	ν_{\parallel} 1425 - 1430 cm ⁻¹	ν_{\perp} 1455-1465 cm ⁻¹	A 1426 cm ⁻¹	E ₁ 1444 cm ⁻¹	E ₁ 1446 cm ⁻¹
Amide I'	θ		91	2	159	92	112
	ν_{\parallel} 1680-1690 cm ⁻¹	61	30	-59			
	ν_{\perp} 1640-1660 cm ⁻¹	177	-87	-175			
	A 1645-1649 cm ⁻¹	20			139	72	92
	E ₁ 1650 cm ⁻¹	60			99	32	52
	E ₁ 1657 cm ⁻¹	69			89	23	43

Table. 5.5.2.1 Calculated angles between the amide I' and II' doorway modes (for frequency ranges) and eigenstates (single frequency). Angles in gray are the angle of the transition dipole relative to the dominate axis of the secondary structure. Bolded angles represent modes with the strongest cross peaks observed in ZZYY 2D IR.

Figure 5.5.2.1 shows the amide II' doorway modes of the idealized AP β sheet and idealized α helix. The color scheme represents the amplitude by the depth of color and the phase, or sign, is depicted as either red or blue. For amide II', two bright states are found that best describe the low and high frequency β -sheet modes, one with amide II' site oscillators in phase through the β strands and across the β strands. Because the splitting of these modes is due to the symmetry of the amide oscillators, these modes

mirror the bright states obtained for amide I'. For the α helix, the bright states also mirror those found for amide I' with A and E_1 symmetry modes with phases aligned parallel and perpendicular to the helix axis, respectively.

The relative angles of the doorway modes are calculated for the amide I' and II' modes of the β sheet and α helix. In regions where the density of states is too low, a single intense eigenstates was selected. Table 5.5.2.1 compares the angles of the β -sheet and α -helical modes of the idealized structures. These results correlate exceptionally well to the experimentally observed cross peak ratios of ZZZZ and ZZYY 2D IR spectra from Fig. 5.4.2.1. As expected the strongest transitions of the amide I' and II' transitions are orthogonal with a calculated inclusive angle of 87° . Similarly, the dominant α -helix mode of amide I' runs along the axis while the amide II' runs orthogonal. This is observed in both the calculated angles of the amide I A mode relative to the E_1 modes of amide II' of 72° and 92° and in the experimental polarization spectra. These results are consistent with those presented by Marsh and co-workers.¹⁵

5.6 Amide II' Spectroscopy of Globular Proteins

As a further test of the sensitivity of the amide II' vibration to protein secondary structure, the spectra of an all α -helical protein, myoglobin, and a α/β protein, ubiquitin, are compared under thermal denaturing conditions. The ability to resolve structural changes of proteins from a native state to a purely unfolded state are of great interest in understanding the pathways and mechanisms of protein folding. To this point, the ability to clearly resolve structural difference of α helices and random coils has been a major challenge in amide I' spectroscopy due to overlapping peaks for these structural forms. Using the amide I'-II' cross peak, a clear transition between α helix to a β sheet is seen in

the aggregation of Myoglobin upon heating to above its unfolding temperature.²⁶ The transition to the unfolded state is seen in the reversible heating of ubiquitin.

5.6.1 Myoglobin

Myoglobin contains 74% α -helix content and is a molecular transport protein, which supplies oxygen to muscles in the human body. Like many helical systems, myoglobin is a non-reversible folder and will aggregate at high temperatures. Recent literature has shown the ability to form amyloid fibrils from myoglobin and is conjectured to form highly ordered AP β -sheet aggregates.²⁶

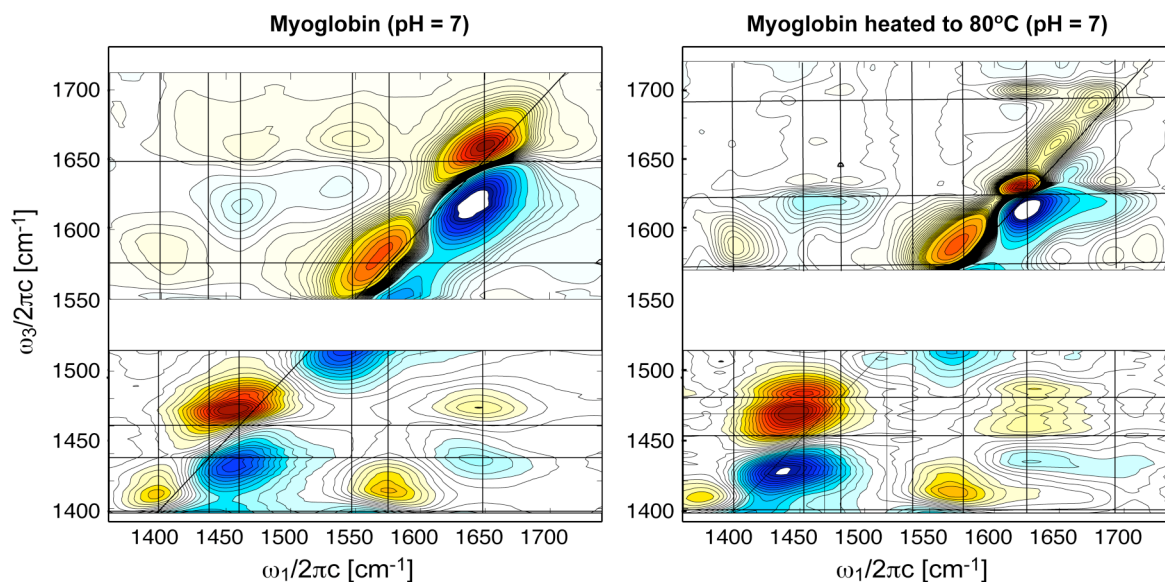


Fig. 5.6.1.1 ZZZY 2D IR Spectra of myoglobin at pH =7 at T = 10°C before (Left) and after (Right) being heated to above the unfolding temperature (T = 80°C). Heated spectra shows aggregation of myoglobin into AP β sheet.

Figure 5.6.1.1, shows the partially exchanged 10°C 2D IR amide I/I' and amide II' spectra of myoglobin and 2D IR spectra of the identical sample heated to at 80°C. The native 2D IR spectra shows the signature amide I' diagonal doublet and a sharp amide II' diagonal transition. This spectra mirrors the idealized helical spectra of PLL in Fig.

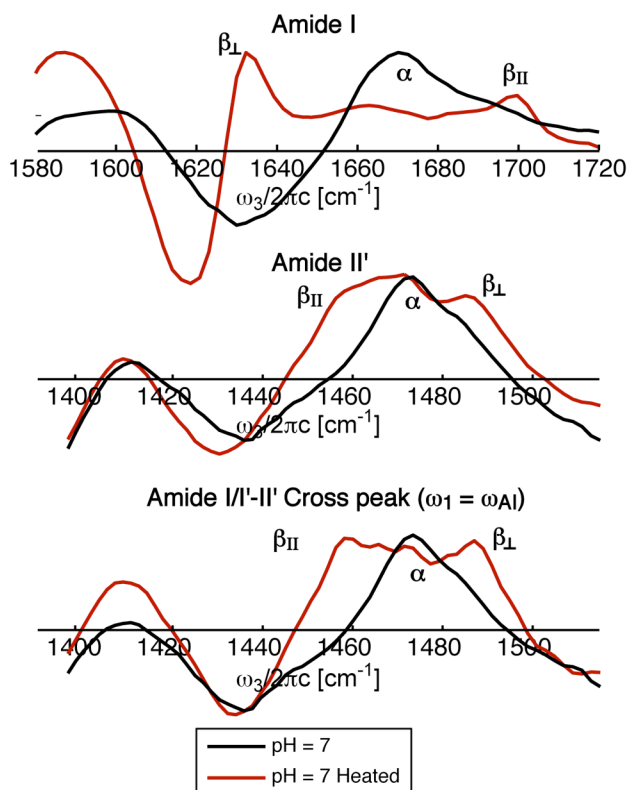


Fig. 5.6.1.2 Projection along ω_1 axis of ZZYY 2D IR Spectra of myoglobin at pH = 7 at $T = 10^\circ\text{C}$ before (Black) and after (Red) being heated to above the unfolding temperature ($T = 80^\circ\text{C}$). Heated spectra shows aggregation of myoglobin into AP β -sheet in the amide I' diagonal (top), amide II' diagonal (middle) and amide I'-II' downward cross peaks (bottom) projections.

5.4.2.1, in even the low intensity amide II' overtone. The downward amide I'/II' cross peak also exhibits the characteristic cross peak of an α helix with a sharp positive peak and a weaker negative peak. Upon heating, a drastic structural transformation is observed. The heated myoglobin spectra strongly mirror the β -sheet form of PLL implying the formation of AP β -sheet aggregates. The ν_{\perp} and ν_{\parallel} modes of the amide I' are apparent in the diagonal region as is the two-peak structure of the amide II' band. There is a significant change in the downward cross peak from the helical form to the β -sheet aggregate. By comparing the projections of the amide I' diagonal, amide II' diagonal and downward cross peak in Fig. 5.6.1.2, the ability to clearly resolve this

structural transition is significant. This provides another clear spectral probe for measuring the rates of transformations from α helices to β sheets, such as predicted to occur in the aggregation of fibrils.

5.6.2 Ubiquitin

To demonstrate the transition from a native folded state to unfolded state of a protein, a reversible folder is desired. Ubiquitin is a heavily studied, reversible folding protein, which contains a mixture of parallel and AP β sheets and a single α helix. The hydrophobic core of the protein is formed by a combination of the β hairpin and α helix that are located in the first 37 amino acids from the N-terminus. To this point, temperature jump experiments have mapped the timescale of unfolding of the β sheet by probing structural changes through the use of amide I' 2D IR spectroscopy;²⁷ however, monitoring changes of the α helix have been difficult due to its overlap with the random coil region.

Upon heating of fully deuterated ubiquitin, a large transition is seen in the amide II' diagonal and cross peaks (Fig. 5.6.2.1). At 5°C, the 2D IR strip shows the presence of a two-peak structure and the appearance of shoulders at 1454 cm^{-1} and 1486 cm^{-1} in the 2D projections imply to the presence of AP β -sheet structure. Little change is seen in the both the 2D and projections upon heating to 20°C, however a substantial transition is observed well above the melting temperature at 80°C. The 2D spectrum shows a merging of the 2 positive peaks in the cross peak region. The projection more clearly shows the loss of the low and high frequency shoulders (1454 and 1486 cm^{-1}). This implies unfolding of the AP β sheet. The significant growth of the overtone, particularly of the cross peak, implies that the amide II' spectrum is dominated by a random coil

conformation. The remaining high-energy peak at 1484 cm^{-1} is the vibrational signature

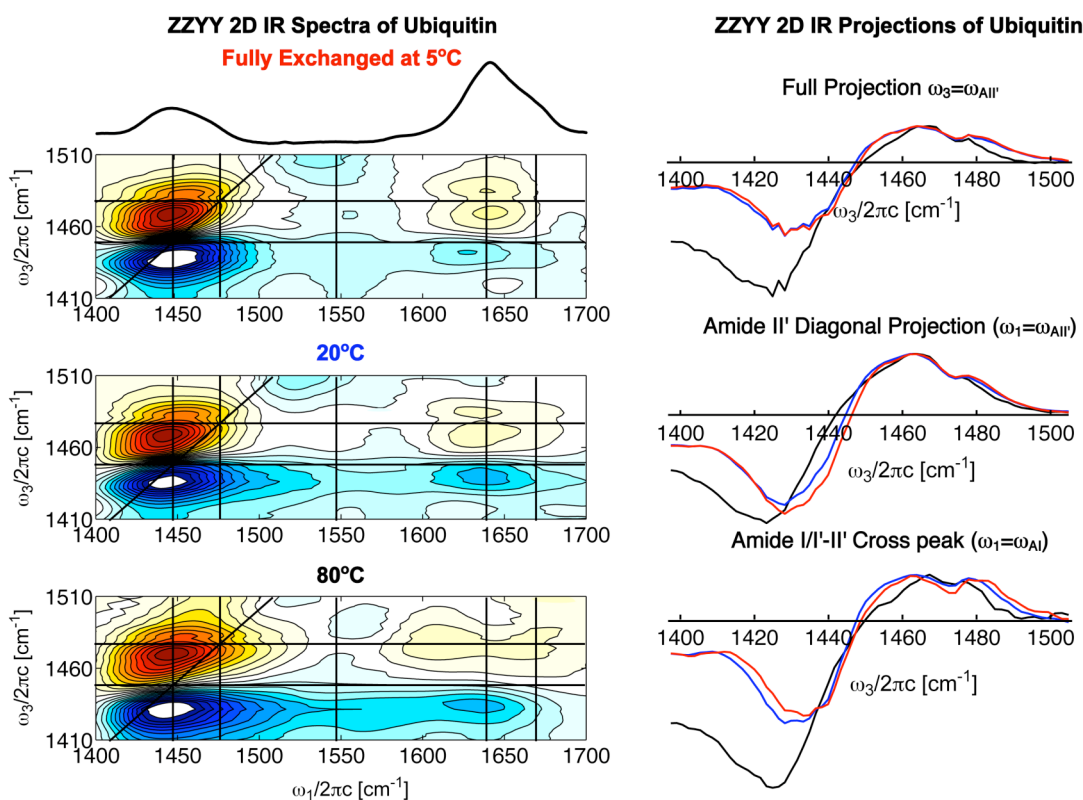


Fig. 5.6.2.1 Temperature dependent Amide II' 2D IR spectra and projections of ubiquitin at $T = 5^\circ\text{C}$ (red), 20°C (blue), and 80°C (black).

of a random coil configuration. The peak at 1471 cm^{-1} is a signature representative of the presence of α helix even at $T = 80^\circ\text{C}$. The presence of this peak implies that the nearest neighbor orientation is conserved. However, we cannot quantify the extent that the helix has “loosened” or that hydrogen-bonded contacts are broken. Performing hydrogen exchange measurements on unfolding intermediates of ubiquitin might be able to elucidate this question and preliminary experiments will be reported in Chapter 8.² The helix of ubiquitin has been shown to be exceptionally stable and these results provide further evidence.^{28,29}

5.7 Conclusion

We have demonstrated that increased structural sensitivity and molecular information can be obtained through multi-mode 2D IR spectroscopy. To this point, the amide I vibrational mode of proteins has predominately provided molecular insight to the protein dynamics through its structural sensitivity. Amide I'-II' 2D IR experiments elucidate the distinct structure sensitivity of the amide II' mode on an idealized system of poly-L-lysine in the β -sheet, α -helix, and random coil conformations. Polarization selective measurements provide direct evidence for a rotation in the molecular reference frame for amide II' of approximately 90° relative to Amide I'. This gives rise to dominate transition dipoles that lie along the β -sheet strands and orthogonal to the helix axis.

Model calculations are performed to gain insight into the molecular origin of the observed amide II' peaks. This model demonstrates that nearest neighbor couplings accurately captures the two band structure of the amide II' mode. The splitting and magnitude of the transitions in the FTIR spectra constrain the sign and magnitude of the coupling. For all secondary structure moieties, negative couplings properly predict the experimental results and coupling magnitudes of -8.5 cm^{-1} for the β sheet and -8.7 for the α helix are found. The random coil coupling term is sample from a Gaussian distribution with an average negative value. Due to this significant nearest neighbor coupling, the amide II' band shows distinct secondary structure sensitivity and provides an additional molecular probe for understanding frequency-structure correlation in proteins.

Extension of this work to globular proteins shows promise for an additional probe of the α -helix. Results of myoglobin show the α -helix to β -sheet transition of the amide II' line shape upon aggregation at high temperatures and ubiquitin demonstrates the

ability to resolve unfolding of the β sheet and spectroscopically isolates the presence of native helical structure at high temperatures. In the next chapter, the structural sensitivity of the amide I' and II' bands will be integrated with the solvent exposure sensitivity of the amide II band. This work presents the ability to isolate stable secondary structure of proteins through hydrogen-deuterium exchange multi-mode 2D IR spectroscopy.

Acknowledgements

I would like to thank Ziad Ganim for the providing the calculated 2D IR and FTIR spectra and performing the doorway mode analysis and Rebecca Nicodemus for the DFT calculations and help in acquiring the amide II' 2D IR data.

References

- (1) Demirdöven, N.; Cheatum, C. M.; Chung, H. S.; Khalil, M.; Knoester, J.; Tokmakoff, A. *J. Am. Chem. Soc.* **2004**, *126*, 7981-7990.
- (2) DeFlores, L. P.; Tokmakoff, A. *J. Am. Chem. Soc.* **2006**, *128*, 16520-16521.
- (3) Mikhonin, A. V.; Bykov, S. V.; Asher, S. A. *J. Phys. Chem. B* **2006**, *110*, 1928-1943.
- (4) Miyazawa, T.; Blout, E. R. *J. Am. Chem. Soc.* **1961**, *83*, 712-719.
- (5) Cheatum, C. M.; Tokmakoff, A.; Knoester, J. *J. Chem. Phys.* **2004**, *120*, 8201-8215.
- (6) Krimm, S.; Bandekar, J. *Adv. Protein Chem.* **1986**, *38*, 181-364.
- (7) Rosenheck, K.; Doty, P. *Proc. Nat. Acad. Sci.* **1961**, *47*, 1775.
- (8) Greenfield, N.; Davidson, B.; Fasman, G. D. *Biochem.* **1967**, *6*, 1630-1637.
- (9) Wooley, S.-Y. C.; Holzwarth, G. *Biochemistry* **1970**, *9*, 3604-3608.
- (10) Davidson, B.; Fasman, G. D. *Biochemistry* **1967**, *6*, 1616-1629.
- (11) DeFlores, L. P.; Ganim, Z.; Ackley, S. F.; Chung, H. S.; Tokmakoff, A. *J. Phys. Chem. B* **2006**, *110*, 18973-18980.
- (12) Ganim, Z.; Chung, H. S.; Smith, A.; DeFlores, L.; Jones, K. C.; Tokmakoff, A. *Acc. Chem. Res.* **2008**.
- (13) Golonzka, O.; Khalil, M.; Demirdöven, N.; Tokmakoff, A. *J. Chem. Phys.* **2001**, *115*, 10814-10828.
- (14) Khalil, M.; Demirdöven, N.; Golonzka, O.; Fecko, C. J.; Tokmakoff, A. *J. Phys. Chem. A* **2000**, *104*, 5211.
- (15) Marsh, D.; Muller, M.; Schmitt, F. *Biophys J.* **2000**, *78*, 2499-2510.

- (16) Miyazawa, T. *Journal of Chemical Physics* **1960**, *32*, 1647-1652.
- (17) Moore, W. H.; Krimm, S. *Proc. Natl. Acad. Sci. USA* **1975**, *72*, 4933-4935.
- (18) Hamm, P.; Lim, M.; Hochstrasser, R. M. *J. Phys. Chem. B* **1998**, *102*, 6123-6138.
- (19) Torii, H.; Tasumi, M. *J. Chem. Phys.* **1992**, *96*, 3379-3387.
- (20) Hayashi, T.; Mukamel, S. *J. Phys. Chem. B.* **2007**, *111*, 11032-11046.
- (21) Ham, S.; Cho, M. *J. Chem. Phys.* **2003**, *118*, 6915-6922.
- (22) Jansen, T. I. C.; Knoester, J. *J. Chem. Phys.* **2006**, *124*, 044502.
- (23) Ganim, Z.; Tokmakoff, A. *Biophys J.* **2006**, *91*, 2636-2646.
- (24) Chung, H. S.; Tokmakoff, A. *Journal of Physical Chemistry B* **2006**, *110*, 2888-2898.
- (25) Torii, H.; Tasumi, M. *J. Chem. Phys.* **1992**, *97*, 92-98.
- (26) Fandrick, M.; Fletcher, M. A.; Dobson, C. M. *Nature* **2001**, *410*.
- (27) Chung, H. S.; Khalil, M.; Smith, A. W.; Tokmakoff, A. *Rev. Sci. Instr.* **2007**, *78*.
- (28) Sosnick, T. R.; Dothager, R. S.; Krantz, B. A. *Proc. Natl. Acad. Sci. USA* **2004**, *101*, 17377-17382.
- (29) Briggs, M. S.; Roder, H. *Proc. Natl. Acad. Sci. USA* **1992**, *89*, 2017-2021.

Chapter 6

Side Chain Absorptions in the Amide Finger Print Region of Proteins

“...it is far better to grasp the Universe as it really is than to persist in delusion, however satisfying and reassuring.”-Carl Sagan

6.1 Two-Dimensional Infrared Spectroscopy of Protein Side Chains

Two-dimensional infrared spectroscopy of the amide finger print region of proteins provides information about protein structure, dynamics and function. As laser technology advances and broader band infrared systems become available, the ability to exploit the full potential of this region becomes possible. The amide I vibration has been an exceptionally valuable probe of protein folding dynamics and shows distinct secondary structural sensitivity. The amide II vibration, less studied but its strengths are demonstrated in this thesis, shows high sensitivity to isotopic substitution of the amide

Table 1a. Side Chain Absorptions in H₂O

Amino Acid		cm ⁻¹ (H ₂ O) < pK _s low pH		cm ⁻¹ (H ₂ O)		cm ⁻¹ (H ₂ O) > pK _s high pH		Mode	pK _s
Arginine	ARG R	460 320	1652 1630	-	-	-	-	$\nu_{as}CN_3H_5^+$ $\nu_sCN_3H_5^+$	11.6 - 12.6
Aspartic Acid	ASP D	-	-	280	1716	-	-	$\nu C=O$ $\nu_{as}COO^-$ ν_sCOO^- δ_sCH_3	4.0 - 4.8
		-	-	-	-	235 256	1577 1402		
Asparagine	ASN N	-	-	320	1677	-	-	$\nu C=O$	
		-	-	150	1617	-	-	δNH_2	
Cysteine	CYS C	-	-	-	2551	-	-	νSH	9.0-9.5
Glutamic Acid	GLU E	-	-	220	1712	-	-	$\nu C=O$	4.4 - 4.6
		-	-	-	-	460 316	1558 1404	$\nu_{as}COO^-$ ν_sCOO^-	
Glutamine	GLN Q	-	-	370	1680	-	-	$\nu C=O$	
		-	-	230	1595	-	-	δNH_2	
		-	-	-	1410	-	-	νCN	
Histidine	HIS H	250 70	1631 1575, 1594	-	-	-	-	$\nu C=C (H_2^+)$ $\nu C=C (H)$	6.0-7.0
		-	-	-	-	-	1439	$\delta CH_3, \nu CN (-)$	
Lysine	LYS K	80 85	1626 1526	-	-	-	-	$\delta_{as}NH_3^+$ $\delta_sNH_3^+$	10.4-11.1
Phenylalanine	PHE F	-	-	80	1494	-	-	νCC ring	
		-	-	-	1460	-	-	$\delta_{as}CH_3$	
Proline	PRO P	-	-	-	1432	-	-	νCN	
		-	-	-	1450	-	-	δCH_2	
Tryptophan	TRP W	-	-	-	1622	-	-	$\nu CC, \nu C=C$	
		-	-	-	1509	-	-	$\nu CN, \delta CH, \delta NH$	
		-	-	-	1496	-	-	$\nu CC, \delta CH$	
		-	-	-	1462	-	-	$\delta CH, \nu CC, \nu CN$	
		-	-	-	1427	-	-	$dNH, \nu CC, \delta CH$	
Tyrosine	TYR Y	120 85 385	1617 1598 1515	-	-	160	1601	$\nu CC, \nu CH$ νCC	9.8 - 10.4
		-	-	-	-	700	1499	$\nu CC, \delta CH$	
		-	-	-	-	580	1270	$\nu CO, \delta CC$	
		200	1250	-	-	-	-	$\nu CO, \delta CC$	

Table 1b. Side Chain Absorptions in D₂O

Amino Acid		cm ⁻¹ (D ₂ O) < pK _s low pH		cm ⁻¹ (D ₂ O)		cm ⁻¹ (D ₂ O) > pK _s high pH		Mode	pK _s (pH)
Arginine	ARG R	460 500	1605 1586	-	-	-	-	$\nu_{as}CN_3D_5^+$ $\nu_sCN_3D_5^+$	11.6 - 12.6
Aspartic Acid	ASP D	-	-	290	1713	-	-	$\nu C=O$	4.0 - 4.8
		-	-	-	-	820	1584	$\nu_{as}COO^-$ ν_sCOO^-	
		-	-	-	-	-	1404		
Asparagine	ASN N	-	-	570	1648	-	-	$\nu C=O$	
Cysteine	CYS C	-	-	-	1849	-	-	νSD	9.0-9.5
Glutamic Acid	GLU E	-	-	280	1706	-	-	$\nu C=O$	4.4 - 4.6
		-	-	-	-	830	1567	$\nu_{as}COO^-$ ν_sCOO^-	
		-	-	-	-	-	1407		
Glutamine	GLN Q	-	-	550	1640	-	-	$\nu C=O$	
		-	-	-	1163	-	-	δND_2	
		-	-	-	1409	-	-	νCN	
Histidine	HIS H	35 70	1600 1569, 1575	-	-	-	-	$\nu C=C (D_2^+)$ $\nu C=C (D)$	6.0-7.0
		-	-	-	-	-	1439	$\delta CD_3, \nu CN (-)$	
Lysine	LYS K	-	1200 1170	-	-	-	-	$\delta_{as}ND_3^+$ $\delta_sND_3^+$	10.4-11.1
Tryptophan	TRP W	-	-	-	1618	-	-	$\nu CC, \nu C=C$	
		-	-	200	1455	-	-	$\delta CD, \nu CC, \nu CN$	
		-	-	-	1382	-	-	$\delta ND, \nu CC, \delta CD$	
Tyrosine	TYR Y	160 50 500	1615 1590 1515	-	-	350	1630	$\nu CC, \nu CD$ νCC	9.8 - 10.4
		-	-	-	-	650	1499	$\nu CC, \delta CD$	
		150	1255	-	-	-	-	$\nu CO, \delta CC$	

Table 6.1.1.1 Extinction coefficients (M⁻¹cm⁻¹) and peak frequencies of amino acids that absorb between 1200 cm⁻¹ and 1800 cm⁻¹ in H₂O and D₂O. Frequencies are tabulated as a function of pH relative to the pK_s value determined from the isolated amino acid. For vibrations with no pH dependence appear in the central column.

proton, and therefore reports directly on solvent accessibility. In addition to the amide vibrations, side chains with carboxyl, aliphatic, and aromatic groups absorb in this region. Side chains play a vital role in protein stability through structural contacts and in function for the catalysis of enzymatic reactions. The vibrational signatures of side chains are strongly influenced by the local protein and solvent environment. Hydrogen bonding will induce spectra shifts as will protonation state and coordination of cations. These factors will also influence absorption coefficients and spectral line widths. Through the use of 2D IR coupling of side chains and the amide backbone vibrations can be exploited to reveal more information about protein structure and enzymatic function. First, however, the side chain vibrational signatures must be identified and characterized. Table 6.1.1.1 details the extinction coefficients and peak frequencies of the amino acid side chains that absorb in the amide fingerprint region as detailed by Barth and co-workers.^{1,2} In this chapter, the 2D IR spectra are presented of aspartic acid, tyrosine and arginine in a number of common proteins and the pH dependence of these tabulated side chain absorptions are compared against FTIR for various globular proteins and β -hairpins.

6.1.1 Aspartic Acid

Aspartic acid plays an important role in enzymatic centers as a general acid and for maintaining the ionic strength and solubility of proteins. The strong absorption coefficient of the carboxyl group of carboxylic acids is due to the highly polar nature of the functional group. Both aspartic acid and glutamic acid have particularly strong absorptions and absorb just about 1700 cm^{-1} when protonated at low pH. At high pH, two vibrations are seen between $1560\text{-}1590\text{ cm}^{-1}$ and at 1410 cm^{-1} due to the symmetric and asymmetric COO^- stretch.

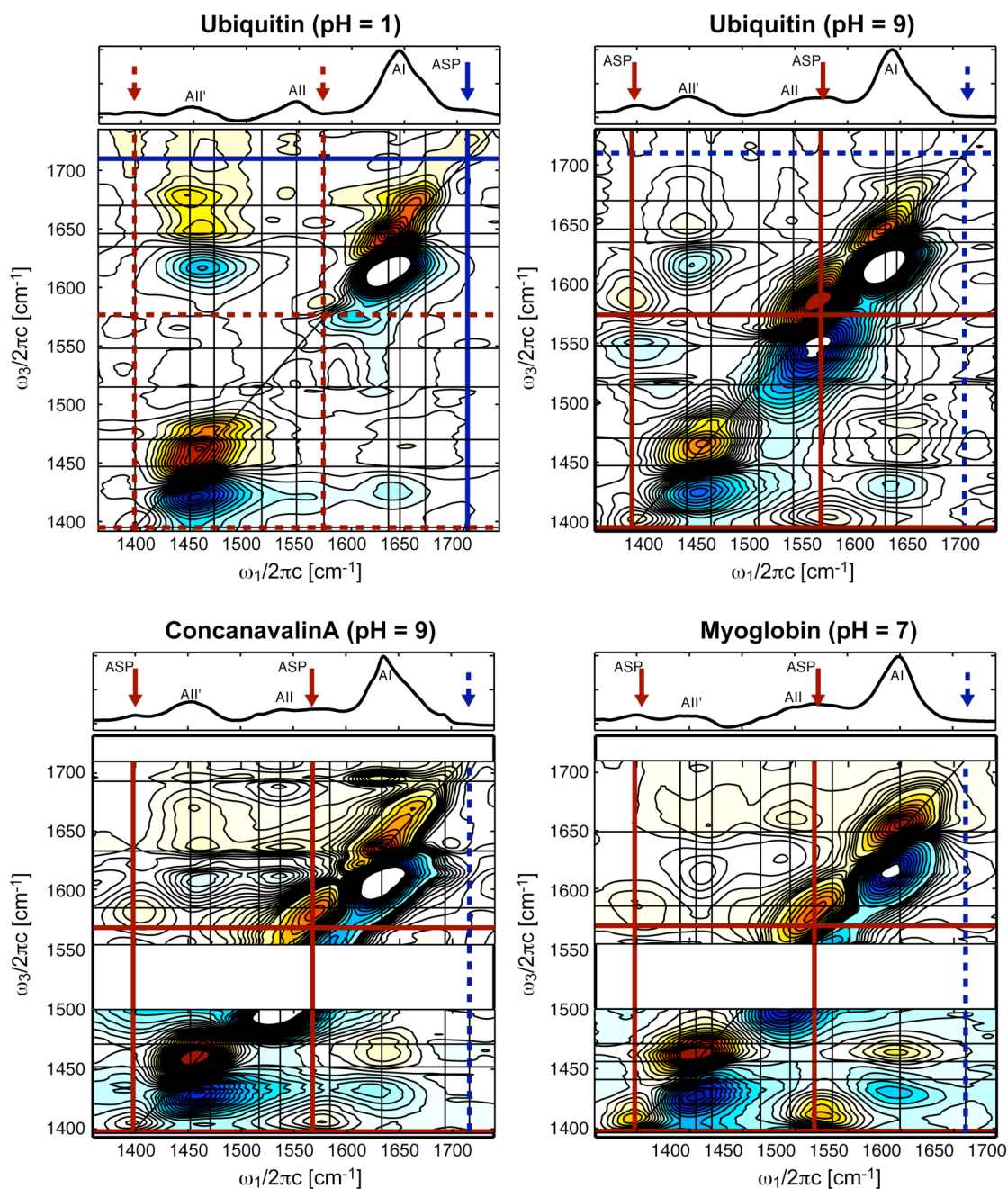


Fig. 6.1.1.1 FTIR and 2DIR spectra showcasing the aspartic acid side chain absorption in ubiquitin, concanavalin A and myoglobin.

Figure 6.1.1.1 shows 2D IR spectra of ubiquitin, concanavalin A and myoglobin, all proteins with a high content of aspartic acid. Figure 6.1.1.a and b show the frequency shift of aspartic acid from a 2 peak structure, confirmed by a intense anti-correlated cross

peak between 1584 and 1390 cm^{-1} to a single peak at 1710 cm^{-1} at low pH. The anti-correlated cross peak, or a tilt of the cross peak perpendicular to the diagonal, confirm coupling between the symmetric and asymmetric vibrations.

6.1.2 Tyrosine

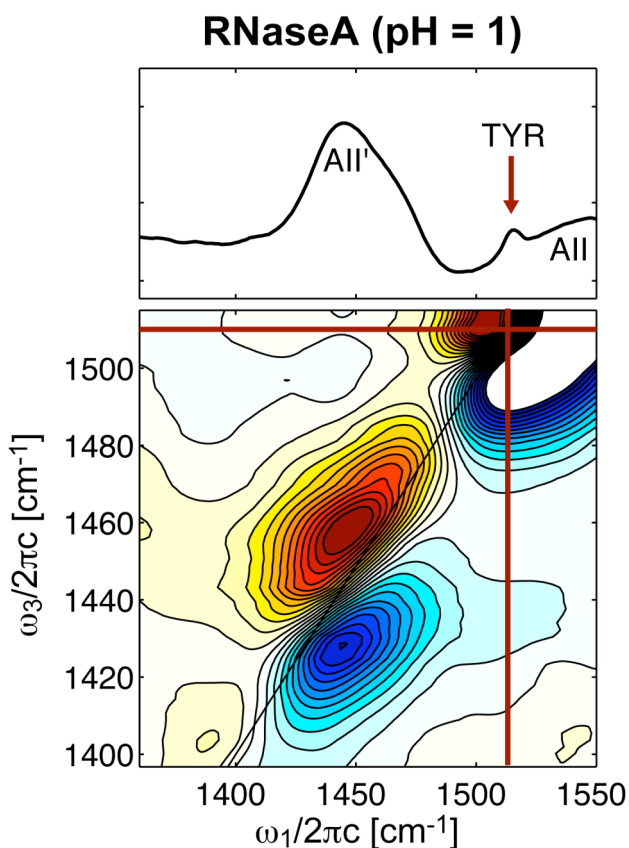


Fig. 6.1.2.1 FTIR and 2DIR spectrum of ribonuclease A exhibiting the tyrosine absorption at 1515 cm^{-1} .

The most prominent of the aromatic side chains in the amide region with a ring mode (ν_{CC}) absorbance around 1515 cm^{-1} is tyrosine. Due to its spectroscopic isolation and narrow and intense line shape, tyrosine is a highly studied side chain particularly for its role in proton and electron transfer reactions. The FTIR spectrum in Fig. 6.1.2.1 shows

a clear sharp feature at 1515 cm^{-1} indicative of the tryrosine ring mode. This is also seen in the amide II' 2D IR spectrum of ribonuclease A.

6.1.3 Arginine

Arginine is a positively charged side chain with a vibrational doublet due to the guanidyl group resonance at 1635 and 1674 cm^{-1} in water. In D_2O , the frequency is shifted to 1580 and 1600 cm^{-1} due to deuteration of the highly labile guanidyl group. The highly polar nature of arginine makes it ideally suited for hydrogen bonded environments and interacting with negatively charged functional groups, and is typically found on the

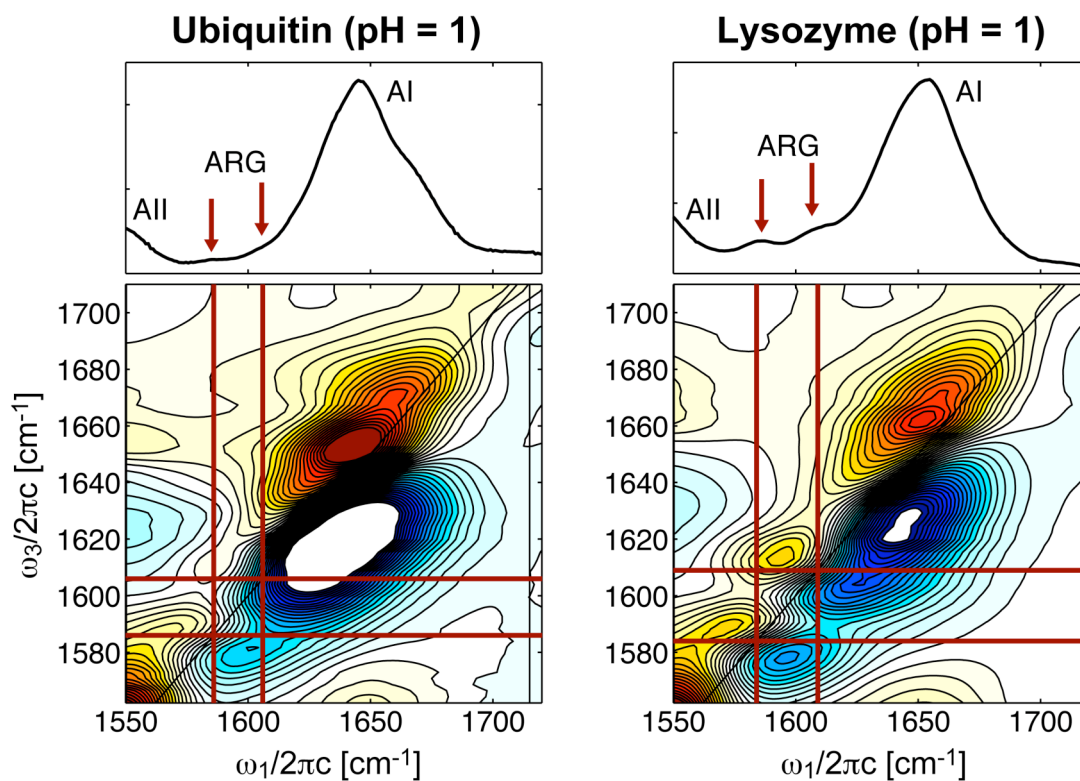


Fig. 6.1.3.1 FTIR and 2D IR spectra of ubiquitin and lysozyme that show the symmetric and asymmetric stretch of the guanidyl group of the arginine side chain.

outside of proteins. This is seen in the protein structure of Fig. 6.1.3.2. Therefore, it is commonly found in the deuterated state in D₂O as a doublet around 1580 and 1600 cm⁻¹ as seen in the vibrational spectrum of Ubiquitin and Lysozyme of Fig. 6.1.3.1 and in the partially and fully exchanged spectra in Fig. 6.1.3.2. Constructive and destructive interference with the amide I and II vibrations shift the relative positions of the vibrations in the 2D surfaces as well as interference with the cross peaks that are present due to coupling of the symmetric and asymmetric mode of the guanidinium group of the side chain.

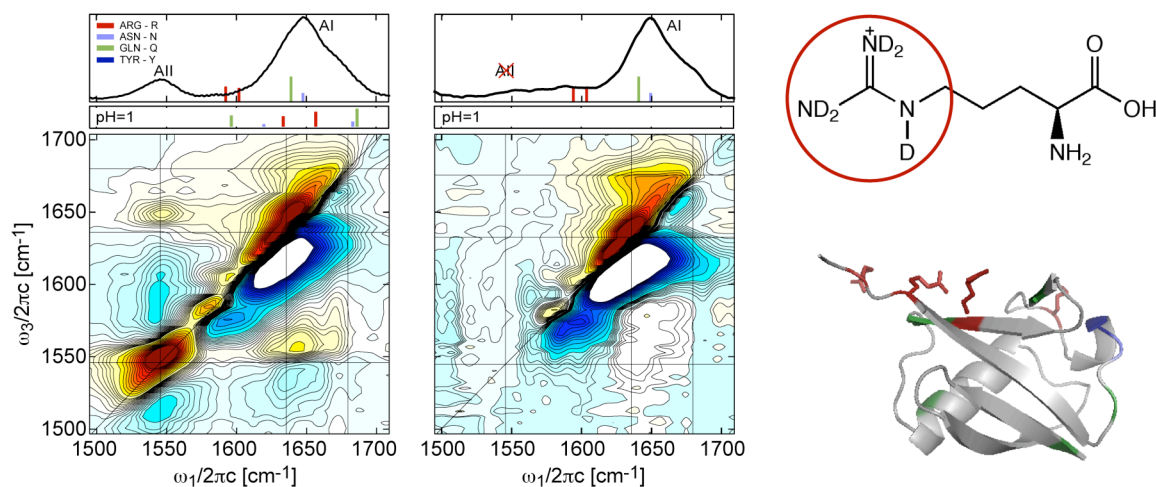


Fig. 6.1.3.2 Position and structure of the guanidyl group in ubiquitin. The guanidinium groups are fully exchanged due to solvent exposure of the protein. The stick spectra shown under the FTIR represent the position of the side chains in D₂O (top) and H₂O (bottom) at pH=1.

6.2 Side Chain Absorptions seen in FTIR Spectroscopy of Proteins and Hairpins

To further illustrate side chain dependence on protein and solvent environment, Table 6.1.1.1 is compared with linear vibrational measurements in the amide fingerprint region. Fig. 6.2.1.1 translates Table 6.1.1.1 into a stick figure illustration of the side chain vibrations in the amide finger print region scaled by extinction coefficients. This figure

also includes the predominant side chains and the molecular structures. Fig 6.2.1.2-6.2.1.11 compare the tabulated frequencies of a number of globular proteins and hairpins against the FTIR spectra. These figures help identify side chains of protonated proteins prepared rapidly at cold temperatures in D₂O. Solvent exposed side chains will exchange and absorb as reflected in Table 1b while those that do not will absorb at frequencies reflected in Table 1a. In addition, Fig 6.2.1.2-6.2.1.6, contain pH dependent FTIR to show spectral shifts of the acidic side chains.

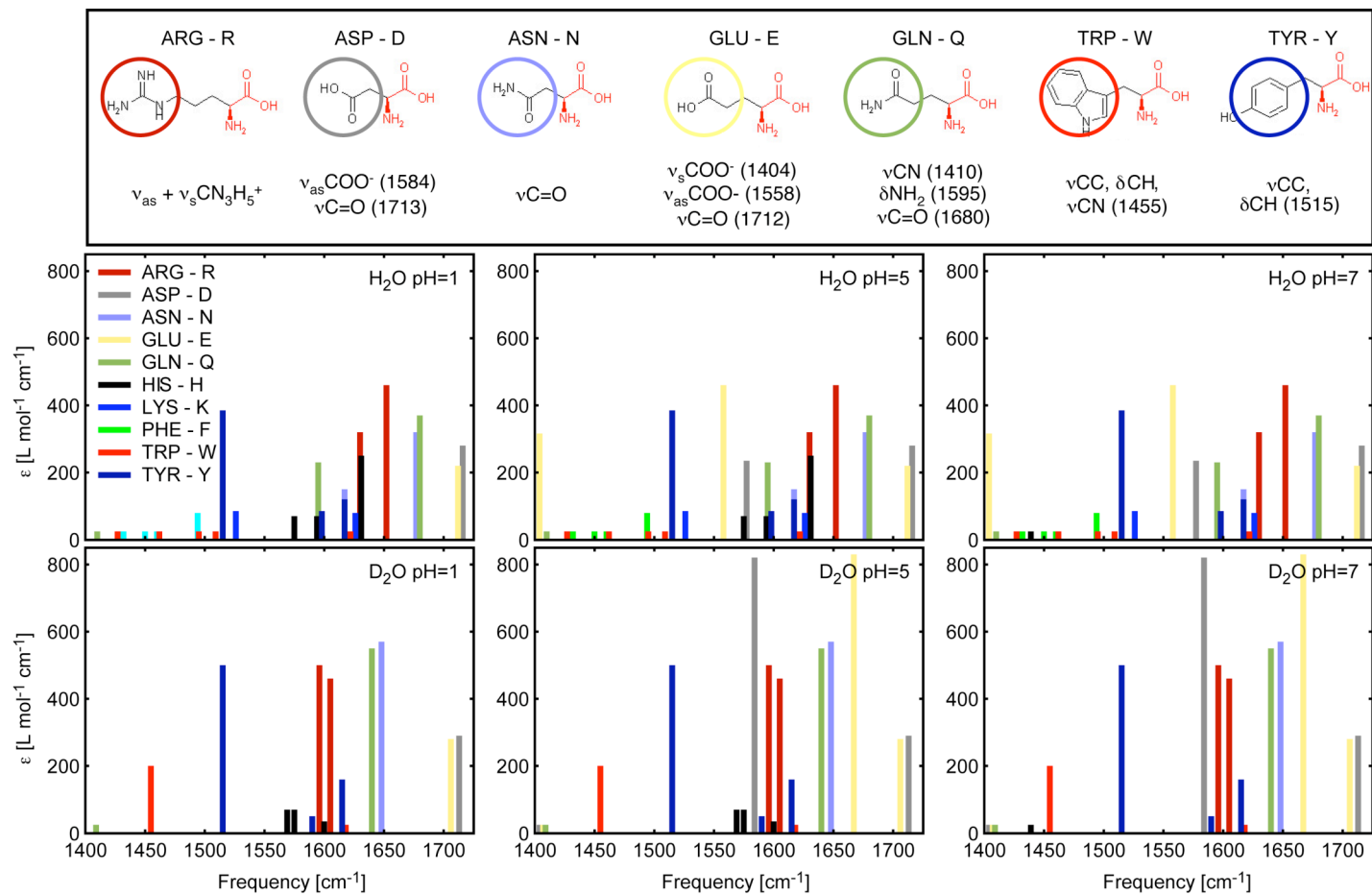


Fig. 6.2.1.1 (Top) Atomic structures of predominant side chains in the amide finger region. (Bottom) Stick plots of side chain absorption from Table 1 in the amide finger fingerprint region as a function of solvent and pH. Major changes occur due to the protonation state of ASP, GLU and HIS. Isotopic sensitivity of the vibrational absorption is seen in TRP, ARG, GLU and ASP.

Concanavalin A

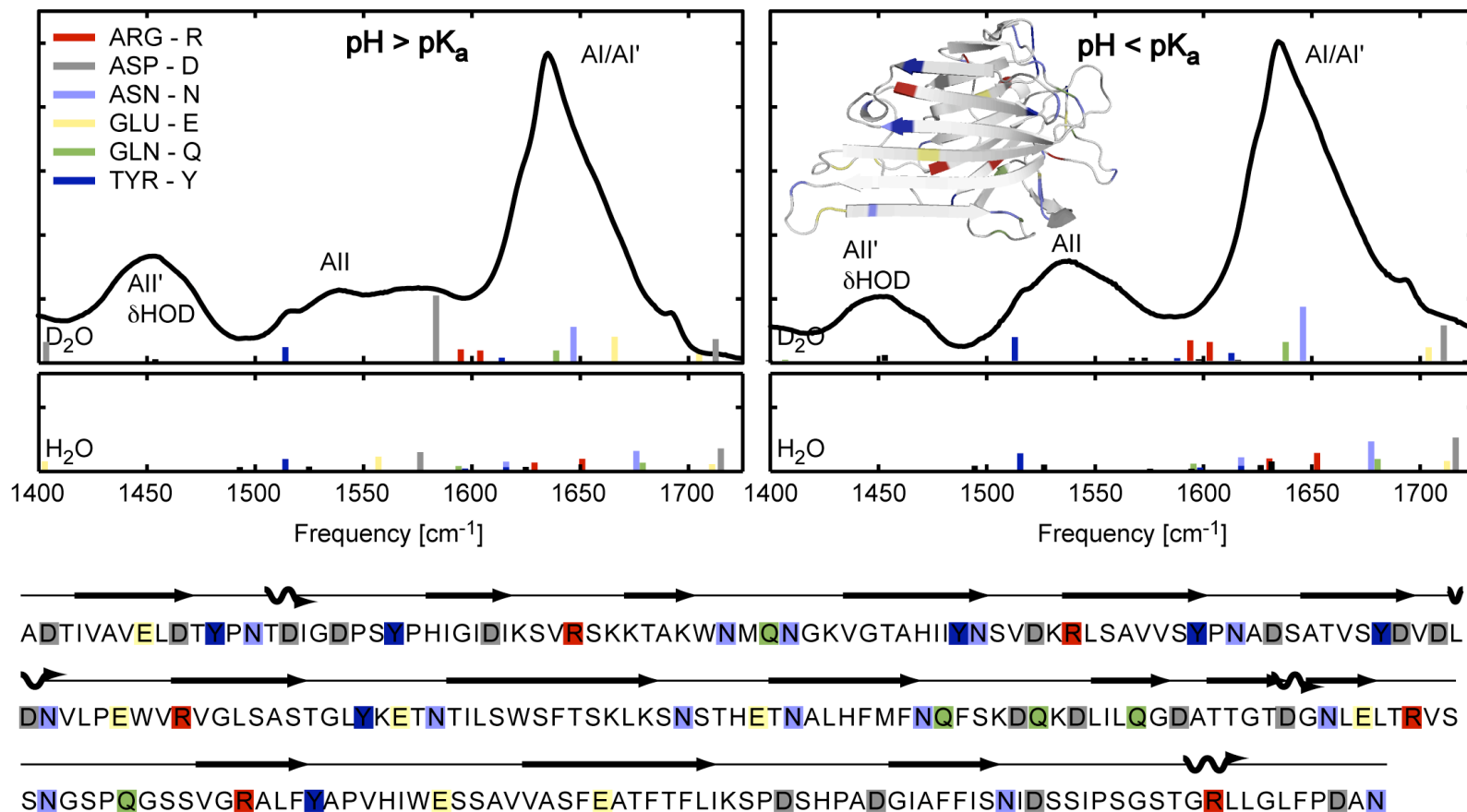


Fig. 6.2.1.2 FTIR of concanavalin A at pH = 9 ($\text{pH} > \text{pK}_a$) and pH = 1 ($\text{pH} < \text{pK}_a$) and the corresponding side chain stick plots from Table 1. Intensities of stick plots are given side chain are scaled relative to the total number of amide I oscillators in the protein assuming an amide I extinction coefficient of $300 \text{ M}^{-1} \text{ cm}^{-1}$.

Ribonuclease A

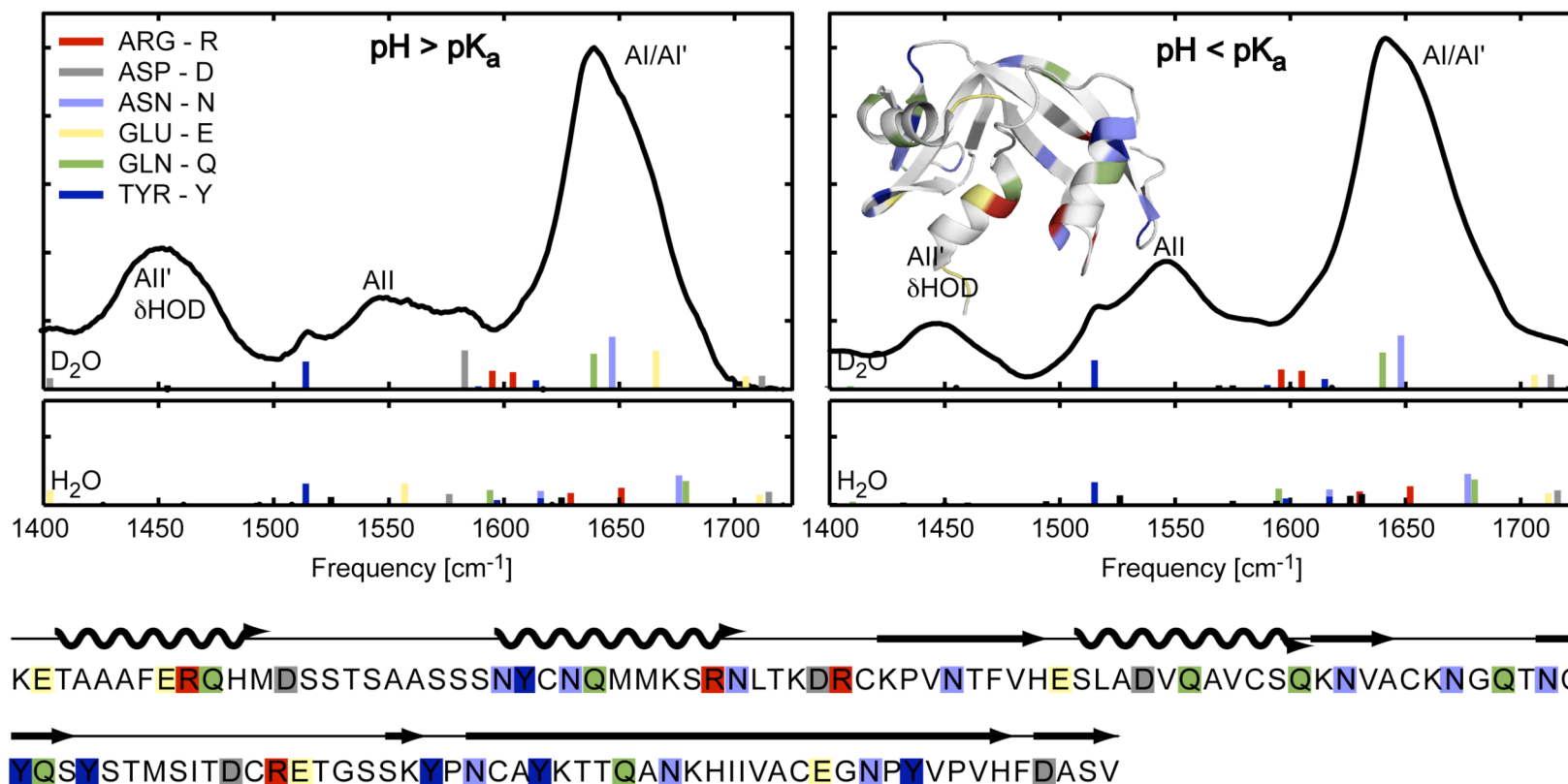


Fig. 6.2.1.3 FTIR of ribonuclease A at pH = 9 ($\text{pH} > \text{pK}_a$) and pH = 1 ($\text{pH} < \text{pK}_a$) and the corresponding side chain stick plots from Table 1. Intensities of stick plots are given side chain are scaled relative to the total number of amide I oscillators in the protein assuming an amide I extinction coefficient of $300 \text{ M}^{-1} \text{ cm}^{-1}$.

Ubiquitin

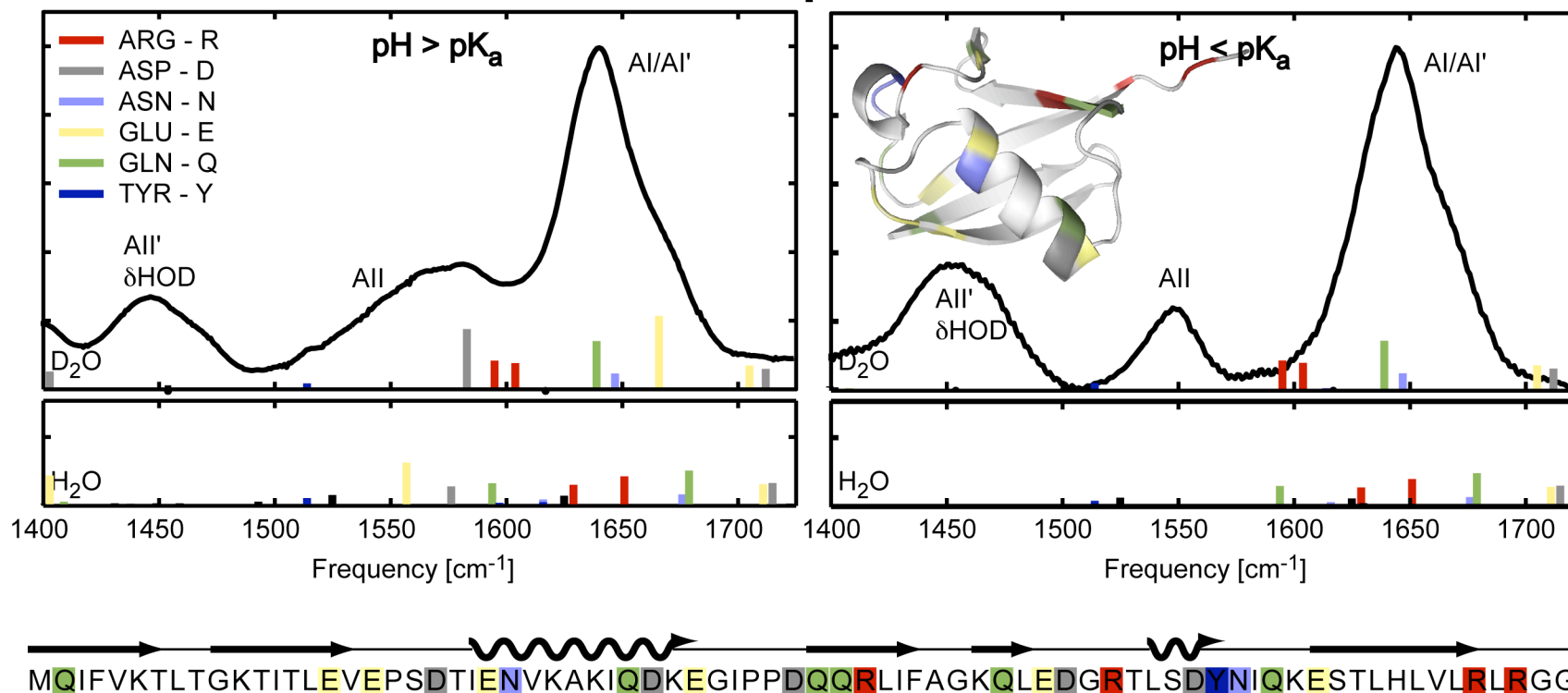


Fig. 6.2.1.4 FTIR of ubiquitin at $\text{pH} = 9$ ($\text{pH} > \text{pK}_a$) and $\text{pH} = 1$ ($\text{pH} < \text{pK}_a$) and the corresponding side chain stick plots from Table 1. Intensities of stick plots are given side chain are scaled relative to the total number of amide I oscillators in the protein assuming an amide I extinction coefficient of $300 \text{ M}^{-1} \text{ cm}^{-1}$.

Lysozyme

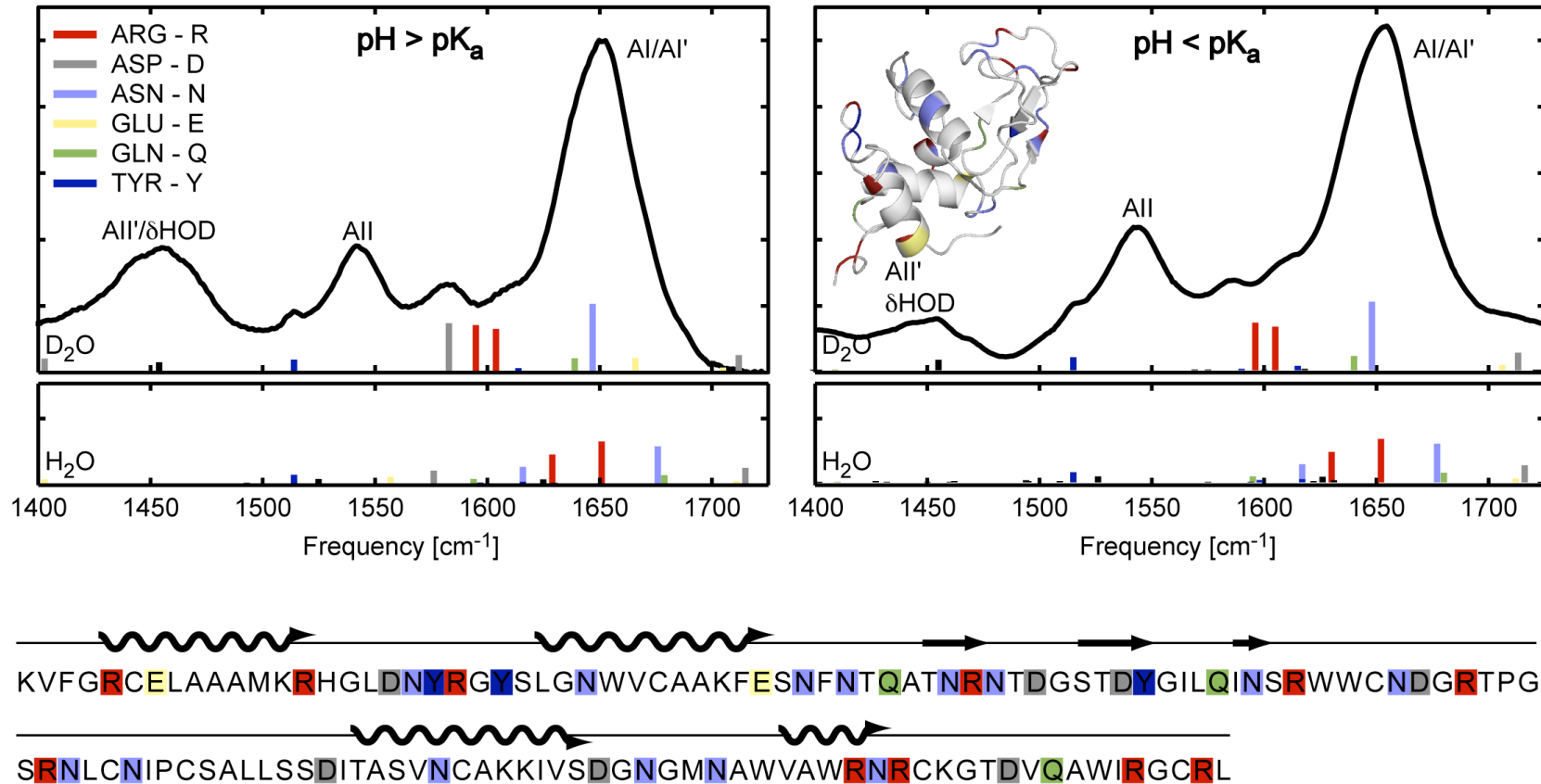


Fig. 6.2.1.5 FTIR of lysozyme at pH = 9 ($\text{pH} > \text{pK}_a$) and pH = 1 ($\text{pH} < \text{pK}_a$) and the corresponding side chain stick plots from Table 1. Intensities of stick plots are given side chain are scaled relative to the total number of amide I oscillators in the protein assuming an amide I extinction coefficient of $300 \text{ M}^{-1} \text{ cm}^{-1}$.

Myoglobin

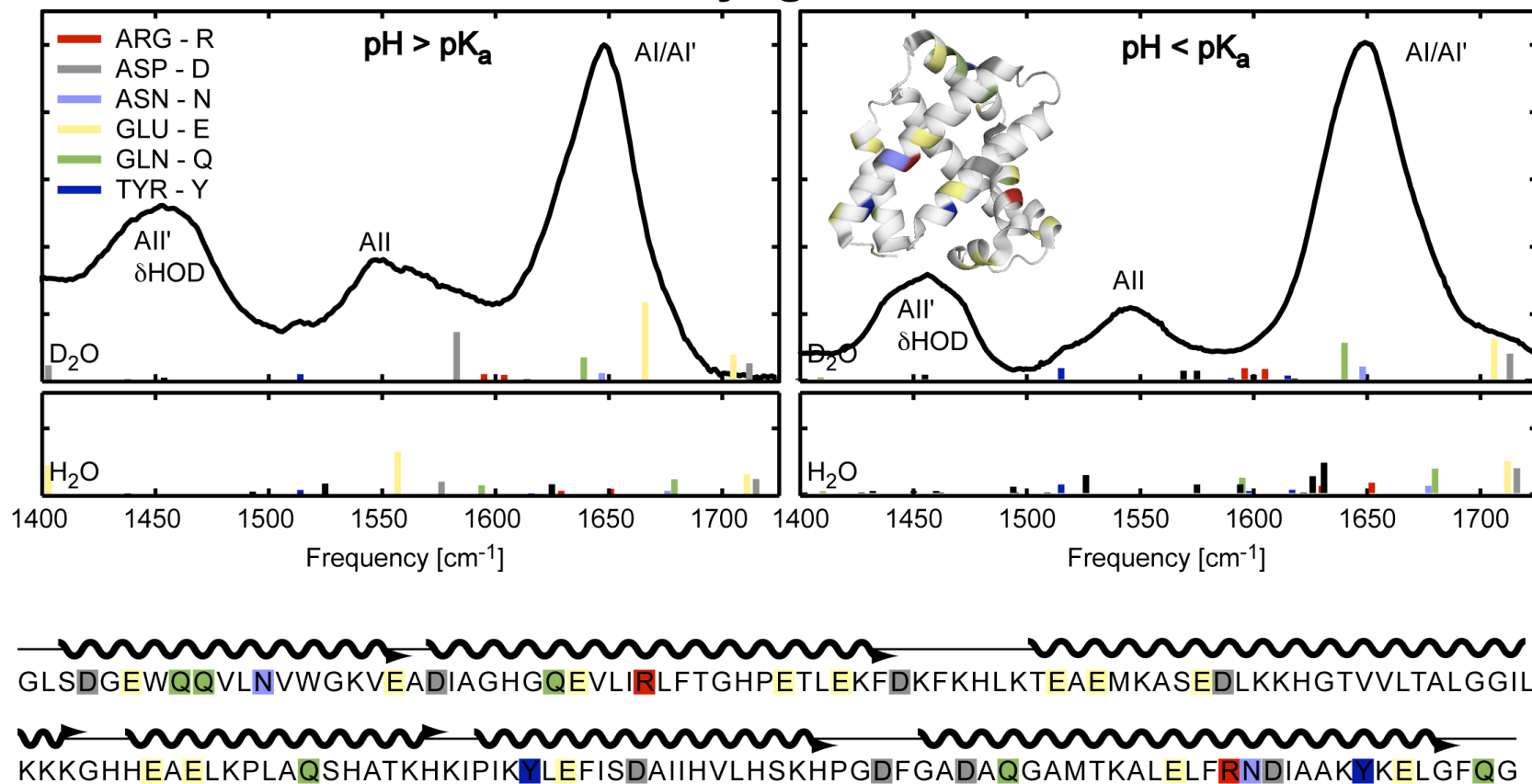


Fig. 6.2.1.6 FTIR of myoglobin at pH = 9 (pH > pK_a) and pH = 1 (pH < pK_a) and the corresponding side chain stick plots from Table 1. Intensities of stick plots are given side chain are scaled relative to the total number of amide I oscillators in the protein assuming an amide I extinction coefficient of 300 M⁻¹cm⁻¹.

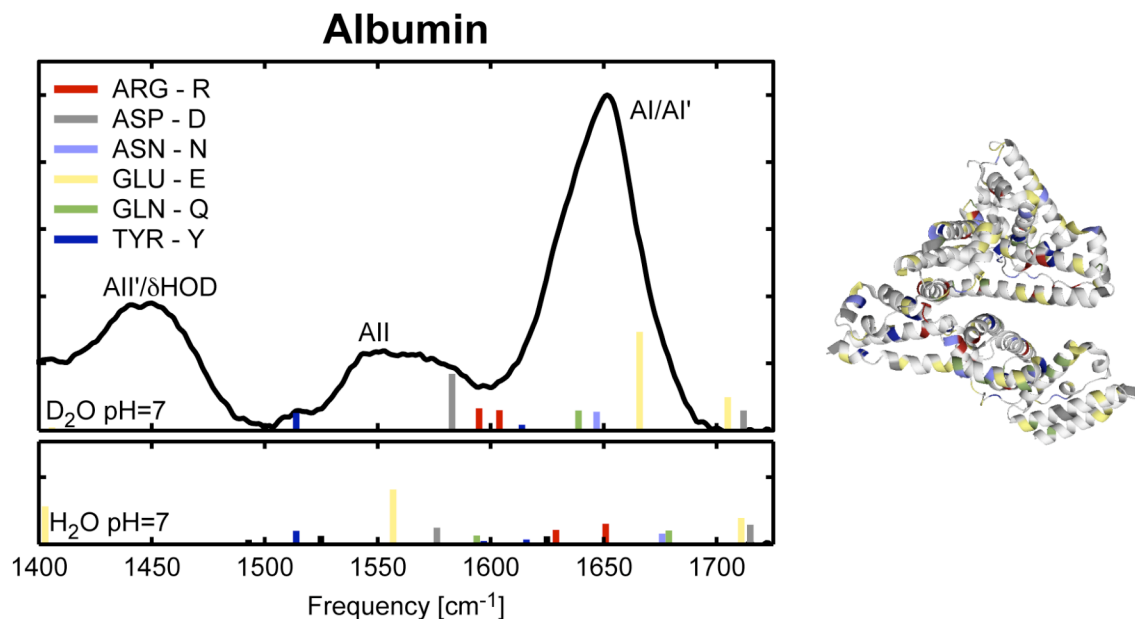


Fig. 6.2.1.8 FTIR of albumin at pH = 7 and the corresponding side chain stick plots from Table 1. Intensities of stick plots are given side chain are scaled relative to the total number of amide I oscillators in the protein assuming an amide I extinction coefficient of $300 \text{ M}^{-1}\text{cm}^{-1}$.

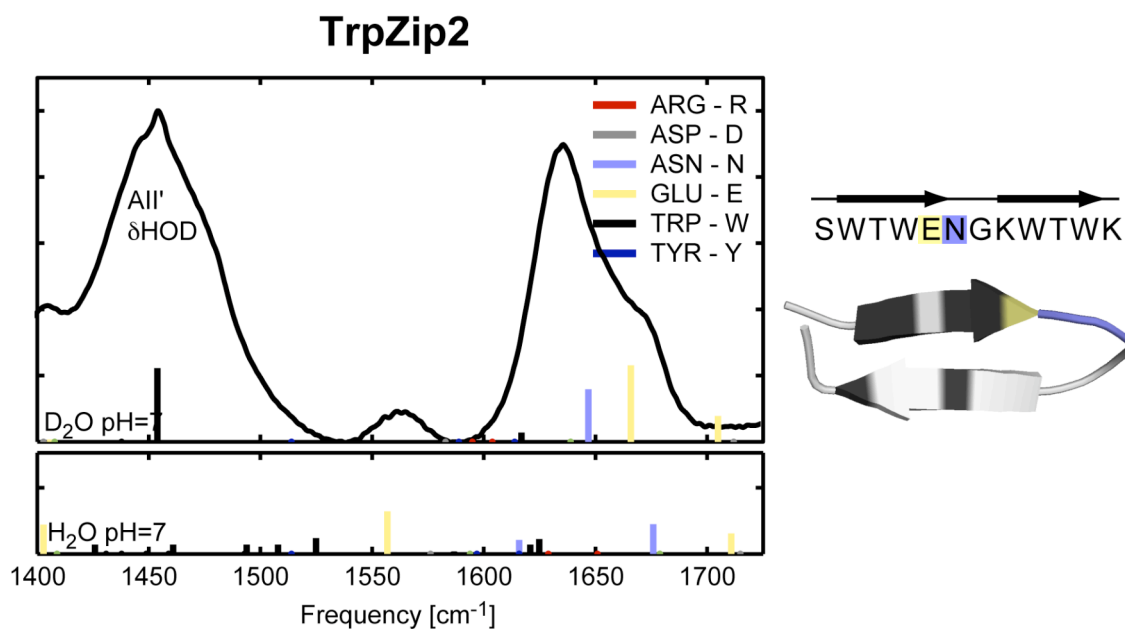


Fig. 6.2.1.9 FTIR of TrpZip2 at pH = 7 and the corresponding side chain stick plots from Table 1. Intensities of stick plots are given side chain are scaled relative to the total number of amide I oscillators in the protein assuming an amide I extinction coefficient of $300 \text{ M}^{-1}\text{cm}^{-1}$.

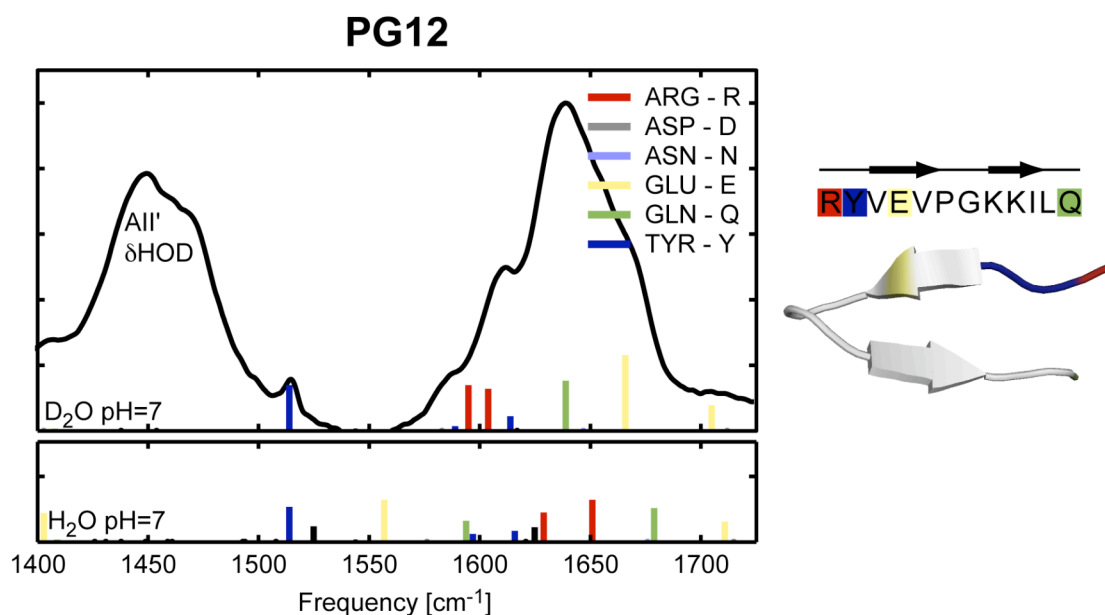


Fig. 6.2.1.10 FTIR of PG12 at pH = 7 and the corresponding side chain stick plots from Table 1. Intensities of stick plots are given side chain are scaled relative to the total number of amide I oscillators in the protein assuming an amide I extinction coefficient of $300 \text{ M}^{-1} \text{ cm}^{-1}$.

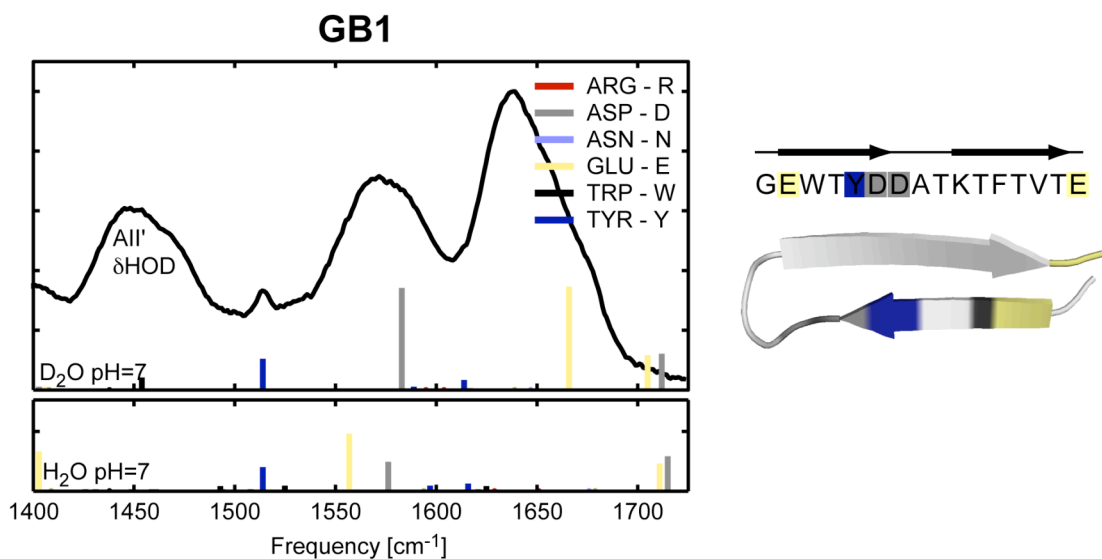


Fig. 6.2.1.11 FTIR of GB1 at pH = 7 and the corresponding side chain stick plots from Table 1. Intensities of stick plots are given side chain are scaled relative to the total number of amide I oscillators in the protein assuming an amide I extinction coefficient of $300 \text{ M}^{-1} \text{ cm}^{-1}$.

References

- (1) Barth, A. *Progress in Biophysics and Molecular Biology* **2000**, 74, 141-1
- (2) Barth, A.; Zscherp, C. *Q. Rev. Biophys* **2002**, 35, 369-430.

Chapter 7

Hydrogen-Deuterium Exchange FTIR of Ubiquitin

*“We make our world significant by the courage of our questions and by the depths of our answers.”
–Carl Sagan*

7.1 Background: Hydrogen-Deuterium Exchange

The protein free energy landscape is a complex surface with local and global minima arising from the large number of degrees of freedom in a protein structure. As proteins grow in size, their energetic, structural and dynamical complexity increases and the ability to study these large systems on a wide range of timescales with sufficient structural resolution becomes significantly more challenging. In addition, techniques that can also provide understanding of the mechanisms and pathways that dictate proteins function and structure become more critical. Two-dimensional Nuclear Magnetic Resonance (2D NMR) has provided a wealth of information about protein structure and

kinetics with atomic resolution on nanosecond or longer time scales. Optical methods have the capability of providing information on much faster timescales (sub-picosecond), and when integrated with a photo-initiation or temperature jump techniques, can provide dynamical insight into protein structural evolution and function. Indirect information about the proteins local interactions can be inferred through line shape analysis. However, in the case of protein folding experiments, though these techniques are exceptionally powerful, neither has the capability of directly probing structural intermediates alone and both require an additional method that can spectroscopically isolate structural elements and intermediates independent of kinetic lifetimes.

Through chemical synthesis, isotopically labeling proteins can provide the desired spectroscopic isolation of single residues or sections of the protein to provide direct information about local couplings and protein interactions across the ensemble. Isotope labeling, however, requires some chemical intuition as to the nature of structural intermediate. What is desired is the ability to address questions about protein stability, solvation and structural intermediates without a preconceived intuition of the protein-folding pathway. 2D NMR hydrogen-deuterium exchange (HX) studies have long been used to understand the kinetics of protein folding^{1,2} and its implementation over the past decade has shown promise to elucidate structural intermediates along the folding trajectory.^{3,4} Later in this chapter, the advancements in HX optical methods, HX 2D IR, will be demonstrated to show the enhanced structural sensitivity of the technique⁵ and it is expected ability to isolate stable structural intermediates.

Figure 7.1.1.0 illustrates the principles that dictate protein hydrogen-exchange kinetics. These principles will be outline in this chapter in detail to elucidate information

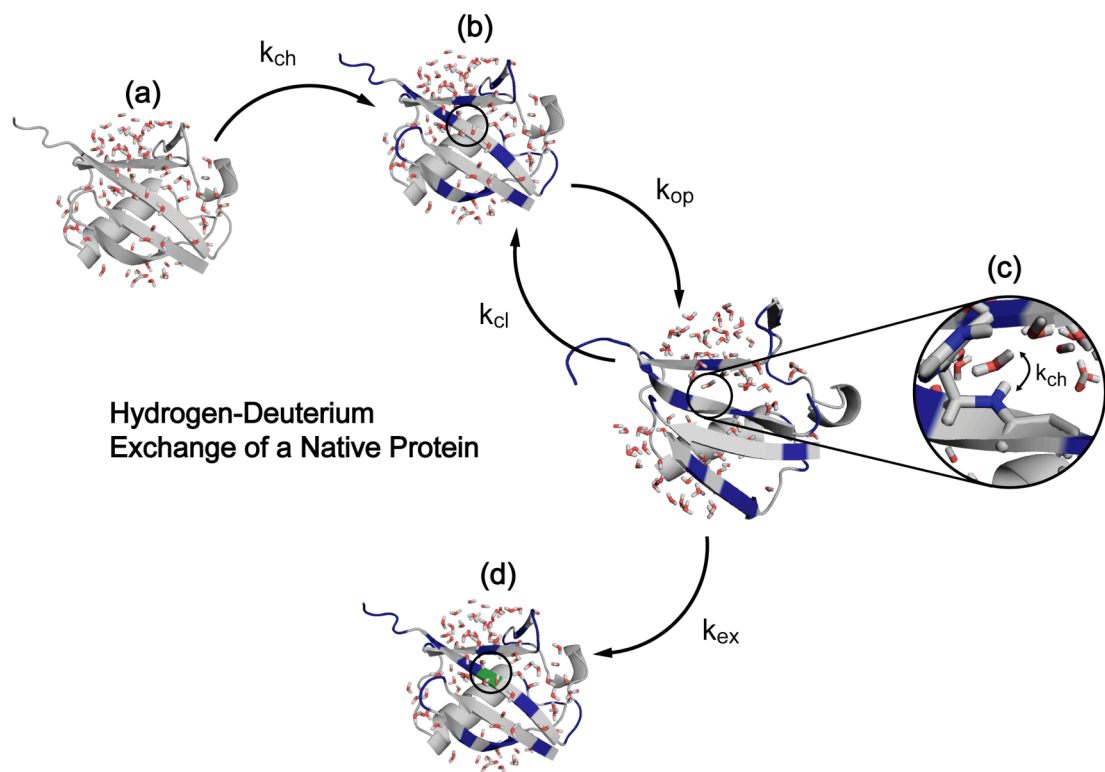


Fig. 7.1.1.0 Illustration of a solvated hydrogenated protein in a bath of D₂O. (a) Exchange of surface protons (blue) or those in highly labile regions ($k_{ch} \sim 10^{-3}$ - 10^{12} s^{-1}) (b) Protein fluctuations lead to opening events through breaking of hydrogen bonds and exposure of imbedded residues to solvent ($k_{op/cl} \sim 10^{-5}$ - 10^{12} s^{-1}) (c) Exchange of an internal proton via water penetration into the protein structure (k_{ch}) (d) The overall exchange of an structurally hindered proton (green) will have a rate constant (k_{ex}) proportional to the chemical exchange and protein dynamics.

about protein solvation and stability that can be extracted through the measurement of the amide backbone proton exchange rates in solution. The rates of exchange are not only dictated by the site specific pK_a of the amino acid, but by induction and steric effects due to primary structure⁶ and solvent accessibility dictated by the local protein structure and dynamics. Fig. 7.1.1.0 shows hydrogenated protein placed in a bath of heavy water (a). Solvent exposed residues will exchange at a rate determined purely by the chemistry of the site (pK_a) giving a snap shot of solvent exposed and inaccessible regions of a protein

(b). The remaining protons are inaccessible to the solvent because they are either embedded within the hydrophobic core or partaking in strong hydrogen bonds of secondary structure. However, even at equilibrium, interior protons exchange due to conformational fluctuations that induced local or global opening events that create access for solvent exposure into the protein structure. Fig. 7.1.1.0c shows a water molecule capable of exchange to a typically embedded proton; however, this exchange is more likely to be acid or base catalyzed. The exchange rate of this site is now determined by the kinetics of both the proton exchange and the accessibility of the proton to solvent due to the protein secondary and tertiary structure. Through measuring these rates, individual sites of proteins can be quantified as inaccessible stable regions or accessible regions of the protein. By altering the pH and temperature of this system, exchange rates can be controlled and effectively hold a protein in the partially exchanged state. Using this unique capability, in which the protein labels itself in a non-perturbative manor, stable structural intermediates can be isolated and identified and will be discussed in more detail in a later section.

7.1.1 Hydrogen Exchange Chemistry

The amide proton of the protein backbone is known to have exceptionally high pK_a values and therefore, solvent exchange with the pure solvent is slow. Based on the observed pH dependence of the amide proton exchange rate, the reaction is catalyzed by a strong acid or base, in this case H_3O^+ and OH^- . The rapid rate of proton transfer was first discussed in detail by Eigen and co-workers.⁷ Eigen's proton transfer theory describes exchange by a three-step process in which a diffusion-limited step creates an acceptor-donor complex that then redistributes the proton among the members of the

complex and in a final step, the proton is transferred. In the case of the amide proton, the final transfer step is typically the rate-determining step due to the large pKa. Fig. 7.1.1.1 depicts the possible mechanism for exchange of the amide proton for acid and based catalyzed exchange. In both cases, diffusion of the deuterium donor is required. It is likely that hydrogen exchange is a concerted process and not step-wise as depicted below, particularly for the rapid exchange at high pH. Tuchsén and Woodward proposed a proton wire mechanism where proton exchange is initiated by an acid catalyst down a “wire” of hydrogen bound amide residues. The final step is the exchange of the last amide proton by water.⁸

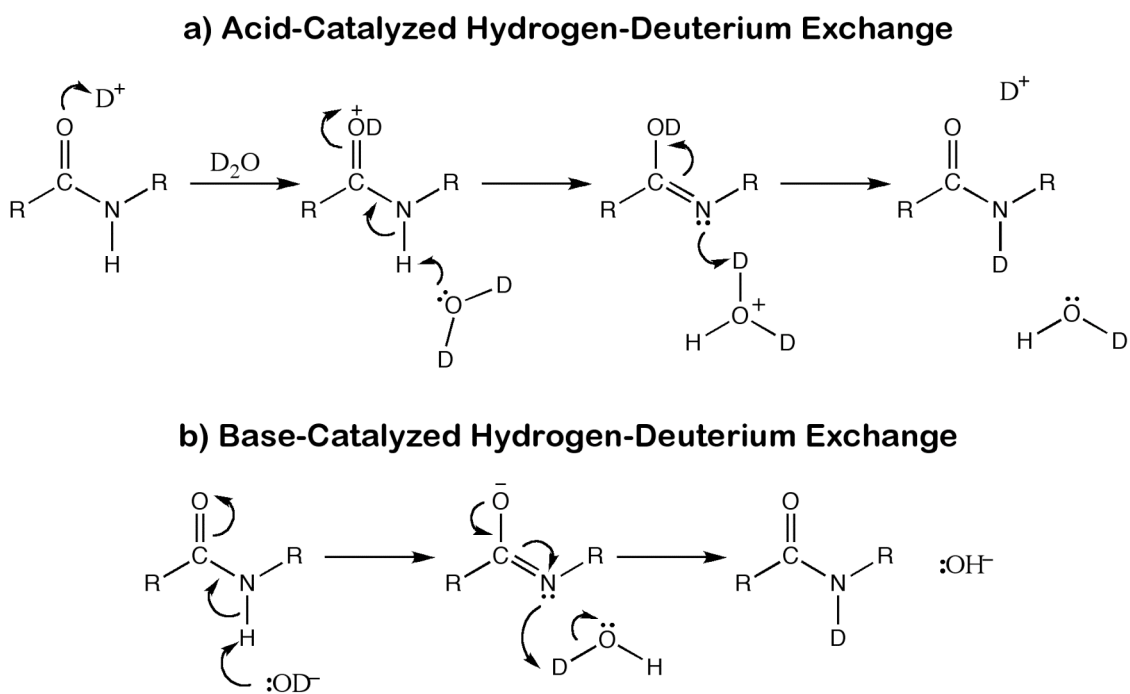


Fig. 7.1.1.1 Possible mechanisms for (a) acid and (b) base catalyzed reactions for hydrogen-deuterium exchange of amide groups in proteins.

Figure 7.1.1.2 shows the pH dependence of acid and base catalysis of the amide proton where the black dotted line is an idealized calculation for a single protein of poly-L-alanine.⁹ At pH_{min} , both the acid and base catalyzed mechanisms significantly contribute to the exchange rate and the point at which water catalyzed exchange becomes important. This value is typically situated at $\text{pH}=4$ for an exposed amide proton. Deviations of pH_{min} are caused by additional effects due to the local structure and neighboring side chains of the amide proton that effect the relative rates for the acid and base catalyzed reactions. This effect is induced by sterics and electrostatics that impede the ability of the catalyst to approach the amide proton. Bai and co-workers have detailed these effects through both theoretical and experimental methods. Their work has been validated on a number of polypeptides in which the experimental rates predicted using the parameterized model. This work is the basis of the hydrogen-deuterium exchange literature and is used actively to predict the protection factors, or the difference between the observed experimental rates and those predicted for the isolated residue.

Deviations from the dotted black curve in Fig. 7.1.1.2 are governed by a large number of chemical phenomena. The primary structure of the protein plays a large role in the observed rate of proton exchange. The sequence results in inductive and electrostatic effects caused by polar side chains that act to increase the acidity of the amide group. Due to the electron withdrawing capability of polar side chains, the amide proton becomes more easily base catalyzed and the base rate of exchange increases while the acid rate decreases. This causes a global shift in pH_{min} to the left, seen as the shift to the red curve of Fig. 7.1.1.2. As side chains become bulkier, the ability for the catalyst to diffuse into the complex is reduced and the overall acid and base rates will decrease. This

is seen as a downward overall shift of the rate versus pH curve (blue trace). Less but still notable contributions to the intrinsic chemical exchange have been documented by others. Isotope corrections to exchange rates is given by Connelly and collaborators.¹⁰ It is also important to note that the ionic strength and buffer solutions can also speed up exchange rates considerably in that the buffer can act to catalyze the proton transfer reaction.¹

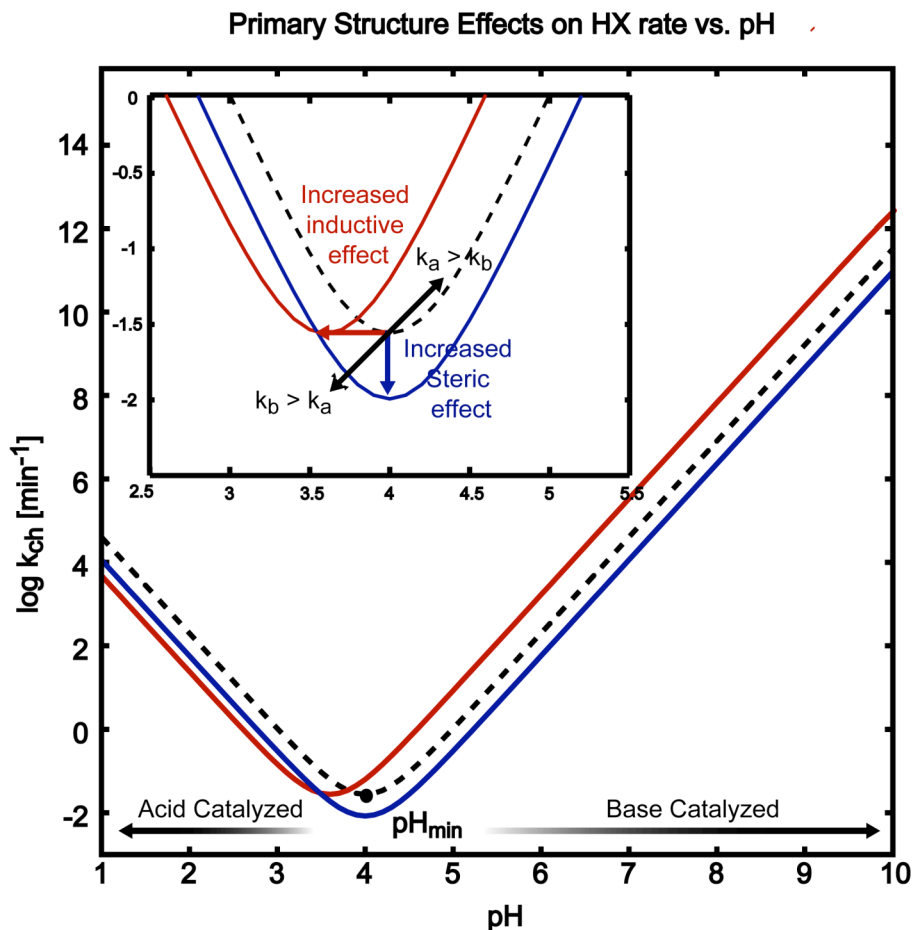
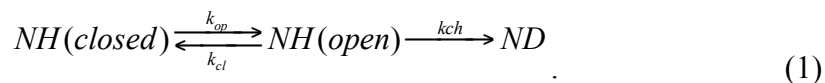


Fig. 7.1.1.2 Effects of primary structure of the calculated hydrogen exchange rate of a disordered homopolymer of poly-L-alanine. At low and high pH, away from pH_{min} , the rate is dominated by the acid and base catalyzed mechanism that scales with the concentration of catalyst. Here k_a and k_b are the acid and base catalyzed rates respectively. As steric effects increase, the overall rate of exchange decreases due to accessibility of catalyst to the exchange site (blue trace and arrow). Inductive effects act to decrease the rate of the acid catalysis mechanism and increase the rate of the base catalysis mechanism due to electron withdrawing effects of the side chain (red trace and arrow). This excludes the effects on exchange due to burial of amino acids in the protein core or residues partaking in hydrogen bonded contacts of secondary structure. Figure adapted from reference.⁶

Despite the influence of primary structure effects, that can slow down proton exchange times of solvent exposed residues to seconds, even minutes, amide protons of proteins in the native state that are involved in secondary structure or imbedded in the interior of the protein experience exchange rate orders of magnitude slower, to the days and even week timescales. The question then arises, how does the secondary and tertiary structure of proteins dictate the observed rate of hydrogen exchange at equilibrium? Therefore what is the role of hydrogen bonding on the exchange rates? And more importantly, what wealth of information can be mined about protein dynamics, stability and structure.

7.1.2 Linderstrom-Lang Steady State Theory of HX Kinetics

In 1958, the two-state model for hydrogen exchange kinetics in proteins was first proposed by Linderstrom-Lang.^{11,12} The exchange rates of amide protons are not only dictated by the site specific chemistry but also by the structure of the surrounding protein. A rapid equilibrium is established between the opening and closing of local protein structure that shields and exposes internal protons from exchange. The reaction that dictates hydrogen exchange is given in Eq. 1



The rates of opening (k_{op}) and closing (k_{cl}) represent structural fluctuations or unfolding transients that attenuate the chemical exchange of the fully accessible amide proton (k_{ch}). The variables that determined the rate of chemical exchange will be discussed in detail in next section and have been tabulated in detail elsewhere.^{6,10} It is important to note that the chemical exchange rate assumes that the open state of the protein is equivalent to the random coil state in which no residual conformation is dictating exchange.

The observed hydrogen exchange rate for a folded protein (k_{ex}) can be predicted from this model under stable conditions for which the rate of opening is much slower than the rate of closing ($k_{op} \ll k_{cl}$) to be as follows:

$$k_{ex} = \frac{k_{op}k_{ch}}{k_{cl} + k_{ch}}, \quad (2)$$

A more general derivation of the hydrogen exchange equation has been addressed by Hvidt and coworkers that include no assumptions about the relative relationship between the intrinsic exchange rates giving a more robust pre-steady state solution.¹³ However, the bulk of the experimental literature assumes a stable protein structure. Much of the exchange kinetics theory mirrors Michaelis-Menten Kinetics for enzyme substrate binding.¹⁴ Similarly the reaction mechanism is dictated by the proteins dynamics in which an equilibrium between structural forms are observed and follows with an irreversible process, however, for hydrogen-exchange, the presence of the “substrate” is not a limiting reagent.

Two limiting cases exist for hydrogen exchange in proteins and are based on the rate of exchange relative to the protein structural dynamics. For the first limiting case, the EX1 limit, the imbedded sites remain exposed to the solvent for a statistically long period of time relative to the fluctuations of the protein structure. Therefore, when the exchange rate is much faster than the protein dynamics ($k_{cl} < k_{ch}$), it follows that buried residues will experience hydrogen exchange rates independent of their intrinsic kinetics. Eq. 2 simplifies into Eq. 3

$$k_{ex}^{EX1} = k_{op}. \quad (3)$$

Here, the observed rate is directly related to the structural opening rate of the protein giving a direct probe of the structural kinetics. Due to the lack of dependence of the

observed hydrogen exchange rate on the intrinsic chemical rate of the amide proton, the observed rate will be pH independent, assuming the protein structure shows minimal destabilization with over the pH range of interest. This limit is achieved with high pH and temperature. Fig. 7.1.2.1 details the pH dependence of the hydrogen exchange rate that increases by an order of magnitude with each pH unit. Eventually the rate is dominated by the protein fluctuations thus approaches the EX1 limit.

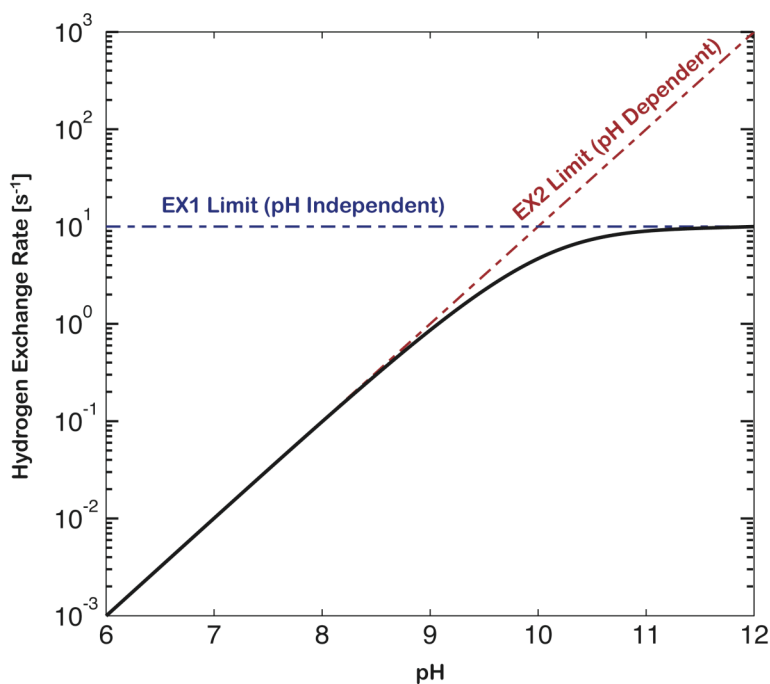


Fig. 7.1.2.1 pH dependence of the hydrogen exchange rate (black curve). The EX1 limit dominates at high pH where the protein fluctuations dictate the exchange rate. At low pH, or the EX2 limit, the exchange shows pH dependence.

In the EX2 limit, the protein dynamics are faster than the chemical exchange of the amide protons ($k_{cl} \gg k_{ch}$). Therefore, every structural opening will *not* lead to a hydrogen exchange event and the observed rate will strongly be dictated by the protein fluctuations. Eq 2 reduces to

$$k_{ex}^{EX2} = \frac{k_{op}}{k_{cl}} k_{ch}. \quad (4)$$

where the scaling term in front of the chemical exchange is defined as the “protection factor,” or K_{op} , of the amide proton.

$$K_{op} = \frac{k_{op}}{k_{cl}} \quad (5)$$

This protection factor reflects the degree of solvent inaccessibility for the specific proton due to burial in the protein or involvement in strong hydrogen bonds of secondary structure. In addition, due to the fact that the observed rate is dependent on chemical exchange, the observed rate will display pH dependence. This limit occurs at low pH and low temperature.

The observed protection factors in the EX2 limit, should be comparable for neighboring sites and provides an additional experimental observable. For folding experiments, the EX1 limit directly reports on the rate of unfolding while in EX2 limit, the rates depend on the equilibrium unfolding and provide information to the free energy level of the individual intermediate forms.

In addition to determining the rates of exchange, the apparent free energy that quantifies the exchange limiting backbone fluctuations is given by

$$\Delta G_{HX} = -RT \ln(K_{op}). \quad (6)$$

From the observed rate of hydrogen exchange, the free energy provides indirect information to the energetics of the system and provides the required insight into the energy needed to structurally disrupt the protein such that the solvating proton or hydroxide can penetrate into the system. Therefore, it is expected that one can infer the mechanisms by which protons exchange in equilibrium via breaking of a single hydrogen bond, the cooperative unfolding of protein sub-regions (local unfolding) or on the global unfolding

of the entire molecule by the magnitude of ΔG_{HX} . In a later section, the sensitivity of the free energy to destabilization conditions, i.e. denaturant and temperature will be discussed.

7.1.3 Mechanism of Hydrogen Exchange in Proteins

Even under conditions that energetically favor the native state structure of proteins, when internal proton exchange rates are slowed drastically by protein sterics, the protein will fully exchange in time. This can be on the days or even minute times scales. Even at equilibrium, the energy landscape is thermally populated giving rise to an inhomogeneous structural environment, so despite high barriers there remains finite probability of unfolding. So the question that arises is what are the mechanisms dictating these exchange rates? What is the manner by which imbedded protons become accessible by the solvent? Can this be due to large amplitude structure transients at equilibrium? If so, what is the magnitude of the structural fluctuations? What are the timescales for opening events to permit exchange? Or does the solvent penetrate into the protein structure exchanging from the interior? These questions are still under considerable debate in the ever expanding hydrogen-exchange community. Currently, there are three major exchange mechanisms under debate that differ based on the amplitudes and timescales of protein motion: Global unfolding, sub-global (or local) unfolding and native state fluctuations. These mechanisms are distinguishable by their thermodynamical parameters and denaturant sensitivity.²

Global Unfolding. For deeply embedded protons with very high protection factors, it is predicted that these exchange via a global opening mechanism or an event with a statistically minor occurrence or one with a very high energetic barrier. This state

is described by a breaking of all internal hydrogen bonds accompanied with full solvation and solvent intercalation into the unfolded structure. The free energy associated with the exchange of these specific embedded hydrogens would report on the enthalpy of denaturation for the protein. Therefore, it is expected that global unfolding would be strongly dependent on structural destabilization conditions including concentration of denaturant and temperature.

Local Unfolding is described by a cooperative rearrangement of local structure that exposes embedded protons to the surface of the protein. This is limited to approximately 10 residues that are typically involved in hydrogen bonded secondary structure.¹⁵ The rates for protons exchanging via sub-global unfolding should experience faster rates than global unfolding or more importantly smaller free energies. At low temperatures and concentrations of denaturant, these local events should be minimally affected however at high temperatures and denaturant concentrations should approach the global unfolding limit. In addition, these events should be distinguishable based on timescales and amplitudes of structure change through molecular dynamics simulations. Local unfolding which involve the opening of neighboring hydrogen bonds in secondary structure require lifetimes that are long enough for catalyzed exchange to occur. Molecular dynamics simulations on helical peptides in methanol predict these relevant timescales of structural openings to be between 40-200 ps.¹⁶

Native state fluctuations allow for small structural openings that permit penetration of solvent into the protein interior and have been described by Woodward and co-workers.¹⁷ These events would be described by much smaller free energies because require less cooperativity and lower amplitude motions of the protein. However, this has

been strongly contested due to the notion that the amplitude of such fluctuations would need to permit the penetration of a solvated hydroxide or hydronium ion to penetrate into the protein interior. This would significantly slow the rates observed.

Global vs. Local Unfolding. A kinetic approach for unfolding experiments, there will be a direct contribution of the local and global unfolding of the protein to the exchange rates of the amide protons. Therefore, similar to understanding the mechanism that dictates hydrogen exchange under native state conditions, the ability to experimentally decipher local and global unfolding is universally required. By controlling the destabilization conditions, through denaturant or temperature, the relative contribution of global and local unfolding events to the exchange kinetics can be manipulated. This is because the hydrogen exchange rate depends on the fraction of the time the amide proton is structurally exposed and that will depend on the rate of local openings plus the rate of global openings scaled by either the denaturant (Eq. 7 and 8) or temperature (Eq. 9 and 10) effects. The expressions for denaturant in the EX2 limit are as follows:

$$\Delta G_{HX}^{Den} = \Delta G_o - \Delta nRT \ln(K_{op,eff}) \quad (7)$$

where

$$K_{op,eff} = K(l)_{op} + K(g,0)_{op} \exp\left(\frac{c_d}{RT}\right) \quad (8)$$

Here, K_{op} is defined in Eq. 5, $K(l)$ and $K(g)$ are the respective rates for local and global unfolding, Δn is the number of denaturant sites, and c_d is the concentration in molarity of denaturant. The expression for the free energy dependence on temperature is

$$\Delta G_{HX}^T = -RT \ln \left[\exp\left(\frac{-\Delta G(l)}{RT}\right) + \exp\left(\frac{-\Delta G(g)}{RT}\right) \right] \quad (9)$$

where

$$\Delta G = \Delta H_m - T\Delta S_m + \Delta C_p \left[(T - T_m) - T \ln \left(\frac{T}{T_m} \right) \right] \quad (10)$$

$\Delta G(g)$ is defined for the two state model as in Eq. 10 and the temperature independence of $\Delta G(l)$ is removed assuming ΔC_p is 0. Fig. 7.1.3.1 shows these relationships between free energy of exchange versus the concentration of denaturant (Fig. 7.1.3.1a) and temperature (Fig. 7.1.3.1b).

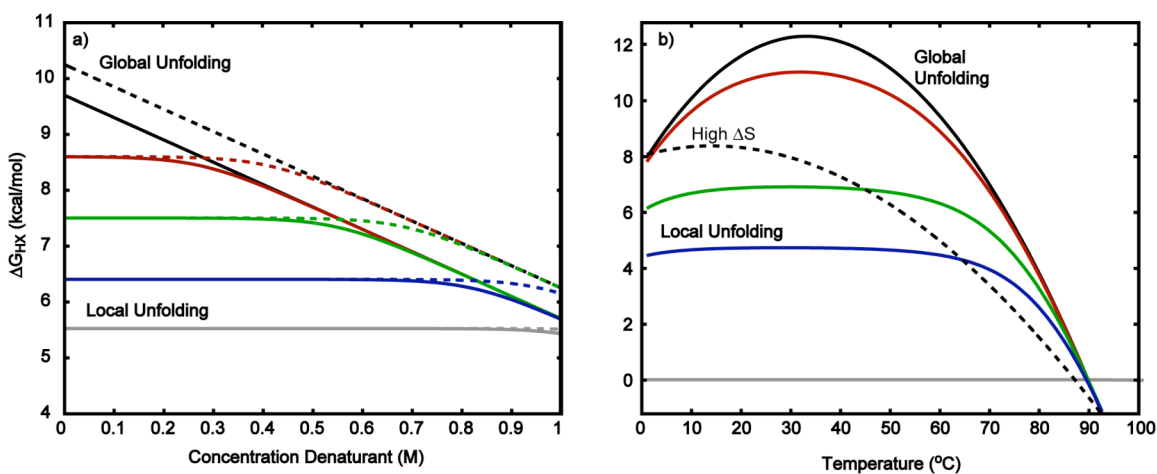


Fig. 7.1.3.1 Free energy dependence on protein destabilization conditions. (a) Free energy as a function of denaturant concentration from Eq. 7 and 8 where $\Delta G_o = 9.7$ kcal/mol, $T = 300$ K, $\Delta n = 4$, $K_{op}(g) = 1$, and $K_{op}(l) = 0, 10^2, 10^4, 10^6, 10^7$. The dotted traces represent the effect of protection of exchangeable sites. (b) Free energy as a function of temperature from Eq. 9 and 10 where $\Delta S = 0.27$ kcal/mol·T, $C_p = 1.8$ kcal/mol·T, $T_m = 77^\circ$ C and $\Delta H = 100, 84, 69$ and 67 kcal/mol. The dotted trace represents the effects on free energy with high entropy.

Fig. 7.1.3.1a shows the change in free energy of hydrogen exchange against low denaturant concentration. The non-linear shape of the lower curves represents exchange of protons with lower activation energies and therefore faster exchange rates. At these low free energies, the curve change minimally versus concentration and the local unfolding mechanism is governing hydrogen exchange. This result is a consequence of

the assumption made in Eq. 8 that $K_{op}(l)$ does not depend on concentration. As the concentration of denaturant increases, the rates dictated by global unfolding begins to dominate equilibrium exchange rates and the curves converge. The major assumption made here is that transient intermediates that expose interior protons have an exchange rate equal to that of the random coil rate for that specific residue. In the limit of residual structure, the rates will be scaled by some additional protection factor. This can be implemented empirically through the introduction of scale factors in front of the rates of opening and closing and is seen in an overall increase of free energy (dotted curved of Fig. 7.1.3.1a).

The temperature dependence of the free energy of exchange is given in Fig. 7.1.3.1b. The top black curve shows inverse parabolic temperature dependence indicative of global unfolding. At high temperatures, the protein structure will destabilize reducing the free energy for exchange. For faster exchanging protons, those that have a inherent higher exposure to solvent, and therefore lower ΔG_{HX} , their temperature dependence flattens out and local structural unfolding events dominate the exchange mechanism as these will depend less on temperature. Again, these curves converge as the temperature exceeds melting transition of the protein. In this limit, the protein a random coil and exchange is dictated by the global unfolding kinetics.

Local unfolding vs. solvent penetration. In the full limit of HX, where the protein is fully destabilized, one sees a small distribution of rates, while under native conditions there is a large distribution of HX rates which report on the local environment of the proton. Within the stable state model are two mechanisms for proton exchange, (1) solvent penetration and (2) local unfolding. These can be differentiated most clearly by

timescales and the amplitude of fluctuations. Solvent penetration involves the entrance of catalyst into the interior of the protein through transient structural openings or through solvent-protein wire exchange.⁸ These rates depend on the access of solvent to the imbedded site, which will be governed by the steric hindrance of the site, the amplitude of the structural modulations and therefore stability of the local protein structure and the intrinsic chemistry of the site. Hydrogen bonding and packing density are the major barriers to exchange of highly buried protons therefore adjacent protons may not have similar rates of exchange.

Molecular dynamics simulations predict modest sized fluctuations with sufficiently long structure opening time scales that support the solvent penetration model.^{16,18} This provides the proper time scale and openings to give water enough time and opportunity to diffuse into the protein. The rates of exchange for this mechanism would be sufficiently fast and results by Tuchsén on BPTI report rapid exchange rates for protons in the hydrophobic core with bulk solvent.⁸ Additional support for the solvent penetration model is seen through comparison of exchange rates of myoglobin and lysozyme protein crystals with condensed phase measurements. The exchange rates of embedded protons experience similar timescales implying exchange is occurring due to minor structural deviations. However, it has been argued by Englander and Kallenbach that the free energy required to shuttle a hydroxide ion into the hydrophobic core would be sufficiently higher than the rates observed.¹⁹

Local unfolding occurs when a small section of hydrogen bound residues, typically those involved in secondary structure, transiently unfolds, exposing the imbedded residues to the bulk solvent. In this mechanism, breaking hydrogen bonds are

the driving force for exchange and requires cooperativity of neighboring amide groups. Correlation between proton exchange rates of adjacent residues partaking in secondary structure implies a local cooperative unfolding event. This correlation arises from the fact that the exchange rate is not only dictated by the depth of burial within the protein but by protection through hydrogen bonded contacts. In contrast to myoglobin and lysozyme crystals, the intermediate and fast exchanging protons of BPTI, show inconsistencies between the crystal and condensed phases.²⁰ This result points to a mechanism that requires large structural changes to occur. In addition, studies using 2D NMR by Wagner and co-workers on BPTL show at sites with different solvent exposure experience similar rates of exchange.²¹ This is due to the cooperativity of local unfolding.

Substantial evidence exists for both the viability of the penetration and local unfolding model. Dill and co-workers developed a purely statistical mechanical model for protein exchange that calls for the existence of both models to explain their results.¹⁵ Both models are predicted based on the small enthalpy required for exchange relative to the full unfolding of the protein. The main differences are whether the exchange is external or internal or if there is correlated exchange between neighboring residues.

Experimental Observables. Native state HX has the capability to detect and characterize folding intermediates that have finite existence under native conditions. Pulsed HX labeling methods isolate stable, dominant folding intermediates that persist longer than timescale of mixing, $>1s$.⁴ Time resolved experiments are performed in the EX2 limit by mapping the decay of the 2D NMR spectra as a function of destabilizing conditions. In the limit that the exchange does not depend on the concentration or degree of denaturing, the exchange is dictated by local fluctuations. These events expose little

new surface area to the bulk solvent. Alternatively, if the leading mechanism for exchange is global unfolding, the time dependence of exchange will strongly depend on the denaturing conditions.

In the EX2 limit, equilibrium exchange experiments detect intermediates via measurement of the equilibrium free energy. For kinetic exchange measurements in the EX1 limit, all the protons will exchange at a rate dictated by the unfolding rate, and not by their site-specific exchange rate or free energy. This is commonly done at high pH and temperature where the exchange rate is on the order of 10^4 s^{-1} . In the presence of denaturant, this will promote K_{op} and will slow the re-closing of the site. Under EX1 conditions, these experiments are difficult to access by NMR due to the high rates of exchange. Ultrafast optical measurements have the ability to resolve chemical exchange dynamics on the ps to ms timescales, and show significant promise to be able to unravel questions of hydrogen-exchange in protein systems. To access these rapid timescales, flow cell techniques will need to be employed due to the irreversibility of the process. The details of using optical techniques will be detailed in the remainder of this chapter and applications using multi-mode 2D IR will be discussed in Chapter 8.

7.2 Hydrogen-Deuterium Exchange Kinetics of Ubiquitin: An FTIR Study

Hydrogen exchange techniques have been applied to a broad range of methods including 1D and 2D NMR,² Mass Spectroscopy,^{22,23} Raman,²⁴ and FTIR.^{19,25} This technique has distinct advantages in its ability to spectroscopically isolate solvent accessible and stable protein structures from solvent exposed and unstable structures. HX FTIR experiments have been shown to improve secondary structure selectivity through restricted multiple regression with particular sensitivity for isolation of helical moieties.²⁶

In this section, the stability of ubiquitin, a mixed α/β protein will be investigated through the use of time dependent and thermally induced hydrogen exchange FTIR spectroscopy.

7.2.1 Temperature Dependent Hydrogen Exchange

Temperature-dependent hydrogen exchange is a technique that characterizes the stability of proteins under thermal denaturation by determination of the temperature (T_{EX}) where all protons have exchanged. The relationship of this temperature to the melting temperature (T_m) of the protein provides the framework for understanding the mechanism of exchange in protein systems. For example, if hydrogen exchange occurs at a temperature where $\Delta T = T_m - T_{EX}$ is large, the mechanism for exchange will be less dependent on global protein dynamics. For ubiquitin, studies have shown that it is an exceptionally stable protein with melting temperatures above 100°C at high pH.²⁷

To characterize ubiquitin's stability, the kinetics of temperature-dependent hydrogen exchange FTIR spectra of the amide finger print region are acquired as a function of time for at pH 1 and pH 9. Fourier transform infrared (FTIR) spectra are taken over the entire amide fingerprint of the protein from 1350 cm^{-1} to 3700 cm^{-1} . This covers all relevant vibrations including the amide I mode which displays sensitivity to secondary structure, the amide II and II' band which represents the contribution of amide protons that are protonated or deuterated and the amide A vibration (NH stretch) that provides similar information to amide II.

Ubiquitin is purchased from Sigma-Aldrich and used without further purification. A DCl in D_2O mixture is used for the low pH solutions while a NaOD in D_2O solution is used for high pH. Samples are prepared at a concentration of 30 mg/mL 3-4 minutes before acquisition of the FTIR spectra. The high concentration is used to improve

signal-to-noise and no effects of aggregation are observed. The sample is placed in a temperature-controlled cell with 1 mm CaF₂ windows and a 50 μm spacer. Spectra are acquired on a Nicolet 380 FTIR spectrometer (Thermo Electron Corporation) at 16 scans per spectra as the temperature of the cell ramped from 5 to 80°C (~1°/min). The cell temperature and spectra are acquired simultaneous and results are presented in Fig. 7.2.1.1.

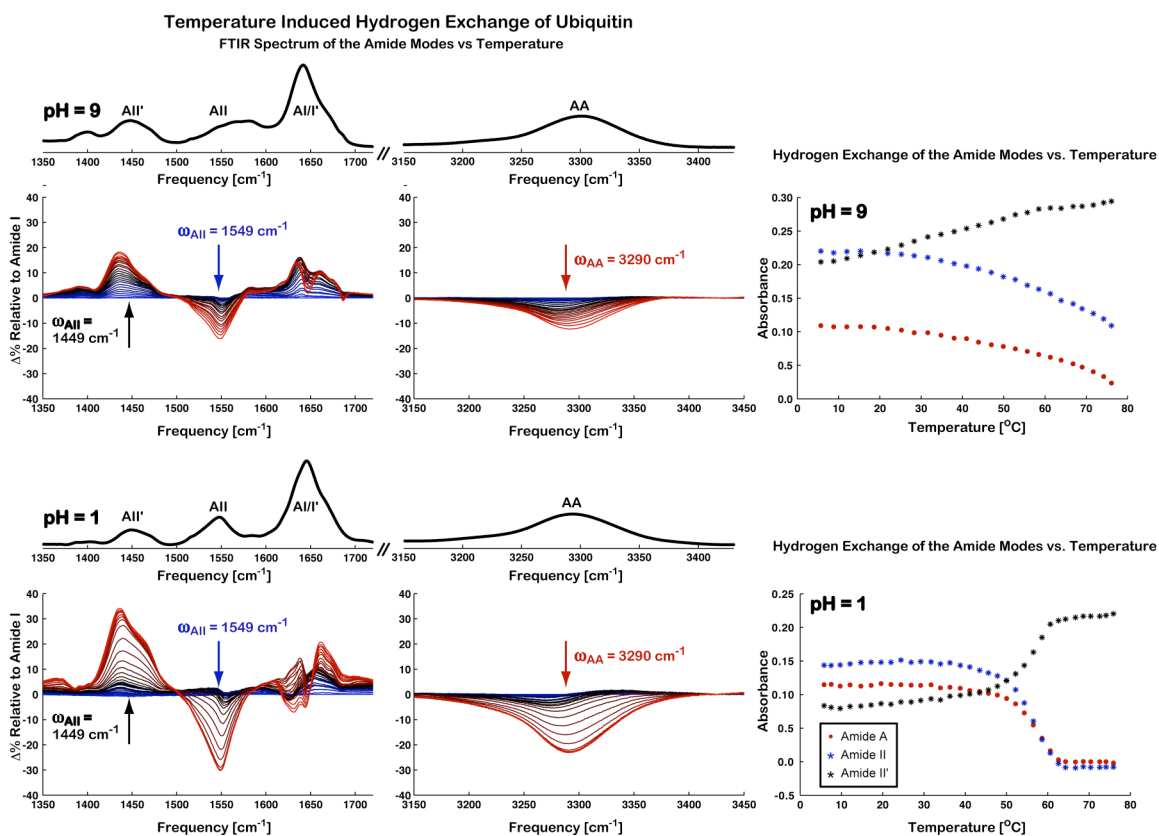


Fig. 7.2.1.1 Temperature induced hydrogen-exchange FTIR spectra of ubiquitin at pH 1 and pH 9. FTIR spectra of partially exchanged ubiquitin of the amide I/II/II' spectral region (left) and amide A mode (middle) and the temperature dependent difference FTIR at pH 9 (top) and pH 1 (bottom) are shown. Note the temperature-dependent difference spectra are colored from cold (blue) to hot (red). The right panel shows the temperature dependent traces of exchange for the amide A (red), amide II (blue) and amide II' (black) bands.

The FTIR spectra of ubiquitin are nearly identical at pH 1 and 9 for the amide vibrations except in the amide II region where the glutamic acid absorption shifts to 1580

cm^{-1} at high pH. To better resolve changes in the FTIR spectra, difference spectra are generated by subtracting the $T = 5^\circ\text{C}$ spectra. Substantial differences are seen in the amide I band upon heating. As expected, an overall shift of $5\text{-}10\text{ cm}^{-1}$ to the red is observed as protons exchange from amide I to I'. In addition, the sharp dip at 1690 cm^{-1} is the result of a concerted amide I to I' shift and unfolding of the AP β sheet as the temperature increases. This observation is most notable at pH 9 where there is a well-defined signature of the extended AP β -sheet. The negative feature at 1645 cm^{-1} arises from the concert shift and loss of the α -helix. In both the pH 1 and 9 spectra, there is a subtle shift of the amide A band to the blue as the temperature increases. This arises from the sensitivity to its local hydrogen bonding environment. As the temperature of the solution increases, the secondary structure is disrupted and hydrogen bonds are broken.

The remaining features in the FTIR difference spectra arise from hydrogen exchange of the amide protons as seen in the synchronized gain of amide II' and loss of amide II and A. The right panel of Fig. 7.2.1.1 show the temperature-dependent peak intensities of the amide II, II' and A modes at high and low pH. A clear transition is seen in the pH 1 trace at a T_{EX} of 58°C . This transition is not observed for pH 9 and is explained by the high melting point of ubiquitin at high pH.²⁸ This result implies that global unfolding is an important mechanism for hydrogen exchange, though does not preclude others. The increase in thermal energy of the system, leads to an increased population of global unfolding events and increases the probability of persisting protons to exchange. This is associated with exposing the hydrophobic core through increasing the internal energy of the system and overcoming enthalpic and entropic propensities.²⁹

The effects of exchange on solvent exposed protons or those that exchange through low energy structural arrangements via local fluctuations³⁰ manifest themselves in these measurements by the initial amplitude of the amide peaks. It is seen that overall, pH 9 has lower initial intensity for amide II and amide A implying that a large fraction of protons have exchange during sample preparation. This result is consistent with the expectation that the rates of chemical exchange will increase at high pH. It should be noted, that simply because a protein is more stable to global unfolding events does not imply that local structure variations are statistically less relevant.

7.2.2 Time Dependence of Hydrogen Exchange

The previous experiment convolves the effects of temperature and time by performing a temperature ramp to examine proton exchange. Even at cold temperatures, a protein will exchange all protons in time. Therefore to disentangle the effects of temperature and time, experiments can be taken as a function of temperature ramp rate or taken as a function of time at a given temperature. This section discusses the time dependent exchange of ubiquitin. Samples were prepared in a similar manner described above, however, the temperature controlled cell was held at a fixed temperature of $T = 30^{\circ}\text{C}$, 40°C and 50°C for the duration of the experiment. Fig. 7.2.2.1 shows the results of the FTIR studies at pH 1 and 9.

In Fig. 7.2.2.1, the left and middle panels display FTIR difference spectra in which time “zero” data is subtracted from all subsequent spectra. Again, the amide I difference spectra of pH 9 exhibit a sharp negative feature at 1690 cm^{-1} . The appearance of this peak in the exchange only spectra imply this is simply a shift of the ν_{II} band of the

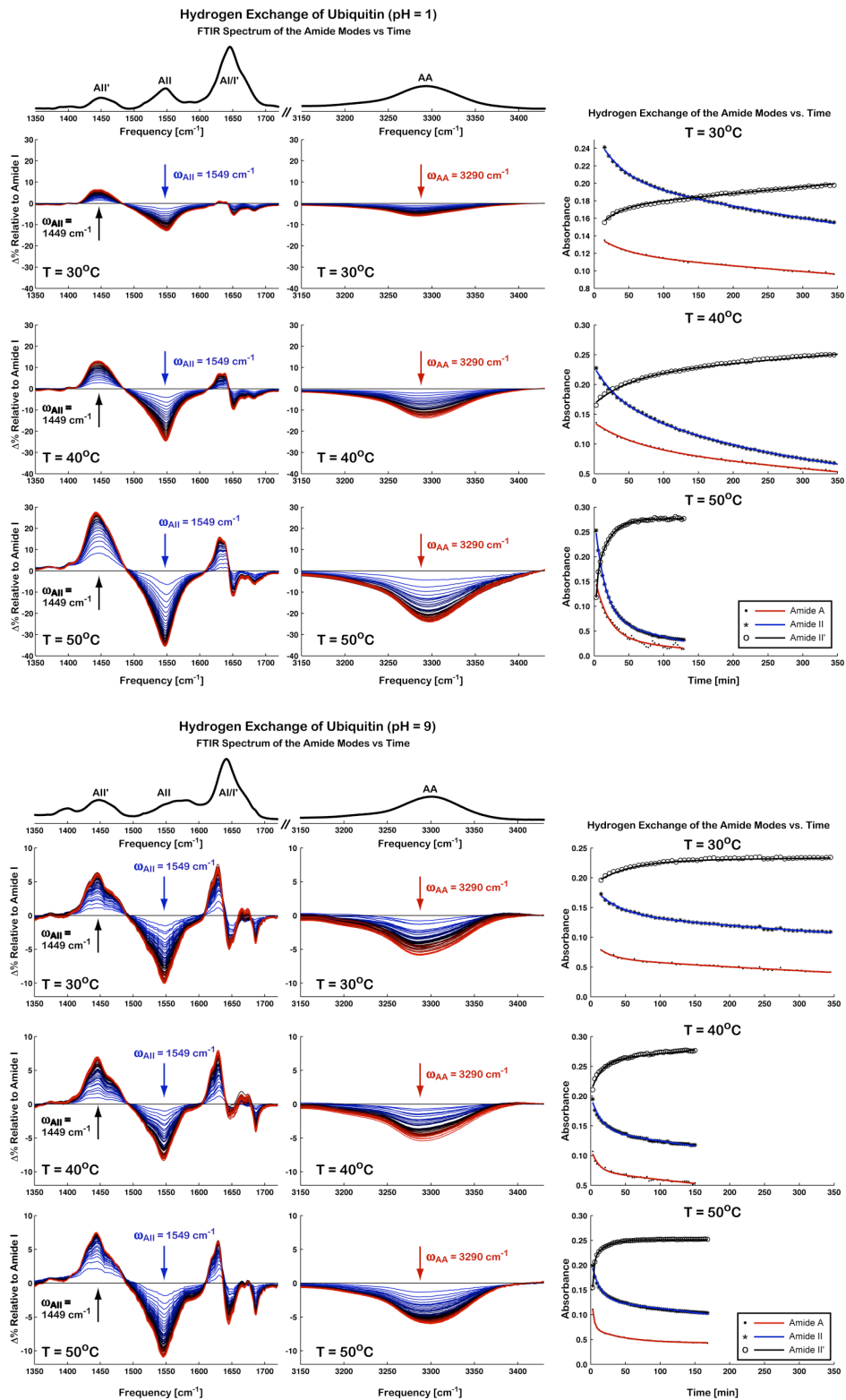


Fig. 7.2.2.1 Time-dependent hydrogen exchange of ubiquitin at pH 9 at T=30°C, 40°C and 50°C

AP β -sheet of ubiquitin from amide I to I'. Similarly, the dispersive feature at 1645 cm^{-1} is observed at both pH 1 and 9. In this experiment, since the temperature is being held constant, the spectral shift of the amide A band is not observed. The peak simply decays as the amide protons of the protein backbone exchange.

The left panel of Fig. 7.2.2.1 displays the kinetics of the amide II, II' and A peak intensity versus time and the normalized bi-exponential fits are tabulated in Table 7.2.2.1. Since the linear FTIR measurement is an ensemble average over a distribution of amide protons in different local environments, the kinetics therefore may be expected to take on a stretched exponential form. The experimental data fits poorly to the stretched exponential and implies that the observed kinetics is dictated by structural conformation mechanism and not simply the local exchange propensities. Therefore, the rates observed in the FTIR measurement report on “global” or “local” protein dynamics and not local chemical kinetics. The effects of chemical kinetics can be indirectly inferred from the initial amplitude of the decays. Universally, the amplitude of the pH 1 decays show that the population of exchange protons is less than that for pH 9. This is expected for the rate of base catalyzed reaction to be faster than acid catalyzed reaction as discussed in the earlier sections. The solvent accessible regions of the proteins are exchanging on timescales faster than the preparation of the sample (minutes). This also will include rapid exchange of labile regions of the protein through described as “local unfolding.” These results show the ability to differentiate between mechanisms based on the temperature dependence of these initial amplitudes by shifting population between the observed timescales.

Table 7.2.2.1 displays all the parameters used to fit the decays of Fig. 7.2.2.1. The short time scales are predicted to be accurate to within 20% of the given value and the longer timescale to no better than 50%. The latter is due to limited data collected for certain measurements and absorption of atmospheric water over the timescale of the measurement. Based on this, the absolute time scales for the second decay are excluded from this discussion till further verification. The amplitudes, however, are noted as important parameters that describe the population of protons that are involved in long timescale structural dynamics. To properly compare these amplitudes, normalized amide II decays for direct comparison of pH and temperature are presented in Fig. 7.2.2.2.

	Conditions	Mode	A ₁	T ₁ [min]	A ₂	T ₂ [min]	B
FTIR pH = 1	T = 30°C	AA	0.14	40	0.79	1412	0.07
		AII	0.22	36	0.74	1170	0.04
		AII'	0.16	27	0.79	1705	0.05
	T = 40°C	AA	0.08	16	0.69	529	0.23
		AII	0.10	20	0.69	455	0.21
		AII'	0.08	24	0.83	347	0.08
	T = 50°C	AA	0.36	17	0.39	434	0.24
		AII	0.43	14	0.37	382	0.20
		AII'	0.51	2	0.38	18	0.11
FTIR pH = 9	T = 30°C	AA	0.30	21	0.70	748	0.00
		AII	0.26	36	0.64	1138	0.10
		AII'	0.20	47	0.30	8241	0.50
	T = 40°C	AA	0.36	10	0.91	633	-0.27
		AII	0.29	15	0.90	1011	-0.19
		AII'	0.23	15	0.82	1361	-0.05
	T = 50°C	AA	0.61	3	0.17	46	0.22
		AII	0.38	2	0.57	599	0.05
		AII'	0.70	2	0.14	18	0.16
2D pH = 1	T = 50°C	AII	0.23	16	0.73	94	0.04

Table 7.2.2.1 Fit parameters from FTIR time-dependent hydrogen exchange of ubiquitin at pH1 and 9 at T=30°C, 40°C and 50°C. Traces are fit to a bi-exponential function equal to $A_1 \exp(-t/T_1) + A_2 \exp(-t/T_2) + B$.

The first timescale of the bi-exponential fit reports on protons with exchange limited by relatively low energy barriers to conformational fluctuations of the protein. For both pH 1 and 9, the rate for exchange increases with temperature, as does the

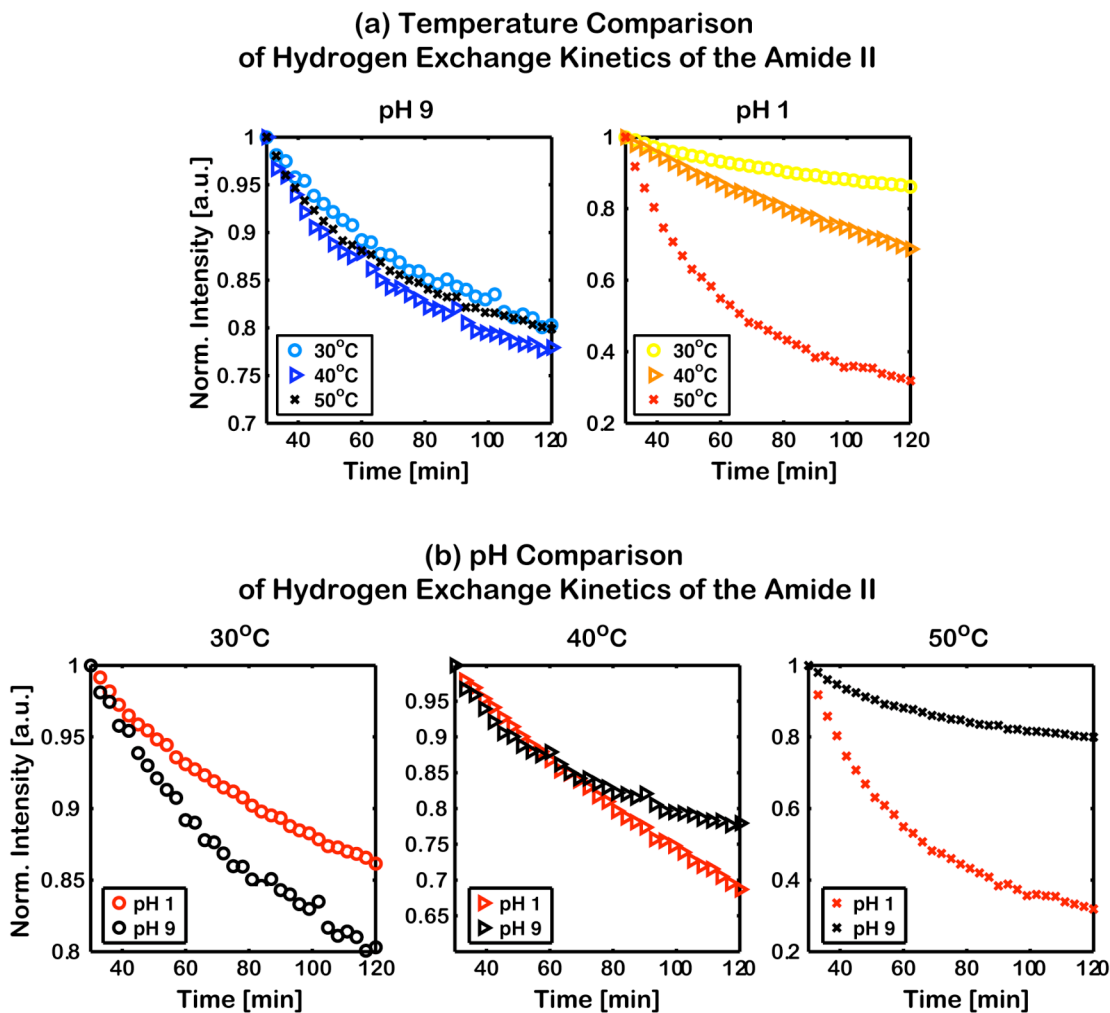


Fig. 7.2.2.2 (a) Normalized hydrogen exchange traces of the amide II mode are plotted for pH 9 (black/blue) and pH 1 (red). pH 1 traces show significant temperature dependence of decay. (b) Direct comparison of pH 1 (red) and 9 (black) hydrogen exchange traces of amide II at $T = 30^{\circ}\text{C}$, 40°C and 50°C .

amplitude of the component. As the temperature increase, a larger population of protons is now accessible to exchange due to increase thermal energy and the amplitude of the second component decreases. Exchange at pH 9 exhibits a more dramatic change in the

amplitude of the first and second component versus temperature. Despite the expected stability of the protein to global unfolding events, the increase in thermal energy in the protein structure allows for the solvents exposed protons to exchange rapidly.

A qualitative examination of the difference FTIR of pH 1 show a more substantial variation across the temperature range studied compared to pH 9. This trend is clearly seen in the pH 1 normalized temperature traces of Fig. 7.2.2.2a. This evidence parallels the results of the previous temperature induced hydrogen exchange experiments that show ubiquitin at pH 1 is approaching its melting point near 50°C. Ubiquitin at pH 9 is substantially more stable on time scales longer than 30 minutes and shows little temperature dependence of versus temperature (Fig. 7.2.2.2a). At low temperatures, or the EX2 limit, the rate of exchange will be pH dependent and the observed rates will be scaled by structural fluctuations of the protein (Eq. 4). At high temperatures, or the EX1 limit, the observed rate of exchange will no longer depend on pH and will be dominated by the protein structural kinetics (Eq. 3). This trend is clearly observed in Fig. 7.2.2.2b where a direct comparison between the amide II decay at pH 1 and 9 are presented. At low temperatures, the pH 9 system exchanges faster than pH 1, however, at high temperatures and inversion of rates is seen in which the pH 1 system decays on a faster timescale than pH 9. This result is due to the increase structural instability of the ubiquitin secondary structure as it approaches its melting transition.

To demonstrate the acquisition of kinetic rates using 2D IR spectroscopy, the time zero slice of the amide II peak is measured versus time in Fig. 7.2.2.3. This slice is related to the projection of the 2D surface onto the ω_3 axis as shown in Fig. 7.2.2.4. The decay of this peak is compared with the FTIR measurements. To a first approximation, it

Hydrogen Exchange of Ubiquitin (pH = 1)

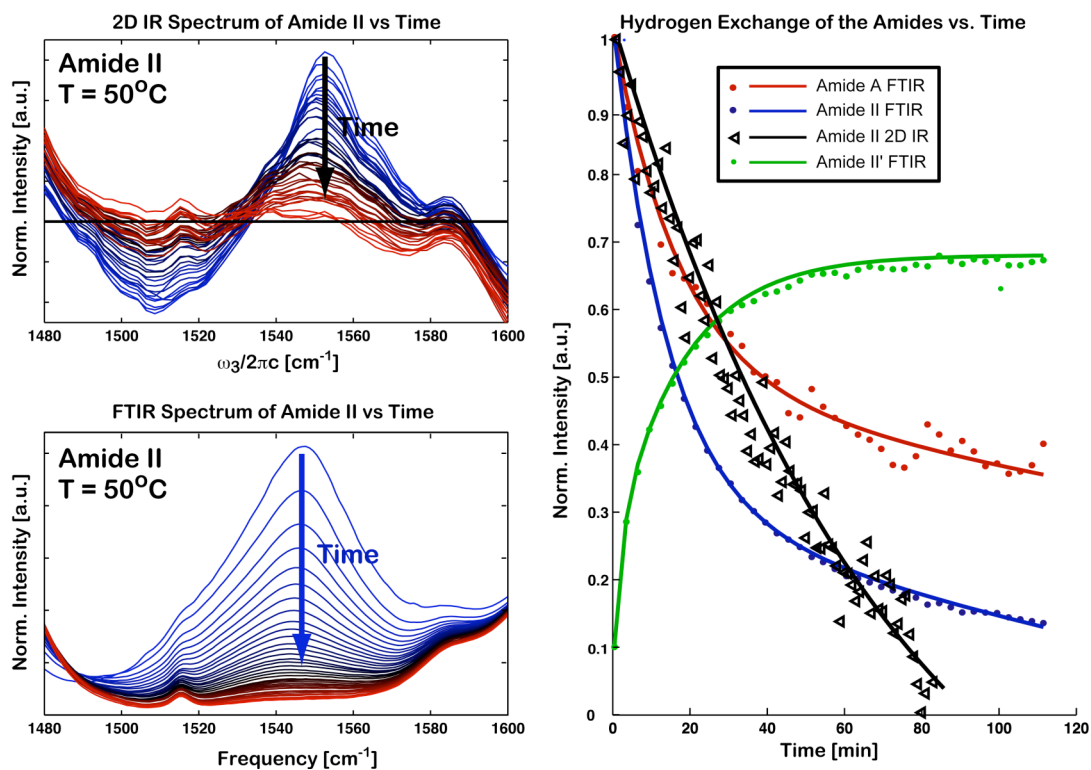


Fig. 7.2.2.3 Comparison of 2D IR projection to FTIR pH 1 and T = 50°C.

is expected that the decays of the amide II 2D IR (black trace) and the amide II FTIR (blue trace) should be identical. However, this is not the case and may arise from non-linear scaling of the transition dipole, interference effects, or background differences due to the solvent contribution.

The apparent synchronization of exchange rates for the amide vibrations and the ability to fit to an exponential form, leads to the conclusion that the exchange observed relies on a cooperative mechanism.⁹ Ideally, the ability to spectroscopically label elements of secondary structure and look at the exchange of each as a function of temperature would further elucidate the mechanisms for exchange. If β sheets and helices

exchange on comparable timescales, global unfolding will dominate the mechanism of exchange. In the next chapter, preliminary results of amide I/II/II' 2D IR spectroscopy explore the use of vibrational coupling to elucidate the structural content of solvent exposed and inaccessible regions of the protein.

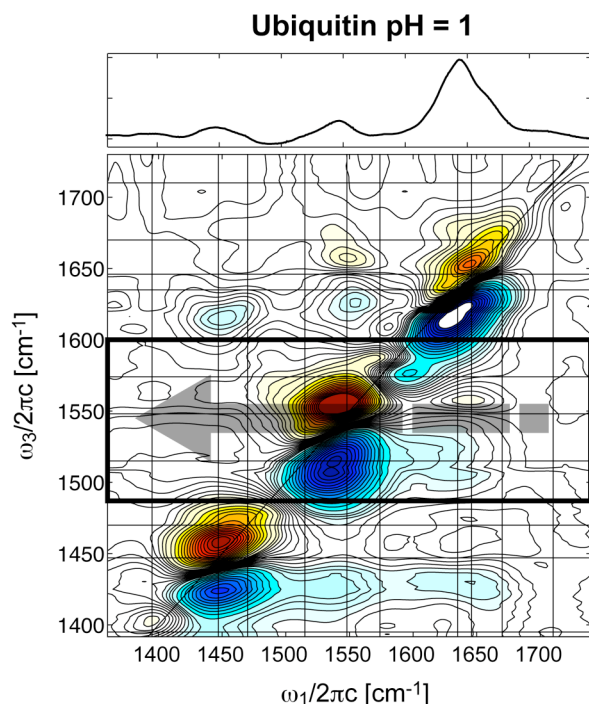


Fig. 7.2.2.4 ZZYY 2D IR spectrum of ubiquitin at pH 1. Arrow represents the related projection of the 2D surface over the amide II region seen in the FTIR kinetic trace of Fig. 7.2.2.3.

7.3 Conclusion

We have demonstrated how the sensitivity of the amide II mode to protonation state of the protein backbone allows FTIR and 2D IR spectroscopy to be used as an effective tool to probe hydrogen exchange kinetics. The ability to determine the influence of local and global unfolding mechanisms can be seen through temperature and pH dependent studies. In the case of NMR, the exchange rate of a single proton can be directly measured and in the limit where the rate is comparable to the T_1 spin relaxation,

magnetization transfer experiments are preformed.² For the optical techniques, the reduced structural sensitivity averages over site-specific exchange rates and, in the experiments discussed in this section, was limited to exchange events after a 3-4 minute sample preparation period. To improve time resolution, stopped flow FTIR experiments can be implemented to measure kinetics of exchange within ms of preparation.³¹

Structural selectivity can be addressed by integration of hydrogen exchange experiments with 2D IR spectroscopy to exploit the distinct advantage of vibrational coupling in which structural correlations to solvent exposure can be measured. Amide I serves as a structurally sensitive vibration and amide II exhibits sensitivity to local solvent environment. The amide I and II mode show significant vibrational coupling.³² Extension of this technique to cover a broader bandwidth, allows for isolation of both solvent exposed and inaccessible regions of the protein to be probed simultaneously. Through the use of 2D IR spectroscopy, the ability to spectroscopically isolate these structures has been realized and will be discussed in detail in Chapter 8.⁵ Furthermore, the extension of ultrafast optical techniques is limited only to the temporal resolution of the molecular system. With proper control over experimental conditions of pH and temperature, picosecond exchange may be observed using ultrafast spectroscopy through amide II-II' exchange spectroscopy.

Acknowledgements

I would like to thank Josh Lessing for providing samples and acquiring the time-dependent hydrogen exchange FTIR kinetics.

References

- (1) Englander, S. W.; Downer, N. W.; Teitelbaum, H. *Annu. Rev. Biochem.* **1972**, *41*, 903-924.
- (2) Dempsey, C. E. *Prog. NMR Spect.* **2001**, *39*, 135-170.
- (3) Krishna, M. M. G.; Hoang, L.; Lin, Y.; Englander, S. W. *Methods* **2004**, *34*, 51.
- (4) Bai, Y. W.; Sosnick, T. R.; Mayne, L.; Englander, S. W. *Science* **1995**, *269*, 192-197.
- (5) DeFlores, L. P.; Tokmakoff, A. *J. Am. Chem. Soc.* **2006**, *128*, 16520-16521.
- (6) Bai, Y. W.; Milne, J. S.; Mayne, L.; Englander, S. W. *Pro. Struct.* **1993**, *17*, 75-86.
- (7) Eigen, M. *Angew. Chem. Internat. Edit.* **1964**, *3*, 1-72.
- (8) Tuchsén, E.; Woodward, J. *J. Mol. Bio.* **1985**, *185*, 421-430.
- (9) Bai, Y.; Milne, C. J.; Mayne, L.; Englander, S. W. *Proteins* **1982**, *20*, 4-14.
- (10) Connelly, G. P.; Bai, Y. W.; Jeng, M. F.; Englander, S. W. *Pro. Struct.* **1993**, *17*, 87-92.
- (11) Linderstrom-Lang, K. *In: Neuberger A, ed. Symposium on Protein Structure* **1958**, London: Methuen.
- (12) Englander, S. W.; Mayne, L.; Bai, Y.; Sosnick, T. R. *Protein Science* **1997**, *6*, 1101-1109.
- (13) Hvidt, A.; Linderstrom-Lang, K. *Trav. Lab Carlsberg (Ser Chim)* **1955**, *29*, 385-402.
- (14) Michaelis, L.; Menten, M. *Biochem. Z.* **1913**, *49*, 333-369.
- (15) Miller, D. W.; Dill, K. A. *Protein Science* **1995**, *4*, 1860-1873.

- (16) Sessions, R. B.; Gibbs, C. E.; Dempsey, C. E. *Biophys J.* **1998**, *74*, 138-152.
- (17) Li, R.; Woodward, C. *Protein Science* **1999**, *8*, 1571-1591.
- (18) Pastore, A.; Harvey, T. S.; Dempsey, C. E.; Campbell, I. D. *Eur. J. Biophys* **1989**, *16*, 363-367.
- (19) Englander, S. W.; Kallenbach, N. R. *Q. Rev. Biophys.* **1983**, *16*, 521-655.
- (20) Kossiakoff, A. A. *Nature* **1982**, *296*, 713-721.
- (21) Wagner, G.; Wuthrich, K. *J. Mol. Bio.* **1982**, *160*, 343-361.
- (22) Englander, S. W. *J. Am. Soc. Mass Spect.* **2006**, *17*, 1481-1489.
- (23) Maier, C. S.; Deinzer, M. L. *Methods in Enzymology* **2005**, *402*, 312.
- (24) Hildebrandt, P.; Vanhecke; Heibel, G.; Mauk, A. G. *Biochem.* **1993**, *32*, 14158–14164.
- (25) Woodward, C.; Hilton, B. D. *Ann. Rev. Biophys. Bioeng.* **1979**, *8*, 99-127.
- (26) Baello, B. I.; Pancoska, P.; Keideling, T. A. *Anal. Biochem.* **2000**, *280*, 46-57.
- (27) Loladze, V. V.; Makhataдзе, G. I. *Protein Science* **2002**, *11*, 174-177.
- (28) Zand, R.; Agrawal, B. B. L.; Goldstein, I. J. *Proc. Nat. Acad. Sci.* **1971**, *68*, 2173.
- (29) Backmann, J.; Schultz, C. P.; Fabian, H.; Hahn, U.; Saenger, W.; Naumann, D. *Proteins: Structure, Function, and Genetics* **1996**, *24*, 379-387.
- (30) Maity, H.; Lim, W. K.; Rumbley, J. N.; Englander, S. W. *Protein Science* **2003**, *12*, 153-160.
- (31) Fabian, H.; Naumann, D. *Methods* **2004**, *34*, 28-40.
- (32) DeFlores, L. P.; Ganim, Z.; Ackley, S. F.; Chung, H. S.; Tokmakoff, A. *J. Phys. Chem. B* **2006**, *110*, 18973-18980.

Chapter 8:

Hydrogen Exchange Multi-Mode Two-Dimensional Infrared (2D IR) Spectroscopy

“It seems to me what is called for is an exquisite balance between two conflicting needs: the most skeptical scrutiny of all hypotheses that are served up to us and at the same time a great openness to new ideas ... If you are only skeptical, then no new ideas make it through to you ... On the other hand, if you are open to the point of gullibility and have not an ounce of skeptical sense in you, then you cannot distinguish the useful ideas from the worthless ones.” –Carl Sagan

Sections of the work presented in this chapter are published in the following paper:

- *L. P. DeFlores and A. Tokmakoff, J. Am. Chem. Soc., Vol. 128, pp. 16520-16521 (2006)*

8.1 Equilibrium Hydrogen Exchange Two-dimensional Infrared Spectroscopy

Hydrogen-deuterium exchange (HX) is a valuable tool for characterizing protein structural stability, solvation and water exposure, and unfolding kinetics.^{1,2} HX is influenced by the site specific pK_A , solvent accessibility to protonated sites and strength

of hydrogen bonding interactions.¹ In the hydrophobic core or strongly hydrogen bound secondary structures, HX rates are dramatically reduced due to shielding of exchangeable sites.¹ NMR methods infer the degree of protection and structural stability from site-specific HX measurements.^{3,4} These can be incorporated into fast-mixing experiments to provide the information about reaction intermediates.¹ IR spectroscopy in conjunction with HX also provides information on solvent exposure of the protein backbone, relying on the strong red shift of the amide II vibration upon deuteration of the peptide group NH.⁵ IR is an appealing technique for kinetic studies, since it can be used in combination with fast unfolding experiments.^{6,7} However, amide II is not otherwise structurally sensitive and is typically overlapped with side-chain absorptions. Using two-dimensional infrared (2DIR) spectroscopy, we have performed HX experiments that combine the solvent-exposure sensitivity of amide II with the secondary-structure sensitivity of amide I. The correlation of transition frequencies in the amide I-II region provides a secondary structure sensitive probe of protein solvent accessibility ideal for studies of protein folding and stability.

2D IR spectroscopy of amide I vibrations has found wide use in the study of protein and small peptide conformation and dynamics.⁸⁻¹³ In the case of proteins, the coupling between amide I vibrations of individual peptide groups leads to excitonic states whose vibrational spectrum reflects the symmetry of underlying secondary structures and the extent of delocalization.^{13,14} In FTIR spectra, anti-parallel β -sheets gives rise to a two-peak amide I signature located at $\sim 1630\text{ cm}^{-1}$ (ν_{\perp}) and $\sim 1690\text{ cm}^{-1}$ (ν_{\parallel}), while α -helical and random coil absorptions overlap in the middle of the amide I band ($\sim 1650\text{ cm}^{-1}$). 2D

IR spectroscopy of proteins has provided a higher level of detail into protein backbone conformation and secondary structure, and is finding use in folding studies.^{15,16}

8.1.1 Amide I/II HX Spectroscopy

Absorptive 2D IR spectra were acquired using methods and instrumentation that is described in detail elsewhere.¹⁷ The experiments used 1 μJ , 90 fs pulsed mid-IR radiation centered at 1600 cm^{-1} . The pulse bandwidth of 185 cm^{-1} (FWHM) is centered to cover both the fundamental ($\nu=0\rightarrow 1$) and anharmonically shifted ($\nu=1\rightarrow 2$) overtones of both the amide I/I' and amide II modes of the proteins shown in Fig. 8.1.1.1 and 8.1.1.3. Data is collected in frequency (ω_3) and time (τ_1) and numerically transformed along τ_1 to obtain ω_1 . The resolution along ω_3 is dictated by grating dispersion and the size of the 64 pixels on the MCT array detector. In this experiment the resolution is 4 cm^{-1} /pixel. ω_1 resolution is determined by the total time delay swept in τ_1 and is 0.5 cm^{-1} . Spectra shown were acquired in the crossed (ZZYY) polarization geometry to enhance to relative intensity of the cross peaks.¹⁸

Two-dimensional infrared spectra were taken of seven protein systems with various degrees of secondary structural motifs: concanavalin A (Con A, β -protein), β -lactoglobulin (BLG, α/β β -sandwich protein), ribonuclease A (RNase A, α/β -protein), ubiquitin (α/β -protein), lysozyme (α/β -protein), myoglobin (α -protein), and serum albumin (α -protein). Experimental conditions were chosen to minimize H/D exchange through the course of data collection (~20 minutes). Samples are held between two CaF_2 windows with a 50 μm spacer in a water-cooled brass sample cell. Proteins were monitored at various temperatures over a two-hour period using FTIR spectroscopy to

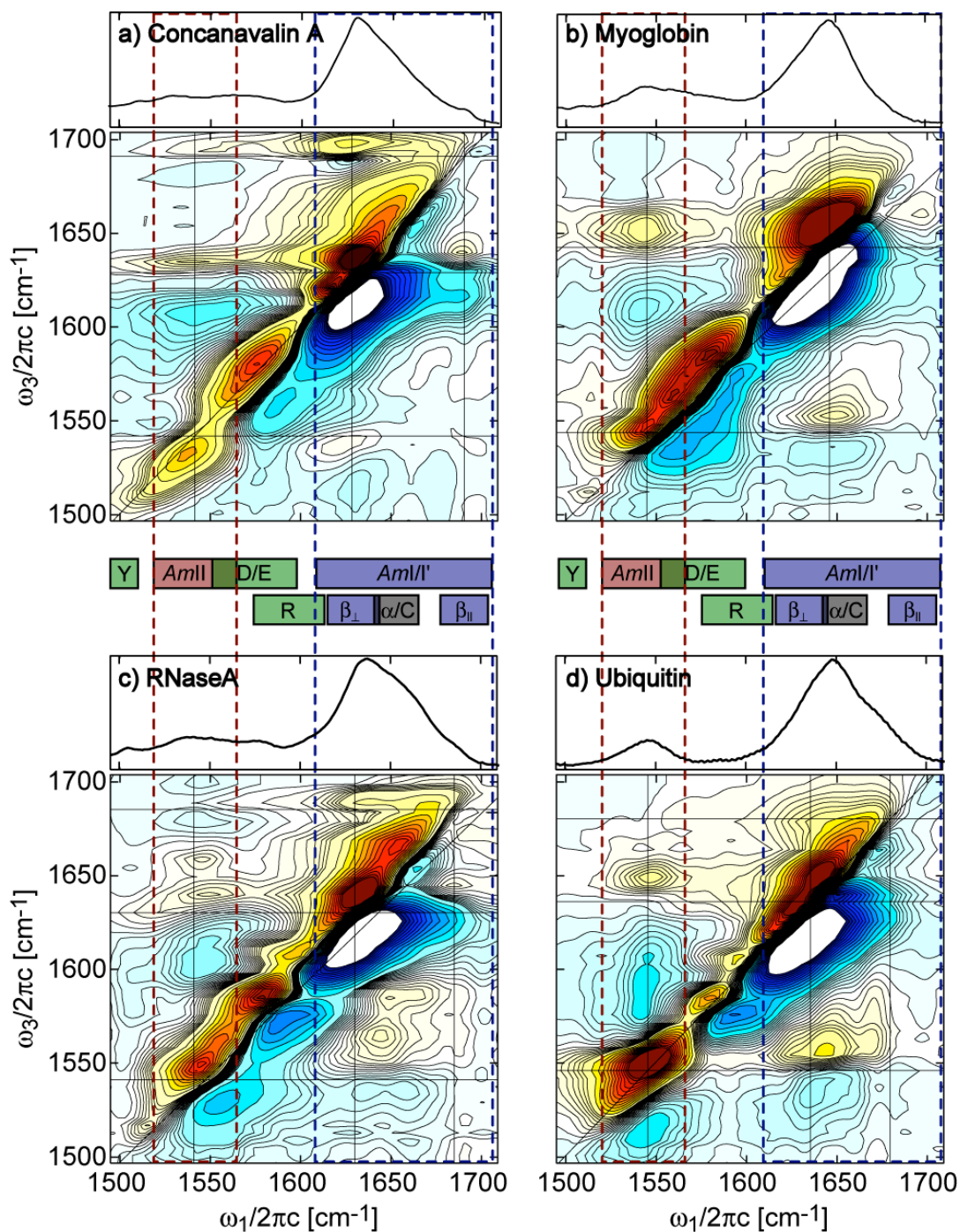


Fig. 8.1.1.1 FTIR and absorptive amide I/I'-II 2DIR spectra of a) Con A, b) myoglobin, c) RNaseA and d) ubiquitin. The spectral regions corresponding to the amide I/I', amide II, and various side chain absorptions are labeled in the middle. Dashes mark the amide I and amide II regions over which the slices in Fig. 8.1.1.3 were integrated. Contour levels are plotted to emphasize the cross peak region of the spectra. Contours for Con A and RNaseA are plotted in 1% increments for $\pm 8\%$ and 4.3% from $\pm 8\%$ to $\pm 60\%$ peak amplitude of the amide I fundamental. Ubiquitin and myoglobin are plotted with 1.5% increments for $\pm 12\%$ and 4% from $\pm 12\%$ to $\pm 60\%$ peak amplitude of the amide I fundamental.

ensure the amide II band did not change. The ideal temperature was determined to be 5°C for all proteins. The samples were rapidly prepared at 10°C to avoid condensation of atmospheric water onto the sample cell and windows, and then cooled to 5°C once in the dry air purged spectrometer. Con A, BLG, RNaseA, and myoglobin were prepared in a pD=7.6 phosphate/D₂O buffer, lysozyme in a pD=5.5 phosphate/D₂O buffer, albumin in a pD=7.3 phosphate/D₂O buffer, and ubiquitin was prepared at pH=1.0 using DCl/D₂O. Sample concentrations ranged between 20-30 mg/ml such that the OD of the amide II transition is ~0.1.

The FTIR and absorptive 2D IR spectra for all proteins are shown in Fig. 8.1.1.2 to show trends in the cross peak region. The 2D IR spectra presented in this manuscript have not been corrected for pulse spectral intensity in either ω_1 or ω_3 dimensions, creating an enhancement of features around 1600 cm⁻¹.

2D IR experiments can be extended to dissect the amide I spectral profile on the basis of the solvent exposure of secondary structures. For proteins immersed in D₂O, buried residues that remain protonated will absorb at ~1550 cm⁻¹ (amide II), while solvent exchanging (deuterated) residues will absorb at ~1450 cm⁻¹ (amide II'). The position and shape of amide I-II cross peaks correlates the secondary structure observed by amide I vibrations with the protonation state of amide II, isolating solvent inaccessible secondary structures and hydrophobic regions of the protein. We have investigated the amide I-II 2D IR spectra for several proteins with varying secondary structure motifs. Fig. 8.1.1.1 shows the results for four proteins: concanavalin A (Con A), myoglobin, ribonuclease A (RNaseA), and ubiquitin. Additional protein spectra are presented in Fig. 8.1.1.2.

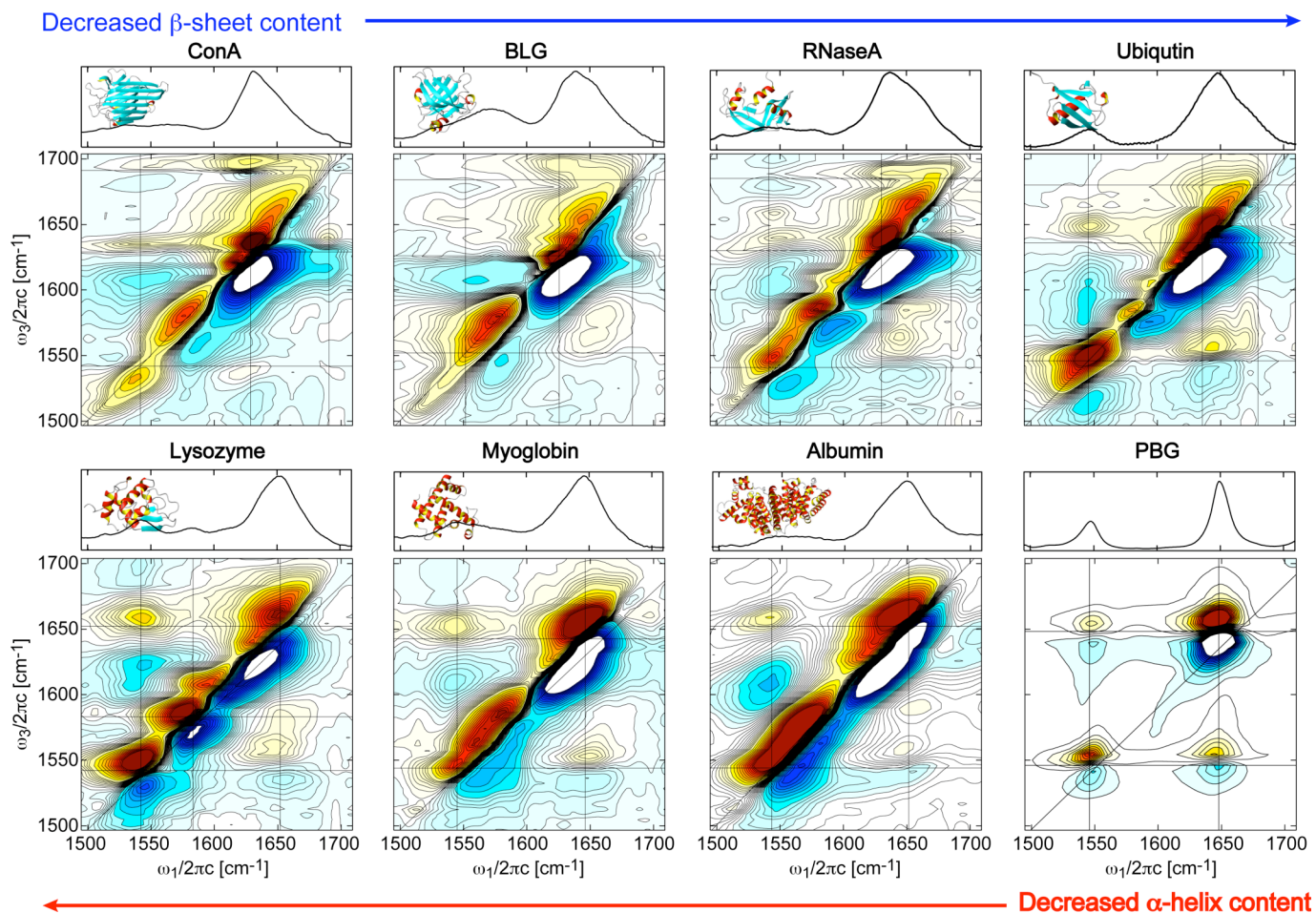


Fig. 8.1.1.2 FTIR and absorptive 2D IR spectra of proteins concanavalin A, β -lactoglobulin, ribonuclease A, ubiquitin, lysozyme, myoglobin, albumin and an idealized α -helix homopolymers PBG in CDCl_3 . Contours for Con A, BLG and RNaseA are plotted in 1% increments for $\pm 8\%$ and 4.3% from $\pm 8\%$ to $\pm 60\%$ peak amplitude of the amide I fundamental. Ubiquitin, lysozyme, myoglobin and albumin are plotted with 1.5% increments for $\pm 12\%$ and 4% from $\pm 12\%$ to $\pm 60\%$ peak amplitude of the amide I fundamental.

Resonances in the 2DIR spectrum correlate the frequency of vibrational excitation ω_1 with the detection frequency ω_3 , and appear as an oppositely signed doublet.¹⁷ The diagonal features ($\omega_1=\omega_3$) can be assigned to components in the FTIR spectrum, and are diagonally elongated as a result of inhomogeneous broadening. Off-diagonal intensity arises from vibrational coupling. The amide I portion of the spectrum contains distinctive line shapes that arise from interference effects and indicate the underlying secondary structure content. “Z”-shaped contour profiles elongated along $\omega_3 = \nu_{\perp}$ and ν_{\parallel} are characteristic of β sheets, and are observed for Con A, RNaseA and ubiquitin.¹⁶ The diagonal amide II peak is observed at $\sim 1550 \text{ cm}^{-1}$, and additional diagonal features between $1550\text{-}1610 \text{ cm}^{-1}$ arise from side chain absorptions by Asp, Glu, Asn, Gln, and Arg.^{19,20} Each of the protein spectra exhibit cross peaks between the amide I and amide II vibrations with strongly varying line shapes. Since amide I and amide II vibrations are anharmonically coupled,²¹ these cross peaks arise from couplings in non-exchanged residues of the protein, and directly reveal the amide I spectrum of the buried, non-exchanging residues and secondary structures of the protein. The cross peaks are observed to extend along ω_1 with the width of amide II, and with ω_3 peaks that pick out components from the amide I diagonal feature.

To analyze these cross peaks slices for $\omega_1=\omega_{\text{AII}}$ integrated over a 30 cm^{-1} window in ω_1 are plotted in Fig. 8.1.1.3. These are compared to the amide I FTIR and the amide I diagonal region projected onto ω_3 . For Con A, a β -protein, the cross peak consists of a pair of vertically displaced doublets at $\omega_3=1630 \text{ cm}^{-1}$ and 1690 cm^{-1} (Fig. 8.1.1.1a) indicative of its anti-parallel β -sheets. The lack of intensity between $1640\text{-}1680 \text{ cm}^{-1}$, seen in the cross peak slice of Con A in Fig. 8.1.1.3, indicates that coil and turn regions at

the edge of the protein have exchanged. The cross peak for myoglobin, an α -protein, shows a highly rounded and intense doublet centered at $\omega_3=1646\text{ cm}^{-1}$. The peak is red-shifted from the main amide I band, suggesting a loss of spectral content from coil contributions. This allows one to clearly isolate secondary structural elements from the random coil and solvent exposed regions of the protein. Previous HX studies on RNase A, an $\alpha+\beta$ protein, concluded that secondary structural elements contain mixed protonation states.⁶ The presence of cross peaks in the 2DIR spectra containing all of the amide I features implies a high degree of secondary structural stability in RNaseA at pH 7 and 5°C. The cross peak slice, Fig. 8.1.1.3, shows distinct signatures of its β sheet and α helices.

For ubiquitin, the 2D spectrum in Fig. 8.1.1.1d and cross-peak slice in Fig. 8.1.1.3, shows a round cross peak centered at the frequency associated with α helices. This indicates that even though ubiquitin has a five-stranded mixed sheet, the β sheet of ubiquitin is relatively labile and exchanges readily under low pH and temperature and the protons of the helix are least susceptible to HX. This conclusion is consistent with ubiquitin unfolding studies, which argue that ubiquitin's mixed β -sheet is partially disordered at the unfolding transition state. The first 37 residues form a tightly folded core consisting of a β hairpin and helix,⁴ whereas the remaining three strands of the sheet are presumed to be less stable and unfold first.¹⁵

The side chain spectral features provide further insight into solvent exposure within these proteins. In the $1570\text{-}1610\text{ cm}^{-1}$ ubiquitin window, a pair of sharp diagonal

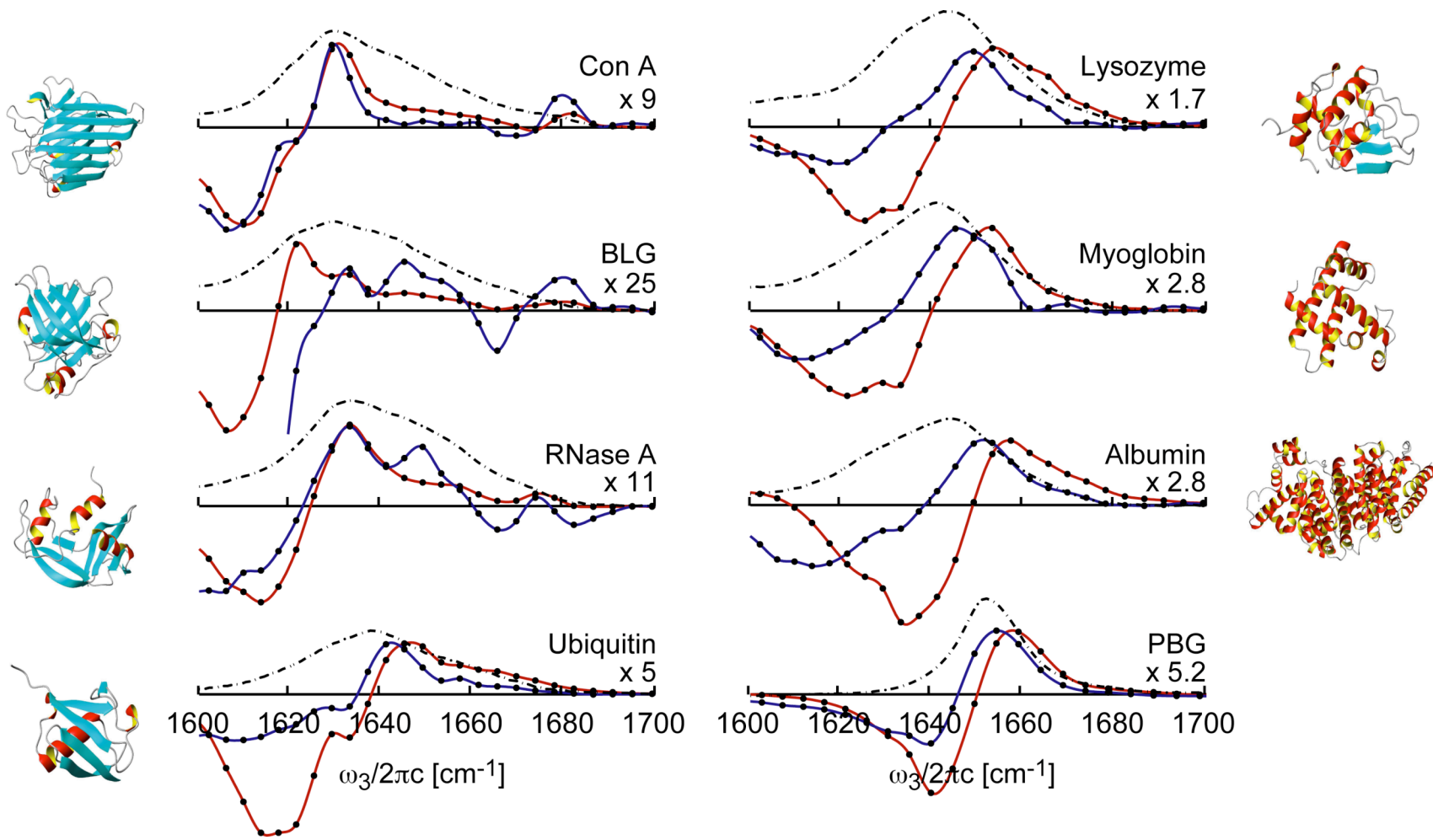


Fig. 8.1.1.3 Normalized slices taken along $\omega_1 = \omega_{AI}$ (blue) overlapped with the amide I slice (red) and amide I FTIR (black dashed).

peaks with ω_3 -elongated ridges, indicating cross peaks, are observed. We assign this feature to the coupled symmetric/asymmetric guanidinium vibrations of the Arg side chains.^{19,20} In the case of ubiquitin, the four arginines present are within the loops and termini of the destabilized β -strands. This is expected for a polar side chain. Similar features are observed in RNaseA and lysozyme.

To confirm the protonation of the peptide groups in amide I/II couplings and the persistence of Arg side chain absorption seen in the 2D IR spectra, consecutive 2DIR spectra of partially and fully exchanged ubiquitin were taken (Fig. 8.1.1.4). The sample was prepared as described above and the partially exchange protein was taken at 5°C. The sample was then heated to 65°C at which the protein fully unfolds and left to exchange for 30 minutes. The temperature was then cooled to 5°C and the fully exchanged spectra were taken (Fig. 8.1.1.4b). These spectra show the loss of the amide II doublet at $\omega_1=\omega_3=1550\text{ cm}^{-1}$. No diagonal or off-diagonal features involving amide II are observed in the fully exchanged spectrum (Fig. 8.1.1.4b). Additionally, the side chain absorption of symmetric/asymmetric guanidinium vibrations of the Arg near $\sim 1585\text{ cm}^{-1}$ persist after complete deuteration of the protein.

In addition to the structural sensitivity of the technique, 2DIR provides information about the protein anharmonic vibrational potential. These spectra, particularly for α proteins, show cross peak splitting that give a large apparent off-diagonal anharmonicity or coupling strength. This feature most likely arises more from the inhomogeneous broadening of amide I; however, this opens questions about the degree of amide mode coupling in proteins.²² Another feature, particularly in the β -sheet containing proteins, is the asymmetry of the upward ($\omega_1<\omega_3$) and downward ($\omega_1>\omega_3$)

cross peaks. The asymmetry can be explained by destructive interference effects between vertically elongated positive and negative cross peaks. The intensity mismatch is less dramatic in the case of myoglobin and ubiquitin.

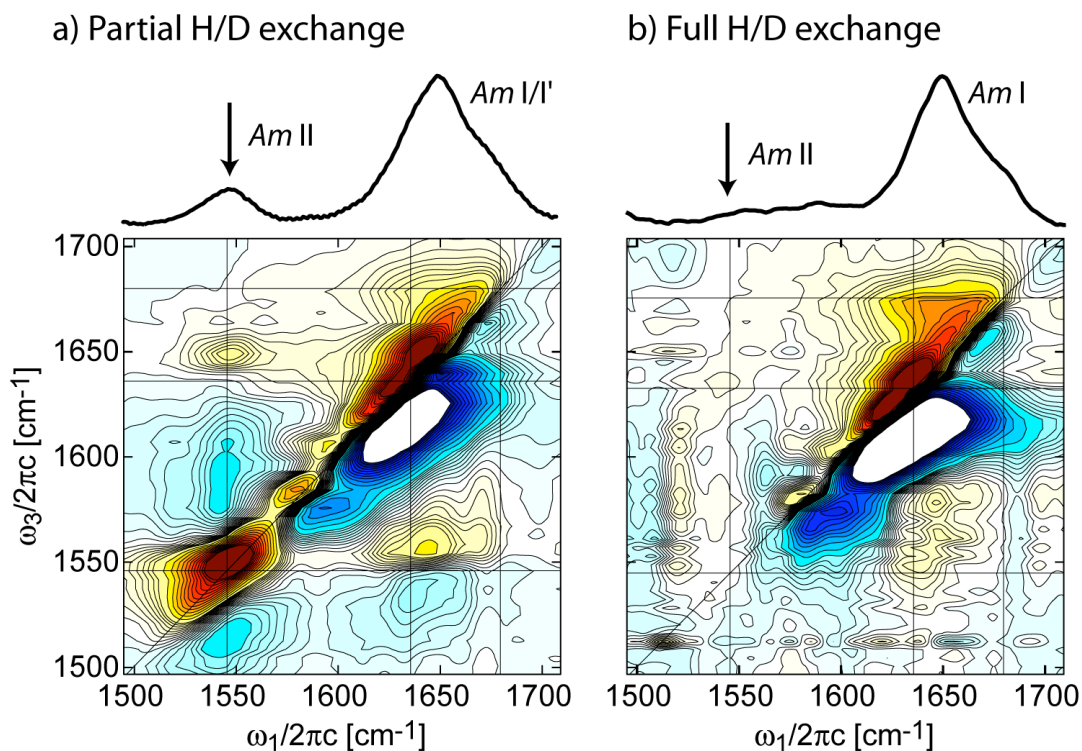


Fig. 8.1.1.4 FTIR and 2DIR spectra of ubiquitin before exchange and after full exchange. Note disappearance of the amide II peak that is only present when the amide mode is protonated.

Hydrogen exchange 2DIR spectroscopy can be used to isolate spectra for buried secondary structure elements through vibrational coupling of the amide I and amide II modes. Coupling of the amide modes in these isolated regions shows distinct spectral features indicative of α -helical and/or β -sheet structure, implying a high degree of stability of hydrogen bonding contacts.

8.1.2 Amide I/II/II' HX Spectroscopy: Monitoring Solvent Accessible and Inaccessible Regions of Proteins Simultaneously

With the experimental advances presented in Chapter 2 and 3, generation of broadband IR pulses allows for the amide I, II, and II' modes to be simultaneously probed. HX multi-mode 2D IR spectroscopy has the capability of isolating solvent accessible and inaccessible regions of proteins by taking advantage of the secondary structure sensitivity of amide I and II' and the intrinsic sensitivity of amide II and II' to protonation state of the protein backbone. When surfaces are collected as a function of time or temperature, the exchange kinetics of secondary structure and the mechanisms that lead to exchange can be unraveled.

In this section, equilibrium 2D IR spectra are taken of partially exchanged proteins at 5°C using the experimental set up outlined in Chapter 3. All proteins, ubiquitin, concanavalin A (ConA), myoglobin, ribonuclease A (RNaseA), and lysozyme are purchased from Sigma-Aldrich and used without further purification. For pH 1 measurements, DCl is mixed in D₂O, for pH 7 a 50 mM phosphate buffer is prepared and for pH 9, 14 M NaOD is diluted in D₂O. Spectra are taken as 120 cm⁻¹ wide strips in ω_3 at 2 cm⁻¹/pixel to improve the resolution for defining secondary structure. For the full ubiquitin surfaces in Fig. 8.1.2.1, consecutive strips are taken at three different monochromator settings of 1650, 1550 and 1450 cm⁻¹ and surfaces are stitched together.

The full 2D IR spectrum of the amide I/I'/II/II' finger print region provides a wealth of information about protein solvation and structure. By using 2D IR, one has the ability to correlate different sensitivities of vibrationally coupled modes through the presence of cross peaks. Each cross peak provides a different vantage point and allows for simultaneous acquisition of information. The intensity of the cross peak depends on

the strength of coupling and the relative angle of the transition dipole moment. The frequency reports on the modes that are coupled.

For the HX experiments, under partial exchange each 2D IR spectra will have the dominate diagonal resonances, the amide I/I', II and II' modes. The amide I/I'-II cross peak, as described in the previous section, will be sensitive to secondary structure that is solvent inaccessible, while the amide I/I'-II' cross peak will isolate residues that have undergone hydrogen-deuterium exchange. The results of Chapter 4 conclude that the amide I'-II' coupling will be stronger than amide I-II due to the local mode composition of the vibrational bands.

The relative angle of the amide II band (assumed to be a localized to the amide group and 65° from the CO bond) will lie 60° and 55° with respect to the amide I/I' ν_\perp and ν_\parallel modes and 95° relative to the amide I A mode of the α -helix. The amide II' band is shown to exhibit secondary structure sensitivity. The two β -sheet amide II' signatures have an inclusive angle of 88° . The dominant amide II' mode along the β strands is calculated to be 86° relative to ν_\perp and 30° relative to ν_\parallel of amide I/I'. The degenerate α -helix E_1 modes of amide II' lie 92° and 112° off the central axis of the helix. This gives a relative angle of 72° and 92° to the A mode of the amide I helix. All angles are tabulated in Table 5.5.2.1. In the ZZYY spectra, purely based on the angular dependence, the amide I/I'-II' cross peak will show strong transition indicative of coupling between the along the strand mode of amide II' and ν_\perp mode of amide I, as well as a strong helical cross peak. The amide I/I'-II cross peak will show strong helical coupling and relatively weaker β -sheet peaks.

Hydrogen Exchange 2D IR Spectroscopy of Ubiquitin at pH 1

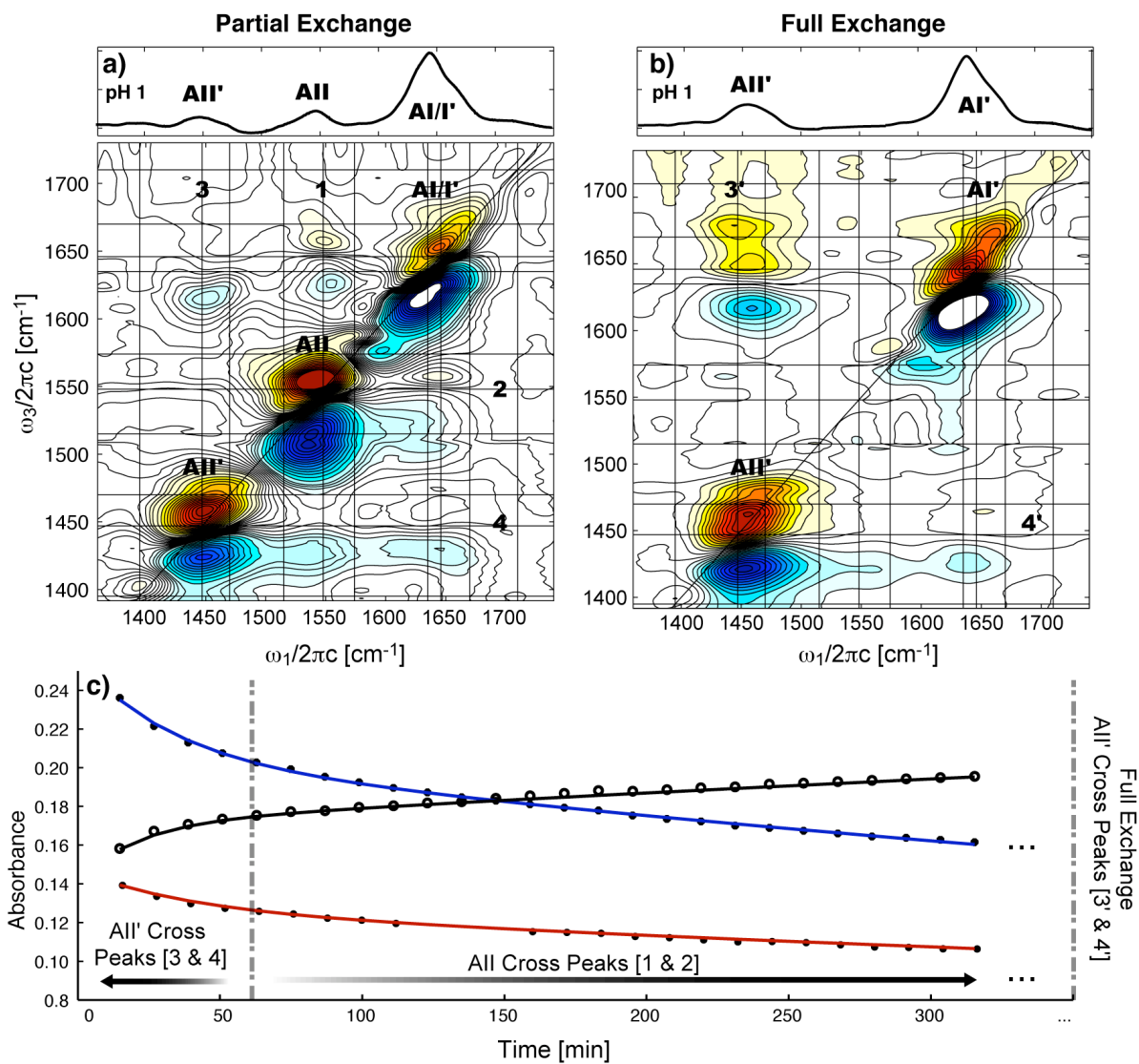


Fig. 8.1.2.1 ZZZY 2D IR Spectra of ubiquitin at pH = 7 (a,b) under partial exchange conditions (5°C) and after full exchange (heated to 80°C and cooled back to 5°C). FTIR kinetic traces of ubiquitin at pH 7 and 30°C. The amide II' cross peaks (3 and 4) report on secondary structure that has exchanged during sample preparation and data acquisition. The amide II cross peaks (1 and 2) report on solvent inaccessible regions of the protein.

Hydrogen Exchange 2D IR Spectroscopy of Ubiquitin at pH 9

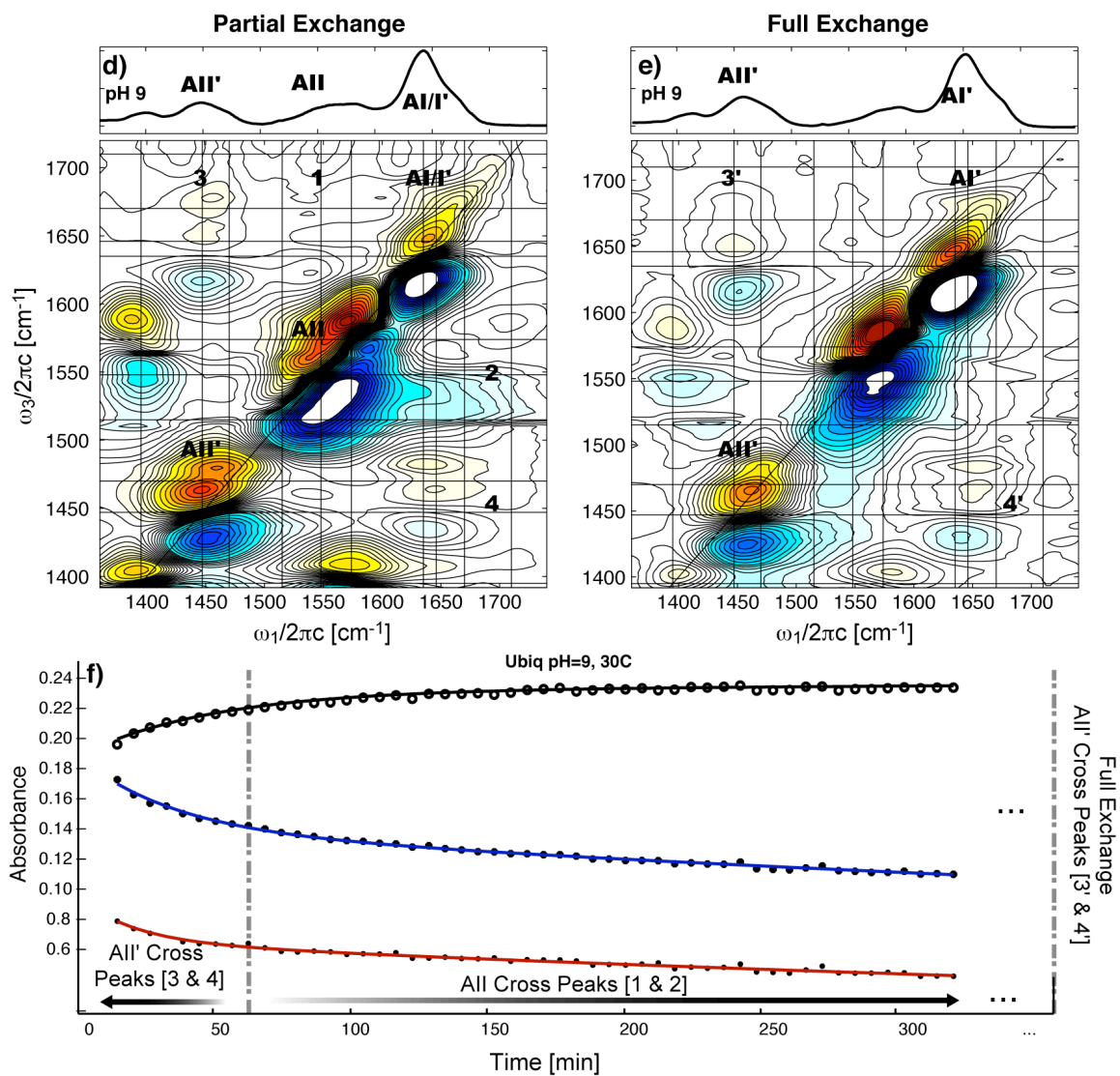


Fig. 8.1.2.2 ZZZY 2D IR Spectra of ubiquitin at pH = 9 (d, e) under partial exchange conditions (5°C) and after full exchange (heated to 80°C and cooled back to 5°C). FTIR kinetic traces of ubiquitin at pH 9 and 30°C. The amide II' cross peaks (3 and 4) report on secondary structure that has exchanged during sample preparation and data acquisition. The amide II cross peaks (1 and 2) report on solvent inaccessible regions of the protein.

In partially exchanged systems, it is likely that isolated amide protons will exchange in the secondary structure. The sensitivity of the amide II' band is derived from the orientation and coupling of nearest neighbors. Therefore, an isolated residue will take on a random coil signature in the amide II' diagonal; however, it will still couple to the secondary structure that it is imbedded in. The cross peak will scale with the product of the square of the transition dipole moments of amide II' and coupled amide I/I' mode. A participation factor, or the population of oscillators that have exchanged, will additionally scale this cross peak. For the case of a single amide proton in ubiquitin, this will be 1 in 76 amide unit. This result is the distinct ability to measure the kinetics of exchange by tracking the growth and disappearance of the cross peaks at a specific frequency versus time or temperature.

To further elucidate the stability of secondary structure elements of ubiquitin, pH dependent 2D IR spectra are taken under partial and full exchange. At pH 6.7, ubiquitin's isoelectric point, the protein is the most stable and has been shown to have melting points exceeding 100°C at higher pH.²³ Results of the FTIR study in Chapter 7, despite the increased stability of pH 9, it is seen that a greater number of amide units exchange rapidly in early time kinetics in sample preparation time.

Figures 8.1.2.1 and 8.1.2.2 shows the full 2D IR amide I/I'/II/II' spectrum of ubiquitin under partial exchange at 5°C and the fully exchange spectra at both pH 1 and 9. Glutamic acid has a symmetric and asymmetric mode at 1400 cm⁻¹ and 1586 cm⁻¹ at pH 9. For the partially exchanged spectra, peaks 1 and 2 are the amide I/I'-II upward and downward cross peaks. These peaks report on solvent inaccessible protons and, therefore, label amide protons that have not exchange prior to experimental acquisition

(approximately 60 minutes). Peaks 3 and 4 report on the amide protons that have exchanged and therefore solvent accessible regions. Peaks 3' and 4' of the fully exchange spectra (Fig. 8.1.2.1b and 8.1.2.2e) report on the coupling of amide I'-II' of the full protein. In these spectra, the amide II diagonal and off-diagonal peaks no longer exist.

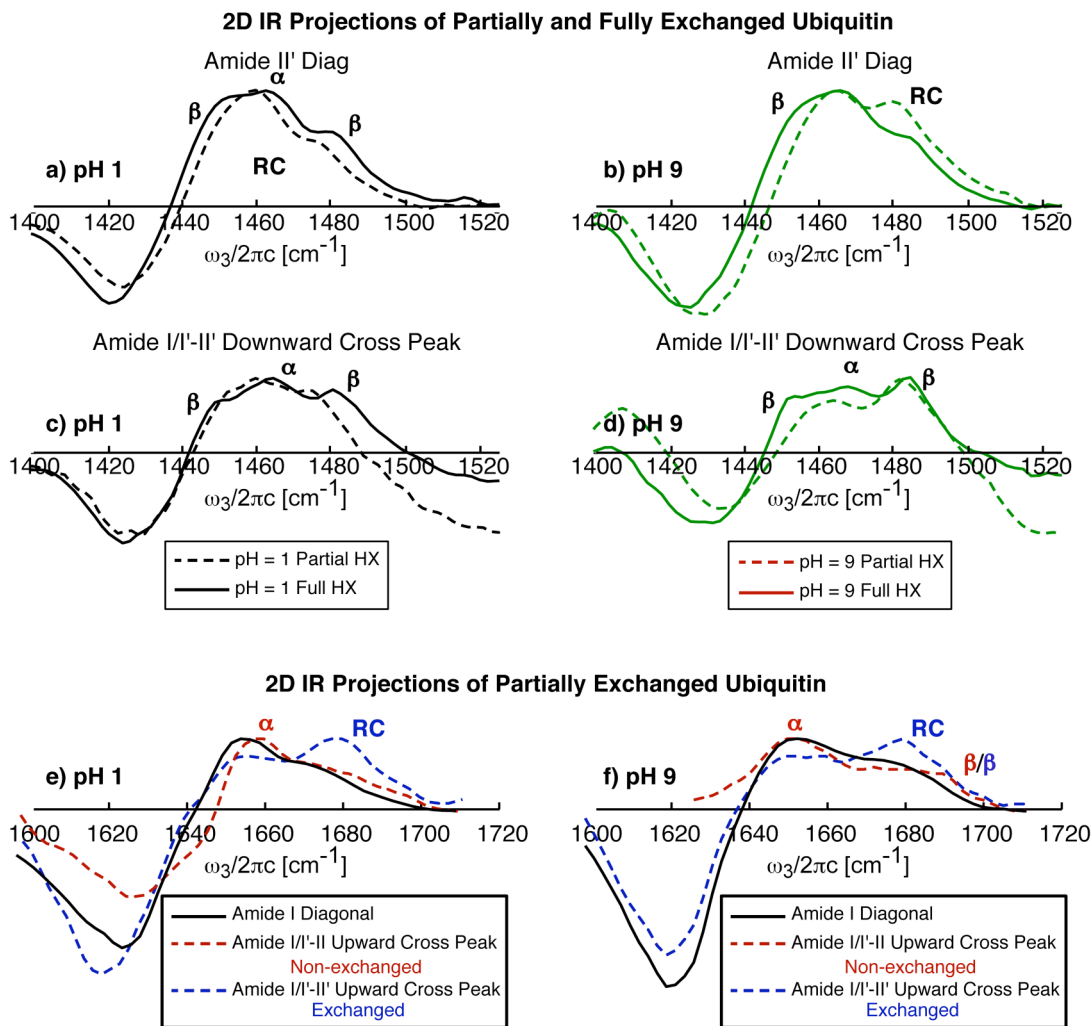


Fig. 8.1.2.3 (a-d) Projection along ω_1 axis of ZZYY 2D IR spectra of ubiquitin at pH = 1 (black) and pH 9 (green) under partial exchange conditions (5°C, dotted) and after full exchange (heated to 80°C and cooled to 5°C, solid). The changes to the projection of the amide II' diagonal (a,b), amide II' and amide I/I'-II' downward cross peak (c,d) show increase β -sheet structure. (e,f) Projection of the amide I' diagonal (black), amide I/I'-II' upward cross peak (red, dotted), amide I/I'-II' upward cross peak (blue, dotted) show partially exchange secondary structure.

Visual inspection of the partially exchanged 2D spectra (Fig. 8.1.2.1a and 8.1.2.2d), directly indicate that pH 9 has exchanged more readily than pH 1 in one hour. This can be seen by directly comparing the relative cross peak intensities of the upward amide II and II' bands (peaks 1 and 3).

To gain further insight into the regions of the protein that have exchanged, the structure of the cross peaks is analyzed. Projections of the amide II' diagonal and the amide I/I'-II and -II' cross peaks (1, 3, 4 and 4') are displayed in Fig. 8.1.2.3. Inspection of the amide II' diagonal for both pH 1 and 9 (Fig. 8.1.2.3 a and b) show a random coil line shape (Chapter 5). Therefore, there is no global exchange of secondary structure. This implies that only random coil regions of the protein, isolated amide units of protein secondary structure or both have exchanged. Upon full exchange, three additional peaks appear that correspond to the exchange of the β sheet (1440 cm^{-1} and 1484 cm^{-1} shoulders) and the α helix at 1470 cm^{-1} . The increased secondary structure content of the amide II' diagonal upon full exchange is also reflected in the upward cross peak seen as a shift of the combination band (negative peak) from 1450 cm^{-1} to 1458 cm^{-1} . This shift reflects the coupling of the deuterated α -helix.

The amide I/I'-II cross peaks (4 and 4') show similar features to the amide II' diagonal. Displacements of peaks along ω_1 projection onto the amide I band provide more insight into exchanged secondary structure. However, the signal-to-noise is insufficient in this data set. Alternatively, the upward cross peak provides identical information.

To determine if isolated residues in secondary structure have exchanged in these systems, the amide I/I' diagonal is compared to the amide I/I'-II and -II' cross peaks in

Fig. 8.1.2.3 e and f. The blue traces, or the amide I/I'-II' cross peak, reports on solvent exposed residues and show clear random coil signatures. As expected, the random coil regions are highly solvated and are expected to rapidly exchange. Additionally, the red traces, or the amide I/I'-II cross peak that report on solvent inaccessible residues, show clear helical features at 1655 cm^{-1} . Helices contain particularly strong hydrogen bonds, and for ubiquitin, the helix is an integral part of the hydrophobic core and is expected to exchange less rapidly due to structural stability. In the pH 9 projections, signatures of partial β -sheet exchange are seen as a small peak near 1690 cm^{-1} . Joining the signature of the amide II' diagonal and the appearance of β -sheet signature in both cross peaks reveals that isolated residues of the β sheet are exchanging. For the low pH system, the broadening seen between the red and blue trace at 1645 cm^{-1} suggests that a significant portion of the β sheet has exchanged. However, due to the structure of the amide II' diagonal, the number of sites exchange still does not provide the proper nearest neighbor structure of amide II' oscillators to generate substantial structural sensitivity.

To identify the residues that are susceptible to exchange, a molecular dynamics simulation of unconstrained ubiquitin at pH 2 in a bath of water is performed.²⁴ A 40 ps second trajectory with a 20 fs step size is analyzed. The distance between each amide proton and surrounding water molecules is calculated to established water proximity. Due to the time scale of the calculation, structural opening events are not observed. Therefore, a threshold of 3 \AA is set for amide proton to water distance. This represents the conditions in which a water molecule is capable of diffusing to the site and exchanging. Fig. 8.1.2.4 presents a histogram of the water proximity per residue number for ubiquitin. Black

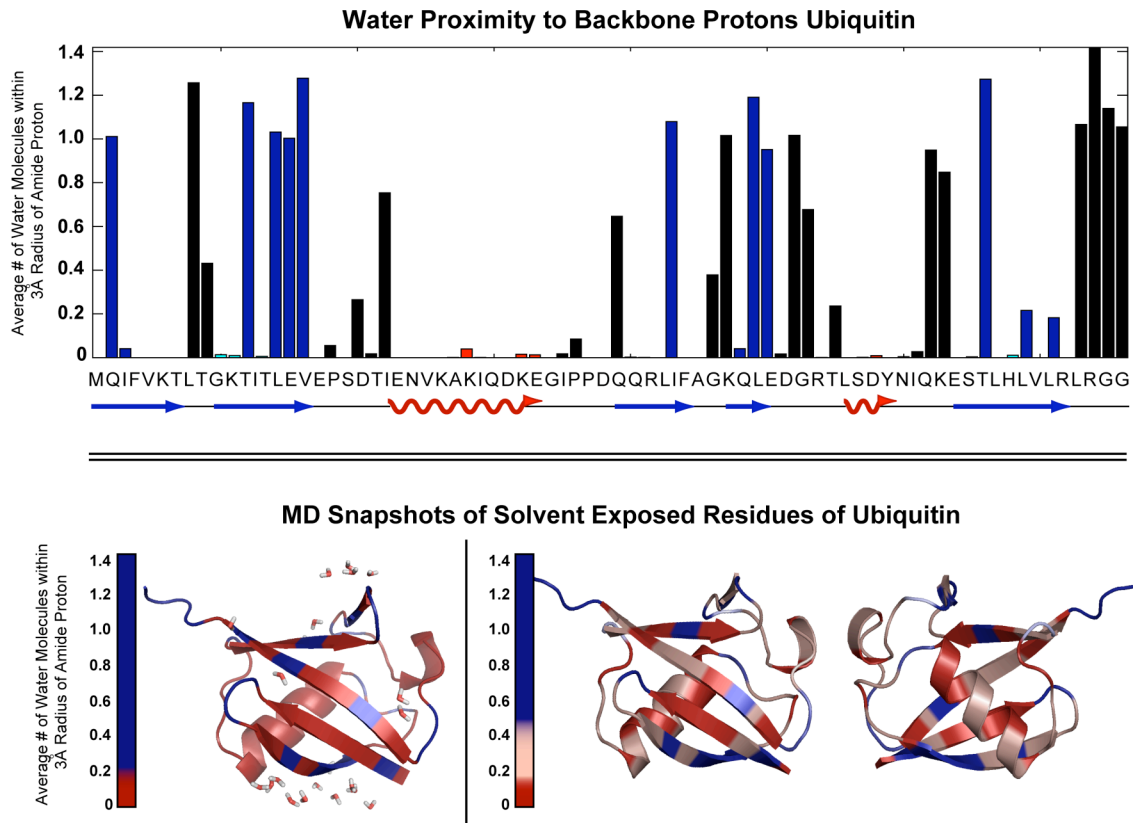


Fig. 8.1.2.4 Tabulated results of water proximity to amide backbone protons from a 40 ps molecular dynamics simulation of Ubiquitin. Bar-plot represents the fraction of water molecules within a 3Å radius of the amide proton. Visualization of the exchange sites is spatially mapped onto the Ubiquitin structure. Results show isolated residues have higher susceptibility to exchange.

represents residues in random coil regions, blue in β -sheet structures and red in α helices.

As expected, random coil regions are highly solvent exposed and helices are poorly solvated in ubiquitin. Below the histogram is a spatial map of water proximity projection onto the ubiquitin structure. The fraction represents the number of molecular within this radius over the simulation time. What is seen in this illustration is that alternating residues of the AP β sheet are more solvent accessible than their nearest neighbor. This arises from the alternating arrangement of the NH bond of the amide backbone. The helical view of the protein shows that only the external face of the helix is capable of

exchange due to water proximity, however, even with amide protons close to the water-protein interface, these sites can be highly protected by the secondary structure and hydrogen bonded contacts.

The joint results of the multi-mode 2D IR spectroscopy, FTIR study and molecular dynamics simulation reveal information about the secondary structure stability of ubiquitin. Mixed exchange of protons in secondary structure is expected based on their relative proximity to the protein surface and structural contacts. Helices are less likely to exchange but destabilization conditions will make them more susceptible to exchange. Ubiquitin is highly stabilized at high pH and exchange is inhibited on the long timescale by this structural stability. Internal protons will persist for days at room temperature. However, at early times, solvent exposed residues that are not only part of random coil regions, but also isolated residues of secondary structure exchange rapidly at pH 9. At low pH, very low exchange of the helix and partial exchange of the β sheet is observed.

In addition to the work on ubiquitin and general survey of proteins with other secondary structure moieties were performed. Figs. 8.1.2.5-8.1.2.8 show the hydrogen-exchange multi-mode spectra of a variety of proteins under partial exchange at 5°C. For each of these spectra, a single stripe was taken at a monochromator position of 1650 cm^{-1} . This provides minimal information about the secondary structure content of solvent accessible and inaccessible residues. It is important to note that the pH 7 solution was the only buffered solvent. It has been seen the buffers further catalyze exchange rates and this is universally seen in these spectra.²⁵

Structural fluctuations play an important role in enzyme-substrate binding. Concanavalin A is a sugar binding protein, therefore, understanding and charactering

structure fluctuations is of great scientific interest. pH dependent conformational changes have previously been studied with ORD and CD measurements. These results suggest that ConA taken on a random coil form at high pH.²⁶ The isoelectric point of Con A is 7.1²⁷ where it should exhibit the most structural stability to hydrogen exchange. Fig. 8.1.2.5 shows the hydrogen-exchange multi-mode 2D IR spectra of ConA at pH 1, 7(buffered) and 9. pH 1 and 7 show exceptionally stable secondary structure. The weak amplitude of the amide II' cross peak at pH 1 represents very little exchange of the amide protons. At pH 7, there is significant exchange of the random coil region; however, the projections show that very little β -sheet content has exchange. At pH 9, increase random coil structure is not observed but a considerable amount of exchange of the β -sheet structure is observed. This result implies that the secondary structure is more labile at high pH.

Myoglobin exhibits very different pH dependence relative to ConA. Myoglobin, a predominately α -helical protein, displays a broadened lines shape in the FTIR spectra of amide I at low pH. Line shape broadening is often attributed to structural heterogeneity. Results of Ymakova suggest that the tertiary structure of myoglobin is broken below pH 4.5 and above 11.5. ORD and CD results predict that nearly half the α -helical content is lost near pH 3.5 and 80% is maintained at a pH of 12.5.²⁸ These results are in good qualitative agreement with the spectra presented in Fig. 8.1.2.6. At low pH, 70% of the normalized cross peak intensity appears in the amide II' band. This implies that the helices are highly labile. At high pH, the opposite is observed; nearly 70% of the normalized intensity is observed in the amide II peak. This confirms more stable and intact secondary structure.

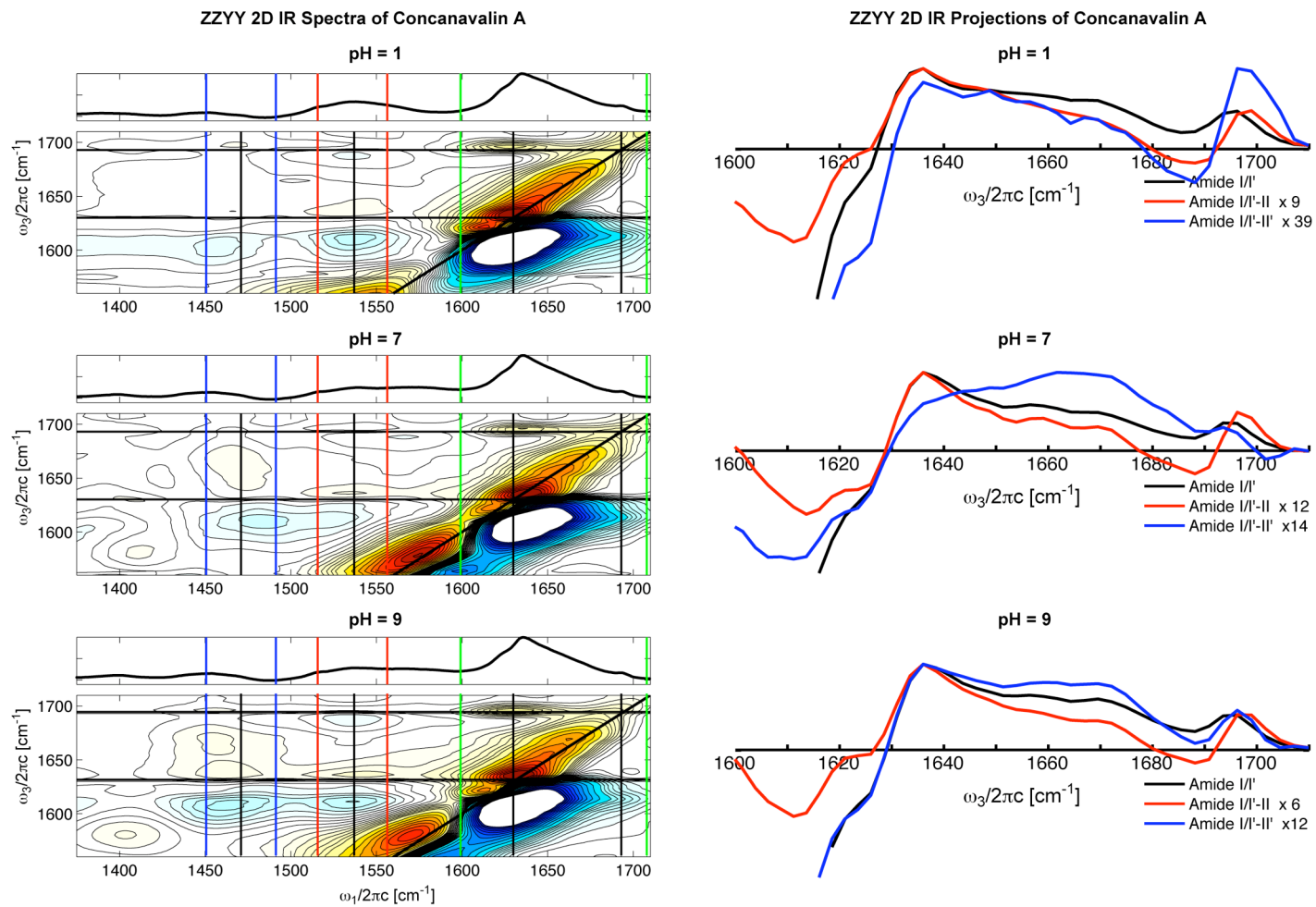


Fig. 8.1.2.5 pH dependence of the AI/II/II' 2D IR spectrum and amide I/I' (green/black), amide II (red), and amide II' (blue) projections of concanavalin A.

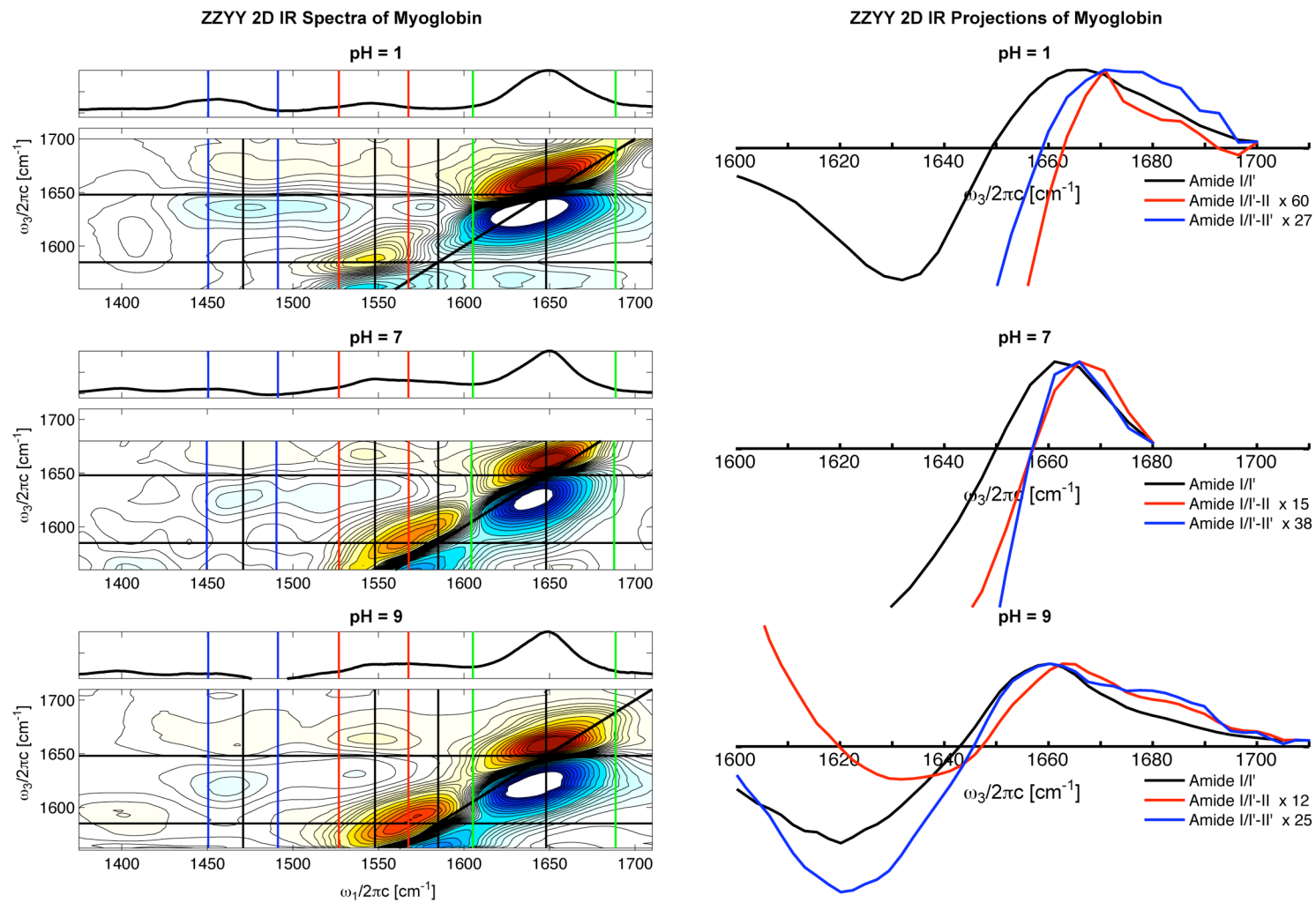


Fig. 8.1.2.6 pH dependence of the AI/II/II' 2D IR spectrum and projections of myoglobin.

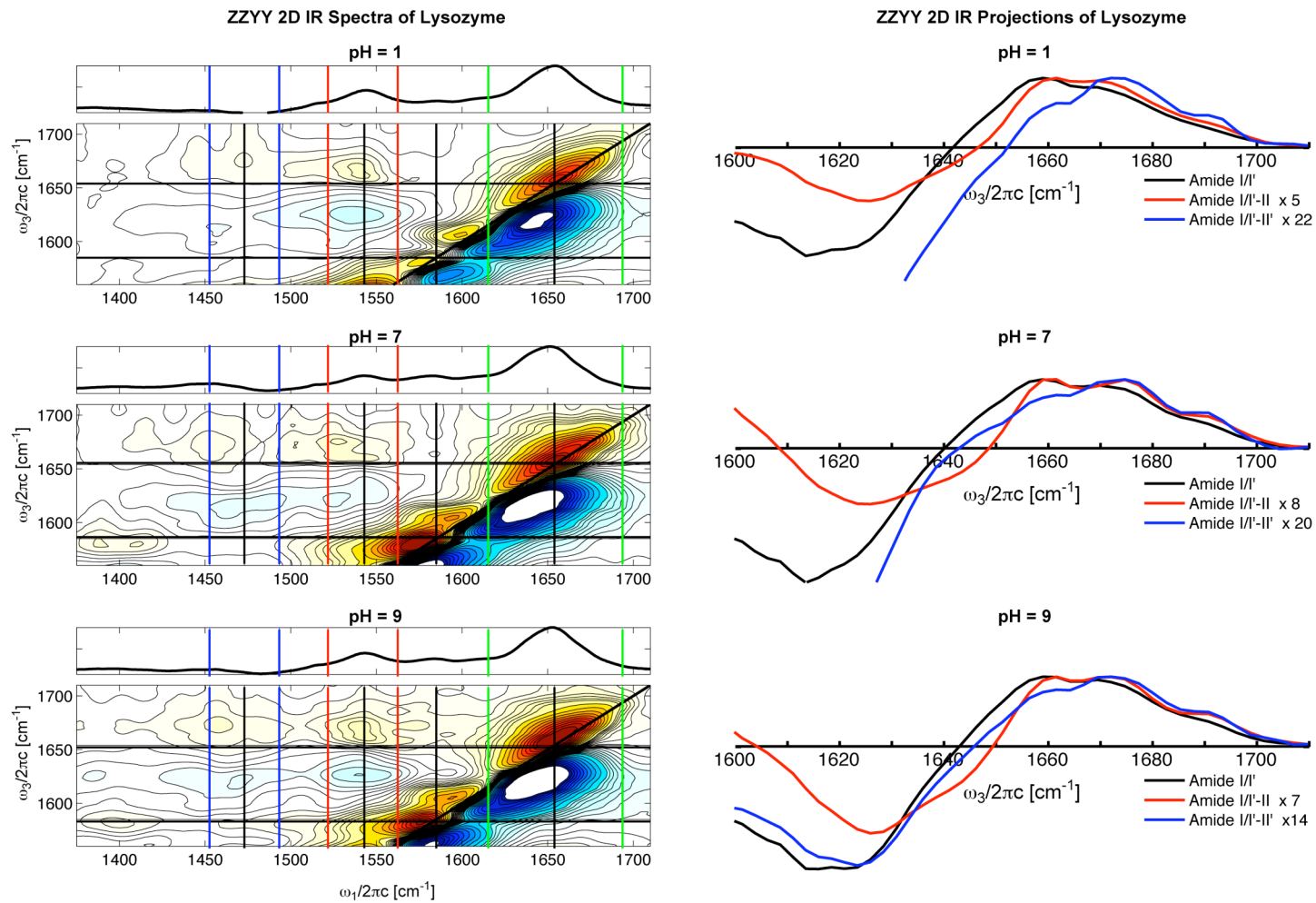


Fig. 8.1.2.7 pH dependence of the AI/II/II' 2D IR spectrum and projections of lysozyme.

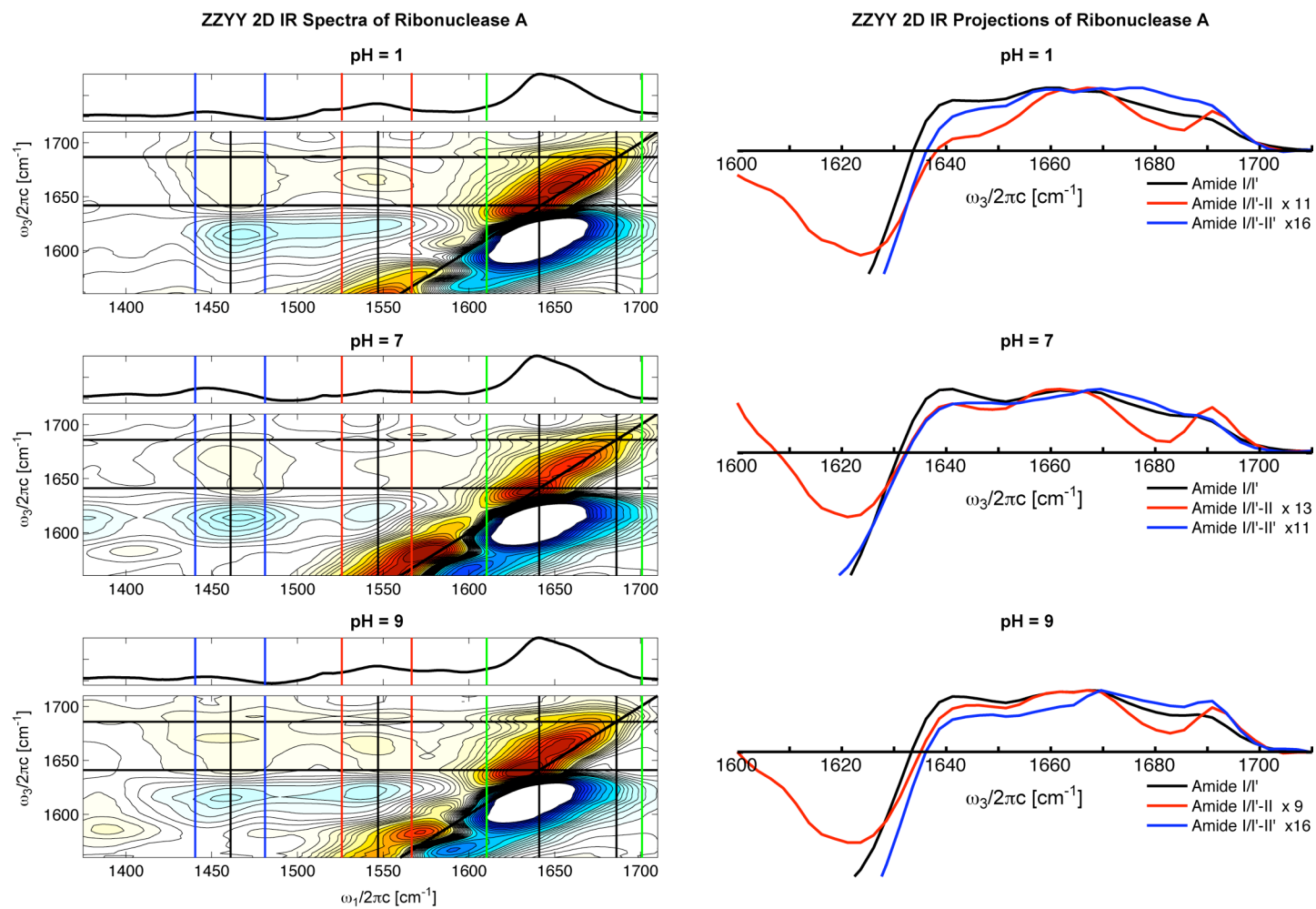


Fig. 8.1.2.8 pH dependence of the AI/II/II' 2D IR spectrum and projections of Ribonuclease A.

Lysozyme and RNaseA are mixed moiety protein containing both helix and β -sheet structures. Across the entire pH range observed in this experiment, lysozyme shows very similar structural stability with a minor increase in exchange at pH 7 (Fig. 8.1.2.7). RNaseA displays similar absolute cross peak intensity similarity to lysozyme. Across the entire pH range, RNaseA shows relatively little change in overall stability. However, at low pH, the relative intensity of the β -sheet and α -helix signatures show that the helix is stabilized at low pH and the β -sheet is more stable at high pH. At pH 9, clear signatures of helix and sheet are seen in the non-exchanged amide II cross peak (Fig. 8.1.2.8).²⁹

8.2 Looking Forward

In this thesis, a methodology for acquiring multi-mode 2D IR spectra to reveal questions about the structural dynamics and stability of proteins through HX experiments is demonstrated. The experimental framework for generation of broadband infrared lasers and a robust new approach to 2D IR spectroscopy has been established. Characterization of the multi-mode spectra was performed on model systems of the vibrational relaxation and coupling. Additionally, the structural sensitivity of the amide II' mode has been observed and quantified for the first time. Integration of these tools has allowed for the structural kinetics of ubiquitin to be observed. Hydrogen-exchange spectroscopy provides information about protein structural fluctuations and solvation through exchange of amide backbone protons.

To further the sensitivity of this measurement, and obtain secondary structure kinetics to reveal information about the mechanisms of exchange via global or sub-global unfolding, rapid acquisition of 2D IR surfaces is desired. Rapid scanning presented in Chapter 3 shows promise in system with sufficiently high signal-to-noise, particularly for

watching structural changes for diagonal resonances. In cases with limited signal-to-noise, 2D IR measurements can be performed with a “narrowband” pump ($<150\text{ cm}^{-1}$) and broadband probe ($>350\text{ cm}^{-1}$). The single pulse delay spectrum, with all pulses timed to zero, can be acquired as a function of time or temperature. This experiment directly generates the projections displayed in Fig. 8.1.2.4-8 in real time. Performing difference experiments, exchange of secondary structure can be observed with high resolution and the kinetics can be mapped to secondary structure. In the case of proteins with congested amide I line shapes, particularly those with mixed moieties, “narrowband” pump dispersed vibrational echo (DVE) measurements can be taken. It has been shown that DVE shows increased sensitivity to loss of secondary structural elements in temperature jump unfolding experiments of ubiquitin.³⁰ A narrowband central frequency of 1450 cm^{-1} will report on the appearance exchanged sites, 1550 cm^{-1} will report on the disappearance of these sites and 1650 cm^{-1} will define the secondary structure of the protein. This allows 2D IR kinetics to be acquired as seen in Chapter 7 for the FTIR measurements.

For exchange experiments in D_2O , the amide II' band will provide information about the binary state of exchange of secondary structure. If experiments are performed in H_2O with a deuterated protein, the amide II' diagonal will report on the exchange of “protected” secondary structure and what composes the most stable species. These experiments can be a simple measurement of the amide II' diagonal resonance. The loss of secondary structure components results from the exchange with the solvent. This approach allows for high signal-to-noise measurements to be made.

To access the exchange timescales faster than the preparation time, rapid mixing experiments need to be performed. Stopped flow experiments with mixing times of sub

ms will allow for faster timescales to be accessed.³¹ However, limited by the single to noise, flow experiments in which the sample probed is being replaced on the timescale of the laser repetition rate can be performed. Using coordinated ultrafast measurements, exchange timescales from microsecond to minutes can be acquired. Additionally, 2D IR spectroscopy has the capability of reporting on chemical exchange in which the time scales of the reaction is on the order of the lifetime of the molecular vibration being probed.³² With proper control of the chemical conditions, including pH and temperature, in a flow cell experiment, exchange of amide protons can directly be measured through the growth of the amide II-II' cross peak. This provides information on hydrogen-exchange on sub-nanosecond timescales.

Ultimately understanding the structural dynamics of proteins along a folding trajectory is desired. However, often the connection between structural stability at equilibrium does not directly translate into the relevant structural intermediates of a folding protein. A significant advance in HX NMR has shown promise in isolating folding structural intermediates through pulse labeling techniques.³ NMR spectra are taken of isolated intermediates, as a function of denaturation and pH, and provide an indirect measure of the folding pathway. Using the techniques described above, similar experiments can be performed with ultrafast optical measurements. Using the structural and protonation state sensitivity of the amide II' band, information about the structural unfolding of solvent exposed residues (in D₂O) and solvent inaccessible residues (in H₂O) can be addressed. Multi-mode two-dimensional infrared spectroscopy drastically improves the structural sensitivity of vibrational techniques through correlation of

vibrational sensitivities. This method allows for more detailed questions in protein dynamics and folding experiment to be answered on all relevant molecular timescales.

Acknowledgements

I would like to thank Rebecca Nicodemus for help in the acquisition of the amide I/I' /II/II' 2D IR spectra and Ziad Ganim for providing the MD simulation of ubiquitin.

References

- (1) Englander, S. W.; Sosnick, T. R.; Englander, J. J.; Mayne, L. C. *Curr. Opin. Struct. Biol.* **1996**, *6*, 18-23.
- (2) Grdadolnik, J.; Marechal, Y. *Applied Spectroscopy* **2005**, *59*, 1357.
- (3) Bai, Y. W.; Sosnick, T. R.; Mayne, L.; Englander, S. W. *Science* **1995**, *269*, 192.
- (4) Briggs, M. S.; Roder, H. *Proc. Natl. Acad. Sci. USA* **1992**, *89*, 2017-2021.
- (5) Krimm, S.; Bandekar, J. *Adv. Protein Chem.* **1986**, *38*, 181-364.
- (6) Dong, A.; Hyslop, R. M.; Pringle, D. L. *Arch. Biochem. Biophys.* **1996**, *333*, 275.
- (7) Wu, Y.; Murayama, K.; Ozaki, Y. *J. Phys. Chem. B* **2001**, *105*, 6251-6259.
- (8) Hamm, P.; Lim, M.; Hochstrasser, R. M. *J. Phys. Chem. B* **1998**, *102*, 6123-6138.
- (9) Woutersen, S.; Hamm, P. *Journal of Physics: Condensed Matter* **2002**, *14*, 1035.
- (10) Mukherjee, P.; Krummel, A. T.; Fulmer, E. C.; Kass, I.; Arkin, I. T.; Zanni, M. T. *Journal of Chemical Physics* **2004**, *120*, 10215-10224.
- (11) Mu, Y.; Stock, G. *J. Phys. Chem. B* **2002**, *106*, 5294-5301.
- (12) Jansen, T. I. C.; Knoester, J. *J. Phys. Chem. B* **2006**, *110*, 22910-22916.
- (13) Abramavicius, D.; Zhuang, W.; Mukamel, S. *J. Phys. Chem. B* **2004**, *108*, 18034.
- (14) Chung, H. S.; Tokmakoff, A. *Journal of Physical Chemistry B* **2006**, *110*, 2888.
- (15) Chung, H. S.; Khalil, M.; Smith, A. W.; Ganim, Z.; Tokmakoff, A. *Proc. Natl. Acad. Sci. USA* **2005**, *102*, 612-617.
- (16) Demirdöven, N.; Cheatum, C. M.; Chung, H. S.; Khalil, M.; Knoester, J.; Tokmakoff, A. *J. Am. Chem. Soc.* **2004**, *126*, 7981-7990.
- (17) Khalil, M.; Demirdöven, N.; Tokmakoff, A. *J. Phys. Chem. A* **2003**, *107*, 5258.

- (18) Golonzka, O.; Khalil, M.; Demirdöven, N.; Tokmakoff, A. *J. Chem. Phys.* **2001**, *115*, 10814-10828.
- (19) Barth, A.; Zscherp, C. *Q. Rev. Biophys* **2002**, *35*, 369-430.
- (20) Chirgadze, Y. N.; Fedorov, O. V.; Trushina, N. P. *Biopolymers* **1975**, *14*, 679.
- (21) DeFlores, L. P.; Ganim, Z.; Ackley, S. F.; Chung, H. S.; Tokmakoff, A. *J. Phys. Chem. B* **2006**, *110*, 18973-18980.
- (22) Hayashi, T.; Zhuang, W.; Mukamel, S. *J. Phys. Chem. A*, *109*, 9757-9759.
- (23) Loladze, V. V.; Makhatadze, G. I. *Protein Science* **2002**, *11*, 174-177.
- (24) Chung, H. S.; Ganim, Z.; Jones, K. C.; Tokmakoff, A. *Proc. Nat. Acad. Sci.* **2007**, *104*, 14237-14242.
- (25) Englander, S. W.; Downer, N. W.; Teitelbaum, H. *Annual Review of Biochemistry* **1972**, *41*, 903-924.
- (26) Zand, R.; Agrawal, B. B. L.; Goldstein, I. J. *PNAS* **1971**, *68*, 2173.
- (27) Agrawal, B. B. L.; Goldstein, I. J. *Biochim Biophys Acta* **1967**, *133*, 376-379.
- (28) Postnikova, G. B.; Komarov, Y. E.; Yumakova, E. M. *Eur. J. Biochem.* **1991**, *198*, 233-239.
- (29) Dong, A.; Hyslop, R. M.; Pringle, D. L. *Arch. Biochem. Biophys.* **1996**, *333*, 275.
- (30) Chung, H. S.; Khalil, M.; Tokmakoff, A. *J. Phys. Chem. B* **2004**, *108*, 15332-15343.
- (31) Fabian, H.; Naumann, D. *Methods* **2004**, *34*, 28-40.
- (32) Kwak, K.; Asbury, J.; Chen, X.; Piletic, I. R.; Fayer, M. D. *Science* **2005**, *309*, 1338-1343.

Appendix 1: Wedges

This appendix contains the design for the optical compression mounts and stage attachments for the ZnSe wedges used for temporal delay of the infrared pulses described in Chapter 2. The optical compression mounts are designed to apply minimum strain across the thin wedge surface to avoid stress induced index effects. Using point compression, via set screws, can cause local stress. Wedges are designed with minimal material to avoid material pulse dispersion. Compression mounts are designed to hold less than 2 mm of the total wedge. Silicon compression material that is 1 mm thick is used to grasp the wedges.

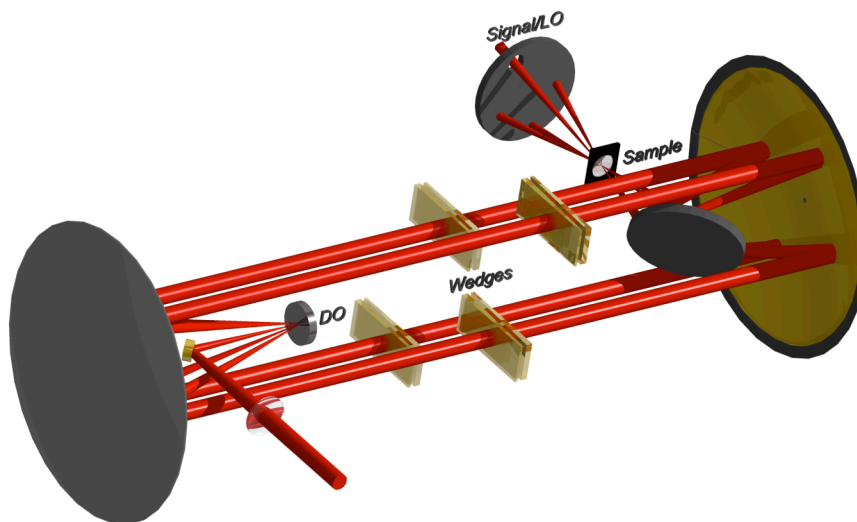


Fig A1.1 Full experimental set up of DO/Wedge 2D IR spectrometer

The wedge pair design in Fig. A1.1 produces an optical delay of $0.1 \mu\text{m}/\text{fs}$ when made of ZnSe which has an index of refraction of ~ 2.4 .

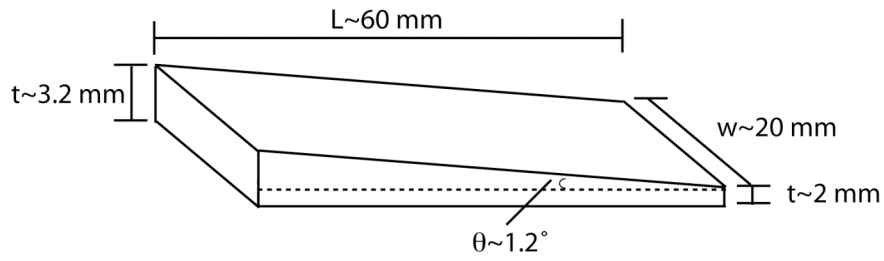


Fig A1.2 Design of the ZnSe wedge used to control pulse delay in experimental set up of Chapter 2.

Wedge Mounts [in]

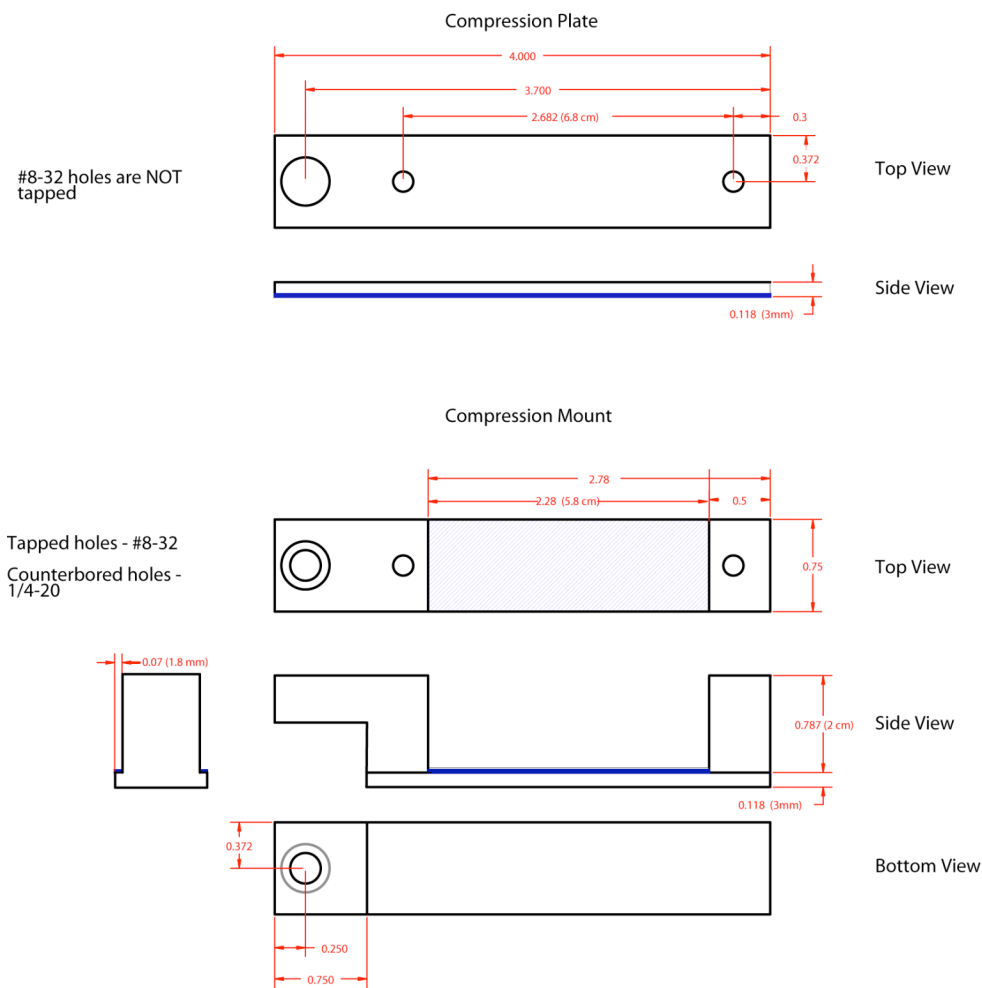
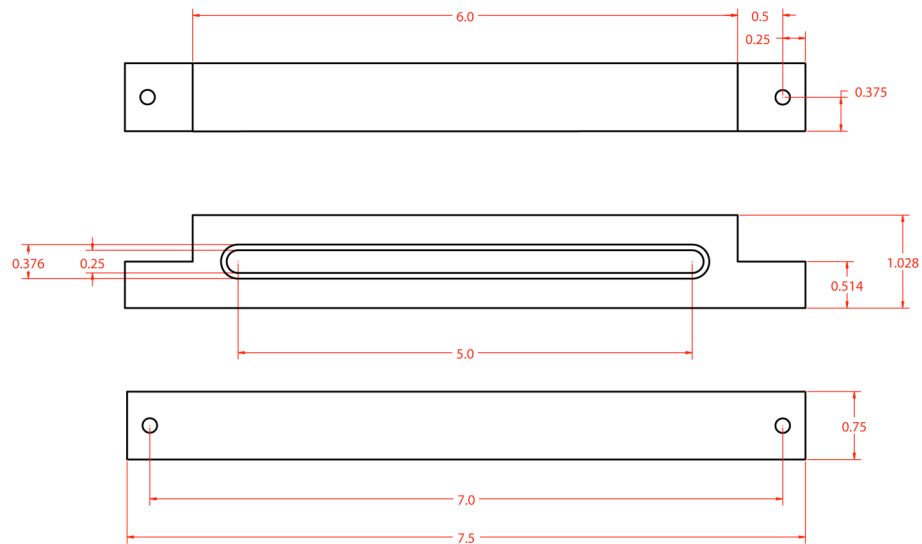


Fig A1.3 Compression mounts for thin wedges with bulk dimensions of 6 cm wide, 2 cm tall and >2 mm thick. Blue lines represent location of silicon compression material.

Horizontal Slide [in]

Cantilever beam to attach wedges to stages (4x)
1/4-20 tapped holes



Vertical Slide [in]

Mount to stage (4x)
1/4-20 tapped holes

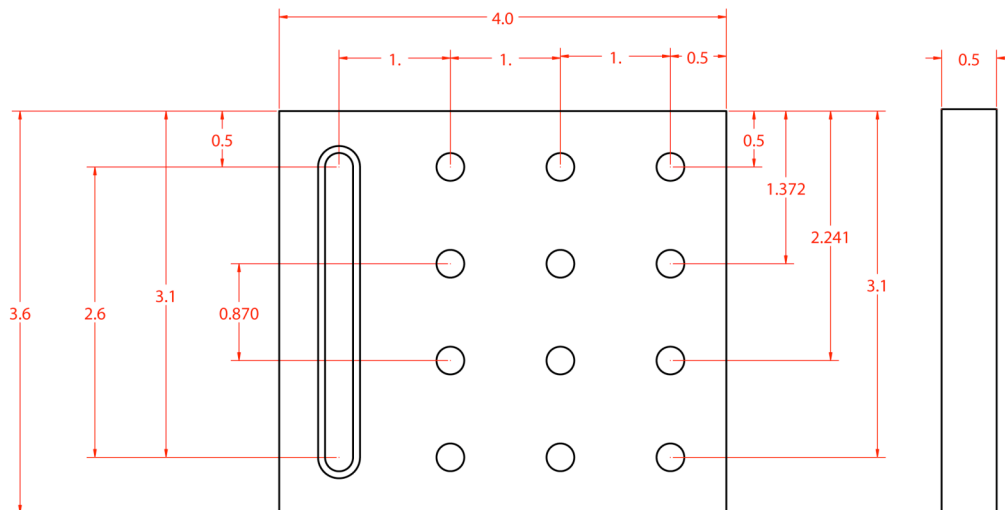


Fig A1.4 Design vertical and horizontal slides for mounting wedges to vertically mounted stages.

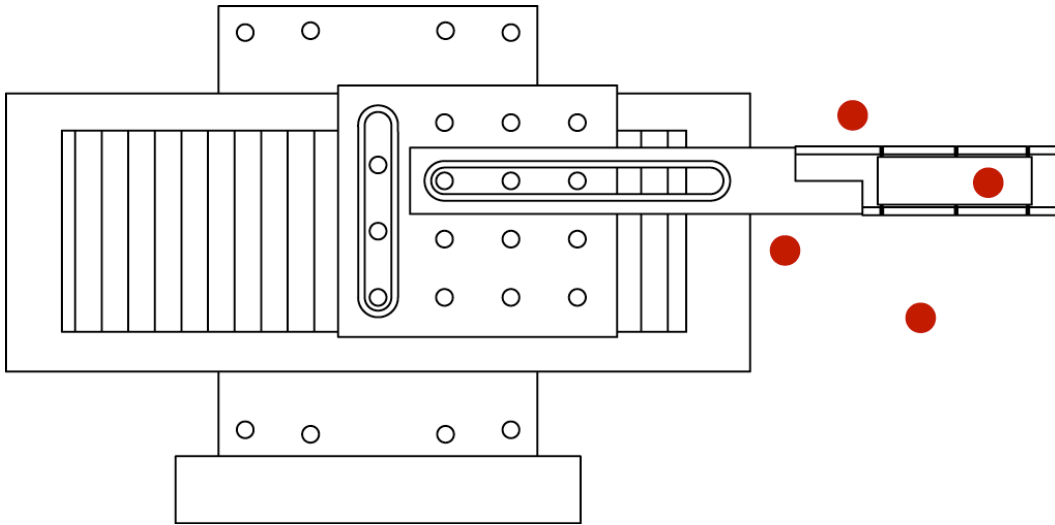


Fig A1.5 Full experimental set up of wedge mounts. The box geometry of the input laser beams is shown (red). The rotation of the box allows for full translation of the wedges.

Curriculum Vitae

856 Massachusetts Ave Apt. 7 • Cambridge, MA 02139
Office: (617) 253-7372 • deflores@mit.edu

Education

Massachusetts Institute of Technology Cambridge, MA

Ph.D. in Physical Chemistry, February 2008

Thesis: Multi-mode Two-dimensional Infrared Spectroscopy of Peptides and Proteins

Advisor: Andrei Tokmakoff

Cornell University Ithaca, NY

B.A. in Chemistry, Magna Cum Laude, January 2002

Honors Thesis: Nanofabrication of Ultra-floppy Silicon Cantilevers Advisor: John A. Marohn

Research

Department of Chemistry, MIT Cambridge, MA

Researcher, 2003-Present Advisor: Andrei Tokmakoff

- Constructed home-built two-dimensional infrared spectrometer including Ti:sapphire oscillator/amplifier, optical parametric amplifier (OPA) and laser diagnostics including second harmonic generation (SHG) autocorrelations and SHG and transient grating (TG) frequency-resolved optical gating (FROG) experiments.
- Designed and constructed a passively stabilized 2D IR spectrometer using diffractive optic interferometer using wedge delay lines and developed new method for acquisition of 2D IR spectra in the pump-probe geometry.
- Studied vibrational coupling and dynamics of peptides and proteins using femtosecond infrared vibrational spectroscopy including heterodyned detected two-dimensional infrared spectroscopy (2D-IR), photon echo spectroscopy and pump-probe spectroscopy.

NASA Centennial Challenge, DeltaX, Space Elevator Tether Team, MIT Cambridge MA

2006-Present

- Developing new material for Space Elevator Tether using carbon nanotube composites
- Skills include chemical synthesis of CNT and functionalization of materials, textiling of tether, chemical and characterization including Raman, tensile strength, and SEM.

George R. Harrison Spectroscopy Laboratory, MIT Cambridge MA

Researcher, 2002-2003 Advisor: Michael S. Feld

- Constructed a quantitative phase-contrast microscope using a spatial light modular (SLM) to reveal structural and dynamical information of Henrietta Lacks (HeLa) and whole red blood cells.

Cornell Nanofabrication Facility and Department of Chemistry, Cornell Ithaca, NY

Researcher, 2000-2002 Advisor: John A. Marohn

- Developed method for batch-fabrication of ultra-floppy silicon cantilevers for use in Magnetic resonance force microscopy (MRFM). Standard employed techniques including optical and e-beam photolithography, chemical vapor deposition, reaction ion etching, and critical point drying.
- Design and constructed a dual-fiber optic interferometer for use MRFM to measure cantilever deflections greater than one optical cycle.

Mars Exploration Rovers, NASA and Department of Astronomy, Cornell Ithaca, NY

Researcher, 1998-2002 Advisor: Steve Squyres and Jim Bell

- Involved in panoramic camera calibration at Jet Propulsion Laboratory, Pasadena, CA
- Develop panoramic camera and mission scenarios and procedures for pre-flight operations.
- Selected flight CCDs for panoramic, hazard avoidance and navigation cameras for the rovers.

Teaching

Massachusetts Institute of Technology, MIT Cambridge, MA
Laboratory Teaching Assistant, Fall 2002 and *Senior Laboratory Teaching Assistant*, Fall 2005

Honors/Awards

Magna Cum Laude, Cornell University 2002
American Microchemical Society Award, Undergraduate Award, 2001
National Society of Collegiate Scholars, Member since 1999

Presentations

1. **L. P. DeFlores**, and Andrei Tokmakoff, "Amide I-II Two-Dimensional Infrared Spectroscopy: Characterizing vibrational couplings and solvation of protein secondary structure" Time Resolved Vibrational Spectroscopy Conference (TRVS XIII), Freising, Germany 2007 (Talk)
2. **L. P. DeFlores**, Z. Ganim, S. F. Ackley and Andrei Tokmakoff, "Anharmonic Nature of the Amide I and II modes" Vibrational Gordon Research Conference, 2006 (Poster)
3. **L. P. DeFlores**, M. F. DeCamp, J. McCracken, and Andrei Tokmakoff, "Solvent effects on the vibrational dynamics of N-methylacetamide," Vibrational Gordon Research Conference, 2004 (Poster)

Publications

1. **L. P. DeFlores** and A. Tokmakoff, "Two Dimensional Fourier Transform Spectroscopy in the pump-probe geometry" *Opt. Lett.* , **32**, 2966 (2007).
2. Z. Ganim, H.S. Chung, A. Smith, **L. P. DeFlores**, K. Jones, and A. Tokmakoff, "Amide I Two-Dimensional Infrared Spectroscopy of Proteins" (Accepted, 2008, *Acc. Chem. Res.*)
3. M.F. Decamp, **L. P. DeFlores**, K. C. Jones, and A. Tokmakoff, "Single-shot two-dimensional infrared spectroscopy" *Opt. Exp.*, **15**(1), 233-241, (2007).
4. **L. P. DeFlores** and A. Tokmakoff, "Water penetration into secondary structure revealed by hydrogen-deuterium exchange 2D IR spectroscopy" *J. Am. Chem. Soc.*, **128**, 16520-16521, (2006).
5. G. Popescu, K. Badizadegan, **L. P. DeFlores**, R. R. Dasari, and M. S. Feld , "Characterization of cell motility by fourier phase microscopy" (Submitted, 2006).
6. **L. P. DeFlores**, Z. Ganim, S. F. Ackley, H. S. Chung, and A. Tokmakoff, "The anharmonic vibrational potential and relaxation pathways of the amide I and II modes of N-methylacetamide," Special Issue "Robert J. Silbey Festschrift" *J. Phys. Chem. B*, **110**, 18973, (2006).
7. M. F. DeCamp, **L. P. DeFlores**, J. M. McCracken, A. Tokmakoff, K. Kwac, and M. Cho, "Amide I vibrational dynamics of N-methylacetamide in polar solvents: The role of electrostatic interactions," *J. Phys. Chem. B*, **109**(21), 11016-11026, (2005).
8. G. Popescu, **L. P. Deflores**, J. C. Vaughan, K. Badizadegan, H. Iwai, R. R. Dasari, and M. S. Feld, "Fourier phase microscopy for investigation of biological structures and dynamics," *Opt. Lett.* **29**, 2503-2505, (2004).
9. N. E. Jenkins, **L. P. DeFlores**, J. Allen, T. N. Ng, S. R. Garner, S.Kuehn, J. M. Dawlaty, and J. A. Marohn, "Batch fabrication and characterization of ultra-sensitive cantilevers with sub-micron magnetic tips," *J. Vac. Sci. Tech. B*. **22**(3), 909-915, (2004).

Patents

L. P. DeFlores and A. Tokmakoff, "Two Dimensional Fourier Transform Spectrometer" (Patent Pending, 2007).